Progress in Oceanography
Article In Press
Acceptation date : October 2018
https://doi.org/10.1016/j.pocean.2018.10.012
https://archimer.ifremer.fr/doc/00461/57290/

Prospects for Future Satellite Estimation of Small-Scale Variability of Ocean Surface Velocity and Vorticity

Chelton Dudley B. [1, *], Schlax Michael G. [1], Samelson Roger M. [1], Thomas Farrar J. [2], Jeroen Molemaker M. [3], McWilliams James C. [3], Gula Jonathan [4]

[1] College of Earth, Ocean and Atmospheric Sciences, Oregon State University, Corvallis, USA
[2] Woods Hole Oceanographic Institution, Woods Hole, USA
[3] Institute of Geophysics and Planetary Physics, Department of Atmospheric and Oceanic Sciences, University of California, Los Angeles, USA
[4] Université de Brest, CNRS, IRD, Ifremer, Laboratoire d'Ocanographie Physique et Spatiale, IUEM, Brest, France

* Corresponding author : Dudley B. Chelton

Abstract :

Recent technological developments have resulted in two techniques for estimating surface velocity with higher resolution than can be achieved from presently available nadir altimeter data: 1) Geostrophically computed estimates from high-resolution SSH measured interferometrically by the wide-swath altimeter on the Surface Water and Ocean Topography (SWOT) Mission with a planned launch in 2021; and 2) Measurements of ocean surface velocity from a Doppler scatterometer mission that is in the early planning stages, referred to here as a Winds and Currents Mission (WaCM). In this study, we conduct an analysis of the effects of uncorrelated measurement errors and sampling errors on the errors of the measured and derived variables of interest (SSH and geostrophically computed velocity and vorticity for SWOT, and surface velocity and vorticity for WaCM). Our analysis includes derivations of analytical expressions for the variances and wavenumber spectra of the errors of the derived variables, which will be useful to other studies based on simulated SWOT and WaCM estimates of velocity and vorticity. We also discuss limitations of the geostrophic approximation that must be used for SWOT estimates of velocity. The errors of SWOT and WaCM estimates of velocity and vorticity at the full resolutions of the measured variables are too large for the unsmoothed estimates to be useful. It will be necessary to smooth the data to reduce the noise variance. We assess the resolution capabilities of smoothed estimates of velocity and vorticity from simulated noisy SWOT and WaCM data based on a high-resolution model of the California Current System (CCS). By our suggested minimum threshold signal-to-noise (S/N) variance ratio of 10 (a standard deviation ratio of 3.16), we conclude that the wavelength resolution capabilities of maps of velocity and vorticity constructed from WaCM data with a swath width of 1200 km are, respectively, about 60 km and 90 km in 4-day averages. For context, the radii of resolvable features are about four times smaller than these mesoscale wavelength resolutions. If the swath width can be increased to 1800 km, the wavelength resolution capabilities of 4-day average maps of surface velocity and vorticity would improve to about 45 km and 70 km, respectively. Reducing the standard deviation of the uncorrelated measurement errors from the baseline value of m s−1 to 0.25 m s−1 would further improve these resolution capabilities to about 20 km and 45 km. SWOT data will allow mapping of the SSH field with far greater accuracy and space-time resolution than are presently

achieved by merging the data from multiple nadir altimeter missions. However, because of its much narrower120-km measurement swath compared with WaCM and the nature of the space-time evolution of the sampling pattern during each 21-day repeat of the SWOT orbit, maps of geostrophically computed velocity and vorticity averaged over the 14-day period that is required for SWOT to observe the full CCS model domain are contaminated by sampling errors that are too large for the estimates to be useful for any amount of smoothing considered here. Reducing the SSH measurement errors would do little to improve SWOT maps of velocity and vorticity. SWOT estimates of these variables are likely to be useful only within individual measurement swaths or with the help of dynamic interpolation from a data assimilation model. By our criterion, in-swath SWOT estimates of velocity and vorticity have wavelength resolution capabilities of about 30 km and 55 km, respectively. In comparison, in-swath estimates of velocity and vorticity from WaCM data with m s−1 have a wavelength resolution capability of about 130 km for both variables. Reducing the WaCM measurement errors to m s−1 would improve the resolution capabilities to about 50 km and 75 km for velocity and vorticity, respectively. These resolutions are somewhat coarser than the in-swath estimates from SWOT data, but the swath width is more than an order of magnitude wider for WaCM. Instantaneous maps of velocity and vorticity constructed in-swath from WaCM data will therefore be much less prone to edge effect problems in the spatially smoothed fields. Depending on the precise value of the threshold adopted for the minimum S/N ratio and on the details of the algorithm used to smooth the SWOT and WaCM data, the resolution capabilities summarized above may be somewhat pessimistic. On the other hand, aspects of measurement errors and sampling errors that have not been accounted for in this study will worsen the resolution capabilities presented here. Another caveat to keep in mind that the resolution capabilities deduced here from simulations of the CCS region during summertime may differ somewhat at other times of year and in other geographical regions where the signal variances and wavenumber spectra of the variables of interest differ from the CCS model used in this study. Our analysis nonetheless provides useful guidelines for the resolutions that can be expected from SWOT and WaCM.

Keywords : Satellite Oceanography, Wide-Swath Altimetry, Doppler Scatterometry, Submesoscale Variability, Mesoscale Variability, Sea Level Measurement, Surface Current Measurement, Relative Vorticity, Geostrophic Approximation

1. Introduction

Presently available global sea-surface height (SSH) fields constructed from satellite altimeter data by Collecte Localis Satellites (CLS) and archived by Archivage, Validation, Interprétation des données des Satellite Océanographiques (AVISO) are able to resolve time scales of about a month and wavelength scales of about 200 km, corresponding to feature radius scales of about 50 km (see Appendix A.3 of Chelton et al., 2011). The 25+ year CLS/AVISO record of SSH fields (Pujol et al., 2016) has been extremely useful for studies of mesoscale eddies, large-scale ocean circulation variability and sea level rise (e.g., Fu et al., 2010; Lee et al., 2010; Willis et al., 2010; Chelton et al., 2011). Notwithstanding the many successful applications of this dataset, it is clear from high-resolution numerical simulations and satellite infrared and visible observations of sea surface temperature (SST) and ocean chlorophyll that energetic variability exists on smaller scales than can be resolved by the CLS/AVISO SSH fields. Of particular interest are wavelength scales smaller than ∼50 km (radius scales less than ∼10 km), which is a commonly used definition for submesoscale variability. Numerical models have shown that submesoscale variability is important to the physics and biology of the ocean (e.g., Capet et al., 2008; Klein and Lepeyre, 2009; Lévy et al., 2001). There is thus a strong interest in high-resolution satellite observations of surface velocity and its associated vorticity to complement the modeling. The objective of this study is to investigate the prospects for future high-resolution satellite measurements of small-scale velocity and vorticity variability.

In addition to the interest in submesoscale variability, much remains to be learned about mesoscale ocean dynamics. Velocity and vorticity can be estimated geostrophically from the CLS/AVISO SSH fields, but with a very coarse spatial resolution imposed by the ∼200 km wavelength resolution limitation of the SSH fields. The improved resolution that is anticipated from the two satellite technologies considered in this study is likely to advance understanding of mesoscale variability in a manner similar to the advances achieved from the CLS/AVISO multi-altimeter merged SSH dataset compared with the single-altimeter observations obtained from TOPEX/Poseidon (see, for example, Fig. 1 of Chelton et al., 2011).

Our particular interest here in satellite estimation of surface velocity and vorticity is motivated in part by their effect on local wind-driven vertical velocities (Ekman pumping). It is well known that surface

*Corresponding author

currents contribute to Ekman pumping in mesoscale eddies through their effects on the relative wind and hence the surface stress. The surface velocity within a rotating eddy generates a curl of the surface stress with sign opposite that of the vorticity of the eddy, thus attenuating the eddy and generating an Ekman pumping velocity that is often larger on mesoscales and smaller scales than that from the curl of the large-scale background wind stress field (e.g., Dewar and Flierl, 1987; Martin and Richards, 2001; McGillicuddy et al., 2007; Gaube et al., 2015). Mesoscale eddies also generate Ekman pumping to an even greater degree through their effects on the gradient of the total vorticity (planetary plus relative vorticity) that generates horizontal divergences of Ekman transport and hence vertical velocities (Stern, 1965; Mahadevan et al., 2008; McGillicuddy et al., 2008; Gaube et al., 2015). This vorticity-gradient-induced Ekman pumping is sometimes referred to as nonlinear Ekman pumping. The two effects of surface currents on Ekman pumping increase rapidly with decreasing scale and increasing Rossby number (see Fig. 7 of Gaube et al., 2015). A small-scale cutoff for this increase presumably exists, but both effects are likely important into at least the upper range of submesoscale variability.

Determination of Ekman pumping on mesoscale and smaller scales thus depends critically on accurate knowledge of the surface ocean velocity at these scales. Recent technology developments have resulted in two techniques for estimating ocean surface velocity that promise higher resolution than is presently achieved from the CLS/AVISO SSH fields. One of these is the Surface Water and Ocean Topography (SWOT) Mission (Alsdorf et al., 2007; Fu and Ferrari, 2008) that is slated for launch in 2021. SWOT will measure SSH altimetrically by radar interferometry (Fu and Rodríguez, 2004) with a footprint size of about 1 km. Surface velocity can then be estimated geostrophically. The other technology for estimating ocean surface velocity is based on the Doppler shift of radar returns from the moving sea surface (Chapron et al., 2005; Rodríguez et al., 2018). An important distinction of Doppler radar systems is that they provide direct measurements of ocean surface velocity, rather than the indirect estimates computed geostrophically from measurements of SSH as in the case of SWOT.

Satellite-based Doppler radar systems for measuring surface ocean currents are in the early stages of development, both in Europe and in the U.S. The European Doppler scatterometer mission concept summarized by Chapron et al. (2005) has evolved to a proposed Doppler radar system called the Sea surface KInematics Multiscale (SKIM) mission (Ardhuin et al., 2018) that has been designed to measure surface currents, ice drift and ocean waves across a swath width of 270 km. A primary goal of SKIM is to measure the wave spectrum. The incidence angles of the SKIM radar measurements have therefore been chosen to be 6° and 12° in order to maximize the sensitivity to surface wave tilt while minimizing the sensitivity to winds. The SKIM radar thus cannot measure surface vector winds.

The Doppler radar in the mission under development in the U.S. will have a much wider measurement swath than SKIM (at least 1200 km, and possibly as much as 1800 km) and will measure radar backscatter at much higher incidence angles that will provide collocated measurements of surface currents and vector winds, but not the wave spectrum. Wind speed and direction are inferred from the roughness of the sea surface by conventional scatterometry (see, for example, Sec. 2 of Chelton and Freilich, 2005, for a summary of the QuikSCAT scatterometer). An aircraft version called DopplerScatt has been built by the National Aeronautics and Space Administration Jet Propulsion Laboratory (NASA/JPL) and has been flown in several field campaigns (Rodríguez et al., 2018) as a proof of concept for a future satellite Doppler scatterometer mission that we refer to in this study as a Winds and Currents Mission (WaCM). In the recent decadal survey of recommended Earth-observing satellite missions by the National Academies of Sciences, Engineering, and Medicine (NASEM, 2018), WaCM was identified as one of seven candidate NASA Earth System Explorer missions. The anticipated performance of WaCM that is assumed in this study (see Sec. 4.2) is supported by the actual performance of the airborne DopplerScatt instrument (Rodríguez et al., 2018).

The collocated WaCM measurements of surface currents and vector winds are expected to have footprint sizes of about 5 km. For the wind measurements, this is much smaller than the footprint sizes of about 25 km for the QuikSCAT and ASCAT scatterometers. The smaller footprint size for WaCM will be achieved with a larger antenna size and the use of a Ka-band radar (35.8 GHz), rather than the Ku-band radar (13.4 GHz) used for QuikSCAT or the C-band radar (5.3 GHz) used for ASCAT. This study considers only the surface ocean velocity estimates. Our baseline simulations of WaCM measurements of surface currents assume a swath width of 1200 km. Recent engineering studies suggest that it may be possible to broaden the swath

width to 1800 km, which would greatly improve the sampling compared with the simulations of WaCM data in this study. The benefits of the wider swath width are investigated as part of this study.

The viability of SWOT and WaCM estimates of surface velocity for investigation of small-scale variability clearly depends on the signal-to-noise ratios of the measurements (SSH for the case of SWOT and surface velocity for the case of WaCM). For SWOT, the utility of the data also depends on the validity of the geostrophic approximation. The objectives of this study are to investigate these issues and assess the resolution capabilities for mapping of the surface velocity and vorticity fields for both SWOT and WaCM. The approach is based on simulated SWOT and WaCM sampling of, respectively, the SSH and surface velocity fields from 30 days of twice-daily snapshots from a high-resolution model of the California Current System (CCS).

Our focus is on the limitations imposed by the baseline science requirements for the cross-swath averaged standard deviations of uncorrelated instrumental measurement errors. In reality, the instrumental errors for both SWOT and WaCM vary across the measurement swaths (see Fig. F1 in Appendix F for the case of SWOT), with smallest errors near the centers of the swaths and increasing errors towards both edges of the swaths. The measurement errors also depend on the significant wave height (see again Fig. F1 for the case of SWOT). The significant wave height (SWH) dependence and cross-track variations of the instrumental errors are not considered in the simulations presented in this study. Rather, we consider the cross-swath average instrumental measurement errors for the conditions of 2-m significant wave height that are specified for the baseline design requirements of the measurement errors.

We note that the error characteristics of SWOT data could have been simulated more accurately and completely for this investigation by using the simulator software available from the SWOT Project Office (Gaultier et al., 2017; see also Qiu et al., 2016; and Gaultier et al., 2016). Simulator software is not available for WaCM. Moreover, the dependencies of WaCM measurement errors on swath location and SWH have not yet been fully quantified, although it is known that WaCM measurement errors will increase toward the edges of the measurement swaths in a manner similar to the cross-track variations of SWOT measurement errors. For consistency in our treatments of SWOT and WaCM measurement errors, we have therefore chosen to use our simpler simulations of SWOT measurement errors to be consistent with our simulations of WaCM measurement errors.

Measurements from both SWOT and WaCM are also subject to larger-scale errors from geophysical corrections for a variety of environmental effects. While important, these larger-scale errors are not addressed in the analysis presented here as they are generally secondary to the effects of uncorrelated instrumental errors for the purposes of estimating surface velocity and vorticity on the mesoscales and submesoscales that are of primary interest in this study.

We are also not able to address the importance of internal gravity waves, which are underrepresented in the CCS model used to simulate SWOT and WaCM data in this study (see Secs. 2 and 3). This internal wave variability is one of several ageostrophic processes that affect the accuracy of SWOT estimates of surface velocity and vorticity. The contributions of ageostrophic processes to contamination of geostrophically computed surface velocity and vorticity from SWOT measurements of SSH cannot be fully assessed from the CCS model used in this study since it was forced with seasonally varying winds, heat fluxes and freshwater fluxes. This issue is addressed to a limited degree in Sec. 3 and Appendix F (see Figs. 10, 11 and F4 below) from a pair of simulations of the Gulf Stream region off the southeastern seaboard of the U.S.

We note that the seasonally forced CCS model that is used in this study may also misrepresent larger-scale geostrophic processes. Mesoscale and submesoscale variability might be stronger with more realistic wind forcing that includes synoptic atmospheric variability. The analysis presented here is based on model simulations for a 30-day period in early summertime. Since weather systems over the CCS are usually not very energetic at this time of year, inclusion of synoptic atmospheric forcing may have only modest effects on the model simulation for the geographical location and time of year considered here. This potential limitation of the model should nonetheless be kept in mind in the interpretation of the results presented in this study.

Because of the various aspects of measurement errors summarized above that are not taken into consideration in this study, the conclusions about the effects of measurement errors presented here are likely somewhat optimistic assessments of the resolution capabilities of SWOT and WaCM. On the other hand, if

the uncorrelated instrumental errors can be reduced from the baseline science requirement values used in our simulations, the effects of instrumental errors in the simulations presented here may prove to be somewhat pessimistic assessments of the resolution capabilities for the baseline consideration of 2-m significant wave height.

The ability to map the space-time evolution of the surface velocity field also depends on the swath width over which the measurements are made. For SWOT, the swath width will be 120 km with a nadir gap of 20 km. For the analysis in Sec. 8, we have assumed that velocity estimates will be obtained by WaCM across a swath width of 1200 km with a nadir gap of 100 km. The sampling coverage in each satellite overpass of a given region will thus be more than an order of magnitude better for WaCM than for SWOT. The SWOT orbit will have an exact repeat period of 21 days. For the simulations in this study, we have assumed that WaCM will have the same 4-day repeat orbit as QuikSCAT. The net effect of the different swath widths and orbit repeat periods for SWOT and WaCM is that a given location within the CCS region considered here is sampled on average about once a day by WaCM and about once a week by SWOT (see Sec. 7). Extending the WaCM swath width to 1800 km with the same nadir gap of 100 km would increase the sampling to an average of about 1.5 samples per day over the CCS model domain. Our analysis includes an assessment of the impact of this improved sampling on the resolution capability of space-time smoothed velocity and vorticity fields constructed from WaCM data.

The resolution limitations of maps of geostrophically computed surface velocity and vorticity constructed from simulated SWOT data have previously been considered by Fu and Ubelmann (2014), Qiu et al. (2016) and Gaultier et al. (2016). In this study, we extend these previous investigations of the resolution capabilities of simulated SWOT data and compare the results with the resolution capabilities of maps of velocity and vorticity constructed from simulated WaCM data. Our approach is more systematic than has been used in past studies. In particular, we propose a specific criterion for defining resolution capability and we partition the mapping errors between instrumental measurement errors and sampling errors. By sampling errors, we mean the errors in mapped fields of surface velocity and vorticity that are imposed by the limited swath widths of the SWOT and WaCM measurements and by the discrete and irregular temporal sampling of the rapidly evolving submesoscale features in the velocity and vorticity fields at a given location. The ability to distinguish between measurement and sampling errors in maps constructed from simulated satellite data provides insight into the relative benefits of reducing the measurement noise versus improving the sampling, either by increasing the measurement swath widths or by combining the measurements from multiple satellites.

This paper is organized as follows. The CCS model from which simulated SWOT and WaCM data are obtained is summarized in Sec. 2. The limitations of the geostrophic approximation that must be used for SWOT estimates of surface velocity and vorticity are discussed in Sec. 3. The uncorrelated measurement errors for SWOT and WaCM and their effects on the errors of the derived quantities (geostrophically computed velocity and vorticity for SWOT and vorticity for WaCM) are examined in detail in Sec. 4, including determination of the wavenumber spectral characteristics of the errors.

The strategy adopted in this study to assess the resolution capabilities for estimates of surface velocity and vorticity from noisy SWOT and WaCM data is presented in Sec. 5. The procedure is first applied in Sec. 6 to instantaneous maps of the velocity and vorticity fields constructed from SWOT and WaCM data for the idealized case of measurement errors alone without consideration of sampling errors from the limited swath widths of the SWOT and WaCM measurements. This analysis of the effects of measurement errors alone can be interpreted as the best possible resolution capabilities within a single measurement swath.

For mapping of the velocity and vorticity fields over regions larger than the width of an individual measurement swath, sampling errors can be as important as, or even more important than, measurement errors to the overall accuracies of the mapped variables. The space-time sampling characteristics of SWOT and WaCM data are summarized in Sec. 7. The combined effects of measurement and sampling errors on the resolution capabilities of maps of surface ocean velocity and vorticity estimated from space-time smoothed SWOT and WaCM data are then investigated in Secs. 8–10.

The conclusion of Sec. 8 is that the resolutions of maps of geostrophically computed velocity and vorticity constructed from SWOT data are limited almost totally by sampling errors. Improving the SWOT measurement accuracy would therefore have very little effect on the resolution capabilities of the variables

considered in this study. The resolutions of maps of velocity and vorticity constructed from WaCM data are primarily limited by measurement errors but sampling errors are not negligible. The benefits of increasing the WaCM swath width (thus reducing the sampling errors) and reducing the WaCM measurement noise are investigated separately and in combination in Sec. 10.

Supporting technical details for the calculations in Secs. 4, 6 and 8–10 are provided in a series of nine appendices.

The error analysis in Sec. 4 merits special mention since the results will be useful to other studies. Analytical expressions for the variances of the errors of SWOT estimates of velocity and vorticity computed geostrophically from SSH are derived in Appendix G.1 in terms of the variance σ_h^2 of the uncorrelated errors of pre-processed SWOT estimates of SSH. By "pre-processed", we mean the satellite data that will be distributed to general users after smoothing of the raw data onboard the satellite, possibly with additional ground-based smoothing to achieve a specified footprint size. The numerical results presented in this study are based on the SSH error standard deviation of $\sigma_h = 2.74$ cm that is derived in Appendix F for the case of pre-processed data with a footprint size of 1 km. It would be straightforward to obtain numerical results from the analytical expressions for any specified value of σ_h.

An analytical expression for the variance of errors of WaCM estimates of vorticity is similarly derived in Appendix G.2 in terms of the variances σ_u^2 and σ_v^2 of the uncorrelated errors of WaCM estimates of each orthogonal velocity component u and v. The result is therefore valid for any application of WaCM data, given specifications of the velocity component error variances. The analysis in this study assumes an equal error standard deviation of $\sigma_{u,v} = 0.354$ m s^{-1} for each velocity component. If the errors of the two velocity components are uncorrelated with each other, this corresponds to current speed errors with a standard deviation of $\sigma_{spd} = 0.50$ m s^{-1}, which is the present baseline design for WaCM.

Our analysis includes determinations of the wavenumber spectral characteristics of errors of velocity and vorticity computed geostrophically from pre-processed SWOT measurements of SSH, as well as the wavenumber spectral characteristics of velocity components and vorticity estimated from pre-processed WaCM data. Analytical expressions for these wavenumber spectra are derived for SWOT and WaCM in Appendix I.1 and Appendix I.3, respectively. Analytical expressions are also derived in Appendix I.2 and Appendix I.4 for the wavenumber spectra of all of the variables of interest after 2-dimensional smoothing is applied in simulated ground-based post-processing. As with the equations for the error variances discussed above, the equations derived in Appendix I for the error spectra are all expressed in terms of the measurement error variances σ_h^2 for SWOT and σ_u^2 and σ_v^2 for WaCM. The results are therefore valid for any specification of the uncorrelated errors of SWOT and WaCM measurements of SSH and surface velocity.

Throughout this study, the surface vorticity fields are computed from the components of the total velocity fields from simulated WaCM data and from the components of surface velocity fields computed geostrophically from simulated SWOT data. We are also interested in the surface ocean velocity fields themselves, which are characterized here by the magnitude of the total or geostrophically computed vector surface velocity field, rather than by the vector component fields. For the 4-day and 14-day time averages considered in Secs. 8–10, the analysis is based on the magnitudes of the vector averaged velocity fields. While it would be straightforward to consider each velocity component separately constructed from instantaneous maps and time averages of simulated SWOT measurements of SSH and WaCM measurements of surface velocity, the results are more difficult to interpret than the scalar velocity magnitude field because of the highly anisotropic and geographically inhomogeneous nature of the velocity field in the CCS region. Because the velocity errors are random in each component, direction errors will generally decrease as the signal-to-noise ratio of satellite estimates of velocity magnitude increases.

2. The CCS Model

A detailed description and validation of the CCS model used in this study can be found in Molemaker et al. (2015). Since the model representation of submesoscale variability is an important consideration for simulating SWOT and WaCM data in this investigation, a summary of the model is provided here. The computational code was ROMS, the Regional Oceanic Modeling System (Shchepetkin and McWilliams,

2005; 2009), which solves the hydrostatic primitive equations for the velocity, potential temperature, and salinity with a seawater equation of state. To simulate local flows in a realistic large-scale environment, the model was configured for the CCS utilizing open boundary conditions and a sequence of three nested subdomains (Marchesiello et al., 2003; Penven et al., 2006).

Because the primary target is submesoscale currents with horizontal scales of < 10 km near the eastern topographic slope, an aggressive approach to nesting was taken with successively finer resolution in a sequence of steps where each "child" grid utilizes "parent" grid data at the open boundaries of the regional domains (Mason et al., 2010). The procedure consists of off-line, one-way nesting from larger to finer scales without feedback from the child grid solution onto the parent grid. It is implicitly assumed that a numerical "zoom" around a specific phenomenon is valid when it has an essentially local dynamical behavior, albeit with important influences from its environment of basin and regional circulation.

Bottom topography was defined from the SRTM30-plus bathymetry dataset based on the 1-minute Smith and Sandwell (1997) global dataset but using higher resolution data where available. A Gaussian smoothing kernel with a width of 4 times the topographic grid spacing was applied to avoid aliasing wherever the topographic data are available at higher resolution than the computational grid. The maximum depth for all grids was set to 6000 m, which is not a serious distortion for the U.S. west coast region. Models formulated with a terrain-following coordinate such as ROMS have computational restrictions with regard to the steepness and roughness of the topography (Beckmann and Haidvogel, 1993). Where the steepness of the topography exceeded these criteria, additional local smoothing was applied. The above procedure results in topography that is increasingly well resolved in the nested grids with successively higher resolution but may differ significantly from the original data in the coarser grids. Following Mason et al. (2010), the topography near the boundaries of the nested domains is matched with the parent topography.

The largest-scale simulation used in this study covers the full Pacific basin (see Fig. 1 of Molemaker et al., 2015). This grid, as well as the nested grids described below, is orthogonal based on an oblique Mercator projection and designed to have nearly uniform spacing in both horizontal dimensions. For the Pacific basin, the grid spacing varies from 12.5 km at the central latitude of the grid to 8.5 km at the north and south extremes of the grid near 40°S and 55°N; this is comparable to what is used in global mesoscale eddy-resolving models.

The simulation was forced at the surface by the QuikSCAT-based mean-monthly Scatterometer Climatology of Ocean Winds (SCOW; Risien and Chelton, 2008), and monthly heat and freshwater fluxes from the Comprehensive Ocean-Atmosphere Data Set (COADS; Da Silva et al., 1994), using a weak feedback from SST (Barnier et al., 1995). The open boundary information and initial state were taken from the Simple Ocean Data Assimilation monthly climatology (SODA; Carton and Giese, 2008). The model SST fields have both gyre-scale contrasts and mesoscale eddy fluctuations visible in regions of high SST gradients (see Figs. 1 and 2 in Molemaker et al., 2015; see also Figs. 1 and 2 below).

The Pacific basin model was spun-up from interpolated SODA data for 2 years, by which time an approximate statistical equilibrium was reached for kinetic energy. The model was then run for an additional 10 years. The mean-monthly climatology over this 10 years was used to force the first nested grid along the U.S. west coast (see Fig. 2 of Molemaker et al., 2015) at its open boundaries. The climatological monthly boundary information from SODA forced the outermost Pacific basin model with a seasonal cycle. Mesoscale eddy activity was passed through boundary conditions to the first nested grid with an update time scale of five days. The successive nested models were boundary forced at increasingly shorter time scales, with boundary updates every 12 hours for the CCS nested model analyzed in this study (see below). This was verified by comparing maps of surface eddy kinetic energy with altimetry-derived eddy kinetic energy. With open boundary conditions in nested grids, it is important to avoid computational artifacts associated with boundary-trapped features (e.g., rim currents) and noisy fields. In the ROMS-to-ROMS nesting interface, these artifacts are largely avoided, even for realistic flows with high mesoscale activity (Mason et al., 2010).

The three nested grids along the U.S. west coast are rotated by a polar angle of 24° so that the x and y axes are aligned approximately cross-shore and alongshore, respectively. As with the grid for the full Pacific basin, each of the three nested grids is discretely orthogonal, and they vary even less in their spacing over their relatively smaller domains. The first nested subdomain has a grid spacing that varies from 4 km to 3.97 km. The grids for the two smaller domains have average horizontal spacings of 1.5 km, and 0.5

km, respectively. The successive levels of grid refinement spontaneously exhibit an increasing amount of submesoscale variability (c.f., Capet et al., 2008).

The importance of the grid resolution for model representation of the submesoscale variability in the inner nested grid is readily apparent from Fig. 1. Submesoscale variability in the SST and vorticity fields is visibly much more energetic with a grid spacing of 0.5 km, even compared with a grid spacing of 1.5 km. The choice of model grid resolution is clearly an important consideration in the assessment of the resolution capabilities of SWOT and WaCM estimates of surface velocity and vorticity. This issue is discussed further in Sec. 11.

In all of the grids, there were 40 stretched vertical levels with a resolution of a few meters near the surface. The time step was 1600 sec for the full Pacific basin model with ∼10 km grid spacing and decreased to 600 sec, 240 sec and 90 sec for the nested models with successively smaller grid spacings of 4 km, 1.5 km and 0.5 km, respectively. Dissipation was imposed in the model by a hyper viscous term, which is a by-product of the 3rd-order upwind advection. The effective hyper viscosity scales with the local velocity and the grid scale. The stepping procedure also includes a damping term that is much smaller than the hyper viscous term.

An important point for this study is that the high dissipation in the model significantly attenuates internal gravity waves compared with observations. While the internal gravity wave energy increases with the increased resolution of each nested grid, it is much weaker than in the real ocean, even at the highest grid resolution. In addition to the high dissipation, the lack of high-frequency atmospheric forcing and the absence of ocean tidal forcing contribute to the weak internal gravity wave energy in the CCS model used in this study. The effects of higher internal gravity wave energy are briefly considered in Sec. 3 from a pair of models of the Gulf Stream region off the southeastern seaboard of the U.S., one with weak internal waves like the CCS model used here and the other with energetic internal waves forced by high-frequency winds and tides (see Figs. 10 and 11 below).

For the investigation of the resolution capabilities of SWOT and WaCM in this study, we consider only the inner nested model, which extends from Point Conception in the south to approximately the Oregon/California border in the north. There are 1200×1800 grid points. With the 0.5-km grid spacing of this inner nested model, this corresponds to 600 km in the cross-shore dimension by 900 km in the alongshore dimension. For the analysis in this study, we consider only the 30-day period from day 141 to day 171, which corresponds to the early summertime period from 21 May through 20 June when submesoscale variability is fully developed. The climatological average wind stress field for the month of June is shown in the right panel of Fig. 2. For this study, the model output was subsampled at intervals of 0.5 days. It will be seen from Fig. 24 below that this sample interval is too coarse to fully resolve the rapidly evolving submesoscale variability. Since the time interval between successive measurements by both SWOT and WaCM is longer than this (see Sec. 7), the rapid evolution of submesoscale variability is even less well resolved in the satellite data.

A representative map of the model SST field on 5 June is shown in the left panel of Fig. 2 for the full domain of the 0.5-km inner nested model in latitude-longitude coordinates. The map reveals a rich distribution of scales of variability. The cold water near the coast is associated with wind-driven upwelling forced by the summertime equatorward winds. The meandering ribbon of upwelled cold water that separates from the coast at the northern corner of the model domain is the core of the equatorward flowing California Current. Submesoscale features are evident along SST fronts throughout the model domain.

The speed and vorticity of the surface currents associated with the SST field in Fig. 2 are shown in the rotated model grid coordinates in Fig. 3. The relative vorticity $\zeta = \partial v/\partial x - \partial u/\partial y$ (referred to hereafter as just the vorticity) was computed from the cross-shore (u, positive onshore) and alongshore (v, positive poleward) velocity components using centered differences on the 0.5 km $\times$ 0.5 km model grid. Except in the alongshore wavenumber spectra in Figs. 13–15 below, the vorticity is normalized throughout this study by the local Coriolis parameter f at each grid point. A mesoscale anticyclonic eddy can be seen in the northwest corner of the Central California Current System (CCCS) region in the bottom panels of Fig. 3. Two additional mesoscale anticyclones and a mesoscale cyclone can be seen in the northwest corner of the full CCS model domain in the top panels. Most of the rest of the model domain is dominated by submesoscale variability, the most energetic of which is associated with the core of the meandering equatorward-flowing

California Current that separates from the coast near Cape Blanco, just to the north of the model domain. Energetic submesoscale features are also associated with two offshore jets, one near the center of the model domain and the other near the southern boundary of the model.

The highly energetic vorticity field at submesoscales in Fig. 3b can be quantified by characterizing the scale dependence of the distribution of the magnitude of the normalized vorticity ζ/f, which can be interpreted as a Rossby number. The scale dependence of $|\zeta|/f$ was determined by isotropic smoothing of the map in the top panel of Fig. 3b using a Parzen smoother (see Appendix A) with successively longer half-power filter cutoff wavelengths ranging from 0 to 150 km. To reduce edge effects in the smoothed fields along the northern, southern and offshore boundaries of the model domain, the analysis throughout the remainder of this study was restricted to the region delineated by the black lines in both panels of Fig. 2.

The distributions of $|\zeta|/f$ from the smoothed fields of normalized vorticity are shown in Fig. 4a as a function of the half-power filter cutoff wavelength of the smoothing. The four solid lines correspond to the 80^{th}, 90^{th}, 95^{th} and 99^{th}-percentile points of the cumulative probability distribution of $|\zeta|/f$. The root mean squared (RMS) value of $|\zeta|/f$ is about 0.5 in the unsmoothed field and decreases to about 0.1 at large scales (see the dashed line in Fig. 4a) and coincides approximately with the 80^{th} percentile point of the distribution at all scales. It would correspond to the 68^{th}-percentile if the distribution were Gaussian. The distribution of Rossby numbers $|\zeta|/f$ in the unsmoothed fields is thus long-tailed toward large magnitudes with values exceeding 0.85 at about 5% of the grid points and exceeding 1.7 at about 1% of the grid points. The high values of $|\zeta|/f$ are concentrated geographically in the regions of strongest ocean velocity (see Fig. 3). Much of the small-scale variability in these regions is thus highly nonlinear and ageostrophic. The long-tailed nature of the distributions of $|\zeta|/f$ decreases rapidly with increasing scale. All of the percentile points and the RMS decrease very slowly for filter cutoff wavelengths longer than about 100 km.

From a close inspection of the vorticity maps in Fig. 3b, it can be seen that small-scale features with positive vorticity are more intense than their counterparts with negative vorticity. This is most easily seen from the enlargement in the bottom panel of Fig. 3b. This asymmetry of the vorticity distribution is quantified as a function of scale in Fig. 4b. At the full resolution of the model grid, the vorticity is skewed toward positive values. This skewness decreases with increasing scale, becoming very small for half-power filter cutoff wavelengths longer than about 50 km. The average values of ζ/f are very close to zero at all scales (see the dashed line in Fig. 4b).

3. Limitations of Geostrophically Computed Velocity

The high incidence of large Rossby numbers $|\zeta|/f$ at small scales in Fig. 4a is indicative of limitations of the validity of the geostrophic approximation. This is investigated in this section from comparisons of the surface currents and vorticity from the total velocity field (as in Fig. 3) with the surface currents and vorticity computed geostrophically from the model SSH fields[1]. The derivatives for the geostrophically computed velocity components $u_g = -gf^{-1}\partial h/\partial y$ and $v_g = gf^{-1}\partial h/\partial x$ were approximated using centered differences of sea surface height h on the 0.5 km $\times$ 0.5 km model grid. The geostrophically computed vorticity $\zeta_g = \partial v_g/\partial x - \partial u_g/\partial y$ was then approximated using centered differences of the geostrophically computed velocity components. Maps of SSH, the magnitudes of geostrophically computed surface velocity and normalized geostrophically computed vorticity are shown in Fig. 5.

To the untrained eye, the existence of energetic submesoscale variability is not easily discerned in the SSH map in Fig. 5a. The preponderance of highly energetic submesoscale variability evident in the map of normalized geostrophically computed vorticity in Fig. 5c attests to the extreme spatial high-pass filtering effects of double differentiation of the SSH fields. Irrespective of the validity of the geostrophic approximation, the ability to estimate vorticity from SWOT measurements of SSH clearly depends critically on the magnitudes of small-scale errors in the SSH measurements. This is investigated in Sec. 6 from consideration

[1]For estimation of surface velocity from SWOT data, it is important to distinguish the velocity computed from SSH data by the geostrophic equations from the truly geostrophic velocity that is valid only for small Rossby number. To clarify this subtle but pedagogically important point, we use the somewhat cumbersome terminology "geostrophically computed velocity" rather than "geostrophic velocity."

of uncorrelated measurement errors alone. The added effects of sampling errors from the limited swath width and discrete overpass times of the SWOT satellite on maps of the spatially and temporally evolving velocity and vorticity fields computed geostrophically from space-time smoothed simulated SWOT data are considered in Sec. 8. In this section, we consider only error-free SSH fields and their spatial derivatives.

Qualitatively, the geostrophically computed surface current speed and the normalized geostrophically computed vorticity in Figs. 5b and c look very similar to the surface current speed and normalized vorticity in Figs. 3a and b that were computed from the total velocity. The vector differences between the total and geostrophically computed surface velocity (referred to hereafter as the ageostrophic velocity[2]) are shown in Fig. 6. From the unsmoothed velocity differences in Fig. 6a, it can be seen that the ageostrophic velocity field on large scales is dominated by the expected wind-driven surface Ekman velocity associated with the climatological wind stress used to force the model. The ageostrophic velocity field smoothed using a Parzen smoother with a half-power filter cutoff wavelength of 150 km is shown in Fig. 6b. These large-scale ageostrophic velocity vectors are predominantly aligned approximately 52° to the right of the equatorward alongshore direction, which is at least qualitatively consistent with expectations from the equatorward alongshore winds during the early summertime period considered in this study (see the right panel of Fig. 2). The magnitudes of these large-scale ageostrophic currents are typically about 0.1 m s^{-1}. For the purposes of the analysis in this section, we will define the 150-km smoothed ageostrophic velocity field in Fig. 6b to be the wind-driven Ekman velocity.

The small-scale features in the ageostrophic velocity field in Fig. 6a that are superimposed on the large-scale wind-driven Ekman velocity field in Fig. 6b coincide with the regions of energetic submesoscale variability noted above from Figs. 3 and 5. This becomes apparent after subtracting the 150-km smoothed ageostrophic velocity field in Fig. 6b from the unsmoothed ageostrophic velocity field in Fig. 6a. The magnitudes of the resulting "non-Ekman ageostrophic velocities" (Fig. 6c) often exceed 0.05 m s^{-1} and differences in excess of 0.15 m s^{-1} are common in regions of the CCS with energetic submesoscale variability.

The scale dependence of the non-Ekman ageostrophic velocities is shown in Fig. 7 for the CCCS region after isotropic smoothing using a Parzen smoother with selected half-power filter cutoff wavelengths ranging from 10 to 80 km. The non-Ekman ageostrophic features diminish in magnitude rather slowly with increasing scale because of the tight clustering of small-scale features. The residual non-Ekman ageostrophic velocities exceed 0.1 m s^{-1} in many small-scale features, even after smoothing with a half-power filter cutoff wavelength of 40 km. Several patches of non-Ekman ageostrophic velocities of 0.3 m s^{-1} still exist with the maximum smoothing of 80 km shown in the bottom right panel of Fig. 7. Bearing in mind the gradual rolloff of the filter transfer function of the Parzen smoother (see Appendix A), the magnitudes of the band-pass filtered non-Ekman ageostrophic velocities in Fig. 7 must be considered lower-bound estimates of the true values. The imperfections of the band-pass filtering become progressively more of an issue as the filter cutoff wavelength approaches the 150 km filter cutoff used to define the Ekman ageostrophic velocity in Fig. 6b from which the smoothed non-Ekman ageostrophic velocity magnitudes in Fig. 7 were derived by band-pass filtering.

The statistics of the scale dependence of the magnitudes of the non-Ekman ageostrophic velocities are summarized in Fig. 8 from the 80^{th}, 90^{th}, 95^{th} and 99^{th}-percentile points in the distributions of the magnitudes of the non-Ekman ageostrophic velocities over the full CCS model domain as functions of half-power filter cutoff wavelength. On all scales, the RMS value corresponds very closely to the 80^{th}-percentile point in the distributions. The distributions of smoothed residual non-Ekman velocities are thus long-tailed toward large magnitudes, especially at small scales. In the unsmoothed fields, the RMS value of the magnitudes of the non-Ekman ageostrophic velocities is about 0.05 m s^{-1} and values in excess of 0.1 m s^{-1} occur at about 5% of the grid points over the full CCS model domain. It is evident from Fig. 6c that high non-Ekman ageostrophic velocities are highly inhomogeneous geographically, occuring over much higher percentages of the grid points within the regions of most energetic submesoscale variability.

[2]The attribution "ageostrophic velocity" is not strictly correct. Some of the apparent velocity structures computed geostrophically from SSH are not representative of actual features in the velocity field. For example, the geostrophically computed velocity field associated with a long-crested internal gravity wave consists of opposing parallel velocity jets that straddle the wave crests and troughs. This is a glaring misrepresentation of the surface manifestation of internal wave velocities. This contamination of SWOT estimates of the surface velocity field is discussed in more detail at the end of this section.

As expected from the maps in Fig. 7, the distribution points of the magnitudes of residual non-Ekman ageostrophic velocities decrease rather slowly with increasing scale. Even after smoothing with a half-power filter cutoff wavelength of 50 km, for example, values in excess of 0.02 m s^{-1} and 0.05 m s^{-1} occur at, respectively, about 20% and 2% of the grid points over the full CCS model domain and at much higher percentages of the grid points within the localized regions of energetic submesoscale variability.

The submesoscale features in the ageostrophic velocity field in Figs. 6 and 7 are attributable mostly to contributions of cyclostrophic motion to the total velocity field in the CCS model used for this study. This can be shown by considering the force balance between geostrophy and centripetal acceleration in the steady-state momentum equation, referred to in meteorology as the gradient wind balance. The cyclostrophic momentum balance for axially symmetric flow in cylindrical coordinates is

$$-fV - \frac{V^2}{R} = -\frac{1}{\rho}\frac{\partial P}{\partial r}, \tag{1}$$

where r is radial distance, R is the radius to the center of curvature, ρ is the water density, P is pressure, and V is the angular velocity, which is defined to be positive for counterclockwise rotation and negative for clockwise rotation. For the northern hemisphere considered here, the angular velocity is thus positive in cyclones and negative in anticyclones.

The momentum equation (1) can be rearranged into the form

$$V_g = V + \frac{V^2}{fR}, \tag{2a}$$

where $V_g = (\rho f)^{-1}\partial P/\partial r$ is the geostrophically computed angular velocity. Since the second term on the right side of (2a) is always positive, it is evident that $V_g > V$ for any nonzero cyclostrophic velocity V. The angular velocity V_g computed geostrophically is thus an overestimate of the positive cyclostrophic velocity in cyclones and an underestimate of the magnitude of the negative cyclostrophic velocity in anticyclones. As a consequence, the vorticity computed geostrophically is overestimated in cyclones and underestimated in anticyclones.

The positive bias of geostrophically computed vorticity can be shown mathematically by rewriting (2a) as

$$V_g = (1 + \epsilon_R)\, V, \tag{2b}$$

where

$$\epsilon_R = \frac{V}{fR} \tag{3}$$

is the Rossby number of the rotational flow. The average relative vorticity within the circular area of the assumed axially symmetric flow with radius R can be obtained from Green's Theorem, which gives

$$\overline{\zeta} = \frac{\oint_C \vec{v}\cdot d\vec{l}}{\int_{A_C} dA} = \frac{V\, 2\pi R}{\pi R^2} = \frac{2V}{R}. \tag{4}$$

It is thus apparent that (3) can be expressed alternatively as

$$\epsilon_R = \frac{1}{2}\frac{\overline{\zeta}}{f}. \tag{5}$$

Multiplication of (2b) by $2/R$ and substitution of (4) for $2V/R$ gives

$$\overline{\zeta}_g = (1 + \epsilon_R)\,\overline{\zeta} = \overline{\zeta} + \frac{1}{2}\frac{\overline{\zeta}^2}{f}, \tag{6}$$

where $\overline{\zeta}_g = 2V_g/R$ is the average vorticity computed geostrophically within the circular area of axially symmetric flow with radius R. Since the second term on the right side of (6) is positive, the geostrophically computed vorticity $\overline{\zeta}_g$ is larger than the true vorticity $\overline{\zeta}$, thus confirming that the geostrophically computed vorticity overestimates the positive vorticity in cyclones and underestimates the magnitude of negative vorticity in anticyclones.

After division of both sides by f, (6) can be rearranged into the form

$$\frac{\overline{\zeta}_g}{f} - \frac{\overline{\zeta}}{f} = \frac{1}{2}\left(\frac{\overline{\zeta}}{f}\right)^2, \tag{7}$$

For cyclostrophic flow, the differences between the normalized geostrophically computed vorticity $\overline{\zeta}_g/f$ and the normalized vorticity $\overline{\zeta}/f$ are thus related quadratically to the latter. The validity of the cyclostrophic relation (7) is shown in the left panels of Fig. 9. The top left panel is a map of $(\zeta_g - \zeta)/f$ in the CCCS region computed from the bottom panels of Figs. 5c and 3b after smoothing with a half-power filter cutoff wavelength of 20 km. The bottom left panel shows binned averages of the normalized differences in the top left panel as a function of the normalized vorticity ζ/f. The curve in the bottom left panel corresponds to the quadratic relation (7). The quadratic fit is quite good. The discrepancies of the binned averages from the theoretical quadratic relation (7) are presumably attributable to deviations of the flow field from the axially symmetric flow assumed in the derivation of (7).

It is noteworthy that the features in the top left panel of Fig. 9 that are most compact and have the largest magnitudes are all positive. This is also evident from the asymmetry of the distribution of adequately sampled bins in the binned scatter plot in the bottom left panel of Fig. 9. The most energetic ageostrophic features in the vorticity field are thus cyclonic and the positive vorticities ζ of these features are overestimated by the geostrophically computed vorticities ζ_g. The lack of compact anticyclonic features is likely because small-scale anticyclones are susceptible to inertial instability (e.g., Rayleigh, 1916; Flierl, 1988; Kloosterziel and van Heijst, 1991; Kloosterziel et al., 2007). The most intense small-scale features in the ageostrophic vorticity field are therefore associated almost exclusively with submesoscale cyclones.

The relevance of cyclostrophic flow can be further investigated from the ratios ζ_g/ζ. For the axially symmetric flow assumed in the derivation above, the ratio obtained from (6) is

$$\frac{\overline{\zeta}_g}{\overline{\zeta}} = 1 + \frac{1}{2}\frac{\overline{\zeta}}{f}. \tag{8}$$

The validity of this cyclostrophic relation is shown in the right panels of Fig. 9. The top right panel is a map of ζ_g/ζ in the CCCS region computed from the bottom panels of Figs. 5c and 3b after smoothing with a half-power filter cutoff wavelength of 20 km. The bottom right panel shows binned averages of the ratios in the top right panel as a function of the normalized vorticity ζ/f. Note again the predominance of positive values of ζ. The line in the bottom right panel corresponds to the linear relation (8). The discrepancies of the binned averages from the theoretical linear relation (8) are again presumably attributable to deviations of the flow field from the axially symmetric flow assumed in the derivation of (8). The differences are especially evident in the regions of large-scale flow where ζ/f is small.

The conclusion of the preceding analysis is that the errors from the effects of cyclostrophic motion on surface velocities computed geostrophically from SWOT data may often exceed 0.1 m s^{-1} in the regions of high velocity where small-scale vorticity magnitudes are strongest. These non-Ekman ageostrophic velocities can mostly be reduced to less than 0.05 m s^{-1} by smoothing with a half-power filter cutoff wavelength of 50 km or more. The small-scale cyclostrophic motions that are responsible for these residual errors in the geostrophic approximation result in geostrophically computed velocities that overestimate the positive vorticity of cyclonic features and underestimate the magnitudes of the negative vorticity of anticyclonic features. The former occurs more commonly than the latter because of the tendency for anticyclonic features to become unstable.

In addition to errors from the existence of small-scale cyclostrophic motions, velocity estimates computed geostrophically from SWOT measurements of SSH will be contaminated by the SSH signatures of

ageostrophic internal gravity waves. Hints of such features are evident from close inspection of Fig. 5c in the form of subtle wavy striations in the geostrophically computed vorticity. These are most clearly seen in the central northern area of weak submesoscale variability in the bottom panel. As discussed in Sec. 2, internal gravity waves are underestimated in the CCS model used in this study. Artifacts from internal waves are therefore likely to be worse in actual geostrophically computed SWOT estimates of velocity than is suggested from Fig. 5c.

Present understanding of the sea-surface height signatures of the oceanic internal gravity wave field is limited, and consequently the extent of this contamination of estimates of surface velocity and vorticity computed geostrophically from SWOT data is not addressed systematically here. Its potential importance can be illustrated, however, through comparison of the ageostrophic velocity fields from two high-resolution ROMS simulations of the Gulf Stream region off the southeastern seaboard of the U.S., both with a grid spacing of 0.75 km $\times$ 0.75 km. Similar to the CCS model used in this study, one of the North Atlantic simulations (referred to here as the LF simulation) was forced at low frequencies with monthly smoothed winds and does not include ocean tides (Gula et al., 2015). The other (referred to here as the HF simulation) was forced at high frequencies with hourly winds and includes boundary forcing by ten ocean tidal constituents. Although the region of the North Atlantic model domain is very different dynamically from the CCS region considered in this study, the availability of the HF and LF simulations provides useful insight into the contamination of SWOT data that can be expected from internal waves forced by high-frequency winds and ocean tides.

Snapshots of the magnitudes of the total surface velocities, the geostrophically computed surface velocities and their differences (the "ageostrophic velocities") over the full model domain are shown in Fig. 10. As in the CCS model used for this study (Figs. 3a and 5b), the geostrophically computed velocity is qualitatively very similar to the total surface velocity in each of the two North Atlantic simulations. Moreover, the total and geostrophically computed velocity fields are qualitatively similar between the two North Atlantic simulations. But the ageostrophic velocity fields are dramatically different in the HF and LF simulations. Features resembling the cyclostrophic motions discussed above from the CCS model are evident in the ageostrophic velocity field from the LF model, especially in the immediate vicinity of the Gulf Stream. Such features are swamped in the HF model by striated internal gravity wave structures. The geostrophically computed velocities associated with these internal waves are a gross misrepresentation of the actual surface velocities associated with internal waves. We nonetheless refer to these striated features as "ageostrophic velocities" since they would be misinterpreted as velocity structures in geostrophically computed SWOT estimates of the velocity field.

To assess the effects of internal gravity waves on SWOT estimates of the surface velocity fields, the "non-Ekman ageostrophic velocity field" was computed from each North Atlantic simulation in the same manner as in Fig. 6c, i.e., as the differences of each of the total ageostrophic velocity fields in the bottom panels of Fig. 10 from their respective 150-km smoothed ageostrophic field (not shown here). The residual velocity fields were then smoothed with various half-power filter cutoff wavelengths as in Fig. 7. The magnitudes of the resulting smoothed non-Ekman ageostrophic velocity fields are shown in Fig. 11 for the region southeast of the Gulf Stream indicated by the boxes in Fig. 10. Features suggestive of internal gravity waves can be faintly seen in the LF simulation with 20-km smoothing but are not readily apparent with higher smoothing. In contrast, internal waves are highly energetic in the HF simulation and decrease in magnitude rather slowly with increased spatial smoothing. Fig. 11 suggests that significant contamination of the geostrophically computed velocity field by the SSH signatures of internal waves persist in some regions even after smoothing with a half-power filter cutoff wavelength of 80 km.

In principle, the internal wave contamination that is evident in Figs. 10 and 11 can be reduced by time averaging as in the simulations of geostrophically computed SWOT estimates of space-time smoothed velocity and vorticity in Sec. 8. In practice, the interleaved sampling pattern during each repeat of the 21-day orbit of SWOT (see Figs. 21–23 below) restricts the geographical distribution of locations with repeat sampling, thus limiting the benefits of time averaging to mitigate contamination by internal gravity waves. Qiu et al. (2018) note that it may be possible to remove some of the internal wave contamination based on model estimates of the stationary part of diurnal and semidiurnal tidal signals. Contamination by nonstationary internal gravity waves is much more problematic.

A thorough analysis of the effects of internal gravity waves on interpretation of geostrophically computed SWOT estimates of space-time smoothed velocity and vorticity is beyond the scope of this study. For present purposes, the contrasting velocity fields from the two North Atlantic simulations in Figs. 10 and 11 serve as a cautionary warning that the assessments of the resolution capabilities for SWOT estimates of velocity and vorticity in Secs. 6, 8 and 9 may be somewhat optimistic since our simulations are based on a CCS model with unrealistically weak internal gravity waves. A rigorous analysis of the effects of contamination of geostrophically computed velocity estimates by internal gravity waves is needed to fully understand the limitations of future use and interpretation of SWOT data.

It should be noted that other effects of synoptic-scale wind forcing besides internal gravity waves may also not be adequately represented in the CCS model used in this study since it was forced by seasonally varying winds. High-frequency wind forcing can also affect mesoscale and submesoscale variability. For this and other reasons, the resolution capabilities of actual SWOT and WaCM data are likely to be somewhat worse than the estimates presented here.

4. The Error Characteristics of Measured and Derived Variables from SWOT and WaCM Data

For our investigation of the resolution capabilities of SWOT and WaCM estimates of surface velocity and vorticity, the measurement characteristics that are of interest are the footprint sizes of the data that will be distributed to general users (referred to here as pre-processed data), the standard deviations of the uncorrelated measurement errors for the specified footprint size, and the space-time sampling patterns that are imposed by the measurement swath width and the orbit configuration for each instrument. The effects of footprint size and uncorrelated measurement errors on SWOT and WaCM estimates of velocity and vorticity are summarized in this section. Discussion of the equally important consideration of sampling patterns on the ability to map the velocity and vorticity fields (especially an issue for SWOT because of its much narrower swath width) is deferred to Secs. 7–10.

4.1. SWOT Errors

The measurement characteristics for the SWOT altimeter are documented in a suite of project reports published by the Jet Propulsion Laboratory and available online at https://swot.jpl.nasa.gov/science/resources/. The most germane of these reports are the Science Requirements Document (Rodríguez and Callahan, 2016), the Onboard Processing and Algorithm Theoretical Basis Document (Peral, 2016), and the Mission Performance and Error Budget Document (Esteban Fernandez, 2017). While the versions of these documents that are listed in the references may undergo revisions between now and the planned launch date in 2021, no major changes are expected in the instrumental measurement errors and orbit configuration that are crucial to the simulations of SWOT data used in this study.

The baseline science requirements for SWOT are for SSH measurements with a footprint size of 1 km on a 1 km $\times$ 1 km grid across the measurement swath. SWOT will also include a nadir altimeter, but that is not considered in this study because it has a very different footprint size and measurement accuracy compared with the Ka-band Radar Interferometer (KaRIn). KaRIn will measure SSH with unprecedented resolution and spatial coverage across two parallel measurement swaths with 50-km widths separated by a 20-km gap centered on the satellite ground track (see Sec. 7).

In addition to uncorrelated errors from instrument noise, the KaRIn estimates of SSH will be contaminated by spatially correlated (long-wavelength) errors from orbit errors and various environmental effects, including significant wave height (SWH) and the effects of dry gases, water vapor and ionospheric free electrons on atmospheric refraction. Of particular note, the validity of the so-called inverted barometer correction of 1 cm hPa^{-1} for sea level pressure effects on SSH is unknown on the small scales measurable by KaRIN. The uncertainties of the sea level pressure fields from the atmospheric model that will be used as a basis for the inverted barometer correction are also unknown on these small scales.

Consideration of the complete error budget for SWOT is beyond the scope of this study. Readers are referred to Rodríguez and Callahan (2016) for a discussion of the present understanding of the various

aspects of SWOT measurement errors. Our focus is on SWOT estimates of small-scale surface velocity and vorticity variability, both of which are spatially high-pass filtered versions of the SSH field (see Fig. 5) since they are computed from spatial derivatives of SSH. With the possible exception of the inverted baraometer correction mentioned above, most of the spatially correlated errors have relatively large scale and are thus expected to be of secondary importance. We therefore consider only the effects of uncorrelated measurement errors in this study.

In its low-resolution mode over the ocean, the raw radar measurements by the KaRIn instrument will have a footprint size of about 100 m. To reduce the measurement errors, while at the same time reducing the unnecessarily large data volume over the ocean, the present official plan as summarized by Peral (2016) and Esteban Fernandez (2017) is to smooth the raw measurements of SSH in an onboard processor to achieve the SWOT science requirements for a footprint size of 1 km for ocean observations[3]. It is shown in Appendix B.1 that this footprint size can be achieved by smoothing the raw measurements using a 2-dimensional Parzen smoother with a half-power filter cutoff wavelength of 2 km. It is further shown in Appendix B.1 that pre-processed SWOT estimates of SSH obtained in this manner are spatially uncorrelated on a 1 km $\times$ 1 km grid.

For the simulations of SWOT data in this study, a critically important characteristic of the pre-processed SWOT estimates of SSH is the standard deviation of the uncorrelated instrumental errors. As discussed in detail in Appendix F, it is not possible to determine this unambiguously from the SWOT documentation. In part, this is because the actual science requirement is specified in terms of the wavenumber spectrum of SSH after 2-dimensional smoothing in ground-based post-processing, rather than in terms of the measurement accuracy itself (see Appendix F). On the few occasions where a standard deviation of the uncorrelated measurement errors is given, the value is inconsistent, probably because the stated value is for an evolving "present best estimate" of what will actually be achieved from SWOT on-orbit, rather than for the baseline science requirement that is considered in this study. The former is slightly better than the science requirement and may continue to improve somewhat as the techniques for processing the KaRIn data are refined between now and the launch date.

The wavenumber spectral specification of the measurement errors in the SWOT science requirements is "reverse engineered" in Appendix F to determine the corresponding standard deviation of the uncorrelated errors of the pre-processed SWOT estimates of SSH. The derived value for the swath-averaged science requirement for conditions of 2-m SWH and a footprint size of 1 km is shown to be $\sigma_h = 2.74$ cm.

The most recent projected estimate of the swath-averaged standard deviation of uncorrelated measurement errors for SWOT on-orbit is about $\sigma_h = 2.4$ cm for 2-m SWH, which is somewhat better than the value of 2.74 cm derived in Appendix F. The dependencies of the present projected estimate of SWOT measurement errors on swath location and SWH are shown in Fig. F1 in Appendix F. Our assumed swath-averaged error standard deviation of $\sigma_h = 2.74$ cm appears to be more representative of the projected estimate for 4-m SWH.

The difference between 2.74 cm and 2.4 cm is a minor distinction for this investigation. A more significant issue is that the analysis presented in this study does not simulate the cross-track variation of the SWOT measurement errors. As shown in Fig. F1, the measurement errors increases toward both edges of the measurement swath, resulting in cross-track variations that are much larger than the difference between 2.74 cm and 2.4 cm. For 2-m SWH, for example, the projected estimates of SSH errors range from 1.9 cm at the center of the swath to 3.0 cm at the inner edge of the swath and more than 4 cm approaching the outer edge of the swath. It will be seen in Secs. 6, 8 and 9 that geostrophically computed SWOT estimates of velocity and vorticity must be smoothed considerably to achieve adequate signal-to-noise ratio. This

[3]The SWOT Algorithm Development Team has recently recommended changing the onboard processing to a smaller footprint size of 0.5 km posted on a 0.25 km $\times$ 0.25 km grid. This higher resolution increases the standard deviation of the uncorrelated measurement errors in the onboard estimates of SSH by a factor of two compared with a footprint size of 1 km. It will be shown in Sec. 6 that even the science requirement of 1-km footprint size used for the simulations in this study exceeds the signal resolution capability by more than an order of magnitude for in-swath SWOT estimates of surface velocity and vorticity computed geostrophically from SSH. The results of the additional smoothing in ground-based post-processing that will be needed to achieve an adequate signal-to-noise ratio would therefore be essentially the same for either footprint size.

smoothing leads to edge effects that would be exacerbated by the larger measurement errors near the swath edges.

As noted in the introduction, the error analysis in this study could have been carried out using the simulator software available from the SWOT Project Office (Gaultier et al., 2017). Analogous simulator software is not available for WaCM. For consistency in our analysis of the effects of SWOT and WaCM measurement errors, we have therefore chosen to simulate the error standard deviation for simulated SWOT data as spatially constant with a swath-averaged value of $\sigma_h = 2.74$ cm. Because our simulations do not account for the higher measurement errors near the edges of the measurement swaths, the analysis presented here likely underestimates the overall effects of measurement errors on space-time smoothed fields of velocity and vorticity constructed geostrophically from SWOT measurements of SSH. The results presented in Secs. 6, 8 and 9 should therefore be considered optimistic assessments of the resolution capabilities of actual SWOT data.

For SWOT, the velocity and vorticity fields that are the focus of this investigation must be estimated geostrophically, which requires differentiation of SSH for velocity and double differentiation of SSH for vorticity. The spatial derivatives are estimated in this study by centered differences of the discrete SSH values. The effects of the uncorrelated errors of SWOT measurements of SSH on geostrophically computed velocity and vorticity are derived in Appendix G.1 using propagation-of-error analysis. The results are summarized in the first column of Table 1, which shows that the $\sigma_h = 2.74$-cm standard deviation of SSH measurement errors for a footprint size of 1 km results in a large standard deviation of 2.17 m s^{-1} for the errors of SWOT estimates of each geostrophically computed velocity component at the central latitude 37°N of the CCS model domain where the Coriolis parameter is $f = 8.77 \times 10^{-5}$ s^{-1}. This error increases by about 11% at the 32.5°N southern corner of the CCS model domain where $f = 7.83 \times 10^{-5}$ s^{-1} and decreases by about 11% at the 42°N northern corner of the model domain where $f = 9.76 \times 10^{-5}$ s^{-1}. The $\sigma_h = 2.74$-cm SSH measurement errors result in an extraordinarily large standard deviation of $39.1f$ for the errors of geostrophically computed SWOT estimates of vorticity at 37°N.

Because of these large errors, SWOT estimates of velocity and vorticity computed geostrophically from the unsmoothed pre-processed data are likely of little value for most oceanographic applications. The errors listed in the first column of Table 1 are much larger than the errors summarized for WaCM estimates of velocity and vorticity in Sec. 4.2 below, but the footprint size of 5 km for pre-processed WaCM estimates of surface velocity is a factor of 5 coarser than the 1-km footprint size for SWOT. The large errors of SWOT estimates of velocity and vorticity obtained from the pre-processed SWOT data can be reduced by smoothing commensurately with the half-power filter cutoff wavelength of 10-km that corresponds to the 5-km footprint size of pre-processed WaCM estimates of surface velocity (see Appendix B.2).

The effects of smoothing the pre-processed SWOT estimates of SSH isotropically with a half-power filter cutoff wavelength of 10 km in ground-based post-processing, i.e., the same smoothing applied in pre-procssing of WaCM estimates of velocity, are derived in Appendix G.3 using propagation-of-error analysis. The results are summarized in the second column of Table 1. The standard deviations of errors of geostrophically computed SWOT estimates of velocity and vorticity are reduced by factors of about 8 and 12, respectively. The resulting uncertainties are comparable to the uncertainties of velocity and vorticity derived below in Sec. 4.2 based on pre-processed WaCM data with the same footprint size of 5 km (see Table 2).

Equations (G.2), (G.5), (G.8), (G.17) and (G.20) [the latter two in combination with (G.2b) and (G.8), respectively] in Appendix G.1 and Appendix G.3 from which the error estimates in the first two columns of Table 1 were computed are all expressed in terms of the variance σ_h^2 of the errors of the pre-processed SWOT estimates of SSH for a footprint size of 1 km. It is therefore straightforward to recompute the standard deviations of the errors of geostrophically computed velocity components and vorticity based on any specified value of σ_h^2 (e.g., the present projected estimate of $\sigma_h = 2.4$ cm, rather than the science requirement of $\sigma_h = 2.74$ cm that is derived in Appendix F and used in Table 1 and throughout the rest of this study).

4.2. WaCM Errors

As WaCM is not yet a proposed NASA mission, there is no formal documentation of the details of the Doppler measurements of surface velocity. The technical aspects of WaCM are essentially the same as

those summarized by Rodríguez et al. (2018) for the NASA aircraft DopplerScatt system. A Doppler radar measures the radial component of velocity parallel to the antenna pointing angle. Estimation of vector velocity requires measurements from multiple look angles. This is achieved using a spinning antenna that measures a given location on the sea surface from several different look angles over a short period of time as the satellite moves along its orbit.

Issues with the geometrical transformations of pooled measurements of radial velocity from multiple look angles to estimate two orthogonal components of velocity are not addressed in our simulations of WaCM data. We have assumed that the two orthogonal velocity components have already been estimated in onboard and ground-based pre-processing of the measurements pooled over 5 km × 5 km areas and that the uncorrelated errors of surface current speed in these pooled estimates have a standard deviation of $\sigma_{spd} = 0.50$ m s^{-1}. In reality, the errors will differ for the two velocity components. Because of limited azimuthal diversity of the Doppler measurements of radial velocity near the swath edges, the errors of the cross-track velocity component increase toward the inner edges of the two parallel measurement swaths. Likewise, the errors of the along-track component increase toward the outer edges of the measurement swaths.

It is shown in Appendix B.2 that an effective footprint size of 5 km can be achieved by smoothing high-resolution data using a 2-dimensional Parzen smoother with a half-power filter cutoff wavelength of 10 km. The estimates of surface velocity that we refer to here as pre-processed WaCM data were therefore simulated from the CCS model output based on isotropic 2-dimensional smoothing of noisy velocity components on the full 0.5 km × 0.5 km resolution of the model grid with a half-power filter cutoff wavelength of 10 km.

Since velocity will be estimated directly by WaCM, the only derived quantity is the vorticity, which is computed from spatial derivatives of the velocity components. We assume throughout this study that the speed measurement uncertainties are equally partitioned between orthogonal velocity components and that the errors of each velocity component are uncorrelated with each other. The $\sigma_{spd} = 0.50$ m s^{-1} standard deviation of speed measurement errors therefore corresponds to a standard deviation of $\sigma_{u,v} = 0.354$ m s^{-1} of the uncorrelated errors of pre-processed WaCM estimates for each orthogonal velocity component u and v.

For a footprint size of 5 km, pre-processed WaCM estimates of surface velocity are spatially uncorrelated on a 5 km × 5 km grid (see Appendix B.2). The effects of the uncorrelated velocity component errors on WaCM estimates of vorticity computed on a 5 km × 5 km grid are derived in Appendix G.2 using propagation-of-error analysis. The results are summarized in the first column of Table 2, which shows that the standard deviation of $\sigma_{u,v} = 0.354$ m s^{-1} for the velocity component errors results in a standard deviation of $0.807f$ for the errors of WaCM estimates of vorticity at the central latitude 37°N of the CCS model domain.

It is advantageous to oversample the WaCM estimates of surface velocity on a 1 km × 1 km grid in order to retain more of the high-wavenumber variability of the vorticity signal in the centered differences used here to estimate the derivatives in the definition of vorticity (see Appendix H). For the simulations in this study, oversampling the WaCM data on a 1 km × 1 km grid has the additional practical advantage of giving a spatial gridding that is equivalent to the 1 km × 1 km gridding assumed here for the pre-processed SWOT data. The footprint size from the filtering in the pre-processing of WaCM data is still 5 km. The standard deviation of the errors of WaCM estimates of each velocity component is therefore still $\sigma_{u,v} = 0.354$ m s^{-1}, but the velocity component errors on a 1 km × 1 km grid are spatially correlated.

The effects of correlation of the measurement errors on the vorticity estimated from WaCM data on a 1 km × 1 km grid are incorporated in the propagation-of-error analysis in Appendix G.2. The results are summarized in the second column of Table 2. The oversampling increases the standard deviation of the vorticity errors by about a factor of 3 to a value of about $2.4f$ at 37°N. While this increase of the errors is undesirable, the standard deviation of the vorticity signal also increases in the centered difference estimates of the derivatives on the oversampled grid. It is shown in Appendix H that this retains more of the short-wavelength vorticity variability where much of the signal variance lies (see Figs. 3b and 4). The net effect of oversampling the WaCM data on a 1 km × 1 km grid is to improve the signal-to-noise ratio, even though the noise standard deviation is higher on the 1 km × 1 km grid.

The standard deviation of the errors of WaCM estimates of velocity with 5-km footprint (i.e., with smoothing with a half-power filter cutoff wavelength of 10 km) in the first two columns of Table 2 is

somewhat larger than the standard deviation of geostrophically computed SWOT estimates of velocity with 10-km smoothing listed in the second column of Table 1. On the other hand, the errors of WaCM estimates of vorticity on a 1 km × 1 km grid are somewhat smaller than the errors of geostrophically computed SWOT estimates of vorticity with 10-km smoothing (compare the bottom element in the second columns of Tables 1 and 2). The apparent contradiction of higher velocity errors but lower vorticity errors for WaCM is attributable to the different wavenumber spectral characteristics of the errors of SWOT and WaCM estimates of the velocity components and vorticity (see Sec. 4.4 below) that arise from the different orders of differentiation required to obtain the estimates.

Equations (G.10), (G.12) and (G.15) in Appendix G.2 from which the error estimates in the first two columns of Table 2 were computed are all expressed in terms of the variances σ_u^2 and σ_v^2 of the errors of the pre-processed WaCM estimates of the velocity components. It is therefore straightforward to recompute the standard deviations of the vorticity errors based on any specified values of σ_u^2 and σ_v^2.

4.3. Error Reductions from Smoothing in Ground-Based Post-Processing

The errors of SWOT and WaCM estimates of velocity and vorticity listed in the first two columns of Tables 1 and 2 are too large for the data to be useful for most applications, even with the 10-km smoothing to achieve a footprint size of 5 km. SWOT and WaCM data will have to be further smoothed in ground-based post-processing to reduce the effects of measurement errors. The reductions of the errors of the measured and derived variables that are achieved with this additional smoothing could be derived analytically, albeit tediously, by the propagation-of-error analysis procedure used in Appendix G.3 for the case of smoothing of the SWOT data with a half-power filter cutoff wavelength of 10 km. For SWOT, this would require determination of the autocorrelations of smoothed SSH errors at the three spatial lags of $2\Delta x$, $2\sqrt{2}\,\Delta x$ and $4\Delta x$ required for Eqs. (G.17a) and (G.21) in Appendix G for each choice of half-power filter cutoff wavelength λ_c. A similar propagation-of-error analysis could be carried out for WaCM estimates of smoothed velocity and vorticity.

The variances of the residual errors after isotropic 2-dimensional smoothing with a given λ_c are much more easily determined for each variable of interest from the analytical expressions for the wavenumber spectra of the measured and derived variables that are derived for SWOT and WaCM in Appendix I.2 and Appendix I.4, respectively.

The procedure for determining the standard deviation of residual errors from the wavenumber spectrum after smoothing in ground-based post-processing is based on Parseval's Theorem, which relates the variance of a variable to the integral of the power spectral density of the variable. For finite record length, this integral becomes the discrete sum (D.1) in Appendix D. The residual error variance after isotropic 2-dimensional smoothing was obtained by integrating the analytical expression for the wavenumber spectra of the residual errors for half-power filter cutoff wavelengths λ_c ranging from 10 km to 150 km. Examples of these wavenumber spectra are presented and discussed below in Sec. 4.4 for $\lambda_c = 20$ km, 50 km and 80 km. The standard deviation of the residual errors is the square root of the residual error variance computed from the integrated spectrum for each choice of λ_c.

The residual error standard deviations obtained in this manner are shown in Fig. 12 for SSH from SWOT (panel a) and for velocity and vorticity (panels b and c, respectively) estimated from both SWOT and WaCM data on 1 km × 1 km grids. These estimates assume complete instantaneous sampling of the full CCS model domain, i.e., without the sampling errors discussed in Secs. 7–10. The errors initially drop very quickly with increased smoothing and then more gradually as the smoothing is further increased. In the case of SSH, the residual errors in Fig. 12a decrease as λ_c^{-1}. The velocity errors in Fig. 12b decrease as λ_c^{-2} and λ_c^{-1} for SWOT and WaCM, respectively. The corresponding vorticity errors in Fig. 12c decrease as λ_c^{-3} and λ_c^{-2}. The more rapid decreases for SWOT than for WaCM are because of attenuation of the variance of the geostrophically computed velocity component errors from the band-pass filtering operation of the response function for centered difference estimates of the geostrophic derivatives (see Appendix H and Appendix I and the discussion in Sec. 4.4 of the wavenumber spectral characteristics of the residual errors of the smoothed variables).

To provide some quantitative numbers for the error reductions achieved with isotropic 2-dimensional smoothing in ground-based post-processing, the values of the standard deviations for the case of a filter

cutoff wavelength of $\lambda_c = 50$ km are listed for SWOT and WaCM in the third columns of Tables 1 and 2, respectively. The errors of SWOT estimates of SSH and geostrophically computed velocity components and vorticity are reduced by factors of 25, 167 and 875, respectively, compared with estimates from the pre-processed SWOT data. Compared with the 10-km smoothing applied to SWOT data in Sec. 4.1 to match the 5-km footprint size of WaCM data (see the second column of Table 1), the errors of geostrophically computed SWOT estimates of velocity and vorticity with 50-km smoothing are further reduced by factors of 21 and 81, respectively. The errors of WaCM estimates of velocity components and vorticity on a 1 km $\times$ 1 km grid with 5-km footprint and 50-km smoothing are reduced by more modest factors of 5 and 20, respectively, compared with the 10-km smoothing in the pre-processing (see the second and third columns of Table 2).

4.4. Wavenumber Spectral Characteristics of the Errors

Alongshore wavenumber spectra of the signals and errors in simulated SWOT and WaCM estimates of the velocity components and vorticity from the CCS model provide insight into the significant challenges in mapping small-scale variability from the satellite data. In the case of SWOT, velocity and vorticity are computed geostrophically and the alongshore wavenumber spectra of SSH signal and errors are also considered. The error spectra provide wavenumber decompositions of the error standard deviations presented in Secs. 4.1–4.3. As noted previously, we consider only the effects of uncorrelated measurement errors in this study since they are the primary limitation for SWOT and WaCM estimates of velocity and vorticity. The error spectra presented below assume a standard deviation of $\sigma_h = 2.74$ cm for the errors of pre-processed SWOT estimates of SSH and a standard deviation of $\sigma_{u,v} = 0.354$ m s^{-1} for the errors of pre-processed WaCM estimates of each velocity component.

A minor caveat to the general applicability of the analytical equations in Appendix I for the theoretical wavenumber spectra of the errors of velocity components and vorticity computed geostrophically from SSH is that they are based on a specified constant value of the Coriolis parameter f. For the calculations in this section, we have used the value of f at the central latitude 37°N of the CCS model domain. At the northern extent of the model domain, the Coriolis parameter is 11% larger than its value at 37°N; at the southern extent, it is 11% smaller.

The use of a constant value of f in the analytical expressions for the geostrophically computed velocity and vorticity error variances is a minor issue in this study. This is confirmed in Figs. 13a,b and 14 below from the very close agreement between the spectra of the errors computed theoretically based on the analytical expressions in Appendix I with constant f (the green lines in each panel of the above-noted figures) and the spectra determined empirically from errors of velocity components and vorticity computed geostrophically from maps of simulated SWOT SSH measurement errors using the local value of f at each grid point (the blue lines in each panel of the figures).

Before presenting the alongshore wavenumber spectra of the variables of interest, we pause to point out one other very minor issue in the error spectra presented for both SWOT and WaCM in Figs. 13–15 below. The 2-dimensional smoothing applied in simulated ground-based post-processing of the SWOT and WaCM error fields from which the error spectra were computed empirically (the blue lines in Figs. 13–15) was applied truly isotropically using a 2-dimensional Parzen weighting function (see Appendix A) that depends only on the radial distance of each data point from the estimation location. It is shown in Appendix C that essentially equivalent isotropic 2-dimensional smoothing can be achieved through sequential 1-dimensional smoothing using the Parzen filter in each of two orthogonal dimensions.

The advantage of sequential 1-dimensional smoothing is that it facilitates the derivations in Appendix I of the analytical expressions for the wavenumber spectral characteristics of residual errors in smoothed fields that are shown by the green lines in Figs. 13–15. The essential equivalence of true isotropic 2-dimensional smoothing and sequential 1-dimensional smoothing can be inferred from these figures by the very close agreement between the theoretical spectra computed from the analytical expressions in Appendix I and the spectra computed empirically from the simulated error fields.

4.4.1. Error Spectra from Pre-Processed SWOT Data

The alongshore wavenumber spectra of error-free SSH from the CCS model and uncorrelated SSH measurement errors from unsmoothed simulated pre-processed SWOT estimates of SSH are shown in the top

panel of Fig. 13a. The spectrum of uncorrelated SSH measurement errors computed empirically from the simulated SWOT data is shown by the blue line. The theoretical spectrum of SSH measurement errors given by the analytical expression (I.2) derived in Appendix I.1 is shown by the green line, which agrees very well with the empirical error spectrum. These error spectra intersect the SSH signal spectrum at a wavenumber of about 0.022 cycle per km (cpkm), which corresponds to a wavelength of about 45 km. The relevance of this intersection of the signal and noise spectra to the resolution capability of SWOT estimates of SSH is discussed later in the context of the interpretation of Fig. 13b.

The alongshore wavenumber spectra of signals and errors for SWOT estimates of cross-shore and alongshore velocity components u_g and v_g computed geostrophically from centered difference estimates of derivatives of simulated pre-processed SWOT estimates of SSH are shown in, respectively, the second and third panels of Fig. 13a. The error spectra computed empirically from the simulated SWOT data based on the local value of the Coriolis parameter f at each grid point are again shown by blue lines in these panels. The analytical expressions (I.5) and (I.10) derived in Appendix I.1 for the error spectra are shown by the green lines, which again agree very well with the empirical error spectra. A notable feature of the v_g spectra is that the spectral power of v_g errors exceeds the spectral power of the v_g signal at all wavenumbers. The v_g signal is thus undetectable from unsmoothed pre-processed SWOT data. In the case of the u_g spectra, the signal power exceeds the error power for wavenumbers below about 0.02 cpkm but this signal variance will be masked in maps of u_g by the order-of-magnitude higher power of the errors at higher wavenumbers.

The dramatic differences between the wavenumber characteristics of the alongshore wavenumber spectra of the errors of u_g and v_g merit some discussion. The spectrum is "white" (constant with alongshore wavenumber) for v_g errors but "blue" (dominated by high alongshore wavenumber variability) for u_g errors. The spatial high-pass filtering of u_g errors implied by this blueness occurs because the white noise SSH is differentiated in the alongshore dimension, i.e., in the same dimension as the wavenumber spectrum. (The dropoff of spectral power at the highest wavenumbers arises because of the response function for the centered difference approximation of the geostrophic derivatives; see Fig. H1 in Appendix H.)

The v_g errors are similarly spatially high-pass filtered, but from differentiation of SSH in the cross-shore dimension. This cross-shore high-pass filtering would be evident in the cross-shore wavenumber spectrum of v_g, but is not manifest in its alongshore wavenumber spectrum because the centered difference estimates of the derivative of SSH in the geostrophic equation for v_g are perpendicular to the alongshore dimension. It is shown in Appendix I, however, that the blueness of the cross-shore spectrum of v_g nonetheless has a large effect on the spectra of error fields smoothed 2-dimensionally in ground-based post-processing. (The cross-shore spectrum of u_g is white for the same reason that the alongshore spectrum of v_g is white, namely that the alongshore centered difference estimates of the derivative of SSH in the geostrophic equation for u_g are perpendicular to the cross-shore dimension.)

The alongshore wavenumber spectra of signal and errors for SWOT estimates of vorticity ζ_g computed geostrophically from second derivatives of simulated pre-processed SWOT estimates of SSH are shown in the bottom panel of Fig. 13a. The spectrum of ζ_g errors computed empirically from the simulated SWOT data (the blue line) again agrees very well with the theoretical spectrum of ζ_g errors (the green line) computed by the analytical expression (I.24) in Appendix I based on the constant value of $f = 8.77 \times 10^{-5}$ s^{-1} at the central latitude 37°N of the CCS model domain. In this case, the error spectra are nearly three orders of magnitude more energetic than the ζ_g signal spectrum at all wavenumbers. The vorticity signal estimated from unsmoothed pre-processed SWOT data is thus completely swamped by the errors at all wavenumbers.

For comparison with the wavenumber spectra of errors of estimates of velocity components and vorticity computed from pre-processed WaCM data that are discussed below, the alongshore wavenumber spectra of signals and errors for SWOT estimates of SSH, u_g, v_g and ζ_g are shown in Fig. 13b for isotropic 2-dimensional smoothing with a half-power filter cutoff wavelength of $\lambda_c = 10$ km in simulated ground-based post-processing of the pre-processed SWOT data. This 10-km smoothing is the same as the smoothing applied in this study to simulate the 5-km footprint size in pre-processing of WaCM data (see Appendix B.2). The error spectra computed empirically from the smoothed SWOT data (the blue line in each panel) again agree very well with the theoretical spectra (the green lines) that were computed by the analytical expressions (I.29), (I.31), (I.33) and (I.35) in Appendix I.2 for isotropic 2-dimensional smoothing with a filter cutoff wavelength $\lambda_c = 10$ km.

Since the wavenumber spectra of error-free SSH, u_g, v_g and ζ_g signals are red, nearby values of each of these variables are correlated. The power of the signal spectra after 2-dimensional smoothing is therefore attenuated only at wavenumbers higher than λ_c^{-1}. (The small attenuation at wavenumbers smaller than λ_c^{-1} is from imperfections of the filter transfer function of the Parzen smoother used here to smooth the 2-dimensional fields of interest.) The spectral power of the errors of SWOT estimates of these variables is also attenuated at wavenumbers higher than λ_c^{-1}. Because the errors are spatially uncorrelated in the cross-shore direction, 2-dimensional smoothing also attenuates the power of the along-track wavenumber spectra of the errors by an additional factor of $2\Delta x/\lambda_c$ at all wavenumbers. This is discussed in detail in Appendix E [see Eq. (E.11)] and Appendix I. For the grid spacing of $\Delta x = 1$ km and filter cutoff wavelength of $\lambda_c = 10$ km, this multiplicative factor is approximately $2\Delta x/\lambda_c = 0.2$. Note that the vorticity errors with 10-km smoothing in the bottom panel of Fig. 13b are still more than an order of magnitude larger than the signal at all wavenumbers.

Because of the overall reduction of the spectral power of the measurement errors at all wavenumbers when applying isotropic 2-dimensional smoothing, the intersection of the smoothed signal and error spectra shifts to higher wavenumbers (shorter wavelengths) with increased smoothing. Recall from Fig. 13a that the unsmoothed SSH signal and error spectra intersect at a wavelength of about 45 km. For the smoothing with the 10-km half-power filter cutoff wavelength used for Fig. 13b, the SSH signal and error spectra intersect at a wavenumber of about 0.03 cpkm, which corresponds to a wavelength of about 33 km.

The intersection of the SSH signal and noise spectra at a wavelength of 33 km in Fig. 13b is surprising in view of the fact that the science requirement for SWOT measurement accuracy was chosen with the intent that the 68$^{\text{th}}$-percentile of the global average SSH signal spectrum intersects the spectrum of uncorrelated measurement errors at a wavelength of 15 km after isotropic 2-dimensional smoothing with a half-power filter cutoff wavelength of 15 km, which is only slightly more than the 10-km smoothing shown in Fig. 13b. With 15-km filtering, the signal spectrum from the CCS model used in this study intersects the noise spectrum at a wavelength of 30 km (see Fig. F3 in Appendix F).

The longer 30-km wavelength of the intersection of the signal and noise spectra found in this study compared with the 15-km wavelength in the specification of the science requirement for the accuracy and resolution of SWOT measurements of SSH occurs because the SSH spectrum from the CCS model falls off as about $l^{-7/2}$ at alongshore wavenumbers l near 1/15 cpkm (see Figs. 13a and F3), which is steeper than the approximate $l^{-5/2}$ rolloff of the assumed 68$^{\text{th}}$-percentile of the global-average SSH wavenumber spectrum upon which the SWOT science requirements are based. The steeper rolloff of the spectrum of SSH from the CCS model reflects both the specifics of the CCS dynamical regime and the absence from the model of other possible physical sources of SSH variance, including, for example, the SSH signatures of internal waves that would flatten the spectral rolloff of the SSH wavenumber spectrum at high wavenumbers.

The uncertainty of the rolloff of the SSH spectrum at wavelengths shorter than the approximate 70-km wavelength resolution limitation of nadir altimeter data (Xu and Fu, 2012) is an important issue for interpretation of SWOT data. Spectra of SSH are shown in Fig. F4 in Appendix F for a region southeast of the Gulf Stream in the two ROMS simulations of the North Atlantic circulation considered in Sec. 3 (see Figs. 10 and 11), one with a weak internal wave field similar to the CCS model and the other with an energetic internal wave field from inclusion of high-frequency wind and tidal forcing. The SSH spectra in the models without and with high-frequency forcing have spectral rolloffs of about l^{-5} and l^{-3}, respectively, at wavenumbers higher than about 1/50 cpkm. Because the flattening of the SSH spectrum from the model with high-frequency forcing occurs only at wavenumbers higher than about 1/50 cpkm, the intersection of the SSH signal spectrum and the noise spectrum for 15-km smoothed SWOT data occurs at only a slightly higher wavenumber (shorter wavelength) than for the model without high-frequency forcing. As for the CCS model used in this study, the SSH spectra from both North Atlantic models intersect the noise spectrum at wavelengths longer than 15 km.

The issue of the uncertainty of the spectral characteristics of SSH at high wavenumbers and its implications for the resolution of SWOT measurements of SSH are discussed further in Appendix F. The conclusion is that the wavenumber spectral characteristics of SSH are not presently known from observations at wavelengths shorter than 70 km and must therefore be inferred from high-resolution models. However, different models give different results (see the discussion in Appendix F). SWOT will provide the first observational

data from which model representations of small-scale SSH variability can be tested.

4.4.2. Error Spectra from Pre-Processed WaCM Data

The alongshore wavenumber spectra of signals and errors of WaCM estimates of velocity components u and v and vorticity ζ are shown in Fig. 13c. As discussed in Sec. 4.2 and in more detail in Appendix I.3, we have assumed that the pre-processed WaCM velocity estimates will be isotropically smoothed with a half-power filter cutoff wavelength of 10 km and oversampled on a 1 km × 1 km grid. As for the case of SWOT considered above, the theoretical error spectra computed by the analytical expression (I.40) for u and v and the analytical expression (I.43) partitioned as (I.46a) and (I.46b) for ζ (the green lines) agree very well with the error spectra computed empirically from the simulated WaCM data (the blue lines). The error spectra for v and ζ are very similar in magnitude and wavenumber characteristics to the spectra of errors of v_g and ζ_g from the simulated SWOT data with 10-km smoothing shown in Fig. 13b. The error spectra for u from pre-processed WaCM data and for u_g from SWOT data with 10-km smoothing applied in post-processing are very different because of the filtering of the first-difference operator used to calculate u_g from SSH, as discussed previously.

4.4.3. Error Spectra from Post-Processed SWOT and WaCM Data

To illustrate the effects of smoothing in ground-based post-processing to improve the signal-to-noise ratio for scientific applications of SWOT and WaCM data, the wavenumber spectral characteristics of the signals and errors for isotropic 2-dimensional smoothing with half-power filter cutoff wavelengths of $\lambda_c = 20$ km, 50 km and 80 km are shown in Figs. 14 and 15 for SWOT and WaCM, respectively. The signal and error spectra are all attenuated at wavenumbers higher than λ_c^{-1}. The 2-dimensional smoothing additionally attenuates the error spectra at all wavenumbers by the factor of $2\Delta x/\lambda_c$ noted above in the discussion of the spectra of SWOT data smoothed with $\lambda_c = 10$ km in Fig. 13b.

An important thing to note from Figs. 14 and 15 is that the noise spectra are attenuated much more quickly than the signal spectra with increased smoothing. Smoothing therefore improves the signal-to-noise variance ratio. This is a key point in our approach to assessing the resolution capability of maps of velocity and vorticity constructed from SWOT and WaCM data.

The effects of isotropic 2-dimensional smoothing of pre-processed SWOT and WaCM data in simulated ground-based post-processing to reduce the effects of uncorrelated measurement errors are examined in Sec. 6 from instantaneous maps of the variables of interest with the same filter cutoff wavelengths of $\lambda_c = 20$ km, 50 km and 80 km used for the spectra on Figs. 14 and 15. The strategy used in this study to define the resolution capabilities from the resulting maps of signals and errors for these and other choices of λ_c is summarized in the next section.

5. A Strategy for Assessing Resolution Capability from Noisy Satellite Observations

The resolution capabilities of SWOT and WaCM estimates of velocity and vorticity are defined in this study by the amount of smoothing required to reduce the errors to achieve a specified signal-to-noise (S/N) ratio. The effects of uncorrelated measurement errors on estimates of surface velocity and vorticity are attenuated in Sec. 6 by isotropic 2-dimensional spatial smoothing of the simulated pre-processed SWOT and WaCM data. In a further effort to suppress noise, temporal averaging is applied in addition to 2-dimensional spatial smoothing of the simulated satellite data in Secs. 8–10.

There is ambiguity in how to define the signal in the S/N metric. We define the S/N ratio based on the spatial variances of the residual signal and residual errors after smoothing. The signal variance is thus defined to be the spatial variance of the true value of the variable of interest after applying the same smoothing that is applied to reduce the errors. An arguably better choice is to compare the spatial variance of the smoothed errors with the spatial variance of the unsmoothed signal. From an observational perspective, however, this strategy would have tenuous relevance to the maps that can be constructed from the error-contaminated satellite observations since it is not possible to reduce the errors by smoothing the observed data without also smoothing the signal.

While the "moving target" of the systematic reduction of signal variance with increased smoothing may not be ideal, this is the only practical approach to assessing the resolution capability of the noisy satellite estimates; the smoothed signal is the best possible estimate of the variable of interest that could be achieved from noisy satellite data after applying a specified amount of smoothing to reduce the effects of uncorrelated measurement errors. Because of spatial correlation of the signal variability as indicated by the redness of the signal wavenumber spectra in Figs. 13–15, the error variance usually decreases more rapidly than the signal variance, in which case the S/N ratio increases with increased smoothing. The preferential attenuation of the error variance compared with the signal variance is evident from the example wavenumber spectra shown in Figs. 14 and 15.

For the case of the uncorrelated measurement errors considered in this study, there is a direct relationship between the signal-to-noise (S/N) variance ratio and the cross correlation between the error-free and noisy fields. To see this, consider $\hat{z}(x,y)$ to be an estimate of a signal $z(x,y)$ contaminated by uncorrelated errors $\epsilon(x,y)$,

$$\hat{z}(x,y) = z(x,y) + \epsilon(x,y).$$

The squared cross correlation between $\hat{z}(x,y)$ and $z(x,y)$ is

$$\begin{aligned}\hat{\rho}^2_{z\hat{z}} &= \frac{\big(\mathrm{Cov}\,[(z+\epsilon),z]\big)^2}{\mathrm{Var}\,[z+\epsilon]\,\mathrm{Var}\,[z]} \\ &= \frac{\big(\mathrm{Cov}\,[z,z] + \mathrm{Cov}\,[z,\epsilon]\big)^2}{\big(\mathrm{Var}\,[z] + 2\,\mathrm{Cov}\,[z,\epsilon] + \mathrm{Var}\,[\epsilon]\big)\mathrm{Var}\,[z]},\end{aligned} \tag{9}$$

where Cov and Var are shorthand notations for the spatial cross covariance and variance. Since the errors ϵ are uncorrelated with the signal z, their cross covariance is $\mathrm{Cov}\,[z,\epsilon] = 0$. And since $\mathrm{Cov}\,[z,z] = \mathrm{Var}\,[z]$, the squared cross correlation can be expressed as

$$\begin{aligned}\hat{\rho}^2_{z\hat{z}} &= \frac{\big(\mathrm{Var}\,[z]\big)^2}{\big(\mathrm{Var}\,[z]\big)^2 + \mathrm{Var}\,[\epsilon]\,\mathrm{Var}\,[z]} \\ &= \frac{1}{1+\gamma^{-2}},\end{aligned} \tag{10a}$$

where

$$\gamma^2 = \frac{\mathrm{Var}\,[z]}{\mathrm{Var}\,[\epsilon]} \tag{10b}$$

is the S/N variance ratio.

Specification of a threshold of minimum S/N variance ratio γ^2 for which the error-contaminated estimates are scientifically useful is somewhat subjective. Example maps are shown in Fig. 16 for $\gamma^2 = 1$, 4 and 10 for the case of normalized vorticity computed from noisy WaCM data, which is considered in detail later in Sec. 6.2. A choice of $\gamma^2 = 1$ (Fig. 16a) is clearly too liberal since any given small-scale feature is as likely to be attributable to noise as to real variability of the signal of interest. A mathematically convenient choice of threshold is $\gamma^2 = 10$, which corresponds to a S/N standard deviation ratio of $\gamma = 3.16$ (Fig. 16c). The signal standard deviation is then about three times larger than the error standard deviation, thus resulting in a clear distinction between the signal and errors in maps of the noisy fields $\hat{z}(x,y)$. For a value of $\gamma^2 = 10$, the squared cross correlation (10a) between the signal z and the noisy estimate $\hat{z}$ is $\hat{\rho}^2_{z\hat{z}} = 1.10^{-1} = 0.91$ so that the cross correlation between z and $\hat{z}$ is $\hat{\rho}_{z\hat{z}} = 0.95$.

A less conservative choice of $\gamma^2 = 4$ for the threshold S/N variance ratio corresponds to a signal standard deviation that is twice as large as the error standard deviation (Fig. 16b). The squared cross correlation between the signal z and the estimate $\hat{z}$ is then $\hat{\rho}^2_{z\hat{z}} = 1/1.25 = 0.80$ so that the cross correlation between z and $\hat{z}$ is $\hat{\rho}_{z\hat{z}} = 0.89$.

Our subjective assessment from visual inspection of maps with varying S/N ratios such as those shown in Fig. 16 is that a S/N standard deviation ratio of $\gamma = 2$ is insufficient to distinguish the signal from the errors

unambiguously. We have therefore adopted the threshold S/N standard deviation ratio of $\gamma = 3.16$ to define the resolution capability in the analysis that follows. Readers can judge for themselves from the examples of error-contaminated maps in Fig. 16 and in the figures in Secs. 6 and 8 whether they consider this threshold to be overly conservative. Since the amount of smoothing required to achieve a specified threshold S/N ratio increases with increasing value of the S/N ratio, lowering the threshold from our preferred choice of $\gamma = 3.16$ yields higher resolution assessments. The relative resolution capabilities of the spatially smoothed instantaneous fields constructed from SWOT versus WaCM data in Sec. 6, or of the spatially smoothed time-averaged fields constructed by either instrument in Secs. 8–10, would not change substantially by adopting a threshold different from $\gamma = 3.16$. In other words, changing the threshold value of γ would not qualitatively alter our conclusions regarding the relative resolution capabilities of SWOT and WaCM.

6. The Effects of Measurement Errors on Estimates of Instantaneous Velocity and Vorticity Fields

The effects of uncorrelated measurement errors are investigated in this section in isolation from the additional effects of sampling errors by assessing the resolution capabilities of maps of velocity and vorticity constructed from simulated SWOT and WaCM data for the idealized scenario of complete sampling of the full CCS domain on each satellite overpass. In reality, of course, the variables of interest can only be estimated within the measurement swaths at the time of each overpass. The analysis of simulated noisy SWOT and WaCM observations in this section must therefore be viewed as the best possible resolution of instantaneous fields that could be achieved within the actual SWOT and WaCM measurement swaths. The effects of sampling errors from the limited swath widths and irregular revisit intervals are investigated separately and in combination with measurement errors in Secs. 8–10 based on simulated time averages of noisy SWOT and WaCM observations.

For the reasons discussed at the end of the introduction, velocity estimates are characterized in this study in terms of the scalar magnitude of the vector-averaged velocity (which is equivalent to the current speed in the instantaneous maps considered in this section), rather than considering each velocity component separately. In the case of SWOT, the adequacy of the geostrophic approximation was discussed in Sec. 3 and this issue is not considered any further in this study. The question addressed for SWOT in this section is thus how the uncorrelated errors of the SSH measurements affect the resolution capabilities of estimates of velocity and vorticity computed geostrophically from SWOT data, irrespective of the accuracy of the geostrophic approximation.

6.1. SWOT

The procedure for simulating pre-processed SWOT estimates of SSH for this study was to smooth the SSH fields on the 0.5 km × 0.5 km grid of the CCS model using an isotropic Parzen smoother with a half-power filter cutoff wavelength of 2 km to mimic the footprint size of 1 km in the baseline science requirements for SWOT (see Appendix B.1). These smoothed SSH fields were then subsampled on a 1 km × 1 km grid over the full CCS model domain. The measurement errors with 2-km smoothing are shown in Appendix B.1 to be uncorrelated for this sample spacing. The errors of SWOT measurements of SSH on this sample grid were simulated by adding Gaussian-distributed random errors with the standard deviation of $\sigma_h = 2.74$ cm derived in Appendix F.

To assess the effects of errors in SWOT measurements of SSH, the estimates of velocity and vorticity that are of interest here were computed geostrophically from the error-free and noisy SSH fields. The results for error-free SSH and geostrophically computed surface velocity and vorticity are shown in the upper left panels of Figs. 17a–c for the CCCS region of the full CCS model domain. As noted previously from Fig. 5, the rich distribution of small-scale variability in the vorticity field in the top left panel of Fig. 17c compared with the smooth SSH field in the top left panel of Fig. 17a from which it was computed is a testament to the extreme spatial high-pass filtering operation of double differentiation to compute the vorticity geostrophically from SSH. Even the single differentiation of SSH to compute the velocity field geostrophically in the upper left panel of Fig. 17b results in considerable small-scale variability compared with the SSH field.

The effects of the $\sigma_h = 2.74$-cm SSH measurement errors on unsmoothed SWOT estimates of SSH and geostrophically computed velocity and vorticity are shown in the lower left panels of Figs. 17a–c. The SSH field has a distinctly speckled appearance but most of the features in the error-free fields are recognizable in the error-contaminated field. In contrast, the geostrophically computed velocity and vorticity signals are completely swamped by the errors. The masking of the velocity and vorticity signals is not surprising in view of the large error standard deviations derived in Sec. 4.1 (see Table 1).

It is clear that the noisy pre-processed SWOT estimates of SSH will have to be smoothed in ground-based post-processing to reduce the errors in geostrophically computed estimates of velocity and vorticity. Illustrative examples of error-free and noisy SSH fields are shown, respectively, in the top and bottom rows of Fig. 17a for smoothing with half-power filter cutoff wavelengths of 20, 50 and 80 km. The uncorrelated SSH measurement errors are quickly mitigated with increased smoothing (see Fig. 12a). A small amount of residual SSH measurement errors is visually apparent with 20-km smoothing but the errors become invisible with 50-km smoothing.

The reduction of errors in SWOT estimates of velocity requires more smoothing than for SSH (Fig. 17b). The residual errors of the velocity field computed geostrophically from the SSH field with 20-km smoothing for which the S/N standard deviation ratio is 1.5 would likely still render the velocity estimates unusable for most applications. The errors in the velocity estimates are essentially eliminated with 50-km smoothing for which the S/N standard deviation ratio is 7.70. Qualitatively, it thus appears that the resolution capability for SWOT estimates of velocity falls somewhere between 20 km and 50 km. This is quantified below.

Because of the amplification of measurement errors by differentiation, even more smoothing is required to obtain useful SWOT estimates of vorticity (Fig. 17c). The signal of interest is completely unrecognizable in the vorticity field computed geostrophically from the SSH field with 20-km smoothing. The noisy field with 50-km smoothing for which the S/N standard deviation ratio is 2.74 still has a somewhat mottled appearance compared with the 50-km smoothed error-free field. For example, the mesoscale anticyclone near the northwest corner of the CCCS region is broken up into multiple smaller-scale features in the noisy field. Numerous other artifacts of the 50-km smoothed measurement errors could easily be misinterpreted as small-scale signals. Qualitatively, it thus appears that the resolution capability for SWOT estimates of vorticity is somewhat coarser than 50 km.

It is noteworthy that the S/N standard deviation ratio of 2.74 for 50-km smoothing falls below our minimum threshold of 3.16, thus providing further rationale for why we advocated the value of 3.16 in Sec. 5 to define the resolution capability. The residual errors diminish very quickly with increased smoothing (see Fig. 12c). The S/N standard deviation ratio of 7.93 achieved by smoothing with a half-power filter cutoff wavelength of 80 km (see the right panels of Fig. 17c) is more than sufficient to eliminate essentially all of the residual errors in the geostrophically computed vorticity field.

To determine the resolution capability of in-swath SWOT estimates of velocity and vorticity, we smoothed the error-free and noisy SSH fields with half-power filter cutoff wavelengths ranging from 10 km to 150 km. We then computed the velocity and vorticity fields geostrophically from these smoothed error-free and noisy SSH fields. The resulting S/N standard deviation ratios are shown as functions of half-power filter cutoff wavelength in Fig. 18a. According to our criterion of a S/N threshold of 3.16, the wavelength resolution capability of in-swath SWOT estimates of instantaneous velocity is approximately 32 km, which falls between the smoothing shown in the second and third columns of Fig. 17b. For in-swath SWOT estimates of vorticity, the S/N threshold of 3.16 implies a resolution capability of approximately 54 km, which is slightly more than the 50-km smoothing shown in the third column of Fig. 17c.

It is shown in Appendix C that the feature resolution capability is approximately half of the wavelength resolution. Fig. 18a thus suggests that SWOT will be able to detect velocity and vorticity features with diameter scales of approximately 16 km and 27 km, respectively, within each measurement swath. These resolution capabilities will be degraded somewhat by edge effects in the smoothing from the fact that the 50-km swath widths of the SWOT measurements (see Sec. 7) are comparable to the half-power filter cutoff wavelengths required to achieve the S/N threshold of 3.16. This is especially an issue for SWOT estimates of vorticity since they require more smoothing than for SWOT estimates of velocity.

6.2. WaCM

A similar procedure was followed to simulate the effects of measurement errors on WaCM estimates of velocity and vorticity. The 5-km footprint size anticipated for pre-processed WaCM estimates of surface velocity was achieved by isotropically smoothing the 0.5 km × 0.5 km gridded surface velocity fields from the CCS model with a half-power filter cutoff wavelength of 10 km (see Appendix B.2). In the baseline design, the measurement errors with this smoothing are uncorrelated with a speed standard deviation of $\sigma_{spd} = 0.50$ m s^{-1} on a 5 km × 5 km grid. Assuming that these speed uncertainties are equally partitioned between two orthogonal velocity components, this corresponds to an error standard deviation of $\sigma_{u,v} = 0.354$ m s^{-1} for each component.

As discussed previously, the simulated WaCM data in this study were oversampled on a 1 km × 1 km grid in order to improve the derivative estimates for calculation of the vorticity signal (see Appendix H). The 10-km smoothing and 1 km × 1 km oversampling were achieved by adding uncorrelated errors with a standard deviation of 3.54 m s^{-1} to each unsmoothed velocity component on the 0.5 km × 0.5 km model grid prior to smoothing and subsampling. This 10-fold increase in noise level compared with the standard deviation of $\sigma_{u,v} = 0.354$ m s^{-1} for the uncorrelated errors of pre-processed WaCM estimates of surface velocity components is commensurate with the 10-fold difference between the 0.5 km × 0.5 km model grid spacing and the 5-km footprint size of the WaCM data.

The effects of the velocity component measurement errors on 10-km smoothed estimates of velocity and vorticity from pre-processed WaCM data are shown in the lower left panels of Figs. 19a and b. The somewhat smoother appearances of the noisy velocity and vorticity fields compared with the lower left panels of Fig. 17b and c for SWOT estimates of velocity and vorticity are because of the 10-km smoothing applied in the pre-processing of WaCM data compared with only 2-km smoothing in pre-processing of SWOT data. The velocity signal of interest is vaguely detectable in the noisy field in the bottom left panel of Fig. 19a but the vorticity signal is completely masked in the bottom left panel of Fig. 19b.

The resolution capabilities of in-swath WaCM estimates of velocity and vorticity were assessed by applying the same smoothing to the error-free and noisy velocity component fields. Examples of the velocity and vorticity fields computed from smoothed velocity fields with and without simulated measurement errors are shown in Figs. 19a and b for half-power filter cutoff wavelengths of 20, 50 and 80 km. For in-swath velocity, the S/N ratio is only 2.30 with the 80-km smoothing shown in the last column of Fig. 19a. According to the S/N=3.16 criterion adopted here, this amount of smoothing is insufficient. The inadequacies of 80-km smoothing are visually apparent from the discrepancies between the smoothed map of error-free velocity in the top right panel and the smoothed map of the velocity signal plus errors in the bottom right panel.

For the case of in-swath vorticity, the S/N ratio is only 1.72 with the 80-km smoothing shown in the last column of Fig. 19b. There are numerous artifacts in the bottom right panel that would be misinterpreted as small-scale vorticity signals.

The S/N standard deviation ratios for velocity and vorticity are shown as functions of the half-power filter cutoff wavelength in Fig. 18b. By the S/N=3.16 threshold adopted here, the wavelength resolutions for in-swath WaCM estimates of velocity and vorticity are coincidentally both approximately 130 km. The more rapid convergence toward this threshold for vorticity compared with velocity is because of the noise attenuation at both high and low wavenumbers in the band-pass filtering operation of the response function for centered difference estimates of the derivatives in the calculation of vorticity (see Appendix H; see also Fig. 15).

A noteworthy feature of the S/N curves for WaCM estimates of velocity and vorticity in Fig. 18b is that they are much flatter than for the SWOT estimates in Fig. 18a. This flatness implies that the standard deviation of the residual errors decreases only slightly faster than the signal with increased smoothing. It also means that the resolution capabilities for WaCM are much more sensitive to the choice of the threshold value of the S/N standard deviation ratio that is used to define resolution capability. Lowering the threshold value from our recommended value of 3.16 to a value of 2, for example, would correspond to much higher resolution capabilities of 67 km and 91 km for WaCM estimates of velocity and vorticity, respectively. For SWOT, the same choice of a threshold S/N value of 2 would only improve the resolution capabilities from 32 km to 24 km for velocity and from 54 km to 44 km for vorticity.

6.3. Discussion of the Effects of Measurement Errors Alone

It is seen from Fig. 18 that the resolution capability of in-swath SWOT estimates of instantaneous velocity and vorticity are superior to those from WaCM data with the baseline noise standard deviation of $\sigma_{spd} = 0.50$ m s^{-1} when considering the effects of measurement errors alone, i.e., by considering the unrealistic case of measurement swaths that sample the entire CCS model domain on each satellite overpass. However, in addition to the limitations of the geostrophic approximation discussed in Sec. 3, SWOT data are severely limited by the narrow measurement swaths (see the top panels of Fig. 20 below). It is shown in Sec. 8 that the sampling errors arising from these narrow measurement swaths are a more significant limitation than measurement errors for mapping the geostrophically computed velocity and vorticity fields over the full CCS model domain considered in this study. But even if SWOT estimates of these variables are considered only within the narrow measurement swaths, the 32-km and 54-km smoothing required to achieve a S/N ratio of 3.16 (see Fig. 18a) for geostrophically computed velocity and vorticity, respectively, will lead to artifacts from edge effects near the edges of the two parallel 50-km measurement swaths.

With its much wider measurement swaths (see the bottom panels of Fig. 20 below for a swath width of 1200 km and Fig. 41 below for a swath width of 1800 km), edge effects are less of an issue for WaCM than for SWOT. Measurement errors are therefore more limiting than sampling errors. This is quantified in Secs. 8–10. The resolution capability of ∼130 km for in-swath WaCM estimates of instantaneous snapshots of velocity and vorticity is coarse for investigations of small-scale variability. But it is much better than the present resolution capability of about 200 km by about 1 month (see Fig. 50 below).

The improved resolutions that could be achieved from WaCM for measurement noise standard deviations smaller than the baseline value of $\sigma_{spd} = 0.50$ m s^{-1} are investigated in Sec. 10.2. If the noise can be reduced to $\sigma_{spd} = 0.25$ m s^{-1}, for example, it is shown that the resolution capabilities of instantaneous snapshot maps of velocity and vorticity constructed from WaCM data would be about 50 km and 74 km, respectively. These values are still coarser than can be achieved in SWOT estimates of velocity and vorticity, but over a swath width that is more than an order of magnitude wider for WaCM and is therefore less prone to edge effects in the smoothed fields.

Thus far, we have considered only the effects of spatial smoothing to mitigate the effects of measurement errors. At least in principle, the residual errors can also be reduced by applying temporal smoothing. In practice, this introduces the additional effects of the sampling errors that are discussed in Sec. 7. The effects of combined space-time smoothing are investigated in Secs. 8–10 where it is shown that temporal smoothing is advantageous for WaCM but, perhaps counterintuitively, detrimental for SWOT.

7. SWOT and WaCM Sampling Characteristics

The sampling characteristics of the SWOT and WaCM radars are fundamentally different. SWOT will measure SSH across a swath width of 120 km with a 20-km gap centered on the satellite ground track, thus resulting in two parallel 50-km swaths. For the purposes of the analysis in Sec. 8, we have assumed that WaCM will have a swath width of 1200 km with a 100-km gap centered on the satellite ground track, thus resulting in two parallel 550-km swaths. Examples of SWOT and WaCM measurement swaths for single simulated satellite overpasses of the CCS model domain are overlaid on a map of the vorticity field in Fig. 20. The factor-of-11 better sampling coverage for WaCM compared with SWOT has a profound effect on the ability to map the space-time evolution of the surface velocity and vorticity fields.

Recent engineering developments indicate that it may be possible to increase the swath width of WaCM to 1800 km, which is a factor-of-17 better coverage than SWOT. The improved sampling afforded by this wider swath and the resulting improvements in the resolution capabilities for time-averaged maps of velocity and vorticity constructed from WaCM data are summarized in Sec. 10.

The limited swath widths and the discrete space-time sampling patterns result in the following three sources of sampling errors that occur independently of the effects of measurement errors considered in Secs. 4 and 6:

1. One form of sampling errors arises from the need to synthesize the measurements from multiple satellite overpasses in order to map the variables of interest over regions larger than the measurement swaths from

a single satellite overpass. The interest in this study is in mapping the velocity and vorticity fields over the full CCS model domain. Because of the rapid evolution of submesoscale features in these variables between the times of different satellite overpasses, spatial discontinuities can occur across the edges of neighboring or overlapping measurement swaths from the different orbits. For example, adjacent pairs of SWOT measurement swaths are sampled about 10 days apart (see the left panel of Fig. 21). Any temporal evolutions of the structure, location and intensity of small-scale features in the regions of overlap will be misinterpreted as spatial variability in time-averaged maps constructed from measurements along multiple satellite overpasses.

2. An equally important and related source of sampling errors arises from differences between the time average of the discretely sampled fields and the true time average. Because of the rapid evolution of submesoscale variability, the estimated time-average is corrupted by unresolved temporal variability between the discrete samples. This is similar to the classical problem of aliasing but this source of sampling errors is more complicated in maps constructed from the measurements from multiple satellite overpasses. The discrete sampling then occurs at different times in different regions of the mapping domain, resulting in a patchwork of different aliasing artifacts.
3. The two sources of sampling errors summarized above can be avoided if the satellite data are smoothed and analyzed on a swath-by-swath basis. But this introduces a third source of sampling errors in the form of edge effects that can occur from incomplete data within the span of the smoother. This type of sampling errors was neglected in Sec. 6 by considering the idealized case of SWOT and WaCM measurement swaths that sample the full CCS model domain on each satellite overpass. An estimate of the spatially smoothed field within an actual measurement swath is imperfect if the distance between the estimation location and a swath edge is less than half of the span of data that are included in the weighting function of the smoother. The imperfections worsen the closer the estimates are to the swath edge. This source of error is worse for some smoothing algorithms than for others and the magnitudes of the errors can depend on the detailed structure of the field near the edge of the dataset. Edge effects are especially problematic when smoothing with a half-power filter cutoff wavelength that is comparable to or larger than the swath width.

All three of the above sources of sampling errors are exacerbated by a narrow swath width and are thus much bigger issues for SWOT than for WaCM. The magnitudes of the first two sources of sampling errors summarized above also depend strongly on the satellite repeat period. SWOT will be launched into a prograde orbit (ascending ground tracks from southwest to northeast) with an inclination of 77.6°, an altitude of 890.3 km and a 21-day exact repeat with 292 orbits per repeat period. As WaCM is in the early stages of planning, the exact orbit has not yet been determined. For the simulations in this study, we have assumed the same orbit configuration as the QuikSCAT satellite, which is a retrograde orbit (ascending ground tracks from southeast to northwest) with an inclination of 98.6°, an altitude of 802.4 km and a 4-day exact repeat with 57 orbits per repeat period.

The effects of the above orbit parameters on the space-time sampling patterns are shown in Fig. 21. The dots in each panel indicate the longitudes and times of ascending ground tracks over a longitudinal range of 25° at a fixed reference latitude. The sampling patterns are similar for the descending ground tracks, except shifted in time by about half a day. The longitudes of the descending ground tracks relative to the longitudes of the ascending ground tracks vary with latitude and are therefore not displayed in Fig. 21.

Consider first the space-time sampling pattern for the WaCM orbit adopted for this study, which is simpler than the sampling pattern for SWOT. As noted above, we assume a swath width of 1200 km for the analysis in 8; the improved sampling for a swath width of 1800 km is considered in Sec. 10.1. As shown in the right panel of Fig. 21, ascending ground tracks cross the western and eastern portions of the CCS model domain (indicated by the vertical dashed lines) approximately one day apart. This is followed by a 2-day gap and then the same pair of ascending ground tracks are sampled again with the same 1-day time separation. During the 2-day gap, the outer portions of a 1200-km WaCM measurement swath from ascending ground tracks outside of the CCS model domain sample small portions of the model domain. In addition, the CCS model domain is sampled twice along descending ground tracks (not shown in Fig. 21) approximately half a day earlier than each ascending ground track. The net result is that nearly every grid

point in the CCS model domain is sampled at least four times by WaCM during each 4-day repeat period (see Fig. 23 below).

The sampling pattern for SWOT is considerably more complicated than for WaCM. From the left panel of Fig. 21, it can be seen that the SWOT ground tracks will map out a grid with a westward-migrating longitude spacing of 2.466° during the first half of each 21-day repeat period. This track spacing is coarse relative to the 120-km span of the two parallel measurement swaths of the SWOT radar. The SWOT ground tracks then map out another grid with the same coarse westward migrating longitude spacing of 2.466° during the second half of the 21-day repeat period. The grid of ground track overpass times from the second half of each repeat period is interleaved spatially half way between the grid from the first half, thus resulting in a longitude spacing of 1.233° of the ground tracks during each 21-day repeat period. Within the longitudinal extent of the CCS model domain, this interleaved pattern of ground tracks results in the two 4-day subcycles indicated by pairs of horizontal dotted lines in Fig. 21. The 4-day subcycles are separated by 6-day gaps in coverage.

In addition to the sampling summarized in the left panel of Fig. 21 for the ascending SWOT orbits, there is analogous sampling on descending orbits. These descending orbits occur about half a day later than the ascending orbits.

With the 120-km span of the two parallel measurement swaths of the SWOT radar and its 77.6° orbit inclination, the 1.233° longitudinal spacing of ground tracks provides very nearly complete coverage of the Earth's surface between about 78°N and 78°S during each 21-day repeat period. The interleaved sampling of the CCS region in two 4-day subcycles separated by 6-day gaps is shown in the left and middle panels of Fig. 22. It can be seen from the right panel of Fig. 22 that there are small diamond-shaped regions that are never sampled by SWOT. These diamond-shaped regions account for about 3% of the area in the CCS region. For context, the thick lines in the right panel of Fig. 22 show the coarse ground track spacing of the 10-day repeat orbit that has been maintained since September 1992 by the TOPEX/Poseidon, Jason-1, Jason-2 and Jason-3 sequence of nadir altimeters. An important aspect of the SWOT sampling over the 21-day repeat period is the characteristic noted previously from the left panel of Fig. 21 that spatially adjacent parallel swaths are sampled about 10 days apart. It will be seen in Sec. 8 that this results in severe artifacts in maps of the variables of interest constructed from multiple satellite overpasses because of the effects of the first of the three sampling errors summarized above.

From the the space-time sampling pattern of the SWOT orbit, there are two natural choices of time scale for SWOT sampling of the CCS model domain considered in this study. About 73% of the region is sampled in each of the two 4-day periods but approximately 14 days are required for SWOT to sample the full CCS region (excluding the above-noted small diamond-shaped regions that are never sampled). Histograms of SWOT and WaCM sampling of the CCS model domain are shown in Fig. 23 for 4-day and 14-day periods. For the case of the 4-day period shown in the top panel, 52% of the grid points in the CCS model are sampled once by SWOT and 27% are not sampled at all. The remaining 21% of the grid points that are sampled twice correspond to the regions of overlap of the measurement swaths from the intersecting ascending and descending ground tracks. During the same 4-day period, about 90% of the model grid points are sampled four times by WaCM for the 1200-km swath considered in this section, and about 9% of the grid points are sampled five times. About 1% of the grid points are sampled only three times by WaCM.

Histograms of the SWOT and WaCM sampling for the 14-day period are shown in the bottom panel of Fig. 23. About half of the CCS model grid points are sampled twice by SWOT during this 14-day period while about 25% and 16% of the grid points are sampled once and three times, respectively. The 3% of the grid points that are never sampled by SWOT correspond to the white diamond-shaped regions in Fig. 22. During the same 14-day period, about 88% of the model grid points are sampled either 13 or 14 times by WaCM. All but about 1% of the remaining grid points are sampled more than 14 times.

The effects of the sampling characteristics summarized above on maps of space-time smoothed velocity and vorticity constructed from simulated SWOT and WaCM data over the CCS model domain are investigated in Secs. 8–10, both separately and in combination with the effects of the measurement errors that were previously considered in isolation in Sec. 6.

8. The Effects of Combined Measurement and Sampling Errors on Estimates of Time-Averaged Velocity and Vorticity Fields

The improvements of the signal-to-noise ratios of SWOT and WaCM estimates of velocity and vorticity that can be achieved from spatial smoothing alone within a single measurement swath were assessed in Sec. 6. Mapping the variables of interest over a domain larger than a single swath of the instrument requires time averaging of measurements from multiple satellite orbits. While time averaging can mitigate the effects of uncorrelated measurement errors, it can also introduce artifacts from the three types of sampling errors discussed in Sec. 7. The question addressed in this section is whether the benefits of the attenuation of measurement errors from time averaging prevail over the added effects of sampling errors. It will be shown that sampling errors are the primary issue for SWOT and measurement errors are the primary issue for WaCM.

Because of the 4-day and 14-day subcycles in the 21-day repeat orbit of SWOT that were discussed in Sec. 7, two natural choices for temporal averaging period are 4 days and 14 days. These are the times required for, respectively, coarse and nearly complete SWOT coverage of the full CCS model domain (see Fig. 22). The 4-day averaging period matches the exact repeat period of the orbit assumed here for WaCM. With the swath width of 1200 km used for the simulations of WaCM data in this section, essentially all of the grid points in the CCS model domain are sampled by WaCM at least four times during each 4-day repeat period (see Fig. 23). In contrast, none of the grid points are sampled more than twice during a 4-day subcycle of the SWOT orbit; about half are sampled only once and about a quarter are not sampled at all. SWOT therefore benefits much less than WaCM from error reduction by time averaging. Moreover, the sampling errors discussed in Sec. 7 are much more severe for SWOT because its swath width is narrower by more than an order of magnitude than the 1200-km swath width of WaCM assumed for the analysis in this section. The benefits of increasing the WaCM swath width to 1800 km are summarized in Sec. 10.

8.1. Time Averages of Error-Free Velocity and Vorticity

Before determining the S/N ratios of SWOT and WaCM estimates of velocity and vorticity from space-time smoothed fields of noisy SSH and velocity components, it is useful to provide context by looking at the effects of time averaging alone on the velocity and vorticity fields of interest. Maps of the magnitude of error-free surface velocity and vorticity from the CCS model at the full 0.5 km $\times$ 0.5 km grid resolution of the model with no spatial smoothing are shown in Fig. 24 for a snapshot and for 4-day and 14-day vector-averaged velocity centered on the time of the snapshot. The two time averages were computed from snapshots of the model output at intervals of 0.5 days.

The periodic structures with very small scales in the vorticity fields in the bottom panels of Figs. 24b and c that are not present in instantaneous maps such as that shown in the bottom panel of Fig. 24a are likely aliasing artifacts from discrete sampling of submesoscale features that are rapidly advected by the strong jet-like currents that are evident in the top panels. Such aliasing issues would not occur if the model output had been saved at a sufficiently fine sample interval, e.g., hourly rather than twice per day. The existence of this aliasing emphasizes how quickly the small-scale variability evolves, thus exposing one of the challenges in mapping submesoscale variability from satellite observations.

Notwithstanding the possible aliasing artifacts, it is visually apparent that the energetic small-scale variance in the instantaneous map in Fig. 24a is dramatically reduced in the 4-day and 14-day averages in Figs. 24b and c. This is quantified by the alongshore wavenumber spectra shown in Fig. 25. In the case of velocity, the variance at the smallest wavenumbers (longest wavelengths) is reduced by modest factors of about 2 and 3 in 4-day and 14-day averages, respectively. The amount of variance attenuation from time averaging alone increases monotonically with increasing wavenumber. At a wavenumber of 0.02 cpkm (a wavelength of 50 km), for example, the variance of the magnitude of the vector-averaged velocity is reduced by about a factor of 4 in the 4-day average and about a factor of 11 in the 14-day average. At a wavelength of 10 km, these reductions of variance increase to factors of about 9 and 49, respectively.

The variance reductions from time averages alone are even greater for vorticity. The vorticity variance at the longest wavelengths is reduced by factors of about 4 and 8 in the 4-day and 14-day averages, respectively.

These variance reductions increase to factors of about 7 and 29 at a wavelength of 50 km and factors of about 16 and 80 at a wavelength of 10 km.

The reductions of variance at the lowest wavenumbers in the time-averaged fields in both panels of Fig. 25 are perhaps surprising. This occurs because the most energetic features with large scales in the alongshore dimension are generally narrow in the cross-shore dimension. The locations of these elongated features evolve quickly in time. Their contributions to the alongshore wavenumber spectrum are thus attenuated in the 4-day and 14-day averaged velocity and vorticity fields.

As summarized in Sec. 5, our metric for defining the resolution capability is based on the square root of the ratio of the spatial variance of the signal to the spatial variance of the total errors. In the space-time smoothed fields considered in Secs. 8.4, 8.5, 9 and 10, the total errors are partitioned between measurement errors and sampling errors. In order for the S/N ratio to improve, the space-time smoothing must attenuate the total error variance more than the amount by which the signal variance is attenuated by the same space-time smoothing.

8.2. The Data Processing Procedure for Assessing Resolution Capability

The procedure for assessing the relative importance of measurement errors and sampling errors and determining the resolution capabilities for SWOT and WaCM estimates of space-time smoothed velocity and vorticity is the following:

Step 1. Twice-daily snapshots of SSH (for simulated SWOT data) and surface velocity (for simulated WaCM data) were constructed on the complete 0.5 km $\times$ 0.5 km model grid in two combinations:

i) The error-free model output of SSH and surface velocity.

ii) The model output of SSH and surface velocity with Gaussian-distributed uncorrelated measurement errors added. To simulate SWOT measurement errors, the uncorrelated errors added to the SSH fields had a standard deviation of 5.48 cm on the 0.5 km $\times$ 0.5 km model grid. To simulate WaCM measurement errors, the uncorrelated errors added to each velocity component had a standard deviation of 3.54 m s^{-1} on the 0.5 km $\times$ 0.5 km model grid. When smoothed in step 2 below to achieve footprint diameters of 1 km and 5 km for SWOT and WaCM, respectively, this yields the desired measurement error standard deviations of $\sigma_h = 2.74$ cm for simulated pre-processed SWOT estimates of SSH and $\sigma_{u,v} = 0.354$ m s^{-1} for simulated pre-processed WaCM estimates of each velocity component.

Step 2. To simulate pre-processing of SWOT data, the twice-daily error-free and noisy SSH fields from step 1 were smoothed isotropically on the 0.5 km $\times$ 0.5 km model grid with a half-power filter cutoff wavelength of 2 km to achieve the desired SWOT footprint diameter of 1 km. To simulate pre-processing of WaCM data, the twice-daily error-free and noisy surface velocity fields from step 1 were similarly smoothed isotropically on the 0.5 km $\times$ 0.5 km model grid with a half-power filter cutoff wavelength of 10 km to achieve the WaCM footprint diameter of 5 km. The smoothed SSH and surface velocity fields on the 0.5 km $\times$ 0.5 km model grid were then subsampled on a 1 km $\times$ 1 km grid to simulate the pre-processed SWOT and WaCM data used throughout the rest of this study.

Step 3. The twice-daily snapshots of simulated pre-processed SWOT estimates of SSH and WaCM estimates of surface velocity from step 2 were sampled on the complete grid and at only the times and locations of the in-swath measurements to obtain maps with four different combinations of signal and simulated measurement and sampling errors for each choice of averaging period (4 days and 14 days):

i) Error-free SSH and surface velocity signals on the complete 1 km $\times$ 1 km grid.

ii) SSH and surface velocity signals plus Gaussian distributed uncorrelated measurement errors on the complete 1 km $\times$ 1 km grid.

iii) Error-free SSH and surface velocity signals sampled only at the 1 km $\times$ 1 km grid points within the measurement swaths at the time of each individual satellite overpass rounded to the nearest 0.5-day time step of the model.

iv) SSH and surface velocity signals plus Gaussian distributed uncorrelated measurement errors sampled only at the 1 km × 1 km grid points within the measurement swaths at the time of each individual satellite overpass rounded to the nearest 0.5-day time step of the model.

Step 4. For each of the two averaging periods considered here (4 days and 14 days), the time-averaged error-free SSH and surface velocity component fields on the 1 km × 1 km grid (map i from step 3) and the time-averaged maps of SSH and surface velocity with the three combinations of errors in maps ii–iv from step 3 (measurement errors alone, sampling errors alone, and combined measurement and sampling errors) were additionally smoothed spatially with half-power filter cutoff wavelengths ranging from 10 to 150 km.

Step 5. Velocity and vorticity were computed geostrophically from each set of four space-time smoothed maps of SSH from step 4 using centered difference estimates of the spatial derivatives in order to assess the resolution capabilities for SWOT. Likewise, vorticity was computed from each set of space-time smoothed maps of surface velocity components from step 4 using centered difference estimates of the spatial derivatives to assess the resolution capabilities for WaCM.

Step 6. The errors for each set of three space-time smoothed fields with measurement and/or sampling errors from step 5 were computed for each variable of interest by subtracting the space-time smoothed error-free value on the complete 1 km × 1 km grid from the space-time smoothed error-contaminated value at each 1 km × 1 km grid point. The sets of three error fields as functions of the half-power filter cutoff wavelength of the spatial smoothing allow assessments of the effects of measurement errors alone, sampling errors alone, and the combination of measurement and sampling errors.

Step 7. The spatial variances of each of the three error fields obtained in step 6 and the spatial variance of the space-time smoothed error-free signals from step 5 were computed from the 1 km × 1 km gridded values for each variable of interest for each of the half-power filter cutoff wavelengths of the spatial smoothing. In the case of SWOT, the 1 km × 1 km grid points outside of the sample swaths during the 4-day and 14-day averaging periods (see Fig. 22) were excluded from the variance calculations. There were no missing grid points in any of the WaCM fields for either time average.

Step 8. The resolution capabilities for SWOT and WaCM estimates of each variable of interest were defined as summarized in Sec. 5 to be the half-power filter cutoff wavelength at which the signal-to-noise variance ratio achieves a value of 10 (i.e., a signal-to-noise standard deviation ratio of 3.16). This half-power filter cutoff wavelength was estimated by linear interpolation between the discretely chosen filter cutoff wavelengths that were applied in step 4.

8.3. SWOT Estimates of Space-Time Smoothed Sea Surface Height

To provide context for understanding the combined effects of measurement and sampling errors on SWOT estimates of surface ocean velocity and vorticity that are the primary interest of this study, it is enlightening to look at time averages of the simulated SWOT measurements of SSH from which surface velocity and vorticity are computed geostrophically in Secs. 8.4 and 8.5.

We first consider the 4-day subcycle of the SWOT orbit with the measurement swaths shown in the left panel of Fig. 22. The four maps of 4-day average SWOT measurements of SSH from step 4 of the procedure summarized in Sec. 8.2 are shown in the top four panels of Fig. 26 for the case of 2-dimensional spatial smoothing with a half-power filter cutoff wavelength of 25 km. The map in the top panel of Fig. 26d simulates the 4-day average SSH field that would be obtained from SWOT data based on the combination of SWOT sampling and measurement errors with a standard deviation of $\sigma_h = 2.74$ cm for a footprint diameter of 1 km. The maps in the top panels of Figs. 26b and c represent the SSH fields that would be obtained from SWOT data if it were possible to isolate, respectively, the measurement errors and sampling errors in real data. The bottom three panels are the differences of each of the three error-contaminated fields in the associated top panels minus the error-free field in Fig. 26a.

The background mottled appearance of the error field in the bottom panel of Fig. 26d represents the residual uncorrelated measurement errors after smoothing with the half-power filter cutoff wavelength of 25 km used for Fig. 26. The most important thing to note is that the largest errors with magnitudes exceeding 1 cm in the bottom panel of Fig. 26d coincide geographically with the largest errors in the bottom

panel of Fig. 26c that includes only the effects of sampling errors. The total errors in Fig. 26d are thus seen to be dominated by sampling errors, at least in the regions of most energetic submesoscale variability in the eastern portion of the CCS model domain.

The 4-day average SSH maps in Fig. 26c and d are affected by two of the three sources of sampling errors discussed in Sec. 7. Some of the sampling errors in the bottom panels of Figs. 26c and d are edge-effect artifacts from incomplete data within the span of the smoother near the edges of the SWOT measurement swaths. But most are aliasing artifacts from inaccurate representation of the 4-day average of the SSH field. As discussed in Sec. 7 from the top panel of Fig. 23, 27% of the CCS model domain is not sampled at all during the 4-day period. These white areas in Figs. 26c and d are sampled over the second 4-day subcycle that begins 6 days later (see the middle panel of Fig. 22). Within the 73% of the CCS model domain that is measured by SWOT during the first 4-day subcycle, 52% of the region is sampled only once and 21% is sampled twice. The latter corresponds to the diamond-shaped areas formed by the intersections of ascending and descending measurement swaths. One or two samples are not adequate to resolve the rapidly evolving submesoscale features during the 4-day averaging period.

Because none of the grid points in the CCS model domain are sampled more than twice and half are sampled only once, time averaging over the 4-day subcycle does little to reduce the measurement errors. Most of the reduction of measurement errors in Fig. 26d is therefore attributable to the 25-km spatial smoothing that reduces the $\sigma_h = 2.74$ cm standard deviation of the uncorrelated noise by about a factor of five (see Appendix D) and results in the background mottled appearance noted above.

It is noteworthy that the SSH errors in the bottom panel of Fig. 26b that includes only the effects of measurement errors are much smaller than the mottled background noise from residual measurement errors in the bottom panel of Fig. 26d, even in the regions of weak submesoscale variability where sampling errors are relatively small in Fig. 26d. This is because the measurement errors in Fig. 26b are much more effectively suppressed by the averaging of the eight individual SSH maps at 0.5-day intervals during the 4-day averaging period. From the sampling characteristics noted above, only 21% of the CCS model domain benefits from temporal averaging of the measurement errors. But those regions are sampled only twice during the 4-day averaging period, thus reducing the measurement noise by half as much as the averaging of eight realizations in Fig. 26b. The remaining 79% of the CCS model domain is sampled only once (52%) or not at all (27%) during the 4-day period and thus do not benefit at all from temporal averaging of the measurement errors.

Intuitively, it may seem that the errors in Fig. 26d can be suppressed by increasing the averaging period to 14 days to increase the number of samples, thus also expanding the SWOT coverage to nearly all of the CCS model domain (see the right panel of Fig. 22). However, because the SWOT sampling consists of only two 4-day subcycles during the 14-day period, measurement errors are only slightly reduced in the longer 14-day average. This is because only about 16% and 1% of the region are sampled three and four times, respectively; about 53% of the CCS model domain is sampled twice during the 14-day period and about 26% is sampled only once.

More importantly than the small reduction of the effects of measurement errors from the modest increase in the numbers of samples at any given location, the longer averaging period of 14 days includes considerably more evolution of the energetic submesoscale features compared with the 4-day averaging period for Fig. 26. The SWOT sampling during during the 14-day period consists of two 4-day subcycles that are interleaved spatially and separated by a 6-day gap. The sampling errors are consequently dramatically worse in the 14-day average SSH field than in the 4-day average SSH field (compare the bottom panels of Figs. 27c and d with the bottom panels of Figs. 26c and d). In addition to the inadequate resolution of the rapidly evolving submesoscale features and the edge effects of smoothing that were both evident in the 4-day average maps in Fig. 26, the third source of sampling errors discussed in Sec. 7 arises in the 14-day average from discontinuities of SSH at the boundaries of spatially adjacent measurement swaths that are separated by about 10 days in time (see the left panel of Fig. 21). It will be seen in Secs. 8.4 and 8.5 that the velocity and vorticity computed geostrophically from centered difference estimates of the derivatives of the SSH field at these boundaries misinterpret temporal variability as spatial variability.

It is clear from Fig. 26 and especially from Fig. 27 that errors from inadequate sampling of rapidly evolving submesoscale features will severely impact the accuracy of geostrophically computed velocity and vorticity fields that are defined in terms of first and second derivatives, respectively, that are approximated

by centered differences of the SSH in space-time smoothed simulated noisy SWOT data. In contrast, the far superior sampling by WaCM and the fact that it measures velocity directly and thus requires only first derivatives of velocity to estimate vorticity, sampling errors are much less of an issue for WaCM than for SWOT. This is shown below from simulated SWOT and WaCM estimates of surface velocity and vorticity in Secs. 8.4 and 8.5, respectively.

8.4. The Resolution Capabilities of Time-Averaged Surface Velocity Fields

As in Sec. 6, the simulated SWOT estimates of velocity in this section neglect the limitations of the geostrophic approximation discussed in Sec. 3. The question addressed here for SWOT is thus how the combined SSH measurement errors and sampling errors affect the resolution capabilities of geostrophically computed SWOT estimates of velocity, irrespective of the accuracy of the geostrophic approximation. It will be seen that the resolutions that can be achieved in SWOT estimates of velocity are so coarse that the geostrophic approximation may not be a major limitation.

The four maps of the magnitudes of 4-day vector-averaged geostrophically computed SWOT estimates of velocity from step 5 of the procedure summarized in Sec. 8.2 are shown in the top four panels of Fig. 28 for the case of spatial smoothing with a half-power filter cutoff wavelength of 25 km. These are the magnitudes of the surface velocity field computed geostrophically from the simulated SWOT estimates of SSH with 25-km smoothing in the top four panels of Fig. 26. The map in the top panel of Fig. 28d simulates the magnitude of the velocity field that would be estimated geostrophically from SWOT data based on the combination of SWOT sampling and simulated measurement errors with a standard deviation of $\sigma_h = 2.74$ cm. The maps in the top panels of Figs. 28b and c represent the magnitudes of the velocity fields[4] that would be obtained from SWOT data contaminated by, respectively, measurement and sampling errors individually. With real observations, it is of course not possible to separate the two sources of errors in space-time smoothed maps. Analogous to Fig. 26, the bottom three panels are the differences of each of the three error-contaminated fields in the associated top panels minus the error-free field in Fig. 28a.

As in the case of the SSH mapping errors in Figs. 26c and d, the largest errors in the velocity fields in the bottom panel of Fig. 28d coincide geographically with the largest errors in the bottom panel of Fig. 28c that includes only the effects of sampling errors. The total errors in Fig. 28d are thus dominated by sampling errors, at least in the regions of most energetic submesoscale variability in the eastern portion of the CCS model domain. These sampling errors arise primarily from inaccurate representation of the 4-day average of the velocity field because of unresolved space-time variability of the rapidly evolving submesoscale features in the SSH field.

While the patterns of the total error field in the bottom panel of Fig. 28d are generally similar to the patterns of sampling errors alone in the bottom panel of Fig. 28c, there is considerably more small-scale variability in the total error field. The small-scale noise in the total error field in the bottom panel of Fig. 28d is much more energetic than the small-scale noise in the map of measurement errors alone in the bottom panel of Fig. 28b. As discussed in Sec. 8.3 from comparisons of the SSH errors in the bottom panels of Figs. 26b and d, this is because the simulated measurement errors in Fig. 28b have been much more effectively suppressed by the averaging of the eight individual maps at 0.5-day intervals during the 4-day averaging period. The effects of measurement errors are even more evident in the total error field for geostrophically computed velocity in the bottom panel of Fig. 28d than in the total error field for SSH in Fig. 26d because the relatively small mottled background noise in the 25-km smoothed SSH field is amplified in the centered difference estimates of the derivatives in the geostrophic equations. This amplification of noise in maps of geostrophically computed velocity constructed from simulated SWOT data has been discussed previously by Pujol et al. (2012) and Gaultier et al. (2016).

As in the case of the SSH fields considered in Sec. 8.3, increasing the averaging time from 4 days to 14 days does not improve the accuracy of SWOT estimates of the surface velocity field (Fig. 29). The sampling errors are even worse in the 14-day averaged geostrophically computed velocity field than in the

[4]For expediency, the magnitude of the estimated vector-averaged velocity fields will be referred to hereafter as velocity fields, with understanding that "velocity" implicitly refers to the magnitude of the time-averaged vector velocity field.

14-day average SSH field in Fig. 27. In addition to sampling errors from inadequate resolution of the rapidly evolving submesoscale velocity field and the edge effects of smoothing that were both evident in the 4-day average maps in Fig. 28, the sampling errors that arise from discontinuities at the boundaries of spatially adjacent measurement swaths that are separated temporally as noted previously by about 10 days in the 14-day average result in misinterpretation of temporal variability as spatial variability in the centered difference estimates of the derivatives of the SSH field at these boundaries. These sampling issues in maps of geostrophically computed velocity constructed from simulated SWOT data have been discussed previously by Gaultier et al. (2016; see their Fig. 5c).

Aside from time averaging that was shown above to be ineffective, the effects of sampling and measurement errors can be suppressed by increasing the spatial smoothing of the SSH field prior to computing the velocity component fields using the geostrophic approximation. The S/N standard deviation ratios as functions of the half-power filter cutoff wavelength are shown in Figs. 30a and b for, respectively, 4-day and 14-day averages of geostrophically computed SWOT estimates of velocity magnitude. The solid lines are the S/N ratios for combined measurement and sampling errors, which represents the total errors in SWOT estimates of velocity. The dotted and dashed lines are, respectively, the S/N ratios for measurement and sampling errors alone, which can be isolated in our simulated SWOT data but of course could not be distinguished in real observational data.

The S/N ratio for measurement errors alone (the dotted lines in Figs. 30a and b) improves rapidly with increased smoothing, intersecting the threshold of 3.16 at a half-power filter cutoff wavelength of about 20 km for 4-day averages and 14 km for 14-day averages. If measurement errors were the only issue in SWOT estimates of surface velocity, these would be the resolution capabilities of 4-day and 14-day averages according to our criterion summarized in Sec. 5. But as noted above from the maps in Figs. 28 and 29, SWOT estimates of surface velocity are more severely affected by sampling errors than measurement errors. This is evident from the dashed lines in Figs. 30a and b by the slow improvement of the S/N ratio for sampling errors alone when the smoothing is increased. The S/N ratio of the total errors (the solid lines in Figs. 30a and b) quickly converges toward the S/N ratio of the sampling errors alone, thus showing the dominance of the effects of sampling errors in the total errors of SWOT estimates of surface velocity.

A peculiarity of Fig. 30a is that the S/N ratios for sampling errors alone and for total errors in estimates of the magnitudes of 4-day averaged velocity asymptote with increased smoothing to a value that is coincidentally just slightly higher than 3.16 for filter cutoff wavelengths longer than about 50 km. This indicates that the signal variance and sampling error variance both decrease at the same rate with high spatial smoothing, resulting in an approximate constant S/N ratio. There is thus no benefit to smoothing with a filter cutoff wavelength longer than about 50 km. According to our criterion, the resolution capability of SWOT estimates of 4-day averaged surface velocity is about 52 km, which corresponds to the wavelength at which the S/N ratio for the total errors (and for sampling errors alone) intersects the threshold of 3.16. The resolution capability worsens to about 132 km in 14-day averages because of the increased sampling errors.

Because of the flatness of the S/N curve, the resolution capability inferred from the S/N ratio is very sensitive to the choice of threshold value of the S/N standard deviation ratio. Lowering the threshold from our recommended value of 3.16 to a value of 2, for example, would improve the estimated resolution capability from 52 km to 28 km in SWOT estimates of 4-day averaged velocity fields.

The results of this analysis indicate that reducing the standard deviation of the uncorrelated measurement errors of SWOT estimates of SSH from the value of $\sigma_h = 2.74$ cm assumed for our calculations would have negligible effect on the resolution capability of maps of geostrophically computed estimates of the time-averaged velocity field constructed from SWOT data. Moreover, time averaging does not improve the S/N ratios of SWOT estimates of surface velocity because the sampling errors from inadequate sampling of rapidly evolving submesocale velocity structures worsens with increasing averaging period. The S/N ratio can be improved by spatial smoothing, but only to a limited degree.

It can thus be concluded that geostrophically computed SWOT estimates of surface velocity will be most useful on a swath-by-swath basis with no time averaging. The resolution capability is then the value of about 32 km deduced in Sec. 6 from Fig. 18, except only within the SWOT measurement swaths rather than for the artificial swaths across the full CCS domain considered in Sec. 6.

As noted in Sec. 6, the 50-km widths of each of the two parallel SWOT measurement swaths will result in some contamination of the swath-by-swath estimates of geostrophically computed velocity from edge effects of the ∼30-km smoothing. It may be possible to utilize the nadir altimeter on the SWOT satellite to help interpolate across the 20-km nadir gap, thus resulting in 30-km smoothed maps of SSH across the full 120-km swath. The different resolution and error characteristics of the nadir altimeter will have to be taken into consideration in order to assess the benefits of this merging of the KaRIN and nadir altimeter data from the SWOT satellite. We have not investigated this in the present study.

The results for WaCM estimates of surface velocity are much more encouraging than for the SWOT estimates considered above. With the factor-of-11 improvement in sampling for the 1200-km swath width considered in this section, sampling errors are much less of an issue for WaCM. The total errors are dominated by measurement errors and time averaging is much more effective at improving the S/N ratio.

The dominance of the effects of measurement errors is readily apparent from the 4-day averaged WaCM estimates of velocity shown in Fig. 31 for the case of spatial smoothing with the same half-power filter cutoff wavelength of 25 km used in Fig. 28 for SWOT estimates of velocity. In contrast to the error maps for SWOT estimates of velocity shown in Fig. 28, the sampling errors shown for WaCM in the bottom panel of Fig. 31c are smaller than the measurement errors shown in the bottom panel of Fig. 31b. The total errors in the bottom panel of Fig. 31d are thus dominated by measurement errors.

The patterns of the total error field in Fig. 31d are generally similar to the patterns of measurement errors alone in Fig. 31b but the magnitudes of the total errors are somewhat larger. This is because the measurement errors alone in the bottom panel of Fig. 31b are more effectively suppressed by the averaging over the eight individual maps at 0.5-day intervals during the 4-day averaging period. As essentially all of the grid points in the CCS model domain are sampled only four times during each 4-day orbit repeat period (see the top panel of Fig. 23), i.e., half as many as the number of twice-daily maps averaged for the bottom panel of Fig. 31b, the residual measurement errors are about $\sqrt{2}$ times larger in the sampled field in the bottom panel of Fig. 31d.

Because sampling errors are less of an issue for WaCM estimates of surface velocity, the total errors can be reduced much more effectively than for SWOT by increasing the averaging period. This is visually evident from the maps of 14-day averages shown in Fig. 32.

The speckled appearance of the velocity estimates in the 4-day average with 25-km smoothing in the top panel of Fig. 31d renders WaCM estimates of surface velocity with this amount of smoothing too noisy for most applications. The S/N standard deviation ratio in this case is only 1.63, which is well below our recommended threshold of 3.16. The velocity estimates in the 14-day average with 25-km smoothing in the top panel of Fig. 32d are still somewhat speckled, but the measurement errors have been reduced enough that the velocity estimates may be useful for many applications. The S/N ratio in this case is 2.89, which is close to our threshold of 3.16.

The effects of noise reduction from spatial smoothing are shown in Figs. 30c and d from the S/N standard deviation ratios as functions of the half-power filter cutoff wavelength for, respectively, 4-day and 14-day averages of WaCM estimates of velocity. The S/N ratios for sampling errors alone (the dashed lines) exceed the threshold of 3.16 for all choices of smoothing, thus showing the secondary importance of sampling errors to the total errors in WaCM estimates of surface velocity. With increased smoothing, the S/N ratios for the case of total errors (the solid lines) parallel the S/N ratios for the case of measurement errors alone (the dotted lines). The small offsets between this pair of lines in both Figs. 30c and d represent the relatively small but not negligible contributions of sampling errors to the total errors. According to our criterion, the resolution capabilities of WaCM estimates of 4-day and 14-day averaged surface velocity are about 58 km and 28 km, respectively. These are significant improvements over the 130-km resolution deduced in Sec. 6 for WaCM estimates of instantaneous velocity fields. It should be kept in mind, however, that the signal variance is reduced at short wavelengths in the time-averaged fields (see Figs. 24 and 25).

8.5. The Resolution Capabilities of Time-Averaged Surface Vorticity Fields

The procedure summarized in Sec. 8.2 and applied in Sec. 8.4 to assess the resolution capabilities of SWOT and WaCM estimates of surface velocity is applied in this section to assess the resolution capabilities

of vorticity estimated from space-time smoothed SWOT and WaCM data. Differentiation of the velocity fields to estimate vorticity amplifies the errors in the velocity fields. It can therefore be anticipated that the resolution capabilities will be worse for vorticity than for velocity. As in Sec. 8.4, the simulated SWOT estimates of vorticity derived from geostrophically computed velocity in this section neglect the limitations of the geostrophic approximation discussed in Sec. 3.

Maps of geostrophically computed SWOT estimates of vorticity are shown for 4-day and 14-day averages in Figs. 33 and 34, respectively, for the case of spatial smoothing with a half-power filter cutoff wavelength of 50 km. The larger smoothing compared with the 25-km smoothing used for the velocity fields in Figs. 28 and 29 is commensurate with the noise amplification from the differentiation to compute vorticity from the geostrophically computed velocity field. Qualitatively, the characteristics of the maps of vorticity errors in the bottom panels of Figs. 33 and 34 are very similar to the characteristics of the maps of velocity errors in the bottom panels of Figs. 28 and 29. The total errors in geostrophically computed SWOT estimates of vorticity are even more dominated by sampling errors than was the case in geostrophically computed SWOT estimates of velocity. This is to be expected because small-scale variability is much more energetic and evolves much more quickly in the vorticity field than in the velocity field. The errors in the SWOT estimates of time-averaged vorticity in the top panels of Figs. 33d and 34d are too large for the SWOT estimates of vorticity to be useful for most applications.

The S/N standard deviation ratios as functions of the half-power filter cutoff wavelength are shown in Figs. 35a and b for, respectively, 4-day and 14-day averages of geostrophically computed SWOT estimates of vorticity. As in the case of SWOT estimates of velocity in Figs. 30a and b, the S/N ratios for the effects of measurement errors alone (the dotted lines) on SWOT estimates of vorticity improve rapidly with increased smoothing, intersecting the threshold of 3.16 at half-power filter cutoff wavelengths of about 38 km and 32 km for 4-day and 14-day averages, respectively. SWOT estimates of vorticity are thus again dominated by sampling errors. In this case, however, the S/N ratios asymptote with increased smoothing to a value of 2 in 4-day averages. In 14-day averages, the S/N ratios increase more gradually to about the same value of 2 for a filter cutoff wavelength of 150 km. The S/N ratios never reach our recommended threshold of 3.16 in either the 4-day or 14-day averages.

Like the geostrophically computed SWOT estimates of velocity considered in Sec. 8.4, we conclude that geostrophically computed SWOT estimates of vorticity will be most useful on a swath-by-swath basis. The resolution capability is then the value of about 54 km deduced in Sec. 6 from Fig. 18, except only within the SWOT measurement swaths. Since the two parallel SWOT measurement swaths each have a width of 50-km, the 54-km half-power filter cutoff wavelength required to achieve a S/N ratio of 3.16 is comparable to the swath width. As discussed in Sec. 6, swath-by-swath estimates of vorticity will therefore be even more contaminated by edge effects of the smoothing than will be the case for swath-by-swath SWOT estimates of surface velocity.

Because of its factor-of-11 improvement in sampling for the 1200-km swath width considered in this section, WaCM estimates of surface vorticity are again much more encouraging than the SWOT estimates considered above. Maps of 4-day and 14-day averages of WaCM estimates of vorticity are shown in Figs. 36 and 37, respectively, for the case of spatial smoothing with the same half-power filter cutoff wavelength of 50 km considered for SWOT in Figs. 33 and 34. The error characteristics for WaCM estimates of vorticity are qualitatively very similar to those of WaCM estimates of velocity in Figs. 31 and 32. Overall, the total errors are dominated by measurement errors (compare the bottom panels of Figs. 36b and d for the case of 4-day averages and the bottom panels of Figs. 37b and d for the case of 14-day averages). Sampling errors are comparable in magnitude to measurement errors in the regions of strongest meandering large-scale currents where submesoscale variability is most energetic. Elsewhere, measurement errors are much larger than sampling errors.

The S/N standard deviation ratios as functions of the half-power filter cutoff wavelength are shown in Figs. 35c and d for, respectively, 4-day and 14-day WaCM estimates of vorticity. The S/N ratios for sampling errors alone (the dashed lines) exceed the threshold of 3.16 for filter cutoff wavelengths of about 25 km in 4-day averages and about 10 km in 14-day averages. Sampling errors are thus of secondary concern and the total errors are dominated by measurement errors for all choices of spatial smoothing. As in Figs. 30c and d for space-time smoothed WaCM estimates of velocity, the small offsets between the S/N ratios for

the case of total errors (the solid lines) and for the case of measurement errors alone (the dotted lines) in both Figs. 35c and d indicate that the effects of sampling errors on the resolution capabilities of space-time smoothed maps of vorticity constructed from WaCM data are not negligible.

By our criterion, the resolution capabilities of WaCM estimates of 4-day and 14-day averaged vorticity with combined measurement and sampling errors are about 86 km and 61 km, respectively. These are significant improvements over the 130-km resolution deduced in Sec. 6 for WaCM estimates of instantaneous vorticity fields. Note again, however, that the signal variance is significantly reduced at short wavelengths in the time averaged fields (see Figs. 24 and 25).

9. Sensitivity of Estimated Resolution Capabilities to the Choice of Smoother

The assessments of resolution capability in Secs. 6, 8.4 and 8.5 were based on the S/N standard deviation ratios computed from error-free and noise-contaminated velocity and vorticity fields smoothed spatially using the Parzen smoother that is summarized in Appendix A. The choice of the Parzen smoother for these calculations was motivated in part by the fact that it will be used in the onboard pre-processing of SWOT data. The Parzen smoother is also very efficient computationally. The degree to which our assessments of resolution capabilities are sensitive to the choice of smoother is investigated in this section from the S/N ratios computed from velocity and vorticity fields smoothed using the quadratic loess smoother that is summarized in Appendix C.

Computationally, the 2-dimensional loess smoother consists of a weighted least squares fit to a quadratic surface (Cleveland and Devlin, 1988). The primary advantages of the loess smoother are that its filter transfer function has smaller sidelobes and rolls off more steeply through the half-power filter cutoff wavelength than does the filter transfer function of the Parzen smoother (see Schlax and Chelton, 1992; see also Fig. C3 in Appendix C). The loess smoother is therefore more effective at attenuating small-scale noise. (It also attenuates more of the small-scale signal variability.)

A disadvantage of the loess smoother is that the weighted least squares fits at each individual grid point are much more computationally intensive than the Parzen smoother. This computational effort increases as the product of the filter cutoff wavelengths in each dimension. The difference in computing time is more than a factor of 50, which was a significant issue in this study because a total of 1200 smoothed maps were required to generate the signal-to-noise graphs in Figs. 18, 30, 35 and 43.

Another disadvantage of the loess smoother is that its total span is 83.5% larger than the span of the Parzen smoother (see Appendix C). This results in potentially more problems with edge-effect artifacts in the smoothed fields.

The S/N standard deviation ratios for SWOT and WaCM estimates of instantaneous snapshots of velocity and vorticity smoothed spatially using the loess smoother are shown as functions of the half-power filter cutoff wavelength in Fig. 38. These S/N graphs are qualitatively similar to those in Fig. 18 based on the Parzen smoother but with somewhat larger values of the S/N standard deviation ratio at all filter cutoff wavelengths. The resolution capabilities inferred from our threshold S/N standard deviation ratio of 3.16 therefore improve, as summarized in Table 3.

The improved resolution capabilities are especially impressive for WaCM estimates of instantaneous snapshots of velocity and vorticity. Because of the flatness of the S/N curves, small increases in the S/N values result in large improvements in the resolution capability inferred from any specified threshold value of S/N ratio. As noted previously from Fig. 18 in Sec. 6.2, the flatness of the S/N curves also implies that the estimated resolution capability is very sensitive to the choice of the threshold value of the S/N standard deviation ratio used to define resolution capability. Lowering the threshold value from our recommended value of 3.16 to a value of 2, for example, would improve the estimated resolution capabilities from 99 km to 47 km for velocity and from 89 km to 59 km for vorticity.

It is important to bear in mind that the estimates of resolution capability in Fig. 38 assume that the measurement swaths sample the entire CCS model domain on each satellite overpass. While this is very nearly achieved by just one side of the two-sided measurement swaths of WaCM, complete coverage of the CCS model domain is a highly idealized representation of SWOT sampling. Because its sampling consists

of two parallel swaths with 50-km width separated by a 20-km nadir gap, in-swath estimates of velocity and vorticity from SWOT measurements of SSH are subject to edge-effect contamination in the smoothed fields. The resolution capabilities suggested from Fig. 38a are therefore optimistic estimates of what will be achieved from in-swath estimates of actual SWOT data.

The S/N standard deviation ratios for 4-day and 14-day averaged estimates of velocity fields computed from simulated SWOT and WaCM data smoothed spatially using the loess smoother are shown as functions of the half-power filter cutoff wavelength in Fig. 39. The results are qualitatively very similar to those obtained in Fig. 30 using the Parzen smoother. The dependencies of the S/N ratios for measurement errors alone, sampling errors alone and combined measurement and sampling errors have very similar characteristics for both smoothing algorithms. The only significant differences are that the S/N ratios increase somewhat faster with increased smoothing and thus intersect our recommended threshold value of 3.16 at somewhat shorter half-power filter cutoff wavelengths. The resolution capabilities of SWOT and WaCM estimates of velocity fields inferred from the loess smoother are consequently somewhat better than those inferred from Fig. 30 based on the Parzen smoother. The resolution capability improves by about 30% and 20% for geostrophically computed SWOT estimates of, respectively, 4-day and 14-day averaged velocity fields, and by about 12% for WaCM estimates of velocity fields for both choices of time averaging (see Table 3).

The S/N standard deviation ratios for 4-day and 14-day averaged SWOT and WaCM estimates of vorticity based on the loess smoother are shown as functions of the half-power filter cutoff wavelength in Fig. 40. As in the case of the space-time smoothed velocity fields considered above, the results are qualitatively very similar to those obtained in Fig. 35 using the Parzen smoother. Recall from Figs. 35a and b that the S/N ratios for SWOT estimates of vorticity inferred from Parzen smoothing never reached the threshold of 3.16. The S/N ratios for sampling errors and combined measurement and sampling errors in SWOT estimates of 4-day averaged vorticity using the loess smoother asymptote with increased smoothing to a value that is coincidentally just slightly higher than 3.16. Because of the flatness of the S/N curve, the resolution capability inferred from this figure is sensitive to the choice of threshold value of the S/N standard deviation ratio. By our criterion of a threshold value of of 3.16, the resolution capability inferred from loess smoothing is about 100 km for 4-day averages (Fig. 40a). The resolution capability worsens to 143 km for 14-day averaged SWOT estimates of velocity (Fig. 40b). As discussed previously, the degradation of resolution capability with increased temporal averaging is from increased sampling errors because of the space-time sampling pattern of the SWOT 21-day exact-repeat orbit that samples the full CCS model domain in two 4-day subcycles that are interleaved spatially and separated by 6-day gaps.

For WaCM, the faster increases of the S/N standard deviation ratios with increased smoothing using the loess smoother result in about 19% improvements in the resolution capabilities of WaCM estimates of both 4-day and 14-day averaged vorticity fields (see Figs. 40c and d and Table 3).

The comparisons in Table 3 of the resolution capabilities of SWOT and WaCM estimates of velocity and vorticity based on the Parzen and loess smoothers provide a measure of how rigorously the resolution capabilities reported here should be interpreted. In addition to the subjectivity of our recommended choice of 3.16 as the minimum threshold value for the S/N standard deviation ratio, the half-power filter cutoff wavelength at which the S/N ratio achieves this threshold changes by 10–40% as summarized in Table 3, depending on the variable of interest, the averaging time, and the choice of smoother. Importantly, however, the relative ranking of resolution capabilities for the two instruments and for the three choices of time averages considered in Figs. 38–40 are insensitive to the details of the smoothing algorithm.

The Parzen smoother and the loess smoother were both applied for all of the calculations in this study. The resolution capabilities will be discussed based on the more conservative estimates obtained from the Parzen smoother.

10. The Benefits of Improved Sampling and Measurement Accuracy for WaCM

A conclusion from Sec. 8 is that measurement errors are a minor concern in space-time smoothed maps of surface velocity and vorticity computed geostrophically from SWOT data. The total errors in these fields are dominated by sampling errors owing to the narrow swath width of SWOT measurements of SSH. Reducing

the SWOT measurement errors would therefore have little effect on the resolution capabilities of space-time smoothed maps of the velocity and vorticity fields computed geostrophically from SWOT data over a domain the size of the CCS. Aside from multiple SWOT instruments operating simultaneously on different satellites in coordinated orbits, the only way to improve the resolution capability would be to reduce the sampling errors by increasing the width of the measurement swath. This might be achievable to a limited degree at increased cost by increasing the power of the transmitted signals. But altimetry is fundamentally restricted to measurements at relatively small incidence angles, and hence narrow swaths, compared with the Doppler scatterometer measurements by WaCM.

In contrast to SWOT, the dominance of the measurement error contribution to the total errors in maps of surface velocity and vorticity constructed from WaCM data implies that the accuracy and resolution capability can be improved by reducing the measurement noise in the WaCM data. For the calculations in Sec. 8, it was assumed that the uncorrelated measurement errors will have a standard deviation of $\sigma_{u,v} = 0.354$ m s^{-1} for each velocity component, which corresponds to a standard deviation of $\sigma_{spd} = 0.50$ m s^{-1} in speed errors. It may be technologically possible to reduce the WaCM measurement errors, thus improving the resolution capabilities for maps of velocity and vorticity fields constructed from WaCM data.

While sampling errors were shown in Sec. 8 to be secondary to measurement errors in determining the resolution capabilities of space-time smoothed maps of velocity and vorticity constructed from WaCM data, they are not negligible. This was evident in Figs. 30c and d and Figs. 35c and d from the small offsets between the S/N ratios for the cases of total errors and measurement errors alone (see also the analogous figures with loess smoothing in Figs. 39c and d and Figs. 40c and d). The resolution capabilities of space-time smoothed maps of velocity and vorticity constructued from WaCM data can thus also be improved by reducing the sampling errors, which can be achieved by increasing the swath width.

The improvements of the resolution capabilities from increasing the swath width and reducing the uncorrelated measurement errors are investigated individually and in combination in this section.

10.1. The Benefits of Increasing the WaCM Measurement Swath to 1800 km

Recent engineering studies have concluded that it may be possible to extend the swath width of WaCM from the 1200-km swath considered for the simulations in Sec. 8 to 1800 km. With the nadir gap of 100 km, WaCM sampling would then consist of a pair of parallel measurement swaths with 850-km widths. The full CCS model domain is more than completely sampled by just one of the parallel measurement swaths on ascending orbits (see the left panel of Fig. 41) and nearly the entire CCS model domain can be sampled with an appropriate choice of orbit ground tracks by just one of the parallel measurement swaths on descending orbits (see the right panel of Fig. 41).

The implications of the improved sampling afforded by the wider swath width of 1800 km are shown by the histograms of WaCM sampling of the CCS model domain in Fig. 42. For the 4-day period shown in the top panel, the average number of samples is about 6.5. For comparison, the average number of samples per 4-day repeat was only about 4 for the 1200-km swath considered in Sec. 8 (see the top panel of Fig. 23). For the 14-day period shown in the bottom panel of Fig. 42, the average number of samples for a swath width of 1800 km is about 23, compared with only about 13.5 for a swath width of 1200 km (see the bottom panel of Fig. 23).

The increased number of WaCM samples during each 4-day and 14-day averaging period reduces the sampling errors because of improved sampling of the rapidly evolving submesocale variability compared with the simulations in Sec. 8. It also reduces the effects of uncorrelated measurement errors somewhat through the time-averaging of a larger number of observations at each grid location over the course of the averaging period. The net effects of the smaller sampling and measurement errors on the S/N standard deviation ratios in space-time smoothed maps of velocity and vorticity with a swath width of 1800 km are shown in Fig. 43. By our criterion, the resolution capabilities of WaCM estimates of 4-day and 14-day averaged surface velocity (Figs. 43a and b) are about 44 km and 21 km, respectively. These are substantial improvements over the resolutions capabilities of 60 km and 28 km deduced in Sec. 8.4 for a swath width of 1200 km (Figs. 30c and d). The resolution capabilities of WaCM estimates of 4-day and 14-day averaged vorticity with a swath width of 1800 km (Figs. 43c and d) are about 70 km and 51 km, respectively, which

are again substantial improvements over the resolutions of 87 km and 62 km deduced in Sec. 8.5 for a swath width of 1200 km (Figs. 35c and d).

A noteworthy feature of Fig. 43 is that the offsets between the S/N ratios for the cases of total errors (the solid lines) and measurement errors alone (the dotted lines) are much smaller for the 1800-km swath width than for the 1200-km swath shown in Figs. 30c and d and Figs. 35c and d. In fact, these two curves in each panel of Fig. 43 are so similar that little would be gained by increasing the WaCM swath width beyond 1800 km. Further improvements in the resolution capabilities of space-time smoothed maps of velocity and vorticity constructed from WaCM data are more effectively achieved by reducing the uncorrelated measurement errors, which is considered in Sec. 10.2.

10.2. The Benefits of Reducing the WaCM Measurement Noise

The resolution capabilities of WaCM estimates of velocity and vorticity that were deduced in Sec. 6 for instantaneous maps and in Secs. 8.4, 8.5 and 10.1 for time-averaged maps were based on an assumed standard deviation of $\sigma_{spd} = 0.50$ m s^{-1} for the speeds of the uncorrelated errors of WaCM measurements of surface velocity. For the simulations throughout this study, these speed uncertainties are assumed to be equally partitioned between each velocity component. Measurement errors could be reduced by increasing the transmit power of the WaCM antenna or by increasing the antenna size. The added cost of these options must be traded off against the scientific benefits of higher resolution maps of velocity and vorticity. To assess the scientific benefits of higher resolution maps, we extended the analyses of Secs. 6, 8.4, 8.5 and 10.1 to determine the resolution capabilities of maps of velocity and vorticity constructed from simulated WaCM data with smaller uncorrelated measurement errors.

The effects of reducing the uncorrelated errors in WaCM measurements of surface velocity can be inferred from the derivations in Appendix I.4 of the effects of measurement errors on the wavenumber spectral contents of smoothed WaCM estimates of velocity component and vorticity fields. It is shown from Eqns. (I.48a) and (I.52), with the latter partitioned as (I.54a) and (I.55a), that the wavenumber spectral values of the errors of smoothed WaCM estimates of, respectively, velocity component and vorticity fields both depend linearly on the variances σ_u^2 and σ_v^2 of the velocity component measurement errors. Since the variance of the smoothed fields is equal to the integral of their wavenumber spectrum according to Parseval's Theorem, the variances of the errors of the smoothed fields decrease linearly with decreasing variance of the velocity component measurement errors.

The S/N standard deviation ratios for smoothed estimates of velocity component and vorticity fields for any particular choice of half-power filter cutoff wavelength increase in inverse proportion to the measurement error standard deviation. The resolution capability defined as in previous sections to be the half-power filter cutoff wavelength at which the S/N standard deviation ratio achieves a value of 3.16 therefore decreases systematically with decreasing measurement error standard deviation, though not necessarily linearly since the signal contribution to the S/N standard deviation ratios does not necessarily vary linearly with filter cutoff wavelength.

We first consider the case of instantaneous snapshot maps of velocity and vorticity that could be obtained from a single overpass of the CCS model domain. The benefits of improving the WaCM measurement accuracy were quantified by repeating the calculations in Sec. 6 of the S/N standard deviation ratios for spatially smoothed WaCM maps of instantaneous velocity and vorticity based on standard deviations of the uncorrelated speed measurement errors ranging from $\sigma_{spd} = 0.10$ m s^{-1} to 0.50 m s^{-1}, which we continue to assume are equally partitioned between the two orthogonal velocity components. As in Sec. 6, we isolate the effects of measurement errors by considering the idealized scenario of complete sampling of the full CCS model domain on each overpass of the WaCM satellite. This is nearly achieved for both ascending and descending orbits for a swath width of 1200 km (Fig. 23) and is essentially achieved for a swath width of 1800 km (Fig. 41). The variances of the error-free signals for each choice of half-power filter cutoff wavelength are unchanged from Sec. 6 in these calculations, but the variances of the errors of the smoothed fields decrease as summarized above.

The dependencies of the resolution capabilities of smoothed maps of WaCM estimates of instantaneous velocity and vorticity on the standard deviation of the speed measurement errors were deduced from graphs

of the S/N standard deviation ratios like those shown in Fig. 18b. The results are shown in Fig. 44 for both Parzen and loess smoothing. As discussed in Sec. 9, the filtering efficiency of the loess smoother improves the resolution capability compared with the Parzen smoother, albeit with higher computational effort. For discussion purposes, we will continue to adopt the more conservative resolution capabilities inferred from the Parzen smoother.

For the sake of specificity in the discussion that follows, the resolution capabilities for the baseline standard deviation of $\sigma_{spd} = 0.50$ m s^{-1} for the uncorrelated speed measurement errors will be compared with the resolutions that could be achieved by halving the noise standard deviation to $\sigma_{spd} = 0.25$ m s^{-1}. The numerical values of the resolution capabilities are listed in Tables 4a and b. The resolution capabilities for other choices of σ_{spd} can be determined graphically from Fig. 44.

Reducing the speed measurement noise to $\sigma_{spd} = 0.25$ m s^{-1} would dramatically improve the resolution capability of instantaneous snapshots of velocity from 130 km to 50 km (see Fig. 44a and Table 4a). The resolution capability of instantaneous snapshots of vorticity would improve from 130 km to 74 km (see Fig. 44b and Table 4b). The benefits of the higher resolution with the smaller measurement noise of 0.25 m s^{-1} for instantaneous snapshots of velocity and vorticity can be seen visually in Fig. 50 below.

The effects of improving the WaCM measurement accuracy on space-time smoothed maps of velocity and vorticity were similarly quantified by repeating the calculations in Secs. 8.4, 8.5 and 10.1 of the S/N standard deviation ratios like those shown in Figs. 30, 35, 38, 39, 40 and 43 for standard deviations of uncorrelated speed measurement errors ranging from $\sigma_{spd} = 0.10$ m s^{-1} to 0.50 m s^{-1}. For space-time smoothed maps, it was shown in Sec. 10.1 that the swath width of the WaCM measurements is also a factor in determining the resolution capability. We therefore estimated the resolution capabilities for both of the swath widths that were considered in Secs. 8.4, 8.5 and 10.1. The results for swath widths of 1200 km and 1800 km are shown, respectively, by the blue and red lines in Fig. 45. The solid and dashed lines are the resolution capabilities inferred based on smoothing using the Parzen and loess smoothers, respectively. For discussion purposes, we again consider the more conservative resolution capabilities inferred from the Parzen smoother.

The dependencies of the resolution capabilities of 4-day averaged WaCM estimates of the surface velocity field on the standard deviation of the speed measurement errors are shown in Fig. 45a. For the baseline standard deviation of $\sigma_{spd} = 0.50$ m s^{-1} assumed in Secs. 8.4 and 10.1 for the uncorrelated speed measurement errors, it was shown from Figs. 30c and 43a that increasing the swath width from 1200 km to 1800 km would improve the resolution capability for 4-day averaged velocity fields from 60 km to 44 km. Reducing the standard deviation of the measurement noise to $\sigma_{spd} = 0.25$ m s^{-1} would further improve this resolution capability to 18 km (see Fig. 45a and Table 4c).

For 14-day averaged velocity fields, it was shown from Figs. 30d and 43b that the resolution capability for a speed measurement noise of $\sigma_{spd} = 0.50$ m s^{-1} would improve from 28 km for a swath width of 1200 km to 21 km for a swath width of 1800 km. Reducing the standard deviation of the speed measurement noise to $\sigma_{spd} = 0.25$ m s^{-1} would further improve the 14-day averaged velocity resolution capability to 10 km (see Fig. 45b and Table 4e), which is the inherent resolution of the pre-processed estimates of surface velocity with a footprint diameter of 5 km for the simulations in this study.

The dependencies of the resolution capabilities of 4-day averaged WaCM estimates of the vorticity field on the speed measurement error standard deviation are shown Fig. 45c. For the baseline standard deviation of $\sigma_{spd} = 0.50$ m s^{-1} for the uncorrelated speed measurement errors, it was shown from Figs. 35c and 43c that increasing the swath width from 1200 km to 1800 km would improve the resolution capability for 4-day averaged vorticity fields from 87 km to 70 km. Reducing the standard deviation of the speed measurement errors to $\sigma_{spd} = 0.25$ m s^{-1} would further improve the resolution capability to 45 km (see Fig. 45c and Table 4d).

For 14-day averaged vorticity fields, it was shown from Figs. 35d and 43d that the resolution capability for a speed measurement noise of $\sigma_{spd} = 0.50$ m s^{-1} would improve from 62 km for a swath width of 1200 km to 51 km for a swath width of 1800 km. Reducing the standard deviation of the speed measurement noise to $\sigma_{spd} = 0.25$ m s^{-1} would further improve the 14-day averaged vorticity resolution capability to 34 km (see Fig. 45d and Table 4f)

While the improved spatial resolution capabilities summarized above for space-time smoothed maps of velocity and vorticity estimated from WaCM data for an increased swath width of 1800 km and a reduction

of the standard deviation of uncorrelated speed measurement errors to 0.25 m s^{-1} are impressive, we note again that much of the small-scale velocity and vorticity signals that are of interest is attenuated in 4-day and 14-day averaged fields, especially the latter (see Figs. 24 and 25). Depending on the application, the coarser spatial resolution of instantaneous snapshot maps of velocity and vorticity constructed from WaCM data (Fig. 44) may be preferable to the higher spatial resolution of the time-averaged maps (see Figs. 48–50 below).

11. Discussion

The preceding analysis has assessed the resolution capabilities of surface ocean velocity and vorticity fields estimated from simulated altimetric measurements of SSH by SWOT and Doppler radar measurements of surface velocity by WaCM. The simulated satellite data for this study were constructed based on the high-resolution model of the California Current System summarized in Sec. 2 with uncorrelated measurement errors added to the SSH and surface velocity fields with the standard deviations in the baseline designs of the SWOT and WaCM instruments.

For SWOT, our analysis includes a derivation of the baseline science requirement for the standard deviation of the uncorrelated errors of the SSH measurements, a number that cannot be found unambiguously in the SWOT documentation. This derivation (see Appendix F) concludes that the requirement for the uncorrelated errors of SWOT measurements of SSH, as specified in the SWOT Science Requirements Document (Rodríguez and Callahan, 2016) in terms of the wavenumber spectrum after smoothing in ground-based post-processing, corresponds to a standard deviation of $\sigma_h = 2.74$ cm for pre-processed SWOT estimates of SSH with a footprint size of 1 km.

Our error analysis includes derivations of analytical expressions for the variances (Appendix G) and the wavenumber spectra (Appendix I) of errors of the estimates of the derived variables (geostrophically computed velocity and vorticity for SWOT and vorticity for WaCM), with and without spatial smoothing. The errors are shown as functions of the half-power filter cutoff wavelength of the smoothing in Fig. 12. The wavenumber spectra shown in Figs. 13–15 quantify the scale dependencies of these errors. The equations for the variances and wavenumber spectra of the errors of the derived variables all depend explicitly on the variance of the uncorrelated measurement errors and are thus applicable to arbitrary specification of measurement noise. This allows an assessment of the degree of improvement in the accuracies of the derived variables that would be achieved by improving the baseline measurement accuracies.

The calculations presented in Secs. 6, 8, 9 and 10.1 are based on the above standard deviation of $\sigma_h = 2.74$ cm for the uncorrelated errors of SWOT measurements of SSH with a footprint size of 1 km, and a standard deviation of $\sigma_{spd} = 0.50$ m s^{-1} for the uncorrelated errors of WaCM measurements of surface ocean velocity with a footprint size of 5 km. The benefits of reducing the measurement noise are investigated for WaCM in Sec. 10.2. Improved measurement accuracy is not considered for SWOT because the total errors in maps of SWOT estimates of velocity and vorticity are so strongly dominated by sampling errors that reducing the measurement errors would offer little benefit.

For WaCM, we have assumed that the uncorrelated speed errors are equally partitioned between the two orthogonal velocity components, thus resulting in a standard deviation of $\sigma_{u,v} = 0.354$ m s^{-1} for each component. In reality, the errors of each velocity component will vary differently across the measurement swaths because of the geometrical transformation issues discussed in Sec. 4.2. For approximation of the derivatives of the velocity components that are required to estimate vorticity from WaCM data, we have further assumed that the velocity estimates with 5 km footprint size are oversampled on a 1 km × 1 km grid. It is shown in Appendix H that 3-point centered differences on this grid retain more of the small-scale signal in the vorticity field without having to resort to centered difference estimates of the derivatives with a wider stencil width on the 5 km × 5 km grid on which the WaCM measurement errors are uncorrelated.

The measurement error standard deviations of $\sigma_h = 2.74$ cm for SWOT and $\sigma_{spd} = 0.50$ m s^{-1} for WaCM are swath-averaged values. It is shown in Fig. F1 of Appendix F that the SWOT measurement errors will increase toward each edge of the measurement swaths and with increasing significant wave height (SWH). The dependencies of the SWOT measurement errors on SWH and swath location are accounted for in the

simulator software available from the SWOT Project Office (Gaultier et al., 2017). WaCM measurement errors also increase toward the edges of the measurement swaths and will depend on SWH. Presently, however, these dependencies of the WaCM measurement errors have not been quantified.

To be consistent in our treatments of the uncorrelated measurement errors for both instruments, we have considered the SWOT and WaCM measurement errors to have uniform standard deviations across the full widths of their measurement swaths. Because we have neglected the increases of measurement errors towards the swath edges, the analysis in this study likely underestimates the overall effects of measurement errors on space-time smoothed estimates of velocity and vorticity fields constructed from SWOT and WaCM data. The results presented in Secs. 6 and 8–10 should therefore be considered optimistic estimates of the resolution capabilities of actual SWOT and WaCM data.

The CCS model used for our assessments of the resolution capabilities of SWOT and WaCM estimates of surface velocity and vorticity has some limitations that should be kept in mind. As summarized in Sec. 2, the model has high dissipation and was forced with seasonally varying winds, heat flux and freshwater flux, and thus omits the significant effects of synoptic atmospheric forcing. The model also lacks tidal forcing. It is therefore likely that internal wave variability, inertial motions and perhaps even mesoscale and submesoscale geostrophic variability are underestimated in the model. In spite of these limitations, the model provides useful comparisons of the resolution capabilities of maps of surface velocity and vorticity constructed from SWOT and WaCM data.

The importance of the grid resolution of the model for proper representation of the effects of submesoscale variability is evident from Fig. 1. Submesoscale variability increases dramatically by increasing the grid resolution from 4 km to the 0.5 km grid spacing of the model used for our simulations. The choice of grid resolution is clearly an important consideration in choosing a model from which to assess the resolution capabilities of SWOT and WaCM estimates of surface velocity and vorticity. For example, Qiu et al. (2016) evaluated the resolution capability of maps of vorticity constructed from simulated SWOT data based on a model of the Kuroshio Extension with a grid spacing of 1/30° (approximately 3 km). The much less energetic submesoscale variability in that model compared with the CCS model used in this study is partly attributable to the coarseness of their model grid. The weaker submesoscale variability in the model output used in the Qiu et al. (2016) study is compounded by the fact that their analysis was based on daily averages rather than instantaneous snapshots of the model output.

The extent to which accurate model representation of submesoscale variability is important in model-based simulations of SWOT and WaCM data depends on the amount of smoothing that must be applied to the simulated satellite data to achieve adequate signal-to-noise ratio in maps of the variables of interest. Given the coarse resolution capabilities inferred from the analysis in Secs. 6 and 8–10 and summarized in Tables 3 and 4, it may not be necessary to use a model with resolution as high as the 0.5-km grid of the CCS model used in this study. It nonetheless seems prudent to use as high a resolution model as possible in order to be sure that aliasing issues from discrete sampling at satellite overpass times are adequately accounted for. To this end, the daily averages analyzed by Qiu et al. (2016) are likely an issue, even for the coarse resolution capabilities of SWOT estimates of geostrophically computed velocity and vorticity. The twice-daily snapshots analyzed in this study are also less than ideal; evidence of aliasing from inadequate sampling of the rapidly evolving submesoscale field was readily apparent from the 4-day and 14-day averages of error-free vorticity in the bottom panels of Fig. 24.

In addition to analysis of the effects of uncorrelated measurement and sampling errors, we also investigated limitations of the geostrophic approximation that must be used to estimate surface velocity and vorticity from SWOT measurements of SSH (Sec. 3). Because of the above-noted underestimation of internal gravity wave energy in the CCS model used in this study, we were not able to use this model to assess the effects of the SSH signatures of internal waves on velocity estimates computed geostrophically from SSH. We did, however, use the CCS model to investigate the effects of ageostrophic variability from cyclostrophic motion, which results in geostrophically computed velocities that overestimate the positive vorticity of cyclonic features and underestimate the magnitude of the negative vorticity of anticyclonic features. The former are more prevalent, presumably because of the tendency for anticyclonic features to become inertially unstable. It was shown in Sec. 3 that the errors from cyclostrophic motion may often exceed 0.1 m s^{-1} but can be reduced to less than 0.05 m s^{-1} by smoothing with a half-power filter cutoff wavelength of 50 km or more.

Contamination of geostrophically computed SWOT estimates of surface velocity by internal gravity waves is an important issue in need of rigorous analysis that is beyond the scope of this study. Some insight into the effects of internal waves on the interpretation of SWOT data was provided in Sec. 3 based on two high-resolution simulations of the ocean circulation southeast of the Gulf Stream in the western North Atlantic (see Figs. 10 and 11). A simulation forced by low-frequency winds and without tides results in ageostrophic submesoscale features similar to the cyclostrophic features found in the CCS model used in this study. The same North Atlantic simulation forced by hourly winds and ocean tides results in a dramatically different geostrophically computed velocity field consisting of internal wave structures that overwhelm the submesoscale velocity structures that are of interest.

The apparent velocity structures computed geostrophically from the SSH signatures of internal waves are a gross misrepresentation of the surface manifestation of the actual internal wave velocities. SWOT data will have to be judiciously smoothed spatially and/or temporally to mitigate contamination of the geostrophically computed velocity estimates by internal gravity waves.

While contamination of SWOT estimates of surface velocity and vorticity by ageostrophic processes is clearly an issue, it should be kept in mind that SWOT was not designed to determine the surface velocity and vorticity fields that are the primary focus of this study. However, many users of SWOT data intend to investigate ocean dynamics from SWOT estimates of velocity and vorticity. The analysis presented in this study provides a useful framework for understanding the limitations of SWOT data for such applications.

It should also be noted that some of the same ageostrophic signals that contaminate SWOT estimates of velocity and vorticity will be considered unwanted "noise" in the context of many applications of the total velocity measured by WaCM. In particular, the surface velocity signatures of internal gravity waves and inertial motions could obscure some of the velocity signals of the mesoscale and submesoscale currents that will be the primary interest in many studies. A sense of the magnitudes of these ageostrophic velocities can be inferred from the modeling result shown in the bottom left panel of Fig. 10. Values exceeding 0.5 m s^{-1} are common. The partitioning of this ageostrophic velocity between inertial motions, internal waves and other ageostrophic processes is presently not well understood.

A point worth emphasizing is that the "contamination" of WaCM data by ageostrophic processes differs fundamentally from the contamination of SWOT data by the same ageostrophic processes. The velocity signatures of inertial motions and internal waves are true velocities. In contrast, the apparent surface velocity field computed geostrophically from the SSH signatures of ageostrophic processes are fictitious velocities that do not exist in nature.

Although the spectral characteristics of SSH at high wavenumbers (short wavelengths) were not a primary focus of this investigation, useful insight into the nature of SSH variance at poorly observed small scales can be obtained from the CCS model used throughout this study and from the above two North Atlantic models considered briefly in Sec. 3 and Appendix F. It is shown in Figs. F3 and F4 that the rolloff at high wavenumbers in the SSH spectra from all three of these models is steeper than the approximate $l^{-5/2}$ dependence on wavenumber l that is assumed in the 68^{th}-percentile global average SSH spectrum that is the basis for defining the science requirements for SWOT measurement accuracy and resolution (Rodríguez and Callahan, 2016). This 68^{th}-percentile wavenumber spectrum is based on extrapolation of along-track SSH spectra from nadir altimetry that resolves variability only down to a wavelength scale of about 70 km (Xu and Fu, 2012). The validity of this extrapolation cannot be determined from presently available observational data and must therefore be inferred from high-resolution ocean circulation models.

A consequence of the steeper rolloff of the wavenumber spectra from the three models considered in this study is that the 68^{th}-percentile spectrum assumed in the SWOT requirements document may overestimate the variance at high wavenumbers, in which case the 15-km resolution of the SWOT data as defined spectrally in the science requirements would be overly optimistic. In particular, the 15-km smoothed white noise spectrum for the SWOT requirement of the standard deviation of $\sigma_h = 2.74$ cm for the uncorrelated measurement errors that is derived for a footprint size of 1 km in Appendix F may intersect the true SSH signal spectrum at a wavelength longer than 15 km. Achieving the science goal of resolving the signal spectrum down to a wavelength of 15 km would then require a higher measurement accuracy in the pre-processed SWOT estimates of SSH, i.e., a smaller standard deviation of the uncorrelated measurement errors.

Since little is known about the spectral characteristics of SSH at wavelengths shorter than 70 km, it is possible that the CCS model used in this study and the two North Atlantic models considered briefly in Sec. 3 and Appendix F underestimate the variance at high wavenumbers. As discussed at the end of Appendix F, the wavenumber spectrum of SSH at wavelengths shorter than 70 km is flatter in the MITgcm model (Rocha et al., 2016; Savage et al., 2017) and thus has higher variance at these high wavenumbers.

The differences between the spectral characteristics of SSH at high wavenumbers from different models underscores how little is known about ocean variability on scales smaller than 70 km. One of the primary contributions of the SWOT mission will be to elucidate the nature of spatial variability of SSH at these smaller scales that have heretofore not been observable from space. This will enable testing of the various model respresentations of small-scale variability of SSH.

Notwithstanding the issues summarized above, the analysis presented in Secs. 6 and 8–10 provides useful insight into the resolution that can be expected in maps of the surface velocity and vorticity fields constructed from SWOT and WaCM data. From simulated SWOT measurements of SSH and WaCM measurements of surface velocity based on the CCS model used in this study, it is shown in Appendix G (see also Tables 1 and 2 and the bottom left panels of Figs. 17b, 17c, 19a and 19b) that the standard deviations of the uncorrelated measurement errors assumed in our analysis result in velocity and vorticity errors that are too large for the SWOT and WaCM data to be useful for oceanographic applications at the full resolutions of the pre-processed data (footprint sizes of 1 km for SWOT and 5 km for WaCM). It will therefore be necessary to smooth the pre-processed satellite data in ground-based post-processing to reduce the effects of uncorrelated measurement errors and improve the signal-to-noise ratios in SWOT and WaCM estimates of velocity and vorticity.

The standard deviations of the errors of the variables of interest decrease rapidly with increased smoothing (see Fig. 12). The signal standard deviations also decrease with increased smoothing, but usually less rapidly than the error variances. The signal-to-noise (S/N) standard deviation ratios therefore generally improve with increased smoothing. From visual inspection of many maps such as the examples shown in Fig. 16 for S/N standard deviation ratios of 1, 2 and 3.16, we recommend a ratio of 3.16 (which corresponds to a S/N variance ratio of 10) as a guideline minimum threshold for maps of velocity and vorticity constructed from SWOT and WaCM data. While subjective, this S/N ratio is sufficiently high to distinguish the signal from the noise unambiguously. For users willing to accept a lower S/N ratio, the corresponding resolution capabilities can be inferred from the graphs in Secs. 6, 8.4, 8.5 and 10.1, specifically Figs. 18, 30, 35, 38, 39, 40 and 43.

In addition to the subjective choice of a threshold S/N standard deviation ratio of 3.16 adopted in this study to define resolution capability, the discussion in Sec. 9 (see also Figs. 44 and 45 in Sec. 10.2) shows that the precise values of the resolution capabilities of SWOT and WaCM estimates of surface velocity and vorticity depend to some extent on the details of the algorithm used to smooth the noisy satellite data. For example, it was shown in Sec. 9 that the resolution capabilities of instantaneous snapshots and space-time smoothed maps of velocity and vorticity that would be inferred based on the loess smoother are better than those inferred from the Parzen smoother (see Table 3) but the relative ranking of resolution capabilities for the two instruments and for the choices of time averages considered in Sec. 9 (instantaneous snapshots and time averages over 4 and 14 days) are insensitive to the details of the smoothing algorithm.

A disadvantage of the loess smoother is that it is more than a factor of 50 more computationally intensive than the Parzen smoother. This was a significant issue in this study since a total of 1200 smoothed maps were required to generate the S/N graphs in Figs. 18, 30, 35 and 43 that are based on Parzen smoothing. Another disadvantage of the loess smoother and other smoothers that attenuate small-scale noise more effectively than the Parzen smoother is that the desirable characteristics of their filter transfer functions (small side lobes and a steep rolloff through the half-power filter cutoff wavenumber) require wider spans of data for each smoothed estimate. Such smoothers are therefore subject to greater edge-effect contamination of smoothed estimates near the edges of the measurement swaths. The assessments of resolution capabilities in this study are based on the more conservative estimates obtained using the Parzen smoother.

We first investigated the effects of measurement errors alone on the resolution capabilities of SWOT and WaCM estimates of surface velocity and vorticity. The analysis in Sec. 6 considered the idealized case of measurement swaths that span the entire CCS model domain on each satellite overpass. This is a highly

unrealistic representation of SWOT sampling, which consists of a 120-km swath with a 20-km nadir gap (see the top panels of Fig. 20). For WaCM, however, most of the CCS model domain is sampled on each overpass by just one of the two parallel measurement swaths for the case of a total swath width of 1200 km (see the bottom panels of Fig. 20). If the total swath width can be extended to 1800 km, essentially all of the CCS model domain would be sampled on each overpass by just one of the two parallel measurement swaths (see Fig. 41).

Based on uncorrelated measurement errors alone without consideration of the limitations of swath width, the conclusion of Sec. 6 is that the resolution capabilities of SWOT estimates of surface velocity and vorticity are substantially better than those of estimates obtained from WaCM with the baseline standard deviation of 0.50 m s^{-1} for the uncorrelated measurement errors (see Table 3). If the WaCM measurement noise can be reduced to 0.25 m s^{-1}, however, the resolution capabilities approach those of SWOT estimates of velocity and vorticity (see Sec. 10.2 and Tables 4a and b), with the distinct advantage of more than an order of magnitude wider measurement swath.

Mapping of the velocity and vorticity fields over domains larger than individual measurement swaths requires combining measurements from multiple satellite overpasses. Space-time smoothing of the satellite data to construct such maps introduces sampling errors in addition to the measurement errors considered in isolation in Sec. 6. As discussed in detail in Sec. 7, sampling errors arise predominantly from inadequate sampling of rapidly evolving submesoscale features in the surface velocity and vorticity fields. To the extent that the CCS model used in this study may underestimate the SSH variance at high wavenumbers as discussed above, our assessment of resolution capabilities for SWOT estimates of velocity and vorticity may be overly optimistic. Because small-scale features generally evolve more rapidly than large-scale features, higher spectral variance at high wavenumbers would likely increase the aliasing artifacts in time-averaged maps of velocity and vorticity constructed from SWOT. This would decrease the signal-to-noise ratio in the time-averaged maps, thus worsening the resolution capabilities.

It is evident from the figures in Secs. 8.4 and 8.5 that the sampling errors summarized in Sec. 7 are much worse for SWOT than for WaCM because of the narrow measurement swath of the SWOT instrument and the space-time sampling pattern of the SWOT orbit; during each 21-day exact-repeat orbit, the full CCS domain considered in this study is observed during two 4-day subcycles that are interleaved spatially and separated temporally by 6-day gaps (see Figs. 21–23). Sptially adjacent swaths are separated in time by 10 days.

Sampling errors are consequently the primary concern in maps of geostrophically computed velocity and vorticity constructed from SWOT data. The sampling errors are so large that our threshold S/N standard deviation ratio of 3.16 is not achieved in either 4-day or 14-day averaged vorticity fields using the Parzen smoother, even with the maximum half-power filter cutoff wavelength of 150 km considered in this study. Moreover, the resolution capability of SWOT estimates of 14-day averages of velocity is substantially worse than in 4-day averages because of the increased sampling errors in the longer time average.

We thus conclude that geostrophically computed SWOT estimates of velocity and vorticity will be useful primarily within individual measurement swaths. But even then, there are likely to be issues from the edge effects of spatial smoothing with a span that is comparable to the 50-km width of each of the two parallel measurement swaths. These edge effects will be exacerbated by the increased measurement errors towards the inner and outer edges of each measurement swath (see Fig. F1) that have not been taken into consideration in this study. To mitigate the multi-faceted effects of sampling errors, mapping of the surface velocity and vorticity fields from SWOT data will likely have to be done with the aid of dynamic interpolation from a data assimilation model, as suggested, for example, by Ubelmann et al. (2015).

12. Space-Time Smoothed SSH Fields from SWOT Data

Because of amplification of errors by the centered-difference approximations of the derivatives required to compute geostrophic velocity and vorticity from SSH, SWOT estimates of the derivative quantities are extremely sensitive to the standard deviation of 2.74 cm of the uncorrelated errors in the SSH measurements on a 1 km $\times$ 1 km grid (see Table 1). As pointed out in Sec. 11, however, SWOT was not designed to map

the surface velocity and vorticity fields that are the focus of this study. It was specifically designed to map the global SSH field with significantly higher resolution than can be achieved from the present constellation of nadir altimeters.

The scientific value of the improved resolution and accuracy of space-time smoothed SSH fields constructed from SWOT data should not be underestimated. Pujol et al. (2012), Fu and Ubelmann (2014) and Gaultier et al. (2016) have previously shown that maps of SSH from SWOT will be superior to the SSH maps from presently available nadir altimeter data. We show this here from simulated altimeter data based on the CCS model used in this study.

Space-time smoothed maps of SSH were constructed from simulated sampling by SWOT and from simulated sampling by nadir altimeters processed in a manner similar that of the "two-sat" SSH fields produced and archived by CLS/AVISO from the merged measurements from two simultaneously operating altimeters. Our intent is not to reproduce all of the details of the CLS/AVISO mapping procedure (see Pujol et al., 2016, and references therein). In view of the conclusion of Sec. 8 that SWOT measurement errors are negligible compared with sampling errors and the fact that sampling errors are much worse for the sparse sampling by two nadir altimeters than for the wide-swath SWOT altimeter, measurement errors were not included in our simplified form of the CLS/AVISO smoothing procedure. Instead, we consider only the effects of sampling errors by constructing a simulated CLS/AVISO SSH map by the following procedure.

The twice-daily SSH fields in the 30-day simulation of the CCS model used in this study were linearly interpolated in space and time to the locations of actual TOPEX/Poseidon and ERS-1 altimeter observations during the period 22 May to 21 June 1993, which corresponds to the same time period as the climatologically forced CCS model simulation. These simulated error-free TOPEX/Poseidon and ERS-1 data were smoothed along the satellite ground tracks with a half-power filter cutoff wavelength of 37 km. The along-track smoothed SSH values were then subsampled at every third point, corresponding to a spacing of about 18 km.

The resolution capability of the CLS/AVISO SSH fields is limited to wavelengths longer than about 200 km and time scales longer than about a month (see Appendix A.3 of Chelton et al., 2011). The subsampled and smoothed SSH values along the TOPEX/Poseidon and ERS-1 ground tracks were therefore smoothed and interpolated to the CCS model grid using a 2-dimensional objective analysis procedure with a half-power filter cutoff wavelength of 200 km in each dimension. To mimic the monthly smoothing in the CLS/AVISO SSH fields, all of the smoothed and subsampled simulated TOPEX/Poseidon and ERS-1 SSH observations within the 30-day period were weighted equally in the 2-dimensional smoothing.

The effects of sampling errors on the 200-km by 30-day smoothed SSH fields constructed from simulated SWOT and nadir altimeter data are shown in Fig. 46. The "true" space-time smoothed SSH field constructed from twice-daily error-free model output is shown in Fig. 46a. The space-time smoothed maps constructed from simulated CLS/AVISO processing of error-free nadir altimeter data and from simulated error-free SWOT data are shown in the top panels of Figs. 46b and c, respectively. The bottom panels show the sampling errors in the maps constructed from the simulated altimeter data.

The superiority of SWOT sampling is visually apparent in Fig. 46 from the smaller sampling errors. The standard deviation of 0.34 cm for the sampling errors in the SWOT map is a factor of 3.2 smaller than the standard deviation of 1.09 cm in the nadir altimeter map. Moreover, the dynamic range of the errors is nearly a factor of four smaller in the SWOT map: the extrema of the sampling errors range from only -1.3 cm to $+1.3$ cm in the SWOT map compared with a range of -6.5 cm to $+3.7$ cm in the nadir altimeter map. The present resolution of 200 km by one month will thus be achieved from SWOT data with much smaller sampling errors than in the presently available CLS/AVISO SSH fields.

It is noteworthy that the CCS region considered in our analysis coincidentally lies within the latitude range of most favorable space-time sampling by SWOT. The mapping errors increase somewhat at higher and lower latitudes, although they are still much smaller than the errors in maps constructed from nadir altimeter data (Pujol et al., 2012; see their Fig. 1 and their Tables 2 and 3).

The simulations in Fig. 46 do not include the effects of uncorrelated measurement errors. As noted above, measurement errors have negligible effect for the 200-km smoothing applied for the simulated SWOT map of SSH Fig. 46c. Uncorrelated measurement errors are a more significant consideration in the simulated "two-sat" CLS/AVISO map of SSH in Fig. 46b because the point-to-point noise in the nadir altimeter

measurements at intervals of 6 km along the satellite ground track has a standard deviation of about 3 cm. This is slightly higher than the $\sigma_h = 2.74$ cm standard deviation of the uncorrelated measurement errors in the pre-processed SWOT estimates of SSH with a smaller footprint size of 1 km. Smoothing the SWOT data 2-dimensionally to a resolution of 6 km (i.e., with a half-power filter cutoff wavelength of 12 km in each dimension – see Appendix B) to be commensurate with the 6-km along-track resolution of nadir altimeter data would reduce the SWOT noise standard deviation by about a factor of six (see Appendix D). The resulting standard deviation of about 0.46 cm for the noise in the 12-km smoothed SWOT data (see Fig. 12a) is more than a factor of six smaller than the 3-cm noise of the nadir altimeter data from which CLS/AVISO maps are constructed. Accounting for the effects of uncorrelated measurement errors in the simulations in Fig. 46 would thus worsen the errors in our simulated CLS/AVISO SSH field compared with the simulated SWOT SSH field.

A complete and rigorous analysis of the improved accuracy and resolution of SSH fields that will be achieved from SWOT data, including consideration of the effects of uncorrelated measurement errors mentioned above as well as orbit errors and other long-wavelength measurement errors, is beyond the scope of this study. Fig. 47 offers a sense of what can be expected from sampling errors alone. The two curves show the standard deviation of the sampling errors from spatially smoothed 30-day and 21-day averages of simulated SWOT data. The 1.09 cm standard deviation from our simulation of the sampling errors in CLS/AVISO SSH fields with 200-km by 30-day smoothing shown in Fig. 46b can be achieved from SWOT data with only 100-km by 21-day smoothing. One application that will especially benefit from the improved accuracy and improved spatial and temporal resolution of SSH fields constructed from SWOT data is the identification and tracking of mesoscale eddies (e.g., Chelton et al., 2011), and more generally, the study of mesoscale ocean dynamics. The smaller sampling errors from SWOT will significantly reduce the mislocation of eddies in presently available SSH fields (see, for example, Fig. 3 of Pascual et al., 2006).

13. Summary and Conclusions

High-resolution global satellite estimates of surface ocean velocity and vorticity would be of broad interest to a wide range of physical, biological and chemical oceanography applications. In this study, we conducted an exhaustive investigation the effects of uncorrelated measurement errors and sampling errors on the resolution capabilities of of instantaneous and space-time smoothed maps of velocity and vorticity fields derived from simulated measurements by two different techniques: 1) Altimetric measurements of SSH by interferometry from the Surface Water and Ocean Topography (SWOT) mission with a planned launch in 2021; and 2) Doppler radar measurements of surface ocean velocity from a future scatterometer mission that we have referred to as a Winds and Currents Mission (WaCM). WaCM is one of seven candidate NASA Earth Systems Explorer missions recommended in the recent decadal survey by the National Academies of Science, Engineering and Medicine (NASEM, 2018).

The results and conclusions of our assessments of the resolution capabilities of SWOT and WaCM estimates of surface ocean velocity and vorticity are summarized below.

13.1. The Analysis Procedures

Our strategy for assessing resolution capability is summarized in detail in Sec. 5. Simulated SWOT and WaCM data were generated based on, respectively, the SSH and surface velocity fields from 30 days of twice-daily output from the CCS model summarized in Sec. 2. Uncorrelated measurement errors with the baseline standard deviations were added to the model simulations of SSH and velocity. For SWOT, we used the error standard deviation of $\sigma_h = 2.74$ cm that is derived for a footprint size of 1 km in Appendix F. For WaCM, we used a baseline standard deviation of $\sigma_{spd} = 0.50$ m s^{-1} for a footprint size of 5 km but we also considered the benefits of smaller measurement errors in Sec. 10.2. Noise-free and noisy SSH and velocity fields on the 0.5 km $\times$ 0.5 km model grid were processed in manners that mimic the pre-processing that will be applied to the SWOT and WaCM data to achieve footprint sizes of 1 km and 5 km, respectively. Maps of noise-free and noisy SSH and velocity fields with these footprint sizes were then constructed on a 1 km $\times$ 1 km grid over the full model domain and on subsampled grids within the measurement swaths at the times and locations of the overpasses of each of the two satellite instruments.

The errors of surface velocity and vorticity fields estimated from the simulated pre-processed SWOT and WaCM data are too large for the estimates to be useful scientifically (see Tables 1 and 2 and the bottom left panels of Figs. 17b, 17c, 19a and 19b). It will be necessary to smooth the pre-processed SWOT and WaCM data in ground-based post-processing to reduce the effects of measurement noise in the maps of the variables of interest in this study. The four combinations of SSH and velocity fields summarized above (noise-free on the full grid, noise-free on the subsampled grid, noisy on the full grid and noisy on the subsampled grid) were successively smoothed with half-power filter cutoff wavelengths ranging from 10 km to 150 km. We also investigated the added benefits of time averaging to reduce the effects of measurement and sampling errors.

For each filter cutoff and each choice of time averaging, we computed the spatial standard deviations of the smoothed noise-free fields and the error fields for the cases of measurement errors alone, sampling errors alone and combined measurement and sampling errors. Our definition of resolution capability is based on the signal-to-noise (S/N) ratios of the standard deviations of the smoothed noise-free fields and the smoothed error fields. The S/N ratios for the cases of measurement errors alone and sampling errors alone allow an assessment of the relative contribution of each type of error to the total errors in maps of velocity and vorticity constructed from the simulated satellite data.

With increased spatial smoothing, the noise standard deviations usually decrease more rapidly than the signal standard deviations. The S/N ratios therefore improve with increased smoothing. Based on visual comparisons of many maps of smoothed noise-free and noisy velocity and vorticity fields constructed from the simulated satellite data (see, for example, Fig. 16), we defined the resolution capability as the half-power filter cutoff wavelength at which the S/N standard deviation ratio reaches a threshold value of 3.16, which corresponds to a S/N variance ratio of 10.

The sensitivity of our assessment of resolution capability to the details of the smoothing algorithm was investigated in Sec. 9 (see also Figs 43 and 44 in Sec. 10.2) from consideration of two different smoothers. The resolution capability inferred based on the loess smoother is better than that inferred based on the Parzen smoother (see Table 3). This is attributable to the more efficient attenuation of small-scale variability because of the better filtering properties of the loess smoother, albeit with more than 50 times more computational effort. The relative rankings of resolution capabilities for the two instruments and for the choices of time averaging considered in this study (instantaneous snapshots and time averages over 4 and 14 days) are insensitive to the details of the smoothing algorithm. We applied both the Parzen smoother and the loess smoother for all of the calculations in this study. Our assessments of resolution capabilities are based on the more conservative estimates inferred from the more computationally efficient Parzen smoother.

13.2. Instantaneous Snapshot Estimates of Velocity and Vorticity

Based on our criterion of a minimum S/N standard deviation ratio of 3.16 and the Parzen smoother, we showed in Sec. 6 that the in-swath resolution capabilities (i.e., the resolution capabilities when measurement errors are the only consideration) for instantaneous snapshot maps of geostrophically computed SWOT estimates of velocity and vorticity would be 32 km and 54 km, respectively, based on the spatial variances of the signals in the CCS model considered in this study (see Table 3). These numbers represent the wavelengths of the features that can be resolved with a S/N standard deviation ratio of 3.16. The corresponding radii of resolvable features are about four times smaller than the wavelength resolution (see Appendix B). The above resolution capabilities for instantaneous maps of SWOT estimates of velocity and vorticity correspond to the upper range of submesoscale variability.

In comparison, the in-swath resolution capabilities for instantaneous maps of velocity and vorticity constructed from WaCM data with the baseline standard deviation of $\sigma_{spd} = 0.50$ m s^{-1} for the uncorrelated measurement errors, equally partitioned between the two velocity components, would be 130 km for both variables (see Table 3). Reducing the WaCM measurement errors to $\sigma_{spd} = 0.25$ m s^{-1} would improve these resolution capabilities to about 50 km and 74 km for instantaneous maps of velocity and vorticity, respectively (see Fig. 44 and Tables 4a and b).

In terms of measurement errors alone, and aside from the limitations of the geostrophic approximation discussed in Sec. 3, velocity and vorticity would thus be estimated in instantaneous snapshots with higher

resolution from SWOT than from WaCM, although only modestly so if the WaCM measurement noise can be reduced to $\sigma_{spd} = 0.25$ m s^{-1}.

An important qualification of the conclusion that the resolution capabilities of in-swath estimates of velocity and vorticity are better for SWOT than for WaCM is that the analysis of the effects of measurement errors alone in Sec. 6 considers the case of measurement swaths that sample the entire CCS model domain and thus neglects any edge effects of the smoothing near the edges of the measurement swaths. With its 120-km swath width and a 20-km nadir gap, it can be seen from the top panels of Fig. 20 that complete coverage of the CCS model domain on a single satellite overpass is a highly idealized representation of SWOT sampling. In addition to its sparse coverage, edge effects will be problematic because the half-power filter cutoff wavelengths of 32 km and 54 km required to achieve a S/N standard deviation ratio of 3.16 for in-swath SWOT estimates of velocity and vorticity are comparable to the width of each parallel measurement swath. The above numbers must therefore be considered the most optimistic possible outlook for the resolution capabilities of velocity and vorticity fields constructed from SWOT data within the confines of a single measurement swath.

In contrast, the idealized complete coverage of the CCS model domain considered for the analysis in Sec. 6 would be very nearly achieved by WaCM for a region of this size. With a total swath width of 1200 km, WaCM coverage would be nearly complete with just one side of the two parallel measurement swaths (see the bottom panels of Fig. 20). WaCM coverage would be essentially complete on each overpass if the swath width can be extended to 1800 km (Fig. 41).

13.3. Space-Time Smoothed Estimates of Velocity and Vorticity

Mapping of the velocity and vorticity fields over a region wider than an individual measurement swath requires space-time smoothing of the satellite data from multiple overpasses of the region of interest. This is especially needed for SWOT because of its narrow 120-km swath width. For both SWOT and WaCM, time averaging can reduce the effects of the measurement errors considered in Sec. 6 but it also introduces the three types of sampling errors that are summarized in Sec. 7. We investigated the effects of combined measurement and sampling errors in Secs. 8–10 for the cases of 4-day and 14-day averages. These choices of time averages correspond to the two subcycles of each repeat of the 21-day SWOT orbit (see Figs. 22 and 23). The 4-day averaging time also corresponds to the exact-repeat period of the WaCM orbit assumed in this study.

The resolution capabilities inferred from the analysis in Sec. 8 for SWOT and WaCM estimates of space-time smoothed velocity and vorticity fields are summarized in Table 3 for a swath width of 1200 km in the case of WaCM. Whereas SWOT outperformed WaCM from the consideration of measurement errors alone in Sec. 6, the relative performance of the two instruments is not so simple for space-time smoothed velocity and vorticity fields. Because of the narrow swath width of SWOT and the space-time sampling pattern of the SWOT 21-day exact-repeat orbit that samples the full CCS model domain in two 4-day subcycles that are interleaved and separated by 6-day gaps with spatially adjacent swaths separated by 10 days, the total errors in maps of geostrophically computed velocity and vorticity constructed from SWOT data are dominated by sampling errors. Improving the measurement accuracy would have very little effect on the total errors in SWOT estimates of space-time smoothed maps of velocity and vorticity.

For velocity, the resolution capability of SWOT estimates of 4-day averages is 52 km based on the Parzen smoother, but with large gaps in the maps because of the sparse SWOT sampling of the CCS model domain during a 4-day period (see Fig. 28). Sampling errors are even worse in SWOT estimates of time-averaged velocity fields over the 14-day period required for SWOT to map the entire CCS model domain; the resolution capability degrades to 132 km. For SWOT estimates of space-time smoothed vorticity fields, sampling errors are so large that the S/N standard deviation ratio never reaches our threshold minimum of 3.16 for either choice of averaging period based on the Parzen smoother.

A conclusion of this study is thus that SWOT will be of limited value for spatially complete mapping of velocity and vorticity fields without the use of a data assimilation model. Its primary contribution will be the SSH mapping capabilities for which it was designed. SWOT will map the global SSH field with accuracy and resolution significantly better than are presently achieved from the merging of SSH measurements from

multiple nadir altimetry missions (see Sec. 12 and Figs. 46 and 47). Among other applications, this will greatly benefit studies of mesoscale eddy dynamics.

For spatially complete global mapping of the surface velocity and vorticity fields, the Doppler radar measurements from a WaCM mission would be far superior to SWOT. With its wider measurement swath and the 4-day orbit repeat period assumed for the simulations of WaCM data in this study, sampling errors are much less of an issue than for SWOT. The effects of measurement errors in instantaneous snapshot maps of the velocity and vorticity can therefore be reduced with time averaging. By our criterion, the resolution capabilities for WaCM estimates of 4-day averaged maps of velocity and vorticity based on a swath width of 1200 km and a standard deviation of $\sigma_{spd} = 0.50$ m s^{-1} for the uncorrelated measurement errors are 60 km and 87 km, respectively, which correspond to the lower range of mesoscale variability. Increasing the swath width to 1800 km would improve these resolution capabilities to 44 km and 70 km (see Sec. 10.1 and Figs. 43a and c).

For both swath widths, the spatial resolutions of WaCM estimates of velocity and vorticity could be further improved by increasing the averaging period, e.g., to the 14-day averaging period considered in Secs. 8–10. It is not clear, however, how much of an advantage the improved spatial resolution in these longer time averages would be since increasing the averaging time also attenuates the smaller-scale velocity and vorticity signals that are of interest (see Figs. 24 and 25).

The fact that measurement noise is the primary source of errors in WaCM maps of the space-time smoothed velocity and vorticity fields means that the resolution capabilities would be improved if the standard deviation of uncorrelated WaCM measurement errors can be reduced from the baseline value of $\sigma_{spd} = 0.50$ m s^{-1} assumed in Secs. 6, 8.4, 8.5, 9 and 10.1. The benefits of improving the WaCM measurement accuracy were investigated in Sec. 10.2 (see Fig. 45). If the measurement errors can be reduced to $\sigma_{spd} = 0.25$ m s^{-1}, for example, with the same footprint size of 5 km, the resolution capabilities for WaCM estimates of 4-day averaged fields based on a swath width of 1800 km would improve from the above-noted 44 km and 70 km to 18 km and 45 km for velocity and vorticity, respectively (see Figs. 45a and c).

The resolution capabilities summarized above for WaCM estimates of 4-day averaged maps of surface velocity and vorticity constructed using the Parzen smoother are listed in Tables 4c and d for the cases of 1200-km and 1800-km swath widths and standard deviations of $\sigma_{spd} = 0.50$ m s^{-1} and 0.25 m s^{-1} for the uncorrelated speed measurement errors. For comparisons, the resolution capabilities of WaCM estimates of velocity and vorticity are also listed for the cases of instantaneous snapshots (Tables 4a and b) and 14-day averages (Tables 4e and f).

13.4. Visual Assessments of the WaCM Resolution Capabilities

The improvements in the resolution of velocity and vorticity maps that would be achieved from WaCM over the present resolution capability of about 200 km by one month in geostrophically computed maps constructed from multi-mission nadir altimeter data are visually apparent from the 4-day averages shown in Figs. 48 and 49 for the CCS region considered in this study. For the purposes of this comparison, we have adopted the more conservative resolution capabilities inferred from Fig. 45 based on Parzen smoothing.

Although lacking the highly energetic submesocale variability that is evident in the instantaneous maps in Fig. 3, the resolutions of about 60 km and 90 km that are attainable in 4-day averaged maps of, respectively, velocity and vorticity (Figs. 48b and 49b) with the baseline standard deviation of $\sigma_{spd} = 0.50$ m s^{-1} for the uncorrelated measurement noise and a swath width of 1200 km are a dramatic improvement over the present capabilities shown in Figs. 48a and 49a. The increased resolutions of about 45 km and 70 km that would be achieved in 4-day averaged maps of velocity and vorticity with a wider swath width of 1800 km are shown in Figs. 48c and 49c. The further improvements to resolutions of about 20 km and 45 km that would be achieved in 4-day averaged maps of velocity and vorticity if the standard deviation of the WaCM uncorrelated measurement noise can be reduced to $\sigma_{spd} = 0.25$ m s^{-1} are shown in Figs. 48d and 49d.

While the 4-day averaging in Figs. 48 and 49 reduces the measurement noise and improves the spatial resolution compared with instantaneous snapshots, the time averaging attenuates the small-scale signal variability that is of interest, as noted above (Fig. 24). Depending on the application, the coarser spatial

resolution capability of the snapshots may be preferable to the 4-day averages. This is visually apparent from Fig. 50, which shows instantaneous snapshot maps of velocity and vorticity with the resolution capabilities that are achievable from WaCM data with measurement error standard deviations of $\sigma_{spd} = 0.50$ m s^{-1} and 0.25 m s^{-1}.

13.5. Final Comments

A qualification of the analysis in Secs. 6 and 8–10 is that we have neglected the effects of correlated measurement errors. Because of the spatial high-pass filtering property of the derivative operator, these long-wavelength errors are secondary to the effects of uncorrelated errors on estimates of the surface ocean velocity and vorticity fields that are the primary interest in this study. A more important limitation is that we considered the uncorrelated measurement errors to be spatially homogeneous across the SWOT and WaCM measurement swaths. In reality, the measurement errors for both instruments increase toward the inner and outer edges of each swath.

Another caveat to our analysis is that we have assumed that the measurement errors of WaCM estimates of surface velocity are equally partitioned between the two orthogonal velocity components. We have thus neglected the geometrical transformation issues associated with the limited azimuthal diversity of the Doppler measurements of radial velocity near the swath edges. Errors of the cross-track velocity component increase toward the inner edges of the two parallel measurement swaths and errors of the along-track component increase toward the outer edges of the measurement swaths.

Because of our incomplete treatment of measurement errors, the assessments of resolution capabilities deduced from the analysis in Secs. 6 and 8–10 are likely to be somewhat optimistic.

We also emphasize that our assessments of resolution capabilities are specific to the CCS region during the summertime, and in particular, to the representation of the CCS surface currents in the ROMS model with 0.5 km × 0.5 km grid resolution used here to simulate SWOT and WaCM data. Since the S/N ratios for WaCM estimates of the velocity and vorticity fields depend predominantly on measurement errors that are relatively homogeneous geographically, the resolution capabilities inferred from this study will improve in regions or at times of more energetic spatial variability of velocity and vorticity. Likewise, the resolution capabilities for WaCM will be degraded when the velocity and vorticity variability is less energetic.

It is less clear how the resolution capabilities will change geographically and seasonally for SWOT because the S/N ratio depends predominantly on sampling errors owing to the narrow measurement swaths. While the signal variance increases when the variability is more energetic, so does the variance of the sampling errors. Depending on the relative increases in signal and sampling error variances, the resolution capabilities may actually worsen for SWOT when the variability is more energetic. Likewise, the sampling error variance may decrease more than the signal variance when the variability is less energetic, thus improving the resolution capabilities for SWOT. The results for SWOT are thus likely to be regionally and seasonally specific.

The immunity of WaCM measurements of surface velocity to errors from the geostrophic approximation that must be used for SWOT estimates of surface velocity is an important advantage of WaCM. In principle, surface divergence and hence vertical velocity can be estimated from WaCM measurements of surface velocity. This cannot be done from SWOT data since geostrophically computed velocity is non-divergent.

In practice, estimation of surface divergence from WaCM data will be challenging since the velocity field is nearly geostrophic on the scales that will be resolvable by WaCM. The non-divergent part of the velocity signal on these scales is therefore weak. In particular, the divergence is much weaker than the vorticity that has been a focus of this study. Divergence and vorticity both involve first derivatives of velocity. The residual noise variance for a given space-time smoothing of divergence will therefore be about the same as the residual noise variance for space-time smoothed vorticity. It can thus be anticipated that the signal-to-noise ratio that is the basis for defining the resolution capability in this study will be smaller for divergence than for vorticity. The resolution capability of WaCM estimates of space-time smoothed surface divergence will therefore be coarser than the resolution capabilities determined for vorticity in Secs. 8–10.

We close by reiterating the important point that WaCM would provide simultaneous measurements of vector winds collocated with the measurements of surface ocean velocity that were considered in this

study. The WaCM measurements of vector winds will have the same footprint size of 5 km as the surface ocean velocity measurements, which is about a factor-of-5 smaller than the footprint size of QuikSCAT measurements of vector winds. The WaCM technology for measurements of both wind velocity and surface current velocity is mature and has been demonstrated from an aircraft version of a Doppler scatterometer that has been built by NASA and flown in several field campaigns over the past year (Rodríguez et al., 2018).

Acknowledgments

We thank Ralph Milliff, Bo Qiu, Ernesto Rodríguez and Lee-Lueng Fu for many helpful editorial comments and suggestions that improved the manuscript. This research was funded by NASA Grants NNX13AD78G, NNX14AM72G, NNX13AE32G, NNX14AM66G, NNX16AH76G, NNX14AM71G and NNX17AH54G. The two North Atlantic Ocean simulations in this study were performed using HPC resources from GENCI-TGCC with support from Grant 2017-A0010107638 for Jonathan Gula.

Appendices

To provide a road map of the unusually large number of appendices (nine total) in this paper and to clarify the logic of the ordering of the appendices, we include here a brief overview of the content of each appendix.

Appendix A provides a detailed description of the Parzen smoother that is the primary filter used in this study to simulate the smoothing applied in the pre-processing of SWOT and WaCM data and the additional smoothing applied in simulated ground-based post-processing of SWOT and WaCM data to reduce the effects of measurement errors in estimates of velocity and vorticity. The filter transfer function for the Parzen smoother that is given by (A.11) and the relationship (A.12b) between the span of the Parzen smoother and the corresponding half-power filter cutoff wavelength are used extensively throughout later appendices.

Appendix B shows that the footprint diameter that is achieved by smoothing a field of uncorrelated white noise with a specified half-power filter cutoff wavelength of λ_c can be characterized as approximately $\lambda_c/2$. The science requirement for SWOT measurements of SSH with a footprint size of 1 km can thus be achieved with isotropic 2-dimensional smoothing using a Parzen smoother with a half-power filter cutoff wavelength of 2 km. The errors of these pre-processed SWOT estimates of SSH are shown to be uncorrelated when sampled on a 1 km $\times$ 1 km grid.

The baseline design assumed here for WaCM measurements of surface velocity components with a footprint size of 5 km can be achieved with isotropic 2-dimensional smoothing using a Parzen smoother with a half-power filter cutoff wavelength of 10 km. While the errors of these pre-processed WaCM estimates of velocity are uncorrelated when sampled on a 5 km $\times$ 5 km grid, it is shown later in Appendix H that it is advantageous to oversample the WaCM data on a 1 km $\times$ 1 km grid because the response function for standard centered difference estimates of derivatives on the finer grid retains more small-scale variability in the vorticity signal.

Appendix C shows that the filter transfer function of the Parzen smoother is almost identical to that of the Gaussian-weighted smoother with an appropriately chosen e-folding scale. A feature of isotropic Gaussian smoothing in two dimensions, i.e., with Gaussian weighting dependent only on the radial distance of the simulated observations from the location of the smoothed estimate, is that it can be applied either as a single 2-dimensional weighted average or as separate 1-dimensional weighted averages in each of two orthogonal dimensions. The close similarity of the Parzen smoother to the Gaussian smoother thus implies that smoothing successively using a 1-dimensional Parzen smoother with the same half-power filter cutoff wavelength in each dimension is essentially equivalent to isotropic 2-dimensional smoothing.

While the Parzen smoothing that was applied to the simulated SWOT and WaCM data in Secs. 6 and 8–10 was implemented truly isotropically, the derivations of analytical expressions for the wavenumber spectral content of 2-dimensionally smoothed fields in Appendix E, Appendix F, Appendix H and

Appendix I and for the theoretical error spectra in Figs. 13–15 in Sec. 4.4, are greatly simplified if the Parzen smoothing is applied 1-dimensionally in each dimension.

Appendix C also includes a comparison of the filter transfer function of the Parzen smoother with that of the quadratic loess smoother. The latter has the desirable property that its filter transfer function rolls off more steeply through the half-power filter cutoff wavelength, but it is much more computationally intensive. It is shown in Sec. 9 and 10.2 that the more effective attenuation of small-scale noise that is achieved with the loess smoother or other smoothers with similar filter transfer function properties improves our assessment of the resolution capability somewhat (see Table 3).

Appendix D determines the reduction of the variance of uncorrelated errors that is achieved by 2-dimensional smoothing. For isotropic smoothing with a half-power filter cutoff wavelength of λ_c, it is shown that the error variance is reduced by the factor $4\Delta x\,\Delta y\,\lambda_c^{-2}$ that is the same as would be achieved by block averaging of measurement errors on a $\Delta x \times \Delta y$ grid with a span of $\lambda_c/2$ in each dimension. This variance reduction factor, which is equivalent to a standard deviation reduction factor of $2(\Delta x \Delta y)^{-1/2}\lambda_c^{-1}$, is used extensively in the derivations in Appendix E, Appendix F, Appendix G and Appendix I.

Appendix E quantifies the effects of 2-dimensional smoothing on the 1-dimensional wavenumber spectrum of 2-dimensional uncorrelated white noise. As in the case of low-pass filtering of a 1-dimensional dataset, 2-dimensional smoothing of a 2-dimensional dataset attenuates the spectral content of the 1-dimensional spectrum at wavenumbers higher than the half-power filter cutoff wavelength λ_c. For uncorrelated noise, the spectral values are also attenuated at all wavenumbers (not just at high wavenumbers) by the constant multiplicative factor of $2\Delta x/\lambda_c$ in (E.11b), where Δx and λ_c are the grid spacing and half-power filter cutoff wavelength in the dimension perpendicular to the dimension of the 1-dimensional spectrum.

The results of Appendix E are used in the derivations of 1-dimensional spectra in Appendix F and Appendix I. In the context of the analysis presented in this paper, the interest is in 1-dimensional spectra in the alongshore dimension. In the context of actual satellite data, the interest is in 1-dimensional spectra in the along-track dimension.

Appendix F determines the variance of the uncorrelated errors of pre-processed SWOT estimates of SSH based on the science requirements for SWOT that are expressed in terms of the intersection of an hypothesized wavenumber spectrum of the SSH signal and the wavenumber spectrum of smoothed uncorrelated noise. The analysis concludes that the error standard deviation for the baseline design is $\sigma_h = 2.74$ cm.

Our derived error standard deviation of $\sigma_h = 2.74$ cm is used throughout this study, including in the propagation-of-error analysis in Appendix G to determine the standard deviations of errors of geostrophically computed SWOT estimates of velocity and vorticity. The derivations of the analytical formulas for the 1-dimensional wavenumber spectra of errors in SWOT estimates of SSH and geostrophically computed velocity and vorticity in Appendix I are also based on an error standard deviation of $\sigma_h = 2.74$ cm. Likewise, the error fields for the simulated SWOT data used in Secs. 4, 6 and 8 are predicated on an error standard deviation of $\sigma_h = 2.74$ cm.

While the specific value of $\sigma_h = 2.74$ cm for the SSH error standard deviation is used for all of the SWOT calculations in this study, the equations for the variances and wavenumber spectra of geostrophically computed SWOT estimates of the velocity components and vorticity that are derived in Appendix G and Appendix I are all expressed in terms of the variance σ_h^2 of the errors of the pre-processed SWOT estimates of SSH. These equations are therefore applicable to any specified value of σ_h^2.

Appendix G applies standard propagation-of-error analysis to derive analytical expressions for the variances of the errors of derivative quantities estimated from the pre-processed SWOT and WaCM data. In the case of SWOT, the velocity components are computed geostrophically from derivatives of SSH. The vorticity is then estimated from derivatives of the geostrophically computed velocity components, i.e., from second derivatives of SSH. In the case of WaCM, the velocity is measured directly and vorticity is obtained from derivatives of the velocity components. The derivatives in this study are all estimated

using standard centered differences (see Appendix H). This finite differencing amplifies the errors in the measured variables.

The equations that are derived in Appendix G are all expressed in terms of the variances of the uncorrelated errors of the pre-processed SWOT and WaCM data. Throughout this study, the error variance of $\sigma_h^2 = (2.74 \text{ cm})^2$ that is derived in Appendix F is used for SWOT estimates of SSH and an error variance of $\sigma_{u,v}^2 = (0.354 \text{ m s}^{-1})^2$ is used for the variances σ_u^2 and σ_v^2 of the errors of WaCM estimates of the two orthogonal velocity components u and v. The equations for the variances of the errors of the derivative quantities (the two geostrophically computed velocity components and vorticity for SWOT and vorticity for WaCM) are applicable to any specified values of σ_h^2 or σ_u^2 and σ_v^2.

Appendix H examines the wavenumber spectral characteristics of the response functions of various centered differences estimates of derivatives applied to the pre-processed SWOT and WaCM data and in combination with smoothing in ground-based post-processing.

For the amount of smoothing that will be required to achieve scientifically useful signal-to-noise ratios in geostrophically computed SWOT estimates of velocity and vorticity obtained from pre-processed SSH on a 1 km × 1 km grid, it is shown that standard centered differencing with a 3-point stencil width provides adequate estimates of derivatives.

For the 5 km × 5 km grid on which the errors of pre-processed WaCM estimates of velocity are uncorrelated, derivatives estimated from centered differences with a 9-point stencil width are significantly better than from standard centered differences with a 3-point stencil width. If the pre-processed WaCM data are oversampled on a 1 km × 1 km grid, however, it is shown that it is not necessary to estimate derivatives with a 9-point stencil for the amount of smoothing that will be required to achieve scientifically useful signal-to-noise ratios in WaCM estimates of vorticity. This is because a 3-point stencil retains considerably more small-scale variability in vorticity estimates when computed on an oversampled 1 km × 1 km grid rather than on a 5 km × 5 km grid. Although a 9-point stencil on a 5 km × 5 km grid retains even more small-scale variability, that portion of the vorticity wavenumber spectrum is attenuated by the spatial smoothing that is required to achieve adequate signal-to-noise ratio. For the resolution capability of WaCM estimates of vorticity deduced from this study, any advantage of the 9-point stencil is therefore lost in WaCM estimates of vorticity computed on an oversampled 1 km × 1 km grid.

Throughout this study, we therefore assume that the pre-processed WaCM data will be available on a 1 km × 1 km grid and derivatives are estimated with a standard 3-point stencil. This oversampling leads to some complications in the derivations of analytical expressions for the standard deviations and wavenumber spectra of errors of the WaCM estimates of velocity and vorticity in Appendix G and Appendix I.

Appendix I derives analytical expressions for the 1-dimensional wavenumber spectra of the errors of all of the variables that are of interest in this study. The analysis begins with derivations in Appendix I.1 of the spectral characteristics of the errors of SSH and geostrophically computed velocity components and vorticity estimated from the pre-processed SWOT data. The effects on the spectral characteristics of the errors after isotropic 2-dimensional smoothing in ground-based post-processing of SWOT data are then derived in Appendix I.2. The analogous derivations for velocity components and vorticity estimated from pre-processed WaCM data and after smoothing in ground-based post-processing are presented in Appendix I.3 and Appendix I.4, respectively. The theoretical error spectra derived in Appendix I are shown in Figs. 13–15 to agree very well with spectra computed empirically from the simulated SWOT and WaCM error fields generated for the analysis in Secs. 6 and 8–10.

As in Appendix G, the equations derived in Appendix I are all expressed in terms of the variances of the uncorrelated measurement errors and the filter transfer function for whatever smoother is applied in the ground-based post-processing. While this study assumes error variances of $\sigma_h^2 = (2.74 \text{ cm})^2$ and $\sigma_u^2 = \sigma_v^2 = (0.354 \text{ m s}^{-1})^2$ for SWOT and WaCM measurements of SSH and the two velocity components, respectively, the equations for the wavenumber spectra of the errors of the derivative quantities (the

geostrophically computed velocity components and vorticity for SWOT and the vorticity for WaCM) are applicable to any specified values of σ_h^2 or σ_u^2 and σ_v^2.

Appendix A. The Parzen Smoother

Parzen smoothing is used extensively throughout this study. It is applied in the first step of our analysis of simulated satellite data to mimic the onboard pre-processing of the raw radar measurements to achieve footprint sizes of 1 km and 5 km for SWOT and WaCM, respectively (see Appendix B). It is subsequently applied to the maps of SSH for SWOT and surface velocity components for WaCM to mimic smoothing in ground-based post-processing to reduce the effects of measurement errors to acceptable levels for the variables of interest in this study (see Appendix C and Appendix D and Secs. 6 and 8–10). To understand the filtering implied at both of these stages of smoothing, and to quantify what is meant by the "footprint size" of pre-processed data (Appendix B) and by "feature resolution" in smoothed fields constructed in ground-based post-processing (Appendix C), the filtering properties of the Parzen smoother are derived in this appendix.

The filtering properties of any smoother can be understood by considering the case of a 1-dimensional spatial series that is continuous. The results can be extended straightforwardly to the case of two dimensions. The results can also be extended to discrete sampling, but the equations become unnecessarily cumbersome for present purposes of characterizing the wavenumber content of the filtered output.

Any linear, space-invariant filter applied to a continuous spatial series $z(x)$ can be written as the convolution

$$\overline{z}(x) = w(x) * z(x) \equiv \int_{-\infty}^{\infty} w(x-s)\, z(s)\, ds, \tag{A.1}$$

where the asterisk is short-hand notation for the convolution integral on the right side of the equation and $w(x)$ is the weighting function of the smoother. The overbar distinguishes the smoothed value $\overline{z}(x)$ from the unfiltered value $z(x)$. The Fourier transform of the weighting function $w(x)$, which is called the filter transfer function of the smoother, is given by

$$W(k) = \int_{-\infty}^{\infty} w(x)\, e^{-i2\pi kx}\, dx \tag{A.2}$$

where k is wavenumber in the x dimension.

The wavenumber contents of the unfiltered and smoothed data are defined by their Fourier transforms, which can be denoted as $Z(k)$ and $\overline{Z}(k)$, respectively. By the Convolution Theorem, the convolution integral (A.1) in the space domain can be expressed as multiplication in the wavenumber domain. The wavenumber content $\overline{Z}(k)$ of the smoothed output $\overline{z}(x)$ is therefore related to the wavenumber content $Z(k)$ of the unfiltered data $z(x)$ by

$$\overline{Z}(k) = W(k)Z(k). \tag{A.3}$$

The filter transfer function $W(k)$ thus defines the wavenumber content of the smoothed output.

In one dimension, any smoother can be characterized by its filter cutoff wavenumber k_c, which is defined here to be the wavenumber at which the squared value of the filter transfer function passes through a value of 0.5. The ideal filter has a filter transfer function that consists of values of 1 for wavenumbers $|k| \le k_c$ and 0 for higher wavenumbers. In practice, the filter transfer functions of real smoothers decrease gradually with increasing wavenumber across the low-wavenumber pass band and rolloff steeply through the filter cutoff wavenumber k_c. Most real smoothers also have undesirable sidelobes at wavenumbers higher than k_c.

For the simple block-average smoother with uniform weighting over a span of L_1 centered on the estimation location, the weighting function is

$$w_1(x) = \frac{1}{L_1}\, \Pi\left(\frac{x}{L_1}\right). \tag{A.4a}$$

The subscript 1 is used here to distinguish this uniform-weighted average from the Parzen weighted average considered below and $\Pi(x/L_1)$ is shorthand notation for the rectangle function defined by

$$\Pi\left(\frac{x}{L_1}\right) \equiv \begin{cases} 1 & \text{if } -L_1/2 \le x \le L_1/2 \\ 0 & \text{otherwise.} \end{cases} \tag{A.4b}$$

The output (A.1) of the uniform-weighted average smoother with weighting function (A.4) is thus

$$\begin{aligned} \overline{z}_1(x) &= \frac{1}{L_1}\int_{-\infty}^{\infty} \Pi\left(\frac{x-s}{L_1}\right) z(s)\, ds \\ &= \frac{1}{L_1}\int_{x-L_1/2}^{x+L_1/2} z(s)\, ds. \end{aligned} \tag{A.5}$$

For discretely sampled values of $z(x)$, the integral on the right side of this equation becomes a discrete sum.

The filter transfer function (A.2) of the uniform-weighted average smoother is

$$\begin{aligned} W_1(k) &= \int_{-\infty}^{\infty} w_1(x)\, e^{-i2\pi kx}\, dx \\ &= \frac{1}{L_1}\int_{-L_1/2}^{L_1/2} e^{-i2\pi kx}\, dx \\ &= \text{sinc}(kL_1), \end{aligned} \tag{A.6a}$$

where $\text{sinc}(kL_1)$ is standard shorthand notation for

$$\text{sinc}(kL_1) \equiv \frac{\sin(\pi kL_1)}{\pi kL_1}. \tag{A.6b}$$

The half-power filter cutoff wavenumber k_c for the uniform-weighted average smoother is the value k_c of the wavenumber k at which the squared value of the filter transfer function (A.6) has a value of 0.5. The solution to this transcendental equation is

$$\begin{aligned} W_1^2(k_c) = \text{sinc}^2(k_cL_1) &= 0.5 \\ \Rightarrow \quad k_c &= \frac{0.443}{L_1}. \end{aligned} \tag{A.7}$$

The weighting function (A.4) and the squared value of the filter transfer function (A.6) of the uniform-weighted average smoother are shown for the case of $L_1 = 1$ km in Fig. A1a. A highly undesirable feature of the simple uniform-weighted average smoother is that its filter transfer function has large sidelobes outside of the main lobe that defines the range of wavenumbers $|k| \le k_c$ that are of interest. According to (A.3), these sidelobes contaminate the frequency content of the smoothed values $\overline{z}(x)$ by admitting considerable variance at wavenumbers higher than the desired half-power filter cutoff wavenumber k_c.

The sidelobes of the uniform-weighted average smoother can be suppressed by replacing the uniform weighting with a tapered weighting. A simple approach to tapering is to apply a succession of uniform-weighted averages. For example, the weighting function for two successive applications of a uniform-weighted average with a span of L_1 can be shown to be equivalent to a single triangular weighted average with a span of $L_2 = 2L_1$. More generally, p successive applications of a uniform-weighted average with a span of L_1 are equivalent to a single weighted average with a span of $L_p = pL_1$ and a weighting function that consists of a piecewise continuous polynomial of order $p - 1$.

Mathematically, the weighting function $w_p(x)$ of p successive applications of a uniform-weighted average smoother with a span of L_1 consists of p self-convolutions of the rectangle weighting function (A.4) of the uniform-weighted average. The Fourier transform of this smoother (i.e., its filter transfer function) is therefore easily determined from the Convolution Theorem to be the multiplicative product of p of the filter transfer functions (A.6) of the uniform-weighted average,

$$W_p(k) = \text{sinc}^p(kL_1). \tag{A.8}$$

The extremum of the j^{th} sidelobe of this filter transfer function has a value of $\mathrm{sinc}^p(k_j L_1)$, where $k_j = (j + 1/2)/L_1,\ j = 1, 2, 3, \ldots$. Since $\mathrm{sinc}^p(k_j L_1) = (-1)^j / \big[([j + 1/2]\pi)\big]^p$, it has a magnitude less than 1 for all j and the sidelobe extrema decrease rapidly in magnitude, both with increasing j and with increasing p. For the case of the dominant $j = 1$ sidelobe, the sinc function has a value of $\mathrm{sinc}(1.5) = \sin(1.5\pi)/(1.5\pi) = -0.212$. The dominant sidelobe of the filter transfer function for p successive applications of the uniform-weighted average thus has a magnitude of $0.212^{\,p}$ and a squared magnitude of $0.212^{\,2p}$.

There is no practical advantage to smoothing with more than $p = 4$ successive applications of a uniform-weighted average since the extremum of the dominant sidelobe of its squared filter transfer function is 4.08×10^{-6}, i.e., an attenuation factor of more than 50 dB. The quadruple pass of the uniform-weighted average is called the Parzen smoother. Mathematically, the weighting function of the Parzen smoother can be written as a quadruple convolution of the weighting function (A.4) of the uniform-weighted average,

$$w_4(x) = \frac{1}{L_1^4}\left[\Pi\left(\frac{x}{L_1}\right) * \Pi\left(\frac{x}{L_1}\right) * \Pi\left(\frac{x}{L_1}\right) * \Pi\left(\frac{x}{L_1}\right)\right], \tag{A.9}$$

where the subscript 4 signifies that the Parzen smoother is equivalent to 4 successive applications of a uniform-weighted average. The output of the Parzen smoother is the convolution

$$\begin{aligned} \overline{z}_4(x) &= w_4(x) * z(x) \\ &= \int_{-\infty}^{\infty} w_4(x - s)\, z(s)\, ds. \end{aligned} \tag{A.10}$$

The filter transfer function (A.8) with $p = 4$ for the Parzen weighting function is

$$W_4(k) = \mathrm{sinc}^4(kL_1) = \mathrm{sinc}^4\left(\frac{kL_4}{4}\right), \tag{A.11}$$

where $L_4 = 4L_1$ and L_1 is the span of each of the four successive applications of the uniform-weighted average. The motivation for introducing L_4 will become apparent below. The half-power filter cutoff wavenumber of the Parzen smoother is defined as in (A.7) to be the value k_c of the wavenumber k at which the squared value of the filter transfer function (A.11) has a value of 0.5. The solution to this transcendental equation is

$$\begin{aligned} W_4^2(k_c) = \mathrm{sinc}^8(k_c L_1) = \mathrm{sinc}^8(k_c L_4/4) = 0.5 \\ \Rightarrow \quad k_c = \frac{0.228}{L_1} = \frac{0.910}{L_4}. \end{aligned} \tag{A.12a}$$

The value of L_4 for a Parzen filter that has a half-power filter cutoff wavelength of $\lambda_c = k_c^{-1}$ is thus

$$L_4 = 0.910\, \lambda_c. \tag{A.12b}$$

While it would be very tedious to calculate the weights of the Parzen smoother from the quadruple convolution (A.9), it is straightforward with the help of integral tables to determine these weights from the inverse Fourier transform of the filter transfer function (A.11). The result is the piecewise cubic polynomial defined by

$$w_4(x) = \begin{cases} \dfrac{8}{3L_4}\left(1 - \dfrac{24x^2}{L_4^2} + \dfrac{48|x|^3}{L_4^3}\right) \\ \quad \text{if } 0 \le |x| \le L_4/4 \\ \dfrac{8}{3L_4}\left(2 - \dfrac{12|x|}{L_4} + \dfrac{24x^2}{L_4^2} - \dfrac{16|x|^3}{L_4^3}\right) \\ \quad \text{if } L_4/4 \le |x| \le L_4/2 \\ 0 \quad \text{if } |x| > L_4/2. \end{cases} \tag{A.13}$$

The Parzen smoother thus has a full span of L_4 that is defined above to be four times larger than the span L_1 of each of the four successive applications of the uniform-weighted smoother upon which it is based.

In principle, the Parzen smoother (A.10) can be implemented either as a succession of four applications of the uniform-weighted average (A.5) with span L_1 or as a single pass of (A.10) with the piecewise cubic weighting (A.13) and a span of $L_4 = 4L_1$. In practice, however, application to discretely sampled data results in small differences in the filtered output by the two procedures. When applied to data with a uniformly spaced sample interval of Δx, for example, an arbitrarily specified value of L_4 can result in a value of $L_1 = L_4/4$ that is a non-integer multiple of Δx. Moreover, it is desirable for the full span of the smoothing to be an odd multiple of Δx so that the weighting function is symmetric. This assures that there is no phase shift at any of the wavenumbers in the filtered output. It is clearly not possible for both L_1 and L_4 to be odd integer multiples of Δx. The preferred implementation of the Parzen smoother with uniformly spaced data is therefore as a single pass of (A.10) with the piecewise cubic weighting (A.13).

The weighting function (A.13) and the square of the filter transfer function (A.11) of the Parzen smoother are shown for the case of $L_4 = 1$ km by the thick lines in Fig. A1b. This is equivalent to a span of $L_1 = L_4/4 = 0.25$ km for each of the four successive applications of the uniform-weighted average (A.5).

For a given value of L_1, it can be noted from (A.7) and (A.12a) that the filter cutoff wavenumber k_c is a factor of $0.228/0.443 = 0.515 \approx 0.5$ smaller for the Parzen smoother than for the single-pass uniform-weighted average smoother. To achieve the same half-power filter cutoff wavenumber k_c with both the uniform-weighted average smoother and the Parzen smoother, the spans of the two smoothers can be adjusted accordingly. A uniformly weighted average with a span of $L_1 = 0.5$ km, for example, has a half-power filter cutoff wavenumber of $k_c = 0.443/0.5 = 0.886$ cpkm (cycles per km). As shown by the thin line in the bottom panel of Fig. A1b, this is very close to the half-power filter cutoff wavenumber of $k_c = 0.910$ cpkm for the Parzen smoother with a span of $L_4 = 1$ km shown by the thick line.

The much smaller sidelobes of the filter transfer function of the Parzen smoother compared with those of the uniform-weighted average smoother (see Fig. A1b) are highly desirable attributes of the Parzen smoother. This improved sidelobe suppression comes at the price of somewhat more gradual rolloff through the filter cutoff wavenumber k_c of the filter transfer function of the Parzen smoother (see the bottom panel of Fig. A1b).

Appendix B. Footprint Size and Pre-Processing of SWOT and WaCM Data

Appendix B.1. SWOT Pre-Processing

The raw radar measurements by the Ka-band Radar Interferometer (KaRIn) instrument on the SWOT satellite in its low-resolution mode over the ocean have a footprint size of about 100 m. The plan as presently summarized in the SWOT onboard processing document (Peral, 2016) is to smooth the raw measurements of SSH onboard the satellite to achieve the science requirement of a footprint size of 1 km for ocean observations. The SWOT Algorithm Development Team has recently recommended changing the onboard processing to a smaller footprint size of 0.5 km posted on a 0.25 km $\times$ 0.25 km grid. The motivation for this increased resolution is to allow improved detection and removal of noisy outliers in the SWOT estimates of SSH.

The rescoping of the SWOT science requirements to a smaller footprint size of 0.5 km with a concomitant factor-of-two increase of the standard deviation of the uncorrelated measurement errors in the onboard estimates of SSH would change some of the details of the simulations of SWOT data in this study. As shown from the figures in Secs. 6 and 8, however, even the science requirement of a footprint size of 1 km that was used for our simulations far exceeds the signal resolution capability for geostrophically computed SWOT estimates of the variables of interest in this study (surface velocity and vorticity). The difference between 1 km and 0.5 km footprint sizes in the onboard pre-processing of SWOT data is therefore irrelevant to the analysis presented in Secs. 6 and 8. The SWOT Algorithm Development Team acknowledges that the 0.5 km footprint size is unnecessarily fine for most applications of SWOT data. The resulting SSH measurements are likely to be smoothed to a wavelength resolution of 2 km $\times$ 2 km in ground-based post-processing for the SWOT dataset that is provided to the general science community. It is shown below that this is equivalent to the wavelength resolution of measurements with a footprint size of 1 km.

The onboard smoothing of the raw SWOT data will be achieved using a Parzen smoother (see Appendix A) in the cross-track direction and a Blackman-Harris smoother in the along-track direction (Peral, 2016). The parameters of each of these smoothers were carefully chosen to have spatial autocorrelation values of 0.5 at the same lag, which is essentially equivalent to having the same half-power filter cutoff wavenumber for both smoothers.

The rationale for applying a different smoother in each dimension in the onboard pre-processing of SWOT data is that the Blackman-Harris smoother has slightly better sidelobe suppression than the Parzen smoother [see Fig. 37 in Peral (2016); see also Harris (1978)]. But for technical reasons related to the hardware implementation of the onboard pre-processing, the Blackman-Harris smoother cannot be applied in the cross-track direction. The better sidelobe suppression of the Blackman-Harris smoother is not enough to make any significant, or even detectable, difference in the smoothed SSH values. For all intents and purposes, the 2-dimensional smoothing of the raw SWOT data could thus be achieved equally well by smoothing with a Parzen window in both dimensions. The filtering properties of the onboard pre-processed estimates of SSH are therefore discussed here in the context of 2-dimensional smoothing with the Parzen smoother that was examined in detail in Appendix A.

The resolution of smoothed estimates of SSH is defined by Peral (2016) as summarized below based on the lagged autocorrelation associated with the smoother applied to the raw data. An expression for this spatial autocorrelation can be derived by noting that the square of the filter transfer function of the smoother is proportional to the wavenumber power spectral density of the low-pass filtered output of the smoother applied to data consisting of uncorrelated (white) noise with unit standard deviation. The autocovariance of this filtered output can be obtained as the inverse Fourier transform of its power spectral density. For white noise input data with unit standard deviation, this autocovariance is equivalent to the autocorrelation.

For a Parzen smoother with a span of L_4 in the x dimension, the autocorrelation is thus the inverse Fourier transform of the square of the filter transfer function (A.11),

$$\begin{aligned}\rho(x) &= \int_{-\infty}^{\infty} \operatorname{sinc}^8\left(\frac{kL_4}{4}\right) e^{i2\pi kx}\, dk \\ &= 2\int_{0}^{\infty} \operatorname{sinc}^8\left(\frac{kL_4}{4}\right) \cos(2\pi kx)\, dk. \end{aligned} \tag{B.1}$$

This can be evaluated with the help of integral tables. The result is a piecewise continuous 7^{th}-order polynomial that is symmetric about lag $x = 0$. This is shown for positive lags x in the bottom panel of Fig. B1a for a span of $L_4 = 2$ km. The associated weighting function and squared filter transfer function are shown, respectively, in the top and middle panels of Fig. B1a.

The minimum scale of features that can be resolved in the smoothed data is defined by Peral (2016) to be the lag at which the autocorrelation decays to a value of 0.5. Although somewhat subjective, this is a reasonable definition. For the Parzen smoother with a span of $L_4 = 2$ km shown in Fig. B1a, the autocorrelation (B.1) decays to a value of 0.5 at a lag of $x = 0.495$ km (see the bottom panel of Fig. B1a). Since the autocorrelation is symmetric about zero lag, this can be interpreted as the radius of features that can be resolved. The feature diameter resolution after filtering with a Parzen smoother with a span of $L_4 = 2$ km is therefore approximately 1 km. This can be considered the footprint diameter of SWOT measurements of SSH smoothed with a half-power filter cutoff wavelength (A.12) of $\lambda_c = k_c^{-1} = L_4/0.910 \approx 2$ km. The autocorrelation for the Parzen smoother with $L_4 = 2$ km decays to a very small value of 0.050 at a radial lag of 1 km (see the bottom panel of Fig. B1a). The resulting smoothed estimates of SSH are therefore essentially uncorrelated when posted on a 1 km $\times$ 1 km grid.

The present official requirement for the pre-processing of SWOT data in the SWOT onboard processing document (Peral, 2016) is for SSH estimates on a 1 km $\times$ 1 km grid to be statistically uncorrelated. From the preceding discussion, this can be achieved using a 2-dimensional Parzen smoother with a span of $L_4 = 2$ km in each dimension. The half-power filter cutoff wavenumber (A.12a) for this span is $k_c = 0.455 \approx 0.5$ cpkm (see the middle panel of Fig. B1a). A wavenumber of 0.5 cpkm is also the Nyquist wavenumber for a sample interval of $\Delta x = 1$ km. The resolution and sampling requirements for the pre-processed SWOT estimates of SSH as stated in the onboard processing document (Peral, 2016) can thus be achieved using a Parzen

smoother with a span of $L_4 = 2$ km in each dimension, and posting the smoothed SSH estimates on a 1 km $\times$ 1 km grid. The estimates of SSH obtained by smoothing with a half-power filter cutoff wavelength of 2 km could be posted on a finer grid, but the resulting gridded values would no longer be statistically uncorrelated.

As discussed at the beginning of this appendix, the onboard processing for SWOT estimates of SSH is likely to change to a smaller footprint size of 0.5 km. Based on the preceding discussion, this can be achieved by smoothing with a half-power filter cutoff wavelength of 1 km. The analysis throughout this study is based on the science requirements for a footprint size of 1 km, which is achieved by smoothing with a half-power filter cutoff wavelength of 2 km as summarized above. None of the conclusions of this study would change if the analysis were based on the smaller footprint size of 0.5 km since the results of the additional smoothing in ground-based post-processing that will be needed to achieve an adequate signal-to-noise ratio would be essentially the same for either footprint size.

Appendix B.2. WaCM Pre-Processing

The WaCM mission is still in the early stages of planning. To reduce the measurement errors, the present plan is to smooth the pooled raw measurements of radial velocity from multiple antenna look angles into 5 km $\times$ 5 km areas from which two orthogonal components of velocity (e.g., along-track and cross-track components) are estimated. The feature resolution of these velocity estimates will thus effectively have a footprint diameter of 5 km). In analogy with the discussion above for pre-processing of SWOT data, this can be achieved using a 2-dimensional Parzen smoother with a half-power filter cutoff wavelength of 10 km. This corresponds to a span of approximately $L_4 = 10$ km (see Fig. B1b). The associated autocorrelation decays to a value of 0.5 at a lag of $x = 2.476$ km, thus corresponding to a feature diameter resolution of approximately 5 km. The autocorrelation for the Parzen smoother with $L_4 = 10$ km decays to a very small value of 0.050 at a radial lag of 5 km (see the bottom panel of Fig. B1b). The resulting smoothed estimates of surface velocity are therefore essentially uncorrelated when posted on a 5 km $\times$ 5 km grid.

The variables that are of primary interest in this study are the surface velocity field itself and the surface vorticity, which is computed from derivatives of the velocity components. For centered-difference estimates of these derivatives, it is shown later in Appendix H that it is advantageous to post the pre-processed WaCM estimates of surface velocity on a grid that is finer than 5 km $\times$ 5 km. For the analysis in this study, the smoothed velocity estimates were posted on a 1 km $\times$ 1 km. The measurement errors are not uncorrelated on this finer grid.

Appendix C. Feature Resolution

Maps of the variables of interest in this study (surface velocity and vorticity) constructed from SWOT and WaCM data pre-processed as summarized in Appendix B are too noisy to be useful for most applications (see the unsmoothed fields in the bottom left panels of Figs. 17a–c and 19a–b). For these variables, it will be necessary to smooth the pre-processed data in ground-based post-processing to mitigate the effects of the uncorrelated measurement errors. The variance of the errors can be reduced to any desired level with sufficient 2-dimensional smoothing. The error reduction factor is derived later in Appendix D. The purpose of this appendix is to quantify the filter cutoff wavelength and the implied feature resolution scale for a given amount of smoothing.

The procedure used in this study to mitigate the effects of measurement errors and increase the signal-to-noise ratio is to apply 2-dimensional smoothing to the noisy estimates of SSH from SWOT and surface velocity components from WaCM. This smoothing can be applied anisotropically, i.e., with different filter cutoff wavenumbers in each of two orthogonal dimensions. For the purposes of the analysis in Secs. 6 and 8–10, however, the 2-dimensional smoothing was applied isotropically. The 2-dimensional weighting function for isotropic smoothing can be expressed as

$$w^{2d}(x, y) = w^{2d}(r), \tag{C.1}$$

where $r = (x^2 + y^2)^{1/2}$ is the radial distance from the estimation location to each data point within the 2-dimensional span of the smoother. It is shown below that 2-dimensional smoothing with the Parzen smoother used in this study is essentially equivalent to separate 1-dimensional smoothing in each of two orthogonal dimensions. The effects of the 2-dimensional smoothing can thus be understood from consideration of the filtering properties of a succession of 1-dimensional smoothing in each dimension. This simplifies the derivation of the wavenumber spectral characteristics of 2-dimensionally smoothed fields presented later in Appendix I.

There are many possible choices of smoothers to reduce errors. While the details of the filter transfer functions differ for the various smoothers, any smoother applied in, say, the x dimension can be characterized by the half-power filter cutoff wavenumber k_c, or equivalently the half-power filter cutoff wavelength $\lambda_c = k_c^{-1}$, that is associated with the particular choice of the parameters of the smoother. For example, the value of k_c for the uniform-weighted average and the Parzen smoother considered in Appendix A is related to the parameters L_1 and L_4 that define the spans of each of these smoothers by (A.7) and (A.12a), respectively. Other smoothers have analogous relations between k_c and the parameters of the smoother; see, for example, the Gaussian and loess smoothers summarized later in this section. The primary distinctions between different smoothers are the steepness of the rolloff of the squared filter transfer function through k_c and the amplitudes of the sidelobes at wavenumbers higher than k_c.

The analyses of resolution capability in Secs. 6 and 8–10 determine the signal-to-noise ratio as a function of isotropic filter cutoff wavelength λ_c for each of the variables of interest (the two components of velocity and vorticity) computed from the simulated satellite data (SSH for SWOT and the two velocity components for WaCM) smoothed with 19 different values of λ_c ranging from 10 km to 200 km. These smoothed fields were generated for instantaneous maps, 4-day averages and 14-day averages of SSH for SWOT and the two velocity components for WaCM for fields constructed from error-free model output, measurement errors alone, sampling errors alone and combined measurement and sampling errors. Together with the pre-processed SWOT and WaCM data smoothed with $\lambda_c = 2$ km and 10 km, respectively, 20 different smoothed maps were computed for each measured variable, each choice of time averaging, each combination of measurement and sampling errors, and two choices of swath width for WaCM (1200 km and 1800 km). A total of 1200 smoothed maps of the simulated satellite data were thus required to generate the signal-to-noise graphs in Figs. 18, 30, 35 and 43.

Because of the computational effort required for these calculations, the standard smoother used throughout this study was the Parzen smoother that is discussed in detail in Appendix A. The Parzen smoother is computationally efficient and very easy to implement as a simple weighted average with weights defined by (A.13). For a given choice of half-power filter cutoff wavenumber k_c and associated wavelength $\lambda_c = k_c^{-1}$, the span of a 1-dimensional Parzen smoother inferred from (A.12b) is

$$\text{Parzen Smoother}: \quad L_4 = 0.910\,\lambda_c \approx \lambda_c. \tag{C.2}$$

The squared filter transfer function for the Parzen smoother is shown in Fig. C1 in log-log format (the standard format used for the wavenumber spectra shown throughout this paper) for filter cutoff wavelengths of $\lambda_c = 20$, 50 and 80 km, corresponding to weighted averages with spans of $L_4 = 18.2$, 45.5 and 72.8 km.

It is useful to compare the Parzen smoother with the Gaussian-weighted smoother for which the weighting function in one dimension is

$$w_G(x) = \frac{1}{\sqrt{\pi}\,L_G}\,e^{-x^2/L_G^2}, \tag{C.3}$$

where L_G defines the e-folding scale of the Gaussian weighting. The normalization factor $\sqrt{\pi}\,L_G$ constrains the weighting function (C.3) to have unit area, as required for unbiased smoothing. As discussed in Appendix A, the filter transfer function of any smoother is defined to be the Fourier transform (A.2) of the weighting function of the smoother. For the Gaussian smoother (C.3), this is

$$W_G(k) = \int_{-\infty}^{\infty} w(x)\,e^{-i2\pi kx}\,dx = e^{-(\pi L_G k)^2}. \tag{C.4}$$

As defined in Appendix A, the half-power filter cutoff wavenumber of the Gaussian smoother is the wavenumber k_c at which the squared value of the filter transfer function (C.4) has a value of 0.5,

$$W_G^2(k_c) = e^{-2(\pi L_G k_c)^2} = 0.5.$$

The parameter L_G of the Gaussian smoother (C.3) is thus related to the desired half-power filter cutoff wavenumber k_c and associated wavelength $\lambda_c = k_c^{-1}$ by

$$L_G = \left(-\frac{\ln(0.5)}{2\pi^2}\right)^{1/2} \frac{1}{k_c} = 0.187\,\lambda_c. \tag{C.5}$$

The squared filter transfer function of the Gaussian smoother is shown in log-log format by the thin line in Fig. C2 for the case of a half-power filter cutoff wavelength of $\lambda_c = 50$ km. For comparison, the thick line is the squared filter transfer function of the Parzen smoother from Fig. C1 for the same half-power filter cutoff wavelength of $\lambda_c = 50$ km. It is evident that the filtering properties of the Parzen smoother are indistinguishable from those of the Gaussian smoother for wavenumbers smaller than about $2k_c$. The two squared filter transfer functions differ somewhat at higher wavenumbers, but the variability at these wavenumbers is attenuated by more than 15 dB relative to the variability at the lower wavenumbers within the pass band of the smoother.

A useful feature of isotropic Gaussian smoothing in two dimensions is that it can be applied either as a single 2-dimensional weighted average or as separate 1-dimensional Gaussian smoothing with the weighting function (C.3) in each of two orthogonal dimensions. This can be seen by noting that the 2-dimensional weighting function (C.1) for the isotropic Gaussian smoother is

$$\begin{aligned} w_G^{2d}(x,y) = w_G^{2d}(r) &= \frac{1}{\pi L_G^2}\, e^{-r^2/L_G^2} \\ &= \frac{1}{\pi L_G^2}\, e^{-(x^2+y^2)/L_G^2}. \end{aligned} \tag{C.6a}$$

The normalization πL_G^2 constrains the 2-dimensional weighting function $w_G^{2d}(r)$ to have unit volume, as required for unbiased smoothing. The right side of (C.6a) can be rewritten as

$$w_G(x,y) = w_G(x)\, w_G(y), \tag{C.6b}$$

where $w_G(x)$ is the 1-dimensional Gaussian weighting function (C.3) in the x dimension and $w_G(y)$ is an analogous expression in the y dimension. At least in principle, the isotropic 2-dimensional Gaussian smoother can thus be applied as separate 1-dimensional Gaussian smoothers in each orthogonal dimension. It is of course not possible to extend the Gaussian weighting to $x, y \to \pm\infty$. The separability (C.6b) is therefore not precisely valid in practice.

Because of the very close similarity between the squared filter transfer functions of the Parzen and Gaussian smoothers (see Fig. C2), and therefore between the weighting functions of the two smoothers that can be obtained from the inverse Fourier transforms of the filter transfer functions, smoothing isotropically with a 2-dimensional Parzen smoother shares the separability property (C.6b) for all intents and purposes. In other words, isotropic 2-dimensional Parzen smoothing can be implemented as separate 1-dimensional Parzen smoothing in each of the two orthogonal dimensions. This property is used in Appendix D, Appendix E and Appendix I (see also Sec. 4) to derive theoretical expressions for the effects of smoothing on the magnitudes and wavenumber spectral characteristics of residual uncorrelated measurement errors after smoothing SWOT and WaCM data in simulated ground-based post-processing.

The very small sidelobes of the filter transfer function of the Parzen smoother, and the lack of sidelobes in the filter transfer function of the Gaussian smoother, are desirable characteristics of any smoother. An undesirable feature of these smoothers is that the rolloffs of their squared filter transfer functions through k_c are gradual compared with some other smoothers. The assessment of resolution capability of SWOT and WaCM data deduced from smoothed fields in Secs. 6 and 8–10 depends to some degree on the details of

the filtering properties of the smoother that is used to suppress the errors. This is apparent in Secs. 9 and 10.2 from the resolution capabilities inferred from the quadratic loess smoother compared with the Parzen smoother. The quadratic loess smoother introduced by Cleveland and Devlin (1988) has better filtering properties than the Gaussian and Parzen smoothers (Schlax and Chelton, 1992).

Mathematically, the quadratic loess smoother is a locally weighted least squares fit of the data to a quadratic function over a span of L_q. The standard weighting for the quadratic loess smoother is the tricubic function used by Cleveland and Devlin (1988). For a given choice of half-power filter cutoff wavelength λ_c, it can be shown that the span for this quadratic loess smoother is

$$\text{Quadratic Loess Smoother}: \quad L_q \approx 1.67\,\lambda_c. \tag{C.7}$$

This is 83.5% larger than the span (C.2) of the Parzen smoother.

The squared filter transfer function for a 1-dimensional quadratic loess smoother is shown in log-log format by the thick dashed line in Fig. C3 for the case of a half-power filter cutoff wavelength of $\lambda_c = 50$ km (i.e., a span of $L_q = 83.5$ km). For comparison, the thick solid line is the squared filter transfer function of the Parzen smoother from Figs. C1 and C2 for the same half-power filter cutoff wavelength of $\lambda_c = 50$ km. While the sidelobes of the quadratic loess smoother with tricubic weighting function are larger than the sidelobes of the Parzen smoother, they occur at wavenumbers closer to the filter cutoff wavenumber k_c and the rolloff of the filter transfer function has much better characteristics for the loess smoother. Specifically, the squared filter transfer function of the loess smoother is somewhat flatter in the pass band and rolls off much more steeply through k_c. At a wavelength of 30 km, for example, i.e., a wavenumber of $k = 0.0333$ cpkm, the squared filter transfer function for the loess smoother is 27.3 times smaller than that of the Parzen smoother (i.e., an attenuation factor of more than 14 dB). Even with its larger-amplitude sidelobes, the magnitude of the squared filter transfer function of the loess smoother is smaller than that of the Parzen smoother at all wavenumbers less than about 0.07 cpkm (a wavelength of about 14 km), by which point both squared filter transfer functions are down by about 50 dB from the values within the pass band of the smoother so that sidelobe contamination is no longer an issue. The inferiority of simple block averages (i.e., uniformly weighted running averages) is readily apparent from the numerous large sidelobes of its squared filter transfer function shown by the thin dashed line in Fig. C3.

The quadratic loess smoother is thus seen to be more effective than the Parzen smoother for attenuating high-wavenumber variability. In addition to the large span (C.7) required to achieve a filter cutoff wavelength λ_c, a disadvantage of the loess smoother is that the least squares fitting procedure is computationally intensive on the 1 km $\times$ 1 km grid used in this study for simulated SWOT and WaCM data, especially for large spans L_q. It is apparent from the figures in Sec. 9 and 10.2, however, that the better noise suppression properties of the loess smoother improves the assessment of resolution capability (see Table 3).

The precise estimates of the resolution capabilities of SWOT and WaCM data thus depend somewhat on the specific details of the smoother used to suppress the effects of measurement errors. However, the relative resolution capabilities of SWOT compared with WaCM do not depend on the choice of smoother used in the analysis.

The formalism developed in Appendix B to define the footprint sizes of the pre-processed SWOT and WaCM data can be used to characterize the feature resolution in smoothed fields constructed in ground-based post-processing with any desired half-power filter cutoff wavenumbers k_c and l_c in the x and y dimensions. For the case of the Parzen smoother, it was shown in Fig. B1 that smoothing in the x dimension with spans of $L_4 = 2$ km for SWOT and $L_4 = 10$ km for WaCM results in an autocorrelations of 0.5 at lags of about 0.5 km and 2.5 km, respectively, and therefore feature diameter resolution scales of about 1 km for SWOT and 5 km for WaCM according to the criterion adopted in Appendix B.

More generally, the feature diameter resolution scale for a Parzen smoother applied in the x dimension with an arbitrary span of L_4 in ground-based post-processing is

$$\text{Feature Diameter Resolution} \approx \frac{L_4}{2}. \tag{C.8a}$$

Since the half-power filter cutoff wavenumber (A.12a) for a Parzen smoother with a span of L_4 is $k_c \approx L_4^{-1}$,

the feature diameter resolution scale (C.8a) can be expressed equivalently as

$$\text{Feature Diameter Resolution} \approx \frac{1}{2k_c}. \tag{C.8b}$$

In terms of half-power filter cutoff wavelength $\lambda_c = k_c^{-1}$, this is

$$\text{Feature Diameter Resolution} \approx \frac{\lambda_c}{2}. \tag{C.8c}$$

Regardless of the specific formulation of the smoothing procedure, the relationships (C.8b) and (C.8c) between feature diameter resolution and filter cutoff wavenumber k_c or wavelength λ_c developed above for the Parzen smoother are approximately applicable to any smoother.

The preceding analysis clarifies the relation between the autocorrelation-based definition (C.8) of feature diameter resolution and the half-power filter cutoff wavelength $\lambda_c = k_c^{-1}$ that is often used by oceanographers to characterize the resolution of filtered fields. From (C.8c), the feature diameter resolution of fields smoothed with a half-power filter cutoff wavenumber k_c is about $\lambda_c/2$. This definition of resolution, which is based on the lag at which the autocorrelation of the smoothed fields decreases to a value of 0.5 as suggested by Peral (2016), is coarser by 25% than the feature diameter resolution of $\lambda_c/2.5$ as defined somewhat subjectively by Chelton et al. (2011) using a different criterion. For consistency with the SWOT documentation, we adopt the Peral (2016) definition in this study.

Appendix D. Error Reduction by Smoothing

Smoothing of the pre-processed SWOT estimates of SSH and WaCM estimates of surface velocity in ground-based post-processing as summarized in Appendix C clearly reduces the variance of the uncorrelated errors. The objective of this appendix is to quantify the reduction that can be achieved with 2-dimensional smoothing for given choices of the half-power filter cutoff wavenumbers k_c and l_c in the x and y dimensions, respectively. The analysis that follows is based on the Parzen smoother, but the results are at least qualitatively applicable to any smoother with parameters calibrated to the same filter cutoff wavenumber in each dimension.

The amount by which filtering 2-dimensionally with the Parzen smoother reduces the variance of uncorrelated errors compared with block averaging, i.e., compared with the uniform-weighted average (A.4), can be derived from consideration of smoothing in one dimension and then extending the results to two dimensions. Consider a 1-dimensional discretely sampled spatial series $\epsilon(x_m)$ of errors at M locations $x_m = m\Delta x,\ m = 0, 1, \ldots, M-1$. It will be assumed that these errors are uncorrelated at the sample spacing of Δx. It was shown in Appendix B that SWOT measurements of SSH smoothed in pre-processing with a half-power filter cutoff wavelength of 2 km are uncorrelated with a spacing of $\Delta x = 1$ km. For WaCM, smoothing of the surface velocity measurements in pre-processing with a half-power filter cutoff wavelength of 10 km are uncorrelated with a spacing of $\Delta x = 5$ km.

The error reduction by smoothing in ground-based post-processing of the pre-processed SWOT and WaCM data can be quantified from the wavenumber spectral characteristics of the filtered errors. Parseval's Theorem for the sample variance σ_ϵ^2 of the uncorrelated errors in one dimension without smoothing can be expressed as

$$\sigma_\epsilon^2 = \sum_{i=1}^{M/2} S_\epsilon^{1d}(k_i)\,\Delta k, \tag{D.1}$$

where $\Delta k = (M\Delta x)^{-1}$ is the Fourier wavenumber interval between independent spectral estimates for a record length of $M\Delta x$ and $S_\epsilon^{1d}(k_i)$ is the 1-sided, 1-dimensional power spectral density of the errors at wavenumber $k_i = i\Delta k$. The zero wavenumber corresponding to the index $i = 0$ is excluded from the sum (D.1) because the power spectral density at zero wavenumber is equivalent to the square of the sample mean value, which does not contribute to the sample variance. The wavenumber $k_{M/2} = (M/2)\Delta k$ at the upper range of the summation in (D.1) corresponds to the Nyquist wavenumber $k_{\mathcal{N}} = (2\Delta x)^{-1}$ that is

the highest resolvable wavenumber for the discrete sample interval Δx. The 1-sided, 1-dimensional power spectral density $S_\epsilon^{1d}(k_i)$ on the right side of (D.1) doubles the power at all wavenumbers except the zero and Nyquist wavenumbers.

Since the errors $\epsilon(x_m)$ are uncorrelated, the wavenumber power spectral density $S_\epsilon^{1d}(k_i)$ is white, i.e., constant at all wavenumbers[5]. The constant white-noise spectral value obtained by passing the constants $S_\epsilon^{1d}(k_i)$ and $\Delta k = (M\Delta x)^{-1}$ through the summation in (D.1) and inverting the equation is thus

$$\begin{aligned} S_\epsilon^{1d}(k_i) &= \frac{\sigma_\epsilon^2}{(M/2)\Delta k} \\ &= \frac{\sigma_\epsilon^2}{k_{\mathcal{N}}}, \quad i = 1, \ldots, M/2. \end{aligned} \tag{D.2}$$

The wavenumber power spectral density after smoothing of the uncorrelated errors $\epsilon(x_m)$ in ground-based post-processing using a linear, space-invariant filter with a filter transfer function $W_{k_c}(k)$ that has a half-power filter cutoff wavenumber k_c can be expressed in terms of the wavenumber spectrum (D.2) of the unfiltered errors by

$$\overline{S}_\epsilon^{1d}(k_i) = \left|W_{k_c}(k_i)\right|^2 S_\epsilon^{1d}(k_i). \tag{D.3a}$$

The overbar distinguishes the spectrum $\overline{S}_\epsilon^{1d}(k_i)$ of the smoothed errors from the spectrum $S_\epsilon^{1d}(k_i)$ of errors in the unfiltered pre-processed data. The filter transfer functions of the uniform-weighted average and the Parzen smoother considered below are given by (A.6) and (A.11), respectively. Since these filter transfer functions are both real (as is the case for any symmetric, linear filter), the absolute value can be omitted from (D.3a). After substituting (D.2) for $S_\epsilon^{1d}(k_i)$, the spectrum (D.3a) of the smoothed white noise can be written as

$$\overline{S}_\epsilon^{1d}(k_i) = \frac{\sigma_\epsilon^2}{k_{\mathcal{N}}} W_{k_c}^2(k_i). \tag{D.3b}$$

Parseval's Theorem for the sample variance of the residual uncorrelated errors after smoothing can be expressed analogous to (D.1) in terms of the 1-sided, 1-dimensional power spectral density (D.3) of the smoothed errors as

$$\overline{\sigma}_\epsilon^2 = \sum_{i=1}^{M/2} \overline{S}_\epsilon^{1d}(k_i)\, \Delta k. \tag{D.4a}$$

The overbar distinguishes the residual variance $\overline{\sigma}_\epsilon^2$ of the smoothed errors from the variance σ_ϵ^2 of the errors of the unsmoothed pre-processed data that is given by (D.1). Substituting (D.3b) into the right side of (D.4a) expresses the variance of the smoothed errors in terms of the variance of the unsmoothed errors as

$$\overline{\sigma}_\epsilon^2 = \frac{\sigma_\epsilon^2}{k_{\mathcal{N}}} \sum_{i=1}^{M/2} W_{k_c}^2(k_i)\, \Delta k. \tag{D.4b}$$

Note again that the wavenumber $k_{M/2}$ at the upper range of the summation is the Nyquist wavenumber $k_{\mathcal{N}} = (2\Delta x)^{-1}$, a point that is important below.

Equation (D.4b) can be interpreted as a discretized statement that the sample variance of smoothed white-noise errors is equal to the integrated area under the squared filter transfer function. This is seen by considering the limit as the record length $M\Delta x$ approaches infinity for fixed sample interval Δx. The wavenumber interval $\Delta k = (M\Delta x)^{-1}$ then becomes an infinitesimally small value dk and the discrete wavenumbers $k_i = i\Delta k$ become continuous. The subscript i can then be dropped and the discrete summation becomes an integral so that (D.4b) can be written as

$$\overline{\sigma}_\epsilon^2 = \alpha\, \sigma_\epsilon^2, \tag{D.5a}$$

[5]The spectral values at wavenumbers $k_i = 0$ and the Nyquist wavenumber $k_i = M/2$ are not doubled in the 1-sided, 1-dimensional spectrum. Since the measurement errors are assumed to have a mean of zero, this detail is unimportant for $k_i = 0$. The non-doubling at $k_i = M/2$ will be ignored to avoid unnecessary lack of clarity in the analysis that follows.

where

$$\alpha = \frac{1}{k_{\mathcal{N}}} \int_0^{k_{\mathcal{N}}} W_{k_c}^2(k)\, dk$$
$$= 2\Delta x \int_0^{k_{\mathcal{N}}} W_{k_c}^2(k)\, dk. \tag{D.5b}$$

The Nyquist wavenumber that defines the upper bound of the integral is imposed by the discrete sample interval Δx, regardless of the record length $M\Delta x$. [As noted above, the zero wavenumber at the lower bound of the integral in (D.5b) must be excluded from the discretized form (D.4b) of this integral since it does not contribute to the sample variance.]

It is well known that 1-dimensional block averaging of L uncorrelated errors $\epsilon(x_m)$ in uniform-weighted averages with a span of $L_1 = L\Delta x$ on a sample grid spacing of Δx on which the errors are statistically uncorrelated reduces the uncorrelated error variance σ_ϵ^2 by a multiplicative factor of

$$\alpha_1 = \frac{1}{L}. \tag{D.6}$$

The subscript 1 indicates that this value for α in the error variance reduction formula (D.5a) is specific to the uniform-weighted average. The integral on the right side of (D.5b) after substituting (D.6) on the left side of the equation is

$$\int_0^{k_{\mathcal{N}}} W_1^2(k)\, dk = \frac{1}{2L\Delta x}, \tag{D.7}$$

where $W_1(k)$ is the filter transfer function (A.6) of the uniform-weighted average with a span of $L_1 = L\Delta x$, which has a half-power filter cutoff wavenumber of $k_c \approx 0.5 L_1^{-1}$ according to (A.7). The explicit dependence of the filter transfer function $W_{k_c}(k)$ on the half-power filter cutoff wavenumber k_c has been dropped in (D.7) in favor of the subscript 1 in order to distinguish this filter transfer function from that of the Parzen smoother considered below.

It can be anticipated from the close agreement of the half-power filter cutoff wavenumbers of the two filter transfer functions in Fig. A1b that the error reduction factor that is achieved using a 1-dimensional Parzen smoother with a span of $L_p = 2L_1 = 2L\Delta x$, i.e., twice the span of the uniform-weighted average smoother, is approximately the same as the error variance reduction factor (D.6) for a 1-dimensional block average of L uncorrelated errors over a span of $L_1 = L\Delta x$. This can be shown to be the case as follows.

An approximate analytical expression for the ratio of the variances $\overline{\sigma}_1^2$ and $\overline{\sigma}_4^2$ of, respectively, uniform-weighted averages with a span of $L_1 = L\Delta x$ and Parzen-weighted averages with a span of $L_4 = 4L_1 = 4L\Delta x$ applied to uncorrelated white noise can be derived from (D.5) by considering the ratio

$$R_L = \frac{\overline{\sigma}_4^2}{\overline{\sigma}_1^2} = \frac{\displaystyle\int_0^{k_{\mathcal{N}}} W_4^2(k)\, dk}{\displaystyle\int_0^{k_{\mathcal{N}}} W_1^2(k)\, dk}$$
$$= \frac{\displaystyle\int_0^{k_{\mathcal{N}}} \mathrm{sinc}^8(kL\Delta x)\, dk}{\displaystyle\int_0^{k_{\mathcal{N}}} \mathrm{sinc}^2(kL\Delta x)\, dk}, \tag{D.8}$$

where $W_4(k)$ is the filter transfer function (A.11) of the Parzen smoother with a span of $L_4 = 4L\Delta x$, which yields $\mathrm{sinc}^4(kL\Delta x)$ on the right side of (A.11) and has a filter cutoff wavenumber of $k_c \approx L_4^{-1}$ according to (A.12a). Exact solutions for the two integrals on the right side of (D.8) cannot be obtained analytically. However, solutions can be found in integral tables if the upper bounds of the two integrals in (D.8) are both

∞ rather than the Nyquist wavenumber $k_{\mathcal{N}}$. The ratio (D.8) can thus be rewritten as

$$R_L = \frac{I_8 - \int_{k_{\mathcal{N}}}^{\infty} \mathrm{sinc}^8(kL\Delta x)\,dk}{I_2 - \int_{k_{\mathcal{N}}}^{\infty} \mathrm{sinc}^2(kL\Delta x)\,dk}, \tag{D.9a}$$

where

$$I_2 = \int_0^{\infty} \mathrm{sinc}^2(kL\Delta x)\,dk = \frac{1}{2L} \tag{D.9b}$$

$$I_8 = \int_0^{\infty} \mathrm{sinc}^8(kL\Delta x)\,dk = \frac{151}{630L}. \tag{D.9c}$$

The solutions (D.9b) and (D.9c) for I_2 and I_8 are derived from the general solution obtained from integral tables for the integral from 0 to ∞ of $\mathrm{sinc}^p(kL\Delta x)$ with $p = 2$ and 8.

Because the sidelobes of $\mathrm{sinc}^8(kL\Delta x)$ decay so much faster than the sidelobes of $\mathrm{sinc}^2(kL\Delta x)$ (see Figs. A1b and C3), the correction term in the numerator of (D.9a) is much smaller than the correction term in the denominator. The ratio of variances of uncorrelated errors smoothed with the Parzen smoother and the uniform-weighted average can therefore be approximated as

$$R_L \;\approx\; \frac{I_8}{I_2 - \int_{k_{\mathcal{N}}}^{\infty} \mathrm{sinc}^2(kL\Delta x)\,dk}, \tag{D.10}$$

By approximating each of the sidelobes of $\mathrm{sinc}^2(kL\Delta x)$ as rectangles, it can be shown with some effort that the correction term in the denominator of this equation is approximately $\pi^{-2}L^{-2}$ for sufficiently large L. The meaning of "sufficiently large" is quantified below in Fig. D1. The ratio (D.10) of the variances of Parzen-weighted and uniform-weighted averages with spans of $4L\Delta x$ and $L\Delta x$, respectively, then becomes

$$R_L \;\approx\; \frac{I_8}{I_2 - \pi^{-2}L^{-2}}, \tag{D.11a}$$

where I_2 and I_8 are defined in terms of L by (D.9b) and (D.9c).

The analytical approximation (D.11a) for R_L is shown by the dots in Fig. D1 for values of L ranging from 2 to 25. For comparison, the solid line corresponds to the exact solution obtained by numerical integrations of the numerator and denominator of (D.8) with $k_{\mathcal{N}} = (2\Delta x)^{-1}$. The analytical approximation is almost imperceptibly too large for $L = 2$ and becomes indistinguishable from the numerical solution for $L > 2$. It is thus seen that the large L approximation (D.11a) is applicable to all practical choices of smoothing of the pre-processed SWOT and WaCM data. The ratio R_L in Fig. D1 has a value of 0.5 for $L = 5$. It is slightly larger for $L < 5$ and slightly smaller for $L > 5$. Over the range 20 km $\leq L \leq$ 200 km considered in this study, the numerical value of (D.11a) decreases from 0.484 to 0.480 and can thus be approximated as

$$R_L \;\approx\; 0.482. \tag{D.11b}$$

For practical purposes, R_L can be considered to have a value of 0.5. In other words, the residual variance $\overline{\sigma}_4^2$ of white-noise errors smoothed using a Parzen smoother with a span of $L_4 = 4L\Delta x$ is approximately half as large as the residual variance $\overline{\sigma}_1^2$ of white-noise errors smoothed using a uniform-weighted average with a span of $L_1 = L\Delta x$. From (D.7) and (D.8) with $R_L \approx 0.5$, the integral in (D.5b) for the Parzen smoother with a span of L_4 is thus

$$\begin{aligned} \int_0^{k_{\mathcal{N}}} W_4^2(k)\,dk &= R_L \int_0^{k_{\mathcal{N}}} W_1^2(k)\,dk \\ &\approx \frac{1}{4L\Delta x} = \frac{1}{L_4}. \end{aligned} \tag{D.12a}$$

Since the half-power filter cutoff wavenumber for the Parzen smoother with a span of L_4 is $k_c = 0.910\, L_4^{-1}$ according to (A.12a), this can be written alternatively as

$$\int_0^{k_{\mathcal{N}}} W_4^2(k)\, dk = \frac{k_c}{0.910} \approx k_c. \tag{D.12b}$$

From the form (D.12a) for the integral on the right side of (D.5b), it is apparent that the multiplicative error variance reduction factor (D.5b) for a 1-dimensional Parzen smoother with a span of $L_4 = 4L\Delta x$ is

$$\alpha_4 \approx \frac{1}{2L} = \frac{2\Delta x}{L_4}. \tag{D.13}$$

This verifies the relationship between the error variance reduction factor for the 1-dimensional Parzen smoother and error variance reduction factor (D.6) for a 1-dimensional block average with a span of $L_1 = L\Delta x$ that was anticipated above prior to considering the ratio R_L defined by (D.8). Namely, smoothing using a Parzen smoother with a span of $L_p = 2L\Delta x$ yields an error variance reduction factor of $\alpha_4 \approx L^{-1}$, which is obtained by substituting L_p for L_4 in (D.13). This is the same as the value (D.6) for α_1 that is obtained from smoothing with a uniform-weighted running average with a span of $L_1 = L\Delta x$.

The above analysis in one dimension can be extended straightforwardly to the case of filtering in two dimensions in the form of separate 1-dimensional smoothing in each of two orthogonal dimensions for a sample grid spacing of $\Delta x \times \Delta y$ on which the errors are statistically uncorrelated. The multiplicative error variance reduction factor α in (D.5a) that is achieved with 2-dimensional smoothing in this manner using Parzen smoothers with spans of $L_4(x)$ in the x dimension and $L_4(y)$ in the y dimension is then just the product of factors of the form (D.13) in each dimension,

$$\alpha_4 \approx \frac{4\Delta x \Delta y}{L_4(x) L_4(y)}. \tag{D.14a}$$

The filtering of the SSH and surface velocity fields from the CCS model with simulated SWOT and WaCM uncorrelated measurement errors in Secs. 6 and 8–10 was applied isotropically with a 2-dimensional weighting function of the form (C.1) that depends only on the radial distance between the estimation location and each data point. In general, this form of 2-dimensional smoothing differs from successive applications of 1-dimensional smoothing in two orthogonal dimensions. It was shown in Appendix C, however, that the two approaches are essentially equivalent for the Parzen smoother with spans $L_4(x) = L_4(y)$ because of its close similarity to Gaussian smoothing. The advantage of smoothing separately in each dimension is that the separability allows the use of the factor (D.14a) to determine the error reduction from 2-dimensional smoothing. Because of the essential equivalence of the two forms of isotropic 2-dimensional smoothing with the Parzen smoother, the error reduction factor (D.14a) is also applicable to the error fields smoothed in Secs. 6 and 8–10 with an isotropic 2-dimensional Parzen weighting function.

To illustrate the effects of this error reduction with a specific example, consider the case of an isotropic Parzen smoother with spans of $L_4(x) = L_4(y) = 14$ km applied to uncorrelated errors on a 1 km $\times$ 1 km grid. Then $L_4(x) = 14\Delta x$ and $L_4(y) = 14\Delta y$. The error variance reduction factor (D.14a) is therefore $\alpha_4 \approx 4/14^2 = 1/49$, i.e., the same as would be achieved by uniform-weighted block averaging over a 7 km $\times$ 7 km area. Recall, however, that the Parzen smoother has much better filtering properties than the uniform-weighted average smoother (see Figs. A1b and C3).

Because the half-power filter cutoff wavenumber (A.12a) for the Parzen smoother is $k_c \approx L_4^{-1}(x)$ in the x dimension and $l_c \approx L_4^{-1}(y)$ in the y dimension, a 2-dimensional span of $L_4(x) \times L_4(y)$ can be expressed alternatively as smoothing with half-power filter cutoff wavenumbers of approximately $k_c^{-1} \times l_c^{-1}$. The expression (D.14a) for the multiplicative reduction factor α in the relation (D.5) for the residual error variance after smoothing the pre-processed estimates with these half-power filter cutoff wavenumbers can thus be written alternatively by substituting $L_4(x) = k_c^{-1}$ and $L_4(y) = l_c^{-1}$ into (D.14a) to get

$$\alpha_4 \approx 4\, \Delta x\, \Delta y\, k_c\, l_c. \tag{D.14b}$$

For the case of isotropic smoothing with a half-power filter wavelength of $\lambda_c = k_c^{-1} = l_c^{-1}$ in each dimension, this becomes

$$\alpha_4 \approx \frac{4\,\Delta x \Delta y}{\lambda_c^2}. \tag{D.14c}$$

The subscript 4 on the multiplicative error variance reduction factor (D.14) to be used in the error reduction formula (D.5) is a reminder that α_4 was derived specifically for the Parzen smoother. However, the form (D.14b) provides an approximate characterization of the reduction of uncorrelated error variance for other smoothers with parameters chosen to give the same filter cutoff wavenumbers k_c and l_c. For isotropic smoothing, the error reduction for any smoother with a half-power filter cutoff wavelength λ_c is given approximately by (D.14c).

Appendix E. One-Dimensional Wavenumber Spectra of 2-Dimensionally Smoothed Uncorrelated Error Fields

The procedure followed in Secs. 6 and 8–10 to improve the signal-to-noise ratio for SWOT and WaCM estimates of the variables considered in this study (surface velocity and vorticity) is to reduce the error variance by isotropic 2-dimensional smoothing of the variable measured by each instrument (SSH for SWOT and velocity components for WaCM). It was shown in Appendix C that the smoothing applied in Secs. 6 and 8–10 using a truly isotropic 2-dimensional Parzen weighting function could be achieved essentially equivalently as successive applications of a 1-dimensional Parzen smoother in each of two orthogonal dimensions. This equivalence allowed the derivation of the error variance reduction factor (D.14b) for separate smoothing with half-power filter cutoff wavenumbers of k_c and l_c in the x and y dimensions.

The equivalence of the two methods of 2-dimensional smoothing is used in this appendix to quantify the effects of isotropic 2-dimensional smoothing on the wavenumber spectrum of residual measurement errors. Of particular interest is the effect of 2-dimensional smoothing on the 1-dimensional wavenumber spectrum[6] of 2-dimensional uncorrelated white noise, which differs in an important way from what would be achieved with a 1-dimensional dataset. The difference is not necessarily intuitive but is needed for the derivation in Appendix F of the standard deviation of uncorrelated errors from the spectral specification of the science requirement for SWOT measurement accuracy. The results are also essential to the interpretation of the spectral analysis of the effects of smoothing in ground-based post-processing that is derived for both SWOT and WaCM in Appendix I (see also Sec. 4.4). We therefore summarize the effects of 2-dimensional smoothing on the 1-dimensional wavenumber spectrum in this appendix.

Consider a 2-dimensional spatial field $\epsilon(x, y)$ of uncorrelated measurement errors (e.g., measurements of SSH by SWOT or measurements of a velocity component by WaCM) at discrete locations (x_m, y_n) for $x_m = m\Delta x,\ m = 0, 1, \ldots M-1$ and $y_n = n\Delta y,\ n = 0, 1, \ldots, N-1$, where Δx and Δy are the sample intervals in the x and y dimensions. It will be assumed that the errors $\epsilon(x_m, y_n)$ are uncorrelated on this sample grid. Analogous to (D.1) for the 1-dimensional case considered in Appendix D, Parseval's Theorem for the relationship between the sample variance σ_ϵ^2 of this error field and its 2-dimensional wavenumber sample power spectral density $S_\epsilon^{2d}(k_i, l_j)$ at wavenumbers $k_i = i(M\Delta x)^{-1}$ and $l_j = j(N\Delta y)^{-1}$ is

$$\sigma_\epsilon^2 = \sum_{\substack{i=-M/2+1 \\ i\neq 0}}^{M/2} \sum_{\substack{j=-N/2+1 \\ j\neq 0}}^{N/2} S_\epsilon^{2d}(k_i, l_j)\,\Delta l\,\Delta k, \tag{E.1}$$

where $\Delta k = (M\Delta x)^{-1}$ and $\Delta l = (N\Delta y)^{-1}$ are the discrete Fourier wavenumber intervals that are defined by the record lengths $M\Delta x$ and $N\Delta y$ in the x and y dimensions. As in the 1-dimensional case (D.1), the zero wavenumbers corresponding to indices $i = j = 0$ are excluded from the sums in (E.1) because the spectral

[6]The direction of the 1-dimensional spectrum could be defined to be along the satellite ground track for the case of actual satellite data or in the alongshore direction for the case of the spectral analysis of the model output considered in Appendix I and Sec. 4.4.

values at these wavenumbers correspond to the squared values of the sample mean in each dimension, which do not contribute to the sample variance σ_ϵ^2. The indices $i = M/2$ and $j = N/2$ that define the upper limits of the summations in (E.1) correspond to the Nyquist wavenumbers $k_\mathcal{N} = (2\Delta x)^{-1}$ and $l_\mathcal{N} = (2\Delta y)^{-1}$ in the x and y dimensions, respectively

The 2-dimensional form (E.1) of Parseval's Theorem can be interpreted as a discretized statement that the sample variance is equal to the volume under the 2-dimensional wavenumber sample power spectral density. Analogous to the procedure followed in one dimension in Appendix D, this is seen by considering the limit as the record lengths $M\Delta x$ and $N\Delta y$ in the x and y dimensions approach infinity for fixed sample intervals Δx and Δy. The wavenumber intervals Δk and Δl then become infinitesimally small values dk and dl and the discrete wavenumbers $k_i = i\Delta k$ and $l_j = j\Delta l$ become continuous. The subscripts i and j can then be dropped and the discrete summations become integrals so that (E.1) can be written in simpler form as[7]

$$\sigma_\epsilon^2 = \int_{-k_\mathcal{N}}^{k_\mathcal{N}} \int_{-l_\mathcal{N}}^{l_\mathcal{N}} S_\epsilon^{2d}(k,l)\, dl\, dk. \tag{E.2}$$

The variance of the discretely sampled error field $\epsilon(x_m, y_n)$ with infinitely long record lengths $M\Delta x$ and $N\Delta y$ in the two dimensions is thus the integrated volume under the 2-dimensional sample power spectral density. A point that is important to the analysis below and in Appendix F is that the ranges of integration are finite. The Nyquist wavenumbers $k_\mathcal{N}$ and $l_\mathcal{N}$ that define the lower and upper bounds of the integrals are imposed by the discrete sample intervals Δx and Δy, regardless of the record lengths $M\Delta x$ and $N\Delta y$.

The integral representation (E.2) of Parseval's Theorem greatly simplifies the notation in the analysis that follows. It should be kept in mind, however, that the observable resolutions Δk and Δl of the wavenumbers k and l in the x and y dimensions will be finite and are imposed by the finite record lengths $M\Delta x$ and $N\Delta y$.

The 2-dimensional wavenumber sample power spectral density $S_\epsilon^{2d}(k,l)$ of 2-dimensional uncorrelated errors is constant (i.e., white) with a value that can be defined to be S_0 at all wavenumbers k and l except $k = 0$ and $l = 0$ at which $S_\epsilon^{2d}(k,l) = 0$ for errors that have a sample mean value of zero. Parseval's Theorem (E.2) then reduces to

$$\sigma_\epsilon^2 = 4k_\mathcal{N} l_\mathcal{N} S_0 = \frac{S_0}{\Delta x \Delta y}.$$

The constant 2-dimensional power spectral density for a specified white noise error variance σ_ϵ^2 obtained by inverting this equation is

$$S_\epsilon^{2d}(k,l) = S_0 = \Delta x\, \Delta y\, \sigma_\epsilon^2, \quad \text{for } -k_\mathcal{N} < k \le k_\mathcal{N} \text{ and } -l_\mathcal{N} < l \le l_\mathcal{N}. \tag{E.3}$$

For the case of errors $\epsilon(x,y)$ of SWOT estimates of SSH in units of cm, the 2-dimensional white-noise spectral value of S_0 has units of $\text{cm}^2/(\text{cpkm})^2$. Similarly for the case of errors $\epsilon(x,y)$ of WaCM estimates of a velocity component in units of m s^{-1}, S_0 has units of $(\text{m s}^{-1})^2/(\text{cpkm})^2$.

The 1-dimensional wavenumber sample power spectral density in the y dimension of a 2-dimensional field can be obtained from the 2-dimensional wavenumber sample power spectral density by integrating over all wavenumbers k in the x dimension. For the 1-sided, 1-dimensional spectrum that combines the power at positive and negative wavenumbers l, this relationship for the 1-dimensional white noise spectrum becomes[8]

[7] The zero wavenumbers $k = l = 0$ that are included in the integral (E.2) must be excluded from the discretized form (E.1) of this integral since they do not contribute to the sample variance. If the errors have a mean of zero, however, inclusion of the zero wavenumbers in (E.2) is an irrelevant point since the spectral values are then zero at $k = 0$ and $l = 0$. The Nyquist wavenumbers $-k_\mathcal{N}$ and $-l_\mathcal{N}$ at the lower range of each of the integrals must also be excluded from (E.2). To simplify the discussion, this minor distinction between the integral and discrete forms of Parseval's Theorem will be ignored in the analysis that follows.

[8] As noted in footnote 5, the spectral values at wavenumbers $l = 0$ and $l_\mathcal{N}$ are not doubled in the 1-sided, 1-dimensional spectrum in (E.4). As in Appendix D, this technicality will be ignored to avoid unnecessary lack of clarity in the analysis that follows.

$$S_\epsilon^{1d}(l) = 2\int_{-k_\mathcal{N}}^{k_\mathcal{N}} S_\epsilon^{2d}(k,l)\,dk = 4k_\mathcal{N}\,S_0 = \frac{2S_0}{\Delta x}, \quad \text{for } 0 < l \le l_\mathcal{N}. \tag{E.4a}$$

From (E.3), this constant 1-sided, 1-dimensional white noise spectrum can be expressed in terms of the uncorrelated error variance σ_ϵ^2 as

$$S_\epsilon^{1d}(l) = 2\Delta y\,\sigma_\epsilon^2, \quad \text{for } 0 < l \le l_\mathcal{N}. \tag{E.4b}$$

If the variance of the 2-dimensional white noise is suppressed by smoothing 2-dimensionally in the form of separate 1-dimensional smoothing with half-power filter cutoff wavenumbers of k_c and l_c in the x and y dimensions, respectively, the 2-dimensional spectrum $\overline{S}_\epsilon^{2d}(k,l)$ of the smoothed error fields is related to the 2-dimensional spectrum $S_\epsilon^{2d}(k,l)$ of the unsmoothed errors by

$$\overline{S}_\epsilon^{2d}(k,l) = W_{k_c}^2(k)\,W_{l_c}^2(l)\,S_\epsilon^{2d}(k,l), \tag{E.5a}$$

where $W_{k_c}(k)$ and $W_{l_c}(l)$ are the filter transfer functions of the smoother in the x and y dimensions, respectively. It has been assumed in (E.5a) that the smoother is symmetric and linear so that the filter transfer functions are real and hence the wavenumber spectrum of the smoothed errors depends on the squares of the filter transfer functions rather than their complex inner products. If the filter cutoff wavenumbers k_c and l_c are the same, separate 1-dimensional smoothing in this manner with 1-dimensional Parzen smoothers in each dimension is essentially equivalent to isotropic smoothing with a 2-dimensional Parzen weighting function that depends only on the radial distance from the estimation location (see Appendix C).

From (E.3), the spectrum (E.5a) of the smoothed error fields can be expressed in terms of the uncorrelated error variance σ_ϵ^2 as

$$\overline{S}_\epsilon^{2d}(k,l) = \Delta x\Delta y\,\sigma_\epsilon^2\,W_{k_c}^2(k)\,W_{l_c}^2(l). \tag{E.5b}$$

As in (E.4a), the 1-sided, 1-dimensional wavenumber spectrum of the smoothed error fields in the y dimension is obtained from $\overline{S}_\epsilon^{2d}(k,l)$ by integrating over all wavenumbers k in the x dimension and doubling the power at each wavenumber except the zero and Nyquist wavenumbers,

$$\overline{S}_\epsilon^{1d}(l) = 2\int_{-k_\mathcal{N}}^{k_\mathcal{N}} \overline{S}_\epsilon^{2d}(k,l)\,dk.$$

From (E.5b), this can be expressed as

$$\begin{aligned}\overline{S}_\epsilon^{1d}(l) &= 2\Delta x\Delta y\,\sigma_\epsilon^2\,W_{l_c}^2(l)\int_{-k_\mathcal{N}}^{k_\mathcal{N}} W_{k_c}^2(k)\,dk \\ &= 4\Delta x\Delta y\,\sigma_\epsilon^2\,W_{l_c}^2(l)\int_{0}^{k_\mathcal{N}} W_{k_c}^2(k)\,dk.\end{aligned} \tag{E.6a}$$

The last expression follows from the fact that $W_{k_c}^2(k)$ is symmetric about $k = 0$.

For the Parzen smoother used in this study, the integral on the right side of (E.6a) was shown by (D.12b) in Appendix D to be approximately equal to the half-power filter cutoff wavenumber k_c. This relation for the integral of the squared filter transfer function holds approximately for any other smoother with smoothing parameters calibrated to the same half-power filter cutoff wavenumber k_c. The 1-sided, 1-dimensional spectrum (E.6a) of smoothed errors therefore simplifies to

$$\overline{S}_\epsilon^{1d}(l) \;\approx\; 4\Delta x\Delta y\,\sigma_\epsilon^2\,k_c\,W_{l_c}^2(l). \tag{E.6b}$$

It is illuminating to contrast the different effects of 2-dimensional smoothing on the 2-dimensional spectrum (E.5b) compared with the 1-sided, 1-dimensional spectrum (E.6b). The two spectra can be expressed in terms of the constant white-noise spectral value S_0 by substituting (E.3) into (E.5b) and (E.6b) to get

$$\overline{S}_\epsilon^{2d}(k,l) = W_{k_c}^2(k)\, W_{l_c}^2(l)\, S_0 \tag{E.7}$$

$$\overline{S}_\epsilon^{1d}(l) = 4\, k_c\, W_{l_c}^2(l)\, S_0. \tag{E.8}$$

The 2-dimensional spectral values $\overline{S}_\epsilon^{2d}(k,l)$ are thus equal to S_0 multiplied by the product of the squared values of the filter transfer functions in each dimension at the particular wavenumbers k and l. In contrast, the 1-dimensional spectral values $\overline{S}_\epsilon^{1d}(l)$ are equal to S_0 multiplied by the squared value of the filter transfer function in only the y dimension with an additional constant multiplicative factor of $4k_c$ at every wavenumber l. A factor of 2 can be accounted for by the doubling of the power in the 1-sided, 1-dimensional spectrum. The additional factor of $2k_c$ represents a constant attenuation that is applied at every wavenumber l. For smoothing in the x dimension with a filter cutoff wavelength of $\lambda_c = k_c^{-1} = 50$ km, for example, this corresponds to an attenuation by a factor of 25 cpkm at every wavenumber[9].

For the benefit of the analysis in Appendix F, and to illustrate the importance of the above distinction between the effects of 2-dimensional smoothing on the 2-dimensional and 1-dimensional spectra, each of these spectra can be compared with their counterparts for the unsmoothed error fields. From (E.5a), the 2-dimensional spectrum of the smoothed error fields is just the 2-dimensional spectrum of the unsmoothed fields multiplied by the squared values of the two filter transfer functions at each wavenumber k and l. Consider an ideal filter with transfer functions given by

$$W_{k_c}(k) = \begin{cases} 1 & \text{if } |k| \le k_c \\ 0 & \text{otherwise} \end{cases} \tag{E.9a}$$

$$W_{l_c}(l) = \begin{cases} 1 & \text{if } |l| \le l_c \\ 0 & \text{otherwise.} \end{cases} \tag{E.9b}$$

The 2-dimensional spectral values of the smoothed error fields are then related to the 2-dimensional spectral values of the unsmoothed error fields by

$$\overline{S}_\epsilon^{2d}(k,l) = \begin{cases} S_\epsilon^{2d}(k,l) & \text{if } |k| \le k_c \text{ and } |l| \le l_c \\ 0 & \text{otherwise.} \end{cases} \tag{E.10}$$

For the case of 1-dimensional spectra, it can be seen from (E.4b) and (E.6b) that the 1-dimensional spectrum of smoothed errors is related to the 1-dimensional spectrum of unsmoothed errors by

$$\overline{S}_\epsilon^{1d}(l) = 2\Delta x\, k_c\, W_{l_c}^2(l)\, S_\epsilon^{1d}(l). \tag{E.11a}$$

For a half-power filter cutoff wavelength of λ_c in the x dimension, this is

$$\overline{S}_\epsilon^{1d}(l) = \frac{2\Delta x}{\lambda_c}\, W_{l_c}^2(l)\, S_\epsilon^{1d}(l). \tag{E.11b}$$

For the ideal filter in the x dimension considered above that has the filter transfer function (E.9a), (E.11a) becomes

$$\overline{S}_\epsilon^{1d}(l) = \begin{cases} 2\Delta x\, k_c\, S_\epsilon^{1d}(l) & \text{for } 0 < l \le l_c \\ 0 & \text{otherwise.} \end{cases} \tag{E.12a}$$

[9]The units on this attenuation factor are because $2k_c$ multiplies the constant 2-dimensional white noise spectral value S_0 on the right side of (E.8), thus assuring the proper units of the 1-dimensional spectrum on the left side of the equation.

For the case of a Parzen smoother, a filter cutoff wavenumber of k_c can be achieved according to (A.12a) with a span of $L_4 \approx k_c^{-1}$. Neglecting the imperfections of the filter transfer function of the Parzen smoother for the sake of illustration, a span of $L_4 = L\Delta x$ expresses (E.12a) as

$$\overline{S}_\epsilon^{1d}(l) = \begin{cases} 2L^{-1} S_\epsilon^{1d}(l) & \text{for } 0 < l \le l_c \\ 0 & \text{otherwise.} \end{cases} \tag{E.12b}$$

The 1-dimensional spectral values at all wavenumbers in the pass band would therefore be attenuated by a factor of $2L^{-1}$.

In contrast to the 2-dimensional spectrum of smoothed error fields that is unchanged in the low-wavenumber pass band $|k| \le k_c$ and $|l| \le l_c$ according to (E.10), the smoothing in the x dimension reduces the 1-dimensional spectral values within the pass band $|l| \le l_c$ in the y dimension by the multiplicative factor of $2\Delta x k_c$ in (E.12a) compared with the 1-dimensional spectrum (E.4b) of the unfiltered errors. This perhaps non-intuitive point is important to the derivation in Appendix F of the error variance of the pre-processed SWOT estimates of SSH from the science requirement specification in terms of the 1-sided, 1-dimensional power spectral density of SWOT data smoothed with the above hypothetical ideal filter.

Appendix F. The Standard Deviation of Uncorrelated Errors in SWOT Estimates of SSH

The variances and wavenumber spectra of the errors of geostrophically computed SWOT estimates of velocity and vorticity derived in Appendix G and Appendix I, and the generation of simulated noisy SWOT measurements of SSH from the CCS model for the analyses of resolution capabilities in Secs. 6 and 8–10, all require knowledge of the variance or standard deviation of the uncorrelated errors in SWOT estimates of SSH. It is difficult to find this information in the SWOT documentation. Several different values are given or indirectly implied in two of the SWOT documents. The Algorithm Theoretical Basis document for the SWOT onboard processor (Peral, 2016) states, in the caption of Fig. 47, that the swath-averaged standard deviation for a significant wave height (SWH) of 2 m is $\sigma_h = 2.54$ cm for the uncorrelated measurement errors of SWOT data[10] smoothed 2-dimensionally onto a 1 km × 1 km grid with an isotropic half-power filter cutoff wavelength of 2 km as summarized in our Appendix B.1. The Mission Performance and Error Budget document (Esteban Fernandez, 2017) gives three different values for the standard deviation of uncorrelated measurement errors for 2-m SWH. The specification of the white-noise contribution to the total error spectrum in the unnumbered first equation in Sec. 5.1 [see also Eq. (F.1) below] can be combined with the unnumbered last equation in Sec. 5.1.1 for the 1-sided, 1-dimensional power spectral density of the uncorrelated SSH measurement errors to deduce a value of $\sigma_h = 2.74$ cm. The swath-averaged standard deviation for 2-m SWH is subsequently stated in Secs. 5.1.3 and 5.4.5 to be 2.5 cm and 2.4 cm, respectively.

Four different values for the standard deviation σ_h of the uncorrelated errors of SWOT measurements of SSH can thus be found in the SWOT documentation. Among these, the value of $\sigma_h = 2.74$ cm is derived below from the wavenumber spectral specification of the science requirements and thus represents the baseline accuracy requirement for uncorrelated errors in SWOT measurements of SSH with a footprint size of 1 km. Although not stated as such, the three smaller values noted above are probably projected estimates (at the time of writing of the various sections of the reports) of the accuracy that will actually be achieved from SWOT in orbit.

Since the baseline requirement for the standard deviation of the uncorrelated measurement errors is not provided in the SWOT documentation, and because this information is crucial for the simulated SWOT sampling of the CCS model output in this study and likely in other studies, an expression for the error standard deviation is derived in this appendix. As in the spectral specification of SWOT measurement accuracy requirements in Rodríguez and Callahan (2016), the standard deviation of uncorrelated measurement

[10] In the preceding appendices, the variance σ_ϵ^2 of uncorrelated errors was denoted generically with the subscript ϵ in order to be applicable to either SWOT or WaCM, which measure different variables. Hereafter, the subscript ϵ is replaced with a symbol that is indicative of the variable of interest. As the focus in this appendix is on the errors of SWOT estimates of SSH, the subscript h is used in place of ϵ. Other symbols are used in Appendix G and Appendix I, depending on the variable of interest (see the discussion in the introduction of Appendix G).

errors derived below is the global swath-averaged value for SWOT estimates of SSH with a footprint size of 1 km in conditions of 2-m SWH. In reality, the measurement errors increase toward each edge of the two parallel measurement swaths. They also increase with increasing SWH, which varies geographically and temporally. The most recent projected estimates of the dependencies of the SWOT measurement errors on swath location and SWH are shown in Fig. F1 (see also Fig. 2.5 of Gaultier et al., 2017).

The required variance σ_h^2 of the uncorrelated errors in the pre-processed SWOT estimates of SSH with a footprint size of 1 km is determined here from the baseline spectral characterization of the SWOT measurement errors that is specified in the SWOT Science Requirements Document (Rodríguez and Callahan, 2016) in terms of the residual errors after smoothing of the pre-processed data with a half-power filter cutoff wavelength of $\lambda_c = 15$ km. The SWOT documentation of what exactly is meant by this smoothing is contradictory. The requirement 2.7.2a in Sec. 2.7 of the Science Requirements Document (Rodríguez and Callahan, 2016) explicitly states that 15-km smoothing is to be performed 2-dimensionally. Consistent with this specification, the Mission Performance and Error Budget document (Esteban Fernandez, 2017) states in Sec. 4.1 that the objective of the SWOT mission is to characterize SSH variability at spatial scales of 15 km and larger. But later in Sec. 5.1.1 of the document, it is stated that the smoothing is to be applied only 1-dimensionally in the cross-track dimension by "an ideal square filter" that is later clarified in Sec. 5.1.2 to be the simple running average filter with the uniform weighting function given by (A.4) in our Appendix A (which was shown in Figs. A.1 and C.3 to be far from ideal in the wavenumber domain).

A rationale for smoothing only in the cross-track dimension is given in the discussion following the last unnumbered equation in Sec. 5.1.1 of Esteban Fernandez (2017) based on consideration only of the along-track wavenumber spectrum of smoothed SSH, as opposed to the resolution of the 2-dimensional SSH fields themselves. While smoothing only in the cross-track dimension is justifiable if the interest is solely in the 1-dimensional along-track wavenumber spectrum, the smoothing would more generally be applied isotropically in two dimensions to achieve the resolution of 15 km. The analysis that follows therefore assumes that the 15-km smoothing is applied in this manner.

In the discussion that follows, we will consider both an idealized filter and a realizable filter that rolls off gradually through the half-power filter cutoff wavenumber. As expressed by (D.5a), smoothing the pre-processed estimates of SSH with half-power filter cutoff wavenumbers of k_c and l_c in the x and y dimensions, respectively, reduces the uncorrelated error variance σ_h^2 by the approximate multiplicative factor (D.14b) of $\alpha = 4\Delta x \Delta y \, k_c l_c$, where Δx and Δy are the sample intervals at which the measurement errors are uncorrelated. For isotropic 2-dimensional smoothing with $k_c = l_c = 1/15$ cpkm and a uniform sample interval of $\Delta x = \Delta y = 1$ km, this multiplicative factor is $\alpha = 4/15^2 = 1/56.25$. The science requirement for measurement accuracy could thus have been specified in terms of the variance $\overline{\sigma}_h^2$ of residual errors after smoothing isotropically with a filter cutoff wavelength of $\lambda_c = 15$ km. The variance of the unsmoothed pre-processed SWOT estimates of SSH that gives this value of $\overline{\sigma}_h^2$ could then be simply calculated as $\sigma_h^2 = \alpha^{-1} \, \overline{\sigma}_h^2 = 56.25 \, \overline{\sigma}_h^2$.

The baseline requirement for instrument noise is instead specified in the Science Requirements Document (Rodríguez and Callahan, 2016) in terms of the 1-sided, 1-dimensional (along-track) wavenumber power spectral density of the residual white-noise contribution to the total SSH measurement errors after smoothing as

$$\overline{S}_h^{1d}(l) = 2 \text{ cm}^2/\text{cpkm}, \quad \text{for } 1/1000 \le l \le 1/15 \text{ cpkm}. \tag{F.1a}$$

The instrumental errors are thus specified explicitly only for wavenumbers l smaller than $l_c = 1/15$ cpkm, i.e., for wavelengths $\lambda = l^{-1}$ longer than the half-power filter cutoff wavelength of $\lambda_c = l_c^{-1} = 15$ km.

For an ideal isotropic 2-dimensional filter, the specification of the spectrum (F.1a) would be extended from the filter cutoff of $l_c = 1/15$ cpkm to the Nyquist wavenumber $l_{\mathcal{N}}$ of the SWOT data as

$$\overline{S}_h^{1d}(l) = 0, \quad \text{for } 1/15 < l \le l_{\mathcal{N}} \text{ cpkm}. \tag{F.1b}$$

For the present official planned footprint size of 1 km and sample grid spacings of $\Delta x = \Delta y = 1$ km for the pre-processed SWOT estimates of SSH as specified in the onboard processing document (Peral, 2016), the

Nyquist wavenumber is $l_{\mathcal{N}} = 0.5$ cpkm. The residual white noise error spectrum (F.1a) and (F.1b) after smoothing with the ideal isotropic 2-dimensional filter is shown by the dashed red line in Fig. F2.

It was shown in Appendix E that the constant 1-sided, 1-dimensional along-track wavenumber spectrum of residual uncorrelated measurement errors after smoothing with half-power filter cutoff wavenumbers of k_c and l_c in the x and y dimensions is related to the variance σ_h^2 of the unsmoothed errors by (E.6b). For the ideal isotropic 2-dimensional filter specified by (F.1a) and (F.1b), the filter transfer function $W_{l_c}(l)$ on the right side of (E.6b) is given by (E.9b). Then (E.6b) simplifies to

$$\overline{S}_h^{1d}(l) = \begin{cases} 4\Delta x\,\Delta y\,k_c\,\sigma_h^2 & \text{if } 0 < l \le l_c \\ 0 & \text{otherwise.} \end{cases} \tag{F.2}$$

Comparing (F.2) with the science requirement (F.1) expresses the variance of the pre-processed SWOT estimates of SSH as

$$\sigma_h^2 = \frac{1 \text{ cm}^2/\text{cpkm}}{2\Delta x\,\Delta y\,k_c}. \tag{F.3a}$$

The units in the numerator of this equation, in combination with the units of the variables in the denominator, assure that the left side of (F.3a) has units of cm^2. For a sample interval of $\Delta x = \Delta y = 1$ km between uncorrelated errors in pre-processed SWOT data and the post-processing half-power filter cutoff wavenumber of $k_c = 1/15$ cpkm in the science requirement specification, this gives a variance of

$$\sigma_h^2 = 7.5 \text{ cm}^2 = (2.74 \text{ cm})^2 \tag{F.3b}$$

for the errors of the pre-processed SWOT estimates of SSH. The requirement for 1 km $\times$ 1 km pre-processed estimates of SSH with isotropic 2-dimensional smoothing with a half-power filter cutoff wavelength of 2 km is therefore that the uncorrelated errors have a standard deviation of $\sigma_h = 2.74$ cm.

As recently recommended by the SWOT Algorithm Development Team (see Appendix B.1), a smaller footprint size of 0.5 km is likely to be adopted in the near future for the onboard pre-processed SWOT estimates of SSH. For pre-processing of the raw SWOT data with a smaller isotropic filter cutoff wavelength of 1 km in order to achieve the footprint size of 0.5 km, the standard deviation (F.3b) of allowed measurement errors would increase by a factor of two.

The overall average measurement error standard deviation of $\sigma_h = 2.74$ cm derived above from the baseline specification (F.1) in terms of the white noise spectrum of the instrumental errors for 2-m SWH is shown as the dashed line in Fig. F1. It is visually apparent that the across-swath average of the most recent projected estimate of the measurement errors that will be achieved by SWOT for 2-m SWH is smaller than 2.74 cm. An overall average of 2.74 cm appears to be more representative of the projected errors for a SWH of about 4 m. If the projected estimates of the measurement error characteristics shown in Fig. F1 are achieved, the results presented in Secs. 6, 8 and 9 may be somewhat pessimistic for 2-m SWH. From the analysis in Sec. 8, however, space-time smoothed maps of the geostrophically computed velocity and vorticity fields are much more susceptible to sampling errors than measurement errors. The distinction between 2.74 cm and the smaller values of 2.54 cm, 2.5 cm and 2.4 cm noted above from the various SWOT documents is therefore a minor issue in the analysis of resolution capability presented in this paper.

The effects of a $\sigma_h = 2.74$ cm standard deviation of errors in pre-processed SWOT data on the standard deviations of errors of geostrophically computed SWOT estimates of velocity and vorticity are quantified in Appendix G using propagation-of-error analysis. The wavenumber spectral characteristics of the errors in SWOT estimates of SSH and geostrophically computed velocity components and vorticity estimated from the pre-processed SWOT data and after additional smoothing in ground-based post-processing are derived in Appendix I.

The uncorrelated measurement errors in the SWOT estimates of SSH are superimposed on spatially correlated (long-wavelength) noise from orbit errors and various environmental effects. The science requirement for these red-noise errors is that they have a 1-sided, 1-dimensional (along-track) power spectral density no larger than

$$\begin{aligned} S_{red}^{1d}(l) &= 0.0125\,l^{-2} \text{ cm}^2/\text{cpkm}, \\ &\text{for } 1/1000 < l < 1/15 \text{ cpkm}, \end{aligned} \tag{F.4}$$

which is shown extrapolated to the Nyquist wavenumber $l_{\mathcal{N}} = 0.5$ cpkm for 1 km $\times$ 1 km sampling by the dotted red line in Fig. F2. It can be seen that smoothing with an ideal isotropic 2-dimensional filter that has a half-power filter cutoff wavelength of $\lambda_c = l_c^{-1} = 15$ km would have very little attenuation effect on the red noise since it has so little power at wavenumbers $l > l_c$. The science requirement specification for the along-track power spectral density of the total measurement errors in the SWOT data is thus given approximately by the sum of the red-noise spectrum (F.4) and the spectrum (F.1) of the residual white noise after ideal low-pass filtering with a half-power filter cutoff wavelength of 15 km. This total measurement error spectrum is shown by the solid red line in Fig. F2.

The analysis above based on isotropic 2-dimensional smoothing neglects the effects of imperfections of the filter transfer function of any realizable low-pass filter that could be applied in practice in ground-based post-processing of the pre-processed SWOT estimates of SSH. Post-launch verification of the SWOT instrument performance as specified spectrally by (F.1) for SWOT data smoothed 2-dimensionally and isotropically as explicitly stated in the Science Requirements Document (Rodríguez and Callahan, 2016) would therefore be subject to imperfections of the filter transfer function. For example, the dashed green line in Fig. F2 shows the 1-sided, 1-dimensional power spectral density of residual white noise errors after smoothing 2-dimensionally using a Parzen smoother with a half-power filter cutoff wavelength of $\lambda_c = k_c^{-1} = l_c^{-1} = 15$ km. The solid green line is the sum of this realizable low-pass filtered white noise spectrum and the red-noise spectrum (F.4). Because of the gradual rolloff of the filter transfer function through the half-power filter cutoff wavelength l_c, the flatness of the residual error spectrum to the value specified by (F.1a) would not be detectable when the pre-processed SWOT data are smoothed 2-dimensionally with a realizable filter. The requirement for uncorrelated measurement errors in the SWOT estimates of SSH that are specified in the Science Requirements Document based on isotropic 2-dimensional smoothing therefore cannot be formally tested in the spectral form (F.1).

The issue of the untestability of the science requirement specification (F.1) in terms of an ideal 2-dimensional filter can be alternatively addressed by "reverse engineering" the science requirement to determine the required wavenumber spectral characteristics of the unfiltered errors of SWOT estimates of SSH. From (E.4b) in Appendix E and the variance (F.3) derived above from (F.1), the along-track white noise spectrum for the uncorrelated errors in the unfiltered pre-processed SWOT estimates of SSH in the baseline design is

$$S_h^{1d}(l) = 2\Delta y\, \sigma_h^2 = 15 \text{ cm}^2/\text{cpkm} \quad \text{for } 0 < l \le l_{\mathcal{N}}, \tag{F.5}$$

where $l_{\mathcal{N}} = (2\Delta y)^{-1}$ is again the Nyquist wavenumber for a sample interval Δy.

The spectrum (F.5) of unfiltered uncorrelated measurement errors is shown by the dashed blue line in Fig. F2 for the case of a footprint size of 1 km and grid spacings of $\Delta x = \Delta y = 1$ km. Except at the short wavelengths over which the total SWOT measurement errors are dominated by the contribution from uncorrelated measurement errors, the wavenumber spectrum of long-wavelength measurement errors shown by the dotted red line in Fig. F2 is approximately the same with and without smoothing with the half-power filter cutoff wavelength of 15 km considered above. The wavenumber spectrum of total errors in the pre-processed SWOT data without smoothing can thus be approximated by the sum of the dashed blue line and the dotted red line, which is shown as the solid blue line in Fig. F2. In contrast to the solid red line that is untestable because it is based on a hypothetical ideal 2-dimensional low-pass filter, the requirement that the wavenumber spectrum of unsmoothed measurement errors be no greater than the solid blue line can be tested in post-launch verification. The specification (F.1) of the SWOT measurement errors based on idealized filtering can thus be tested indirectly from the along-track spectrum of unfiltered SWOT data.

The preceding analysis is based on the science requirements as specified by Rodríguez and Callahan (2016) in terms of isotropic 2-dimensional smoothing with a half-power filter cutoff wavelength of 15 km in each dimension. As noted previously, the Mission Performance and Error Budget document (Esteban Fernandez, 2017) specifies smoothing only 1-dimensionally in the cross-track dimension. In that case, the wavenumber power spectral density would be attenuated uniformly at all wavenumbers by the factor $\alpha = 1/56.25$ derived above without the gradual rolloff at high wavenumbers that would occur with along-track smoothing in

addition to the cross-track smoothing. This is true regardless of the imperfections of the filtering in the cross-track dimension, i.e., perpendicular to the along-track dimension of the 1-dimensional wavenumber spectrum.

The along-track wavenumber spectrum of this cross-track 1-dimensionally smoothed SSH extends uniformly to the Nyquist wavenumber $l_{\mathcal{N}} = (2\Delta y)^{-1}$ cpkm with the value of $\overline{S}_h^{1d}(l) = 2$ cm^2/cpkm in the spectral specification (F.1) of the science requirements for the uncorrelated measurement errors. However, the specification in the unnumbered first equation of Sec. 5.1 of Esteban Fernandez (2017) [equivalent to our Eq. (F.1a)] considers only the portion of this attenuated spectrum for wavenumbers smaller than 1/15 cpkm. This is effectively equivalent to assuming idealized isotropic smoothing in both the cross-track and along-track dimensions, as in our analysis above, with the distinction that the SWOT performance on-orbit can be tested spectrally if only 1-dimensional cross-track smoothing is applied. This cross-track smoothing can only be applied across the narrow 50-km swath on each side of the satellite ground track.

We note again that testability of the science requirement for SWOT measurement accuracy would be a moot issue if the uncorrelated measurement errors had been specified in terms of the variance σ_h^2 given by (F.3b) derived above for the pre-processed SWOT estimates of SSH with a footprint size of 1 km. It would then be straightforward to test the SWOT performance either from the noise in the SSH fields or spectrally from (F.5) without the need for ground-based post-processing to smooth either 2-dimensionally or 1-dimensionally (cross-track) with a half-power filter cutoff wavelength of $\lambda_c = 15$ km.

It is enlightening to compare the 68$^{\text{th}}$-percentile SSH wavenumber spectrum upon which the science requirement for SWOT measurement accuracy is based with the alongshore wavenumber spectrum of SSH from the CCS model used throughout this study. The two spectra are shown in Fig. F3 along with the empirical and theoretical spectra of residual SSH measurement errors after isotropic 2-dimensional smoothing with a half-power filter cutoff wavelength of $\lambda_c = 15$ km (see Appendix I.2 for the details of the calculation of the theoretical error spectrum). As discussed above, the science requirement is for the SSH signal and error spectra with 15-km smoothing to intersect at a wavenumber of 0.067 cpkm (a wavelength of 15 km). It is evident from Fig. F3 that the SSH signal spectrum from the CCS model used in this study intersects the error spectrum at a smaller wavenumber of about 0.033 cpkm, which corresponds to a wavelength of about 30 km. At this wavelength, the spectral power in the CCS model is about a factor of 5 less energetic than the spectral power in the assumed 68$^{\text{th}}$-percentile spectrum.

The discrepancy between the intersections of the white-noise spectrum for SWOT measurement errors with 15-km isotropic 2-dimensional smoothing and the two SSH signal spectra shown in Fig. F3 raises a question about whether the spectral specification of the science requirements for SWOT will be achieved for the actual SSH spectrum. The difference occurs because the CCS model spectrum rolls off more steeply toward high wavenumbers than does the 68$^{\text{th}}$-percentile spectrum assumed in the Science Requirements Document. In the wavenumber range from about 0.003 cpkm to 0.1 cpkm (wavelengths from 300 km to 10 km), the dependence of the CCS model spectrum on alongshore wavenumber l is approximately $l^{-7/2}$ compared with a rolloff of about $l^{-5/2}$ for the assumed 68$^{\text{th}}$-percentile SSH spectrum.

The flatter assumed 68$^{\text{th}}$-percentile wavenumber spectrum is based on extrapolation of along-track SSH spectra from nadir altimetry that resolves variability only down to wavelength scales of about 70 km (Xu and Fu, 2012). The validity of this extrapolation is unknown since observational data are not presently available to determine the SSH spectrum on these scales. Velocity measurements by acoustic Doppler current profilers can be inverted by assuming geostrophy (see, for example, Fig. 4 of Rocha et al., 2016). Such inversions omit the SSH signals from internal gravity waves and other small-scale ageostrophic processes. The spectral characteristics at wavelengths shorter than 70 km must therefore be inferred from high-resolution ocean circulation models.

The contributions of internal gravity waves and other small-scale ageostrophic processes to the spatial variability of SSH will flatten the spectrum (i.e., increase the variance) at high wavenumbers. Some insight into their effects on the wavenumber spectrum of SSH can be gained from the pair of North Atlantic simulations shown in Figs. 10 and 11 of Sec. 3. The wavenumber rolloff in the SSH spectrum computed from the model forced by monthly winds and no ocean tides (the LF simulation) is about l^{-5} over all wavenumbers in the region southeast of the Gulf Stream (Fig. F4). Up to a wavenumber of about 1/50 cpkm, the spectral

rolloff is also about l^{-5} in the model forced by high-frequency winds and ocean tides (the HF simulation). At higher wavenumbers, however, the spectral rolloff in the HF model flattens to about l^{-3}. The spectra from both the HF model and the LF model intersect the error spectrum at about the same 30-km wavelength as the spectrum from the CCS model shown in Fig. F3.

On the other hand, Savage et al. (2017) found flatter spectral rolloffs between l^{-2} and l^{-1} at wavenumbers between 1/70 cpkm and 1/30 cpkm in high-resolution versions of the Massachusetts Institute of Technology general circulation model (MITgcm) for a wide range of dynamical regimes (see also Rocha et al., 2016). They attribute most of this flattening of the SSH spectrum to internal gravity waves. Depending on the signal power levels, a consequence of the flatter spectral rolloffs is that the SSH signal spectra from the MITgcm model can intersect the noise spectrum for 15-km smoothed SWOT data at shorter wavelengths than from the three ROMS models considered in Figs. F3 and F4.

The details of the wavenumber spectral characteristics of SSH thus apparently differ from one model to another and likely from one region to another. These differences are apparently attributable to a variety of technical details of the model formulations. One of the primary contributions of the SWOT mission will be to provide the first observational evidence from which the wavenumber spectral characteristics of SSH as represented in the various models can be tested.

Appendix G. The Standard Deviations of the Errors of SWOT and WaCM Estimates of Derivative Quantities

The variables of interest in this study include derivatives of the basic measurements by SWOT and WaCM. For SWOT, the velocity must be computed geostrophically from derivatives of the noisy SSH measurements and the vorticity must be estimated from additional derivatives of the geostrophically computed velocity estimates, i.e., double differentiation of the noisy SSH measurements. For WaCM, the velocity will be measured directly and vorticity will be computed from derivatives of the noisy velocity component measurements. Estimation of these derivatives by finite differencing of the gridded fields of the variable measured by each instrument amplifies the errors in the measured variables. The effects of these error amplifications on the uncertainties of the SWOT and WaCM estimates of the derivative fields are quantified in this appendix using standard propagation-of-error analysis.

Throughout this appendix, errors are denoted by ϵ with a subscript symbol that is indicative of the variable of interest and the variances of these errors are denoted by σ^2 with the same subscript. As in Appendix F, the subscript h is used in Appendix G.1 to indicate the errors of pre-processed SWOT estimates of SSH. The subscripts u_g, v_g and ζ_g are used in Appendix G.1 to indicate the errors of geostrophically computed SWOT estimates of the two velocity components and vorticity. Similarly, the subscripts u, v and ζ are used in Appendix G.2 to indicate the errors of WaCM estimates of the two velocity components and vorticity. As in Appendix E and Appendix F, overbars are used in Appendix G.3 to indicate the variances of residual errors after 2-dimensional smoothing of the pre-processed SWOT data.

An important point to note is that the expressions (G.2b), (G.5) and (G.8) derived below for the variances of the errors of geostrophically computed SWOT estimates of the x and y components of velocity and vorticity are all expressed in terms of the variance σ_h^2 of the pre-processed SWOT estimates of SSH. The value of $\sigma_h^2 = (2.74 \text{ cm})^2$ that is derived for a footprint size of 1 km in Appendix F is used in the applications of these equations in Sec. 4.1, but the same equations can be used for any specified value of σ_h^2. Likewise, the expression (G.15) derived below for the variance of errors of WaCM estimates of vorticity is expressed in terms of the variances σ_u^2 and σ_v^2 of WaCM estimates of the x and y components of velocity. A value of $\sigma_u^2 = \sigma_v^2 = (0.354 \text{ m s}^{-1})^2$ for a footprint size of 5 km is used in the application of this equation in Sec. 4.2, but the same equation can be used for any specified values of σ_u^2 and σ_v^2.

As noted previously, the uncorrelated measurement errors for both SWOT and WaCM will vary in the cross-track direction and will depend on significant wave height. The constant values of $\sigma_h = 2.74$ cm and $\sigma_u = \sigma_v = 0.354$ m s^{-1} used throughout this study are the average values across the measurement swaths. In actuality, these errors increase toward the edges of the swaths as shown in Fig. F1 for the case of SWOT. Because we have neglected the cross-track variations of instrumental noise, the effects of uncorrelated errors

on the resolution capabilities of SWOT and WaCM estimates of the variables of interest are likely to be underestimated in Secs. 6 and 8–10. In other words, the resolution capabilities inferred from the analysis in this study are likely somewhat optimistic.

Appendix G.1. Geostrophically Computed SWOT Estimates of Velocity and Vorticity with 1-km Footprint

The standard deviation of the uncorrelated instrumental noise contribution to the pre-processed SWOT measurements of SSH was derived in Appendix F from the wavenumber spectral specification (F.1) in the baseline requirement for SWOT measurement errors. For measurements with a footprint size of 1 km, the derived value of the standard deviation for the baseline design is $\sigma_h = 2.74$ cm. It is shown in the bottom panel of Fig. B1a that SWOT SSH measurement errors with a footprint size of 1 km are essentially uncorrelated on a $\Delta x \times \Delta y = 1$ km $\times$ 1 km grid.

The error $\epsilon_{v_g}(x, y)$ of the alongshore component of geostrophically computed velocity $v = gf^{-1}\partial h/\partial x$ at grid location (x, y) estimated from cross-shore centered differences of the height errors at the adjacent grid locations in the x dimension is

$$\epsilon_{v_g}(x, y) = \frac{g}{f}\,\frac{\epsilon_h(x + \Delta x, y) - \epsilon_h(x - \Delta x, y)}{2\Delta x}. \tag{G.1}$$

Since the height errors are are assumed here to be spatially homogeneous, the variance of these alongshore geostrophically computed velocity errors obtained by propagation-of-error analysis is

$$\sigma^2_{v_g} = \frac{g^2}{f^2}\,\frac{\sigma^2_h}{2\Delta x^2}\Big[1 - \rho_h(2\Delta x)\Big], \tag{G.2a}$$

where $\rho_h(2\Delta x)$ is the autocorrelation of the SSH measurements at a spatial lag of $2\Delta x$. This lagged autocorrelation is essentially zero since the height errors for a footprint size of 1 km are essentially uncorrelated on a 1 km $\times$ 1 km grid as noted above from the bottom panel of Fig. B1a. The variance of the alongshore geostrophically computed velocity errors is therefore

$$\sigma^2_{v_g} = \frac{g^2}{f^2}\,\frac{\sigma^2_h}{2\Delta x^2}. \tag{G.2b}$$

The Coriolis parameter at the central latitude 37°N of the CCS model domain is $f = 8.77 \times 10^{-5}$ s^{-1}. For gravitational acceleration $g = 9.81$ m s^{-2}, an SSH error variance of $\sigma^2_h = (2.74\text{ cm})^2$ and a grid spacing of $\Delta x = 1$ km, the standard deviation of the errors of the alongshore geostrophically computed velocity component is

$$\sigma_{v_g}(37°\text{N}) = 2.17\text{ m s}^{-1}. \tag{G.3}$$

The error $\epsilon_{u_g}(x, y)$ of the cross-shore component of geostrophically computed velocity $u = -gf^{-1}\partial h/\partial y$ at grid location (x, y) estimated similarly from alongshore centered differences of the height errors at the adjacent grid locations in the y dimension is

$$\epsilon_{u_g}(x, y) = \\ -\frac{g}{f}\,\frac{\epsilon_h(x, y + \Delta y) - \epsilon_h(x, y - \Delta y)}{2\Delta y}. \tag{G.4}$$

Analogous to the derivation of (G.2b), the variance of these cross-shore geostrophically computed velocity errors on a 1 km $\times$ 1 km grid is

$$\sigma^2_{u_g} = \frac{g^2}{f^2}\,\frac{\sigma^2_h}{2\Delta y^2}. \tag{G.5}$$

For a uniform grid spacing $\Delta x = \Delta y = 1$ km, the cross-shore geostrophically computed velocity errors $\epsilon_{u_g}(x, y)$ at the central latitude 37°N of the CCS model domain have the same standard deviation (G.3) as the alongshore velocity errors,

$$\sigma_{u_g}(37°\text{N}) = 2.17\text{ m s}^{-1}. \tag{G.6}$$

The error $\epsilon_{\zeta_g}(x,y)$ of the vorticity $\zeta_g = \partial v_g/\partial x - \partial u_g/\partial y$ at grid location (x,y) calculated from centered differences of the geostrophically computed velocity component errors is

$$\epsilon_{\zeta_g}(x,y) = \frac{\epsilon_{v_g}(x+\Delta x,y) - \epsilon_{v_g}(x-\Delta x,y)}{2\Delta x} - \frac{\epsilon_{u_g}(x,y+\Delta y) - \epsilon_{u_g}(x,y-\Delta y)}{2\Delta y}. \tag{G.7a}$$

From the expressions (G.1) and (G.4) for the geostrophically computed velocity component errors calculated from centered differences of heights, (G.7a) can be written as the sum of four centered differences of height errors with center points at $(x+\Delta x,y)$, $(x-\Delta x,y)$, $(x,y+\Delta y)$ and $(x,y-\Delta y)$,

$$\begin{aligned}\epsilon_{\zeta_g}(x,y) = \frac{g}{f}\frac{1}{2\Delta x}\left[\frac{\epsilon_h(x+2\Delta x,y) - \epsilon_h(x,y)}{2\Delta x} - \frac{\epsilon_h(x,y) - \epsilon_h(x-2\Delta x,y)}{2\Delta x}\right] \\ + \frac{g}{f}\frac{1}{2\Delta y}\left[\frac{\epsilon_h(x,y+2\Delta y) - \epsilon_h(x,y)}{2\Delta y} - \frac{\epsilon_h(x,y) - \epsilon_h(x,y-2\Delta y)}{2\Delta y}\right].\end{aligned} \tag{G.7b}$$

For a uniform grid spacing $\Delta y = \Delta x$, this simplifies to

$$\begin{aligned}\epsilon_{\zeta_g}(x,y) = \frac{g}{f}\frac{1}{4\Delta x^2}\Big[&\epsilon_h(x+2\Delta x,y) \\ &+ \epsilon_h(x-2\Delta x,y) \\ &- 4\epsilon_h(x,y) \\ &+ \epsilon_h(x,y+2\Delta y) \\ &+ \epsilon_h(x,y-2\Delta y)\Big].\end{aligned} \tag{G.7c}$$

For the 1 km × 1 km grid on which SWOT estimates of SSH are uncorrelated, the variance of the errors of SWOT estimates of ζ_g obtained by propagation-of-error analysis is

$$\sigma^2_{\zeta_g} = \frac{g^2}{f^2}\frac{20\,\sigma_h^2}{(4\Delta x^2)^2}. \tag{G.8}$$

At the central latitude 37°N of the CCS model domain, the standard deviation of the errors of geostrophically computed SWOT estimates of vorticity is thus

$$\sigma_{\zeta_g}(37^\circ\mathrm{N}) = 3.43 \times 10^{-3}\,\mathrm{s}^{-1}. \tag{G.9a}$$

Compared with the planetary vorticity of $f = 8.77 \times 10^{-5}$ s^{-1} at 37°N, this standard deviation of the geostrophically computed vorticity errors is

$$\sigma_{\zeta_g}(37^\circ\mathrm{N}) = 39.1 f. \tag{G.9b}$$

The uncertainties (G.3) and (G.6) of geostrophically computed SWOT estimates of velocity and the uncertainty (G.9) of geostrophically computed SWOT estimates of vorticity are very large compared with the oceanographic signals of interest. Clearly the SWOT data must be smoothed spatially and/or temporally to achieve scientifically useful estimates of geostrophically computed velocity and vorticity. This is discussed further in Appendix G.3 and Sec. 4.

Appendix G.2. WaCM Estimates of Vorticity with 5-km Footprint

In the baseline design, the standard deviation of speed uncertainties in WaCM estimates of surface velocity for a footprint size of 5 km (i.e., after isotropic smoothing the raw WaCM measurements with a half-power filter cutoff wavelength of 10 km) is $\sigma_{spd} = 0.50$ m s^{-1}. WaCM estimates of velocity with a footprint size of 5 km are essentially uncorrelated on a $\Delta x \times \Delta y = 5$ km $\times$ 5 km grid (see the bottom panel of Fig. B1b). We will assume that the errors of the two velocity components are uncorrelated with each other.

In general, the standard deviations σ_u and σ_v of the errors of the 10-km smoothed velocity estimates differ for the two orthogonal velocity components u and v. In Secs. 6 and 8–10, we have assumed that the speed uncertainties are equally partitioned between u and v. The standard deviations σ_u and σ_v are then both equal to a value $\sigma_{u,v}$ that is related to the baseline design of $\sigma_{spd} = 0.50$ m s^{-1} by

$$\sigma_{u,v} = \frac{\sigma_{spd}}{\sqrt{2}} = 0.354 \text{ m s}^{-1}. \tag{G.10}$$

In the analysis that follows, we allow for the possibility of different error standard deviations for each velocity component.

The errors of WaCM estimates of vorticity $\zeta = \partial v/\partial x - \partial u/\partial y$ can be calculated from centered differences of the velocity errors,

$$\begin{aligned}\epsilon_\zeta(x,y) = &\frac{\epsilon_v(x+\Delta x, y) - \epsilon_v(x-\Delta x, y)}{2\Delta x} \\ &- \frac{\epsilon_u(x, y+\Delta y) - \epsilon_u(x, y-\Delta y)}{2\Delta y}.\end{aligned} \tag{G.11}$$

Since the u and v measurement errors are assumed to be spatially homogeneous, uncorrelated with each other, and individually uncorrelated spatially on the 5 km $\times$ 5 km grid, the variance of the errors of ζ obtained by propagation-of-error analysis for a grid spacing of $\Delta x \times \Delta y = 5$ km $\times$ 5 km on which the velocity component errors are uncorrelated is

$$\sigma_\zeta^2 = \frac{\sigma_v^2}{2\Delta x^2} + \frac{\sigma_u^2}{2\Delta y^2}. \tag{G.12}$$

For equal partitioning of the speed uncertainties between the u and v velocity components with standard deviations given by (G.10), the standard deviation (G.12) of the errors of WaCM estimates of vorticity for a uniform 5 km $\times$ 5 km grid is

$$\sigma_\zeta\Big|_{5\text{km}} = 7.08 \times 10^{-5} \text{ s}^{-1}. \tag{G.13a}$$

Compared with the planetary vorticity of $f = 8.77 \times 10^{-5}$ s^{-1} at the central latitude 37°N of the CCS model domain, this is

$$\sigma_\zeta(37°\text{N})\Big|_{5\text{km}} = 0.807 f. \tag{G.13b}$$

It is shown in Appendix H that it is advantageous to oversample the WaCM data on a grid spacing of $\Delta x = \Delta y = 1$ km because the response function of centered differences on the finer grid retains more of the high wavenumber variability in the vorticity signal. The footprint size from the filtering in the pre-processing of WaCM data is still 5 km. The standard deviations of the errors of WaCM estimates of the velocity components are therefore still σ_u^2 and σ_v^2, but the velocity component errors on a 1 km $\times$ 1 km grid are spatially correlated. We will continue to assume, however, that the errors of the two velocity components are uncorrelated with each other, even on the oversampled $\Delta x \times \Delta y = 1$ km $\times$ 1 km grid. The variance of the vorticity errors (G.11) then becomes

$$\begin{aligned}\sigma_\zeta^2\Big|_{1\text{km}} = &\frac{\sigma_v^2}{2\Delta x^2}\Big[1 - \rho_v(2\Delta x)\Big] \\ &+ \frac{\sigma_u^2}{2\Delta y^2}\Big[1 - \rho_u(2\Delta y)\Big],\end{aligned} \tag{G.14}$$

where $\rho_v(2\Delta x)$ and $\rho_u(2\Delta y)$ are the autocorrelations of, respectively, the alongshore velocity errors ϵ_v at a spatial lag of $2\Delta x$ and the cross-shore velocity errors ϵ_u at a spatial lag of $2\Delta y$.

For the Parzen smoother with a half-power filter cutoff wavelength of 10 km in the baseline design for pre-processing, the autocorrelations of errors of u and v at a lag of 2 km are about 0.638 (see the bottom panel of Fig. B1b). The variance (G.14) of the errors of WaCM estimates of vorticity on the oversampled 1 km × 1 km grid then becomes

$$\sigma_\zeta^2\Big|_{1\text{km}} = \frac{0.362\,\sigma_v^2}{2\Delta x^2} + \frac{0.362\,\sigma_u^2}{2\Delta y^2}. \tag{G.15}$$

Because of the smaller values of Δx and Δy in the denominators on the right side of (G.15) compared with their values in the denominators on the right side of (G.12), the standard deviation of vorticity errors is larger on the oversampled 1 km × 1 km grid. This is the case despite the smaller factor of 0.362 in the numerators of (G.15) that arises from the spatial correlations of the errors on the 1 km × 1 km grid.

For equal partitioning of the speed uncertainties between the u and v velocity components with standard deviations (G.10), the standard deviation of the errors of WaCM estimates of vorticity on the oversampled 1 km × 1 km grid is

$$\sigma_\zeta\Big|_{1\text{km}} = 2.13 \times 10^{-4}\ \text{s}^{-1}. \tag{G.16a}$$

Compared with the planetary vorticity of $f = 8.77 \times 10^{-5}\ \text{s}^{-1}$ at the central latitude 37°N of the CCS model domain, this is

$$\sigma_\zeta(37°\text{N})\Big|_{1\text{km}} = 2.43f. \tag{G.16b}$$

Appendix G.3. Geostrophically Computed SWOT Estimates of Velocity and Vorticity with 5-km Footprint

The standard deviation (G.10) of velocity component errors from WaCM is much smaller than the standard deviations (G.3) and (G.6) of the errors of geostrophically computed velocity components estimated from SWOT measurements of SSH. Likewise, the standard deviation (G.16) of the errors of WaCM estimates of vorticity on a 1 km × 1 km grid is much smaller than the standard deviation (G.9) of the errors of geostrophically computed vorticity estimated from SWOT data on a 1 km × 1 km grid. It must be kept in mind, however, that the footprint size is five times coarser for the pre-processed WaCM measurements of surface velocity than for the pre-processed SWOT measurements of SSH. In this section, we quantify the reduction of the errors of geostrophically computed SWOT estimates of velocity and vorticity that can be achieved in ground-based post-processing by smoothing in a manner that is commensurate with the smoothing with the same half-power filter cutoff wavelength of 10 km planned for the pre-processing of WaCM data.

Consider first the errors of SWOT estimates of the velocity component v_g computed geostrophically from centered differences of SWOT estimates of SSH smoothed using the same Parzen smoother with a half-power filter cutoff wavelength of 10 km considered in Appendix G.2 for the pre-processing of WaCM data. The expression analogous to (G.2a) for the variance of the resulting smoothed estimates of v_g is

$$\begin{aligned}\overline{\sigma}_{v_g}^2 &= \frac{g^2}{f^2}\frac{\overline{\sigma}_h^2}{2\Delta x^2}\Big[1 - \overline{\rho}_h(2\Delta x)\Big] \\ &= \frac{\overline{\sigma}_h^2}{\sigma_h^2}\Big[1 - \overline{\rho}_h(2\Delta x)\Big]\sigma_{v_g}^2,\end{aligned} \tag{G.17a}$$

where the overbar on $\overline{\sigma}_h^2$ distinguishes the variance of the smoothed SSH errors from the variance σ_h^2 of the pre-processed SWOT estimates of SSH and $\sigma_{v_g}^2$ on the right side of (G.17a) is the variance (G.2b) of the errors of unsmoothed SWOT estimates of v_g. The term $\overline{\rho}_h(2\Delta x)$ in the square brackets is the autocorrelation of the smoothed estimates of SSH at a lag of $2\Delta x$.

Whereas the lagged autocorrelation was zero at nonzero lags for the case of unsmoothed SSH data considered in (G.2b), it is nonzero after smoothing with a half-power filter cutoff wavelength of 10 km. As

noted in Appendix G.2 from the bottom panel of Fig. B1b, this autocorrelation for the case of the Parzen smoother used here has a value of about 0.638 at a lag of $2\Delta x = 2$ km. And from (D.14c) in Appendix D, smoothing of the errors of the pre-processed estimates of SSH with a half-power filter cutoff wavelength of 10 km reduces the SSH error variance by approximately a factor of 25. Then $\overline{\sigma}_h^2/\sigma_h^2 \approx 0.040$ and (G.17a) becomes

$$\overline{\sigma}_{v_g}^2 = 0.0145\,\sigma_{v_g}^2. \tag{G.17b}$$

From (G.2b), the variance of the errors of the unsmoothed SWOT estimates of v_g is $\sigma_{v_g}^2 = (2.17 \text{ m s}^{-1})^2$ at the central latitude 37°N of the CCS model domain. The standard deviation of the errors of SWOT estimates of the velocity component v_g computed geostrophically from smoothed SSH at 37°N is therefore

$$\overline{\sigma}_{v_g}(37°\text{N}) = 0.261 \text{ m s}^{-1}. \tag{G.18}$$

The standard deviation $\overline{\sigma}_{u_g}$ of the errors of SWOT estimates of the velocity component u_g computed geostrophically from smoothed SSH is the same as $\overline{\sigma}_{v_g}$. Smoothing the pre-processed SWOT estimates of SSH with the same half-power filter cutoff wavelength of 10 km that is planned for pre-processed WaCM estimates of surface velocity thus reduces the error standard deviations (G.3) and (G.6) by more than a factor of 8. Moreover, the standard deviations of the errors of u_g and v_g computed geostrophically from the smoothed SWOT estimates of SSH are somewhat smaller than the standard deviations (G.10) of pre-processed WaCM estimates of the two velocity components.

Derivation of the standard deviation of the errors of estimates of vorticity computed geostrophically from smoothed SWOT estimates of SSH is tedious. Analogous to (G.7c), the errors of the geostrophically computed vorticity estimated from smoothed SWOT data can be expressed as

$$\begin{aligned}\overline{\epsilon}_{\zeta_g}(x,y) = \frac{g}{f}\frac{1}{4\Delta x^2}\Big[&\overline{\epsilon}_h(x+2\Delta x, y)\\ &+ \overline{\epsilon}_h(x-2\Delta x, y)\\ &- 4\overline{\epsilon}_h(x,y)\\ &+ \overline{\epsilon}_h(x, y+2\Delta y)\\ &+ \overline{\epsilon}_h(x, y-2\Delta y)\Big],\end{aligned} \tag{G.19}$$

where the overbars indicate the errors after smoothing of the SWOT data with the same half-power filter cutoff wavelength of 10 km considered in Appendix G.2 for pre-processing of WaCM data. Whereas the errors ϵ_h of the pre-processed SWOT estimates of SSH were uncorrelated in (G.7c), the errors $\overline{\epsilon}_h$ of smoothed SSH are correlated.

Assuming that the error statistics are spatially homogeneous, the variance of the errors (G.19) of

smoothed geostrophically computed vorticity after grouping of terms is

$$\begin{aligned}\overline{\sigma}^2_{\zeta_g} = \frac{g^2}{f^2}\,\frac{\overline{\sigma}^2_h}{(4\Delta x^2)^2}\Big[&20 + \overline{\rho}_h(0,4\Delta y)\\ &+ 2\,\overline{\rho}_h(-2\Delta x, 2\Delta y)\\ &- 8\,\overline{\rho}_h(0,2\Delta y)\\ &+ 2\,\overline{\rho}_h(2\Delta x, 2\Delta y)\\ &+ \overline{\rho}_h(-4\Delta x, 0)\\ &- 8\,\overline{\rho}_h(-2\Delta x, 0)\\ &- 8\,\overline{\rho}_h(2\Delta x, 0)\\ &+ \overline{\rho}_h(4\Delta x, 0)\\ &+ 2\,\overline{\rho}_h(-2\Delta x, -2\Delta y)\\ &- 8\,\overline{\rho}_h(0, -2\Delta y)\\ &+ 2\,\overline{\rho}_h(2\Delta x, -2\Delta y)\\ &+ \overline{\rho}_h(0, -4\Delta y)\Big],\end{aligned}$$

where $\overline{\rho}_h(m\Delta x, n\Delta y)$ is the 2-dimensional lagged autocorrelation between the errors of smoothed SWOT estimates of SSH separated by $m\Delta x$ in the x dimension and $n\Delta y$ in the y dimension. The overbars on these lagged autocorrelations again indicate that they are based on the smoothed SWOT estimates of SSH. Because the 2-dimensional smoothing is applied isotropically, the lagged autocorrelations in the above expression are symmetric about zero lag and $\overline{\rho}_h(m\Delta x, n\Delta y)$ depends only on the radial distance $\left[(m\Delta x)^2 + (n\Delta y)^2\right]^{1/2}$. The variance of the smoothed geostrophically computed vorticity errors can then be written in terms of 1-dimensional lagged autocorrelations as

$$\begin{aligned}\overline{\sigma}^2_{\zeta_g} = \frac{g^2}{f^2}\,\frac{\overline{\sigma}^2_h}{(4\Delta x^2)^2}\Big[&20 + 2\,\overline{\rho}_h(4\Delta x)\\ &- 16\,\overline{\rho}_h(2\Delta x)\\ &+ 8\,\overline{\rho}_h(2\sqrt{\Delta x^2 + \Delta y^2})\\ &- 16\,\overline{\rho}_h(2\Delta y)\\ &+ 2\,\overline{\rho}_h(4\Delta y)\Big].\end{aligned} \tag{G.20}$$

For a uniform grid spacing $\Delta y = \Delta x$, this simplifies to

$$\begin{aligned}\overline{\sigma}^2_{\zeta_g} &= \frac{g^2}{f^2}\,\frac{\overline{\sigma}^2_h}{(4\Delta x^2)^2}\Big[20 + 4\,\overline{\rho}_h(4\Delta x)\\ &\qquad - 32\,\overline{\rho}_h(2\Delta x) + 8\,\overline{\rho}_h(2\sqrt{2}\Delta x)\Big]\\ &= \frac{\overline{\sigma}^2_h}{\sigma^2_h}\Big[1 + \frac{1}{5}\,\overline{\rho}_h(4\Delta x) - \frac{8}{5}\,\overline{\rho}_h(2\Delta x)\\ &\qquad + \frac{2}{5}\,\overline{\rho}_h(2\sqrt{2}\Delta x)\Big]\,\sigma^2_{\zeta_g},\end{aligned} \tag{G.21}$$

where $\sigma^2_{\zeta_g}$ is the variance (G.8) of the errors of unsmoothed SWOT estimates of ζ_g. As noted above in the derivation of (G.17b), $\overline{\sigma}^2_h/\sigma^2_h \approx 0.040$ for Parzen smoothing of the errors with a filter cutoff wavelength of 10 km. For the grid spacing $\Delta x = \Delta y = 1$ km of SWOT data, the autocorrelations of smoothed SSH at lags of 2 km, $2\sqrt{2} = 2.828$ km and 4 km are about 0.638, 0.403 and 0.155, respectively (see the bottom panel of

Fig. B1b). The variance (G.21) of vorticity estimates computed geostrophically from SWOT estimates of SSH smoothed using a Parzen smoother with a half-power filter cutoff wavelength of 10 km is therefore

$$\overline{\sigma}^2_{\zeta_g} = 0.00684\,\sigma^2_{\zeta_g}. \tag{G.22}$$

From (G.9), the variance of vorticity errors computed from unsmoothed SSH is $\sigma^2_{\zeta_g} = (3.43 \times 10^{-3}\ \mathrm{s}^{-1})^2$. The standard deviation of the errors of SWOT estimates of vorticity computed geostrophically from 10-km smoothed SSH is therefore

$$\overline{\sigma}_{\zeta_g} = 2.84 \times 10^{-4}\ \mathrm{s}^{-1}. \tag{G.23a}$$

At the central latitude 37°N of the CCS model domain where $f = 8.77 \times 10^{-5}\ \mathrm{s}^{-1}$, this is

$$\overline{\sigma}_{\zeta_g}(37°\mathrm{N}) = 3.23f. \tag{G.23b}$$

Smoothing the pre-processed SWOT estimates of SSH with the same half-power filter cutoff wavelength of 10 km that is planned for pre-processed WaCM estimates of surface velocity thus reduces the standard deviation (G.9) of geostrophically computed vorticity estimates by more than a factor of 12. The standard deviation (G.23) of these geostrophically computed SWOT estimates of vorticity is only slightly higher than the standard deviation (G.16) of WaCM estimates of vorticity computed from 10-km smoothed velocity estimates on a 1 km × 1 km grid.

Even with 10-km smoothing, the standard deviations of the errors of the estimates of velocity and vorticity from SWOT in (G.18) and (G.23) and from WaCM in (G.10) and (G.16) are much larger than the oceanographic signals of interest. Clearly, these errors must be further reduced with additional spatial and/or temporal smoothing. The effects of spatial smoothing on the variances of residual errors of SWOT and WaCM estimates of velocity components and vorticity are discussed in Sec. 4.3 (see Fig. 12).

Appendix H. The Filter Transfer Functions for Smoothed Centered Difference Estimates of Derivatives

The quantities of interest in this study of the resolution capabilities of SWOT and WaCM include variables that require spatial differentiation of the variables measured by the two instruments. In the case of SWOT, the SSH measurements must be differentiated once to estimate velocity components geostrophically and a second time to estimate vorticity geostrophically. In the case of WaCM, the surface velocity measurements must be differentiated once to obtain surface vorticity. These derivatives must be approximated from the discretely sampled data using finite difference methods. The effects of finite differencing on the wavenumber spectral content of the estimated derivative fields are quantified in this appendix, both from the pre-processed data and with subsequent spatial smoothing in ground-based post-processing.

The standard procedure for estimating derivatives $z'(x)$ from gridded values of a 1-dimensional variable $z(x)$ is from centered differences of $z(x)$ at the adjacent grid locations,

$$z'_{3pt}(x) = \frac{1}{2\Delta x}\Big[z(x+\Delta x) - z(x-\Delta x)\Big]. \tag{H.1}$$

This finite difference spans across three adjacent points, referred to as the stencil width of the derivative estimate. To distinguish this standard centered difference estimate of derivatives from the estimate considered below based on a stencil width of nine points, (H.1) will be referred to in this appendix as a 3-point centered difference. As this is a linear filter, it can be written in the form (A.1) of a convolution when applied to a continuous spatial series $z(x)$. For discrete sampling at an interval Δx, this convolution integral can be written as a discrete convolution but the equations in the analysis that follows become more cumbersome without providing any improved insight into the filtering properties of centered difference estimates of derivatives.

The filter weighting function in the convolution integral (A.1) for the 3-point centered difference filter (H.1) can be determined by the impulse response method (Bracewell, 1978), which gives

$$w_{3pt}(x) = \frac{1}{2\Delta x}\Big[\delta(x+\Delta x) - \delta(x-\Delta x)\Big], \tag{H.2}$$

where $\delta(x)$ is the Dirac delta, which can be visualized as having a value of infinity at $x = 0$ and zero elsewhere and unit area. The corresponding filter transfer function obtained analytically as the Fourier transform (A.2) of the filter weighting function (H.2) is

$$W_{3pt}(k) = \frac{1}{2\Delta x}\int_{-\infty}^{\infty}\Big[\delta(x+\Delta x)-\delta(x-\Delta x)\Big]\,e^{-i2\pi kx}\,dx.$$

Using the sifting property of the Dirac delta reduces this to

$$\begin{aligned} W_{3pt}(k) &= \frac{1}{2\Delta x}\left[e^{+i2\pi k\Delta x}-e^{-i2\pi k\Delta x}\right] \\ &= i\,\frac{\sin(2\pi k\Delta x)}{\Delta x}. \end{aligned} \tag{H.3a}$$

Substitution of Euler's formula $i = e^{i\pi/2}$ expresses the response function for 3-point centered differences in the standard form of $A\,e^{i\phi}$,

$$W_{3pt}(k) = \frac{\sin(2\pi k\Delta x)}{\Delta x}\,e^{i\pi/2}. \tag{H.3b}$$

The 3-point centered differencing thus introduces a quadrature phase shift of $\phi = \pi/2$ at each wavenumber k with an amplitude of $A = \sin(2\pi k\Delta x)/\Delta x$. This filter transfer function is more commonly referred to in the literature as the response function of the finite difference estimate of the derivative. The squared magnitude of the complex response function (H.3) is

$$\begin{aligned} \big|W_{3pt}(k)\big|^2 &= W^*_{3pt}(k)\,W_{3pt}(k) \\ &= \frac{\sin^2(2\pi k\Delta x)}{\Delta x^2}, \end{aligned} \tag{H.4}$$

where the asterisk denotes the complex conjugate.

For the pre-processing of SWOT and WaCM data with half-power filter cutoff wavelengths of 2 km and 10 km, respectively, the minimum gridding of the pre-processed data to avoid aliasing of the resolved variability (wavelengths longer than 2 km for SWOT and 10 km for WaCM) is 1 km for SWOT and 5 km for WaCM. We will therefore consider centered differences for these two choices of Δx.

The squared response function (H.4) is shown in log-log format in Fig. H1 by the thick and thin solid lines for the cases of $\Delta x = 1$ km and 5 km, respectively. It is assumed in this figure that there is no spectral power at wavenumbers higher than the Nyquist wavenumbers for the sample intervals of 1 km and 5 km, which are $k_{max} = 0.5$ cpkm and 0.1 cpkm, respectively. The response functions have therefore both been truncated at k_{max} in Fig. H1, thus eliminating irrelevant aliases of the response function. The squared response functions for both 3-point centered differences considered in Fig. H1 rise monotonically to a maximum of Δx^{-2} at a wavenumber of $k = (4\Delta x)^{-1}$ and then drop monotonically to zero at the respective Nyquist wavenumber $(2\Delta x)^{-1}$.

Although generally viewed as a high-pass filter, it can be seen from Fig. H1 that the response function for 3-point centered differences is actually a band-pass filter. [Note that the logarithmic abscissa in Fig. H1 distorts the $\sin^2$ dependence on wavenumber k in (H.4)]. The attenuation of variability at low wavenumbers is the 3-point centered difference representation of the squared filter transfer function $(2\pi k)^2$ of high-pass filtering from differentiation of a continuous variable $z(x)$, which is shown as the short dashed line in Fig. H1. The attenuation of the variability at the highest wavenumbers for 3-point centered difference estimates of the derivative arises from the smoothing implied by the differencing between grid points separated by $2\Delta x$. An undesirable characteristic of the 3-point centered difference filter is thus that the variability at the highest wavenumbers is attenuated compared with the squared filter transfer function $(2\pi k)^2$ of the true derivative. This high-wavenumber attenuation can be reduced and the overall accuracy of the derivative estimate can be improved by increasing the number of grid points that are used in the estimate, i.e., the stencil width of the derivative estimate (see, for example, Arbic et al., 2012).

The general centered difference estimate with a stencil width of M points can be written as

$$z'_{Mpt}(x) = \sum_{m=1}^{(M-1)/2} a_m \Big[z(x+m\Delta x) - z(x-m\Delta x) \Big], \tag{H.5}$$

where the weights a_m differ for each choice of M. For the centered differences (H.1) with a 3-point stencil, i.e., for $M = 3$, there is only one term in the sum (H.5) and the weight is $a_1 = (2\Delta x)^{-1}$. Stencil widths greater than $M = 9$ are seldom used in practice. The weights for estimates of the derivatives with a 9-point stencil (referred to in this appendix as 9-point centered differences) can be shown to be

$$a_1 = \frac{4}{5\Delta x} \tag{H.6a}$$

$$a_2 = -\frac{1}{5\Delta x} \tag{H.6b}$$

$$a_3 = \frac{4}{105\Delta x} \tag{H.6c}$$

$$a_4 = -\frac{1}{280\Delta x}. \tag{H.6d}$$

Analogous to the relationship between (H.1) and (H.3a) for the 3-point centered difference, the filter transfer function (response function) obtained by the impulse response method for the general M-point centered difference estimate (H.5) of the derivative is

$$W_{Mpt}(k) = 2\,i \sum_{m=1}^{(M-1)/2} a_m \sin(2\pi f m \Delta x). \tag{H.7}$$

For the case of $M = 3$, this reduces to (H.3a). The square of the response function (H.7) for 9-point centered difference estimates of the derivative is shown in Fig. H1 for the cases of $\Delta x = 1$ km and 5 km (the thick and thin dashed lines, respectively). Compared with the response functions for the standard 3-point centered differences, the 9-point stencils retain significantly more high-wavenumber variability of the true derivative shown by the short dashed line.

The disadvantage of stencils wider than $M = 3$ is that they have larger "edge effects." Because of missing terms in the summation (H.5), centered differences cannot be computed closer than $(M-1)/2$ points from the ends of the data record. This problem could be addressed by ratcheting down to successively narrower stencils at the ends of the data record, but the price paid for such a procedure is that the filter transfer function changes for each of the successively reduced stencils.

The degree to which it is advantageous to estimate derivatives using a wider stencil in this study depends on the subsequent processing of the derivative fields. The derivative variables of interest here are surface velocity and vorticity computed geostrophically from pre-processed SWOT estimates of SSH (the latter computed from second derivatives of SSH) and the vorticity computed from pre-processed WaCM estimates of surface velocity. It is shown in Secs. 6 and 8–10 that maps of these variables must be smoothed in ground-based post-processing to mitigate the effects of measurement errors.

The combined effects of centered differencing and smoothing on the wavenumber spectral content $S_{z'}(k)$ of a derivative variable $z'(x)$ can be expressed in terms of the product of the square of the response function (H.7) of the centered differencing and the squared filter transfer function of the smoother,

$$\overline{S}_{z'}(k) = \left|W_{Mpt}(k)\right|^2 \left|W_{k_c}(k)\right|^2 S_z(k), \tag{H.8a}$$

where $S_z(k)$ is the wavenumber spectrum of the pre-processed satellite data (SSH for SWOT and surface velocity components for WaCM), $W_{k_c}(k)$ is the filter transfer function of the particular choice of smoother

with a half-power filter cutoff wavenumber k_c, and $\overline{S}_{z'}(k)$ is the wavenumber spectrum of centered differences of smoothed values of the variable $z(x)$. For the Parzen smoother considered in detail in Appendix A, Appendix B and Appendix C, the filter transfer function $W_{k_c}(k)$ is given by (A.11) with a span L_4 that is related to k_c by (A.12a), $L_4 = 0.910\,k_c^{-1} \approx k_c^{-1}$. Since the Parzen smoother is symmetric and real, its transfer function is also symmetric and real. But from (H.3) and (H.7), the response function $W_{Mpt}(k)$ for centered differencing is complex. Then (H.8a) can be written as

$$\overline{S}_{z'}(k) = \left|W_{Mpt}(k)\right|^2 W_{k_c}^2(k)\, S_z(k). \tag{H.8b}$$

Examples of the filter transfer function $|W_{Mpt}(k)|^2\, W_{k_c}^2(k)$ for combined M-point centered differencing and spatial smoothing are shown in Fig. H2 for Parzen smoothing with half-power filter cutoff wavelengths of $\lambda_c = k_c^{-1} = 20$, 50 and 80 km (corresponding to wavenumbers of $k_c = 0.05$, 0.02 and 0.0125 cpkm, see Fig. C1) with 3-point and 9-point centered difference estimates of the derivatives for grid spacings of $\Delta x = 1$ km and 5 km (see Fig. H1). Several conclusions can be drawn from Fig. H2:

1. For the SWOT grid spacing of $\Delta x = 1$ km, the filter transfer functions for spatial smoothing combined with 3-point or 9-point centered differencing (the thick solid and thick dashed lines, respectively) are virtually indistinguishable for any of the choices of smoothing shown in Fig. H2. Since the signal-to-noise ratios for SWOT estimates of any of the derivative quantities of interest in this study are inadequate for smoothing with filter cutoff wavelengths less than 20 km, it can be concluded that the 9-point centered differencing offers no advantage over 3-point centered differencing for SWOT data on a 1 km × 1 km grid.
2. For a grid spacing of $\Delta x = 5$ km relevant to WaCM, the filter transfer functions for spatial smoothing combined with 3-point or 9-point centered differencing (the thin solid and thin dashed lines, respectively) differ significantly for $\lambda_c = 20$ km. Centered differencing with a stencil width of 9 points on a 5 km grid thus retains significantly more of the high-wavenumber content of the derivatives and therefore gives improved estimates of the derivatives with this choice of smoothing on a 5 km grid with $\lambda_c = 20$ km. The 9-point stencil offers a very slight improvement for $\lambda_c = 50$ km and no detectable improvement for $\lambda_c = 80$ km. It can be concluded that, for filter cutoff wavelengths $\lambda_c \lesssim 60$ km, it would be advantageous to use 9-point centered differencing if the pre-processed WaCM data are posted on a 5 km × 5 km grid.
3. Although gridding of pre-processed WaCM data on a 5 km × 5 km Nyquist-sampled grid is sufficient to avoid aliasing as discussed in Appendix B, the pre-processed data can be posted on a finer grid. While "oversampling" the WaCM data in this manner offers no advantage for mapping of the surface velocity components, it is evident from Fig. H2 that it is advantageous for mapping of the velocity component derivative fields from which vorticity is computed. This is seen for the case of $\lambda_c = 20$ km in the top panel of Fig. H2 from the fact that the combined effects of the filter transfer function of the smoother and the response functions for both 3-point and 9-point centered differences with $\Delta x = 1$ km (the thick solid and thick dashed lines) retain more of the high-wavenumber content of the derivatives than either 3-point or 9-point centered differences with $\Delta x = 5$ km (the thin solid and dashed lines). This implies that 3-point centered differencing of pre-processed WaCM data on an oversampled 1 km × 1 km grid (the thick solid line) gives better estimates of the derivatives than can be obtained even from 9-point centered differencing on the Nyquist-sampled 5 km × 5 km grid (the thin dashed line). For $\lambda_c \approx 40$ km (slightly shorter than the case of $\lambda_c = 50$ km shown in the middle panel of Fig. H2), the filter transfer functions for 3-point centered differences with $\Delta x = 1$ km are still slightly better than for 3-point centered differences with $\Delta x = 5$ km but become indistinguishable from 9-point centered differences with $\Delta x = 5$ km. For $\lambda_c \gtrsim 80$ km, all of the centered difference estimates of derivatives considered here give essentially equivalent results.

On the basis of the conclusions above deduced from Fig. H2, it is preferable for the purposes of WaCM estimates of small-scale vorticity signal variability to grid the pre-processed WaCM data on the same 1 km × 1 km grid as SWOT rather than on the 5 km × 5 km grid that satisfies Nyquist sampling of pre-processed WaCM data. Moreover, for both WaCM and SWOT, a 3-point stencil width for centered

differencing on the 1 km × 1 km grid is adequate for the filter cutoff wavelengths of $\lambda_c \gtrsim 20$ km that are relevant to signal estimation in the assessments of the resolution capability of derivative fields in Secs. 6 and 8–10.

The above conclusion that oversampling the WaCM data on a 1 km × 1 km grid is preferable to Nyquist sampling on a 5 km × 5 km grid was deduced from consideration of the effects of sampling and centered difference stencil width on preservation of the small-scale (high-wavenumber) signal contributions to the WaCM estimates of velocity component derivatives for calculation of vorticity. The same considerations apply to the error contributions to derivative estimates from WaCM data. Note, however, that the finer gridding accentuates the noise at high wavenumbers. For the case of white noise and red signal in the velocity measurements, it is preferable to attenuate the small-scale variability in the error field. The conflicting goals of signal preservation and noise suppression at high wavenumbers complicate the choice of the best gridding of the WaCM data for mapping of the vorticity field.

From simulations, we found that the noise suppression from 5 km × 5 km gridding is more beneficial than signal preservation in the signal-to-noise ratio of velocity component derivative fields smoothed with half-power filter cutoff wavelengths less than about 25 km. For larger smoothing scales, the advantage of signal preservation from 1 km × 1 km gridding is more beneficial. Since the analysis in Secs. 6 and 8–10 concludes that wavelength scales smaller than about 25 km cannot be adequately resolved in vorticity maps constructed from WaCM measurements of surface velocity,[11] oversampling on a 1 km × 1 km grid is preferable for the simulations presented in this study. A practical advantage of this oversampling is that the grid for simulated WaCM data then matches the 1 km × 1 km grid of the simulated SWOT data.

Appendix I. The Wavenumber Spectral Characteristics of the Errors of SWOT and WaCM Estimates of Velocity and Vorticity

Analytical expressions are derived in this appendix for the 1-dimensional wavenumber spectra of errors of estimates of each of the variables of interest in this study (SSH, two orthogonal velocity components and vorticity) based on the unsmoothed pre-processed estimates of SSH for SWOT and velocity for WaCM, as well as on SSH and velocity fields smoothed in ground-based post-processing. A noteworthy feature of the analysis is that the equation for each of the wavenumber spectra derived in this appendix is expressed in terms of the variance of the pre-processed data. The equations can therefore accommodate variances of the uncorrelated measurement errors (SSH for SWOT and surface velocity components for WaCM) that differ from the present baseline specifications.

In the case of SWOT, the relevant equations for the wavenumber spectra of unsmoothed fields are (I.2a), (I.5a), (I.10a) and (I.24a) for, respectively, the errors of SWOT estimates of SSH, the x and y components of geostrophically computed velocity and geostrophically computed vorticity. These equations are all expressed in terms of the variance σ_h^2 of the pre-processed SWOT estimate of SSH. The analogous equations for the wavenumber spectra of smoothed SWOT estimates of these variables are (I.29a), (I.31a), (I.33a) and (I.35b). The value of $\sigma_h^2 = (2.74 \text{ cm})^2$ that is derived in Appendix F is used in the applications of these equations in Sec. 4.4, but the above-referenced equations can be used for any specified value of σ_h^2.

A limitation of the formulas derived below for the wavenumber spectra of errors of geostrophically computed SWOT estimates of velocity and vorticity is that they require the use of a constant value of the Coriolis parameter f. The theoretical spectra for these errors that are shown in Figs. 13a, 13b and 14 are based on the value of $f = 8.77 \times 10^{-5}$ s^{-1} at the central latitude 37°N of the CCS model domain. Over the latitude range of the CCS model (see the left panel of Fig. 2a), f varies from 7.83×10^{-5} s^{-1} at the 32.5°N southern corner of the model domain to 9.76×10^{-5} s^{-1} at the 42°N northern corner of the model domain. Compared with its value at 37°N, the Coriolis parameter is 11% larger at 42°N and 11% smaller at 32.5°N. This small variation of f and the fact that f varies approximately linearly over the latitudinal range of the

[11] It can be seen from Figs. 44c and d that the resolution capability of vorticity maps constructed from WaCM data would exceed 25 km if the standard deviation of speed measurement errors could be reduced sufficiently to about 0.1 m s^{-1}. At the present time, such measurement accuracy does not seem technologically feasible.

CCS model domain result in negligibly small differences between the theoretical and empirical spectra that are based on the local value of f at each grid point (see Figs. 13a, 13b and 14).

In the case of WaCM, the relevant equations for the wavenumber spectra of the errors of unsmoothed velocity component and vorticity fields are, respectively, (I.40b) and (I.43), with the latter partitioned as (I.45b) and (I.46a). These equations are all expressed in terms of the variances σ_u^2 and σ_v^2 of the errors of WaCM estimates of the u and v components of velocity. The analogous equations for the wavenumber spectra of the errors of WaCM estimates of smoothed velocity component and vorticity fields are, respectively, (I.48a) and (I.52), with the latter partitioned as (I.54a) and (I.55a). A value of $\sigma_{u,v}^2 = (0.354 \text{ m s}^{-1})^2$ is used for both σ_u^2 and σ_v^2 in the application of these equations in Sec. 4.4, but the above-referenced equations can be used for any specified values of σ_u^2 and σ_v^2. This fact is used in Sec. 10.2 to determine how much the resolution capability of WaCM estimates of velocity and vorticity would improve if engineering efforts can reduce the measurement error variance $\sigma_{u,v}^2$.

Appendix I.1. Errors of SSH and Geostrophically Computed Velocity and Vorticity from Unsmoothed SWOT Data

The 2-dimensional wavenumber power spectral density of a spatially uncorrelated error field is constant at all wavenumbers k and l in the x and y dimensions, respectively, which correspond to the cross-shore and alongshore dimensions for the CCS model domain considered here. For the case of uncorrelated instrumental errors with variance σ_h^2 for SWOT estimates of SSH, this constant (white) power spectral density is related to σ_h^2 by Eq. (E.3) in Appendix E, which is repeated here for convenience,

$$S_h^{2d}(k,l) = \frac{\sigma_h^2}{4k_{\mathcal{N}} l_{\mathcal{N}}} = \Delta x \Delta y \, \sigma_h^2, \tag{I.1}$$

where $k_{\mathcal{N}} = (2\Delta x)^{-1}$ and $l_{\mathcal{N}} = (2\Delta y)^{-1}$ are the Nyquist wavenumbers for the sample intervals of Δx and Δy. The errors of pre-processed SWOT estimates of SSH obtained as summarized in Appendix B.1 by smoothing the raw SWOT data with a half-power filter cutoff wavelength of 2 km in each dimension are uncorrelated for a grid spacing of $\Delta x \times \Delta y = 1 \text{ km} \times 1 \text{ km}$. The variance of the errors of these pre-processed SWOT estimates of SSH that is derived in Appendix F is $\sigma_h^2 = (2.74 \text{ cm})^2$.

The 1-sided, 1-dimensional alongshore power spectral density of the errors of the pre-processed SWOT estimates of SSH is given by (E.4), which can be expressed in terms of σ_h^2 as[12]

$$\begin{aligned} S_h^{1d}(l) &= 2 \int_{-k_{\mathcal{N}}}^{k_{\mathcal{N}}} S_{ssh}^{2d}(k,l) \, dk \\ &= 4\Delta x \Delta y \, k_{\mathcal{N}} \, \sigma_h^2 \\ &= 2\Delta y \, \sigma_h^2. \end{aligned} \tag{I.2a}$$

For $\sigma_h^2 = (2.74 \text{ cm})^2$, the 1-dimensional alongshore spectrum (I.2a) of SSH measurement errors in the baseline design is

$$S_h^{1d}(l) = 15.0 \text{ cm}^2/\text{cpkm}. \tag{I.2b}$$

The 2-dimensional wavenumber spectrum of the errors of cross-shore velocity u_g computed geostrophically from centered differences of the errors of pre-processed SWOT estimates of SSH can be determined analytically from the 2-dimensional spectrum (I.1) of SWOT SSH measurement errors by

$$\begin{aligned} S_{u_g}^{2d}(k,l) &= \frac{g^2}{f^2} \left|W_{3pt}(l)\right|^2 S_h^{2d}(k,l) \\ &= \frac{g^2}{f^2} \, \Delta x \Delta y \, \sigma_h^2 \left|W_{3pt}(l)\right|^2, \end{aligned} \tag{I.3}$$

[12] As noted in footnotes 5 and 8, the spectral values at wavenumbers $l = 0$ and $l_{\mathcal{N}}$ are not doubled in the 1-sided, 1-dimensional spectrum. In the interest of clarity in the analysis that follows, this technical detail will again be ignored as in Appendix D and Appendix E.

where $W_{3pt}(l)$ is the response function for the alongshore derivative in the geostrophic relation $u_g = -gf^{-1}\partial h/\partial y$ estimated from alongshore centered differences with a 3-point stencil width. It is shown in Appendix H that $W_{3pt}(l)$ is given by (H.3a), which is repeated here for convenience,

$$W_{3pt}(l) = i\,\frac{\sin(2\pi\Delta y\, l)}{\Delta y}. \tag{I.4}$$

The 1-sided, 1-dimensional alongshore spectrum of u_g errors obtained from the 2-dimensional spectrum (I.3) as in (I.2a) by integrating over all cross-shore wavenumbers k and doubling the power at each wavenumber l is

$$\begin{aligned} S^{1d}_{u_g}(l) &= 2\int_{-k_\mathcal{N}}^{k_\mathcal{N}} S^{2d}_{u_g}(k,l)\,dk \\ &= \frac{g^2}{f^2}\,2\Delta y\,\sigma_h^2\;|W_{3pt}(l)|^2 \qquad \text{(I.5a)} \\ &= \frac{g^2}{f^2}\;|W_{3pt}(l)|^2\,S^{1d}_h(l), \qquad \text{(I.5b)} \end{aligned}$$

where $|W_{3pt}(l)|^2 = \Delta y^{-2}\sin^2(2\pi\Delta y\, l)$ is the squared magnitude of (I.4). The form (I.5b) for $S^{1d}_{u_g}(l)$ follows from (I.2a).

The wavenumber spectrum of the errors of alongshore velocity v_g computed geostrophically from the errors of pre-processed SWOT estimates of SSH can be determined analytically following a procedure similar to that used above for the wavenumber spectrum of the errors of the cross-shore geostrophically computed velocity u_g. In this case, however, the cross-shore derivative in the geostrophic relation $v_g = gf^{-1}\partial h/\partial x$ is estimated by centered differences with a 3-point stencil in the cross-shore direction, rather than in the alongshore direction. The response function for these cross-shore centered differences is the same as (I.4), except with alongshore grid spacing Δy and wavenumber l replaced with their cross-shore counterparts Δx and k,

$$W_{3pt}(k) = i\,\frac{\sin(2\pi\Delta x\, k)}{\Delta x}. \tag{I.6}$$

The 2-dimensional wavenumber spectrum of v_g errors obtained from cross-shore centered differences of the pre-processed SSH errors is thus related to the 2-dimensional spectrum (I.1) of SWOT SSH measurement errors by

$$\begin{aligned} S^{2d}_{v_g}(k,l) &= \frac{g^2}{f^2}\;|W_{3pt}(k)|^2\,S^{2d}_h(k,l) \\ &= \frac{g^2}{f^2}\,\Delta x\Delta y\,\sigma_h^2\;|W_{3pt}(k)|^2\,. \end{aligned} \tag{I.7}$$

The 1-sided, 1-dimensional alongshore spectrum of the errors of geostrophically computed alongshore velocity v_g is

$$\begin{aligned} S^{1d}_{v_g}(l) &= 2\int_{-k_\mathcal{N}}^{k_\mathcal{N}} S^{2d}_{v_g}(k,l)\,dk \\ &= \frac{g^2}{f^2}\,4\Delta x\Delta y\,\sigma_h^2\int_0^{k_\mathcal{N}} |W_{3pt}(k)|^2\;dk \qquad \text{(I.8a)} \\ &= \frac{g^2}{f^2}\,2\Delta x\,S^{1d}_h(l)\int_0^{k_\mathcal{N}} |W_{3pt}(k)|^2\;dk. \qquad \text{(I.8b)} \end{aligned}$$

The last expression follows from (I.2a) and both forms for $S^{1d}_{v_g}(l)$ use the fact that $|W_{3pt}(k)|^2$ is symmetric about $k = 0$. With the definition (I.6) of $W_{3pt}(k)$ and the transformation of variables $k' = 2\pi\Delta x\, k$, the

integral on the right sides of (I.8a) and (I.8b) is

$$\int_0^{k_{\mathcal{N}}} |W_{3pt}(k)|^2 \, dk = \frac{1}{2\pi\Delta x^3} \int_0^{\pi} \sin^2(k') \, dk' = \frac{1}{4\Delta x^3}. \tag{I.9}$$

Then (I.8a) and (I.8b) become

$$S^{1d}_{v_g}(l) = \frac{g^2}{f^2} \frac{\Delta y}{\Delta x^2} \sigma_h^2 \tag{I.10a}$$

$$= \frac{g^2}{f^2} \frac{1}{2\Delta x^2} S^{1d}_h(l). \tag{I.10b}$$

The expression (G.7b) in Appendix G for the errors of ζ_g in terms of finite differences of the uncorrelated errors of pre-processed SWOT estimates of SSH can be written as

$$\epsilon_{\zeta_g}(x,y) = \epsilon_1(x,y) + \epsilon_2(x,y) + \epsilon_3(x,y) + \epsilon_4(x,y), \tag{I.11}$$

where

$$\epsilon_1(x,y) = \frac{g}{f} \frac{1}{2\Delta x} \frac{\epsilon_h(x+2\Delta x,y) - \epsilon_h(x,y)}{2\Delta x} \tag{I.12a}$$

$$\epsilon_2(x,y) = -\frac{g}{f} \frac{1}{2\Delta x} \frac{\epsilon_h(x,y) - \epsilon_h(x-2\Delta x,y)}{2\Delta x} \tag{I.12b}$$

$$\epsilon_3(x,y) = \frac{g}{f} \frac{1}{2\Delta y} \frac{\epsilon_h(x,y+2\Delta y) - \epsilon_h(x,y)}{2\Delta y} \tag{I.12c}$$

$$\epsilon_4(x,y) = -\frac{g}{f} \frac{1}{2\Delta y} \frac{\epsilon_h(x,y) - \epsilon_h(x,y-2\Delta y)}{2\Delta y}. \tag{I.12d}$$

The contributions $\epsilon_1(x,y)$ and $\epsilon_2(x,y)$ correspond to centered cross-shore differences of SSH errors at $(x+\Delta x, y)$ and $(x-\Delta x, y)$, respectively. Similarly, the contributions $\epsilon_3(x,y)$ and $\epsilon_4(x,y)$ correspond to centered alongshore differences of SSH errors at $(x, y+\Delta y)$ and $(x, y-\Delta y)$, respectively.

It was shown in Appendix H that 1-dimensional centered differences can be written as convolution integrals. For the 2-dimensional fields considered here, centered cross-shore differences at (x,y) can be written as the convolution

$$\frac{\epsilon_h(x+\Delta x,y) - \epsilon_h(x-\Delta x,y)}{2\Delta x} = w_{3pt}(x) * \epsilon_h(x,y), \tag{I.13a}$$

where, analogous to (H.2), the filter weighting function for a 2-dimensional field of SSH errors is

$$w_{3pt}(x) = \frac{1}{2\Delta x}\Big[\delta(x+\Delta x,y) - \delta(x-\Delta x,y)\Big]. \tag{I.13b}$$

The similar expression for centered alongshore differences at (x, y) is

$$\frac{\epsilon_h(x, y + \Delta y) - \epsilon_h(x, y - \Delta y)}{2\Delta y} = w_{3pt}(y) * \epsilon_h(x, y), \tag{I.14a}$$

where

$$w_{3pt}(y) = \frac{1}{2\Delta y}\Big[\delta(x, y + \Delta y) - \delta(x, y - \Delta y)\Big]. \tag{I.14b}$$

The response functions (filter transfer functions) obtained as in (H.3a) as the Fourier transforms of (I.13b) and (I.14b) are given by (I.6) and (I.4), respectively,

The four contributions (I.12a)–(I.12d) to $\epsilon_{\zeta_g}(x, y)$ can be written as shifted convolution integrals similar to (I.13a) and (I.14a),

$$\epsilon_1(x, y) = \frac{g}{f}\,\frac{1}{2\Delta x}\, w_{3pt}(x - \Delta x) * \epsilon_h(x, y) \tag{I.15a}$$

$$\epsilon_2(x, y) = -\frac{g}{f}\,\frac{1}{2\Delta x}\, w_{3pt}(x + \Delta x) * \epsilon_h(x, y) \tag{I.15b}$$

$$\epsilon_3(x, y) = \frac{g}{f}\,\frac{1}{2\Delta y}\, w_{3pt}(y - \Delta y) * \epsilon_h(x, y) \tag{I.15c}$$

$$\epsilon_4(x, y) = -\frac{g}{f}\,\frac{1}{2\Delta y}\, w_{3pt}(y + \Delta y) * \epsilon_h(x, y). \tag{I.15d}$$

The weighting functions on the right sides of (I.15a) and (I.15b) are cross-shore-shifted versions of the weighting function (I.13b) of centered cross-shore differences at (x, y). Likewise, the weighting functions on the right sides of (I.15c) and (I.15d) are alongshore-shifted versions of the weighting function (I.14b) of centered alongshore differences at (x, y). By the Shift Theorem, the Fourier transforms of these shifted weighting functions are

$$\mathcal{F}\left[w_{3pt}(x \pm \Delta x)\right] = e^{\pm i2\pi\Delta x\, k} W_{3pt}(k) \tag{I.16}$$

$$\mathcal{F}\left[w_{3pt}(y \pm \Delta y)\right] = e^{\pm i2\pi\Delta y\, l} W_{3pt}(l), \tag{I.17}$$

where $\mathcal{F}$ indicates the Fourier transform and $W_{3pt}(k)$ and $W_{3pt}(l)$ are given by (I.6) and (I.4). The shifted weighting functions in the convolution integrals (I.15a)–(I.15d) thus result in phase rotations of the Fourier transforms $W_{3pt}(k)$ and $W_{3pt}(l)$.

The results above can be used to determine the Fourier transform of the vorticity errors (I.11). This Fourier transform can be written as the sum of the Fourier transforms of each of the four terms on the right side of (I.11),

$$\mathcal{F}\left[\zeta_g(k, l)\right] = \mathcal{F}_1(k, l) + \mathcal{F}_2(k, l) + \mathcal{F}_3(k, l) + \mathcal{F}_4(k, l). \tag{I.18}$$

By the Convolution Theorem and the response functions (I.16) and (I.17) of the shifted centered differences, the four Fourier transforms on the right side of (I.18) are

$$\mathcal{F}_1(k, l) = \frac{g}{f}\,\frac{1}{2\Delta x} e^{i2\pi\Delta x\, k}\, W_{3pt}(k)\mathcal{F}\left[h(k, l)\right] \tag{I.19a}$$

$$\mathcal{F}_2(k, l) = -\frac{g}{f}\,\frac{1}{2\Delta x} e^{-i2\pi\Delta x\, k}\, W_{3pt}(k)\mathcal{F}\left[h(k, l)\right] \tag{I.19b}$$

$$\mathcal{F}_3(k,l) = \frac{g}{f}\,\frac{1}{2\Delta y} e^{i2\pi\Delta y\, l}\, W_{3pt}(l)\mathcal{F}\left[h(k,l)\right] \tag{I.19c}$$

$$\mathcal{F}_4(k,l) = -\,\frac{g}{f}\,\frac{1}{2\Delta y} e^{-i2\pi\Delta y\, l}\, W_{3pt}(l)\mathcal{F}\left[h(k,l)\right], \tag{I.19d}$$

where $\mathcal{F}\left[h(k,l)\right]$ is the Fourier transform of the SSH errors. Then (I.18) becomes

$$\begin{aligned}
&\mathcal{F}\left[\zeta_g(k,l)\right] \\
&= \frac{g}{f}\,\mathcal{F}\left[h(k,l)\right]\left[\left(\frac{e^{i2\pi\Delta x\, k} - e^{-i2\pi\Delta x\, k}}{2\Delta x}\right) W_{3pt}(k)\right. \\
&\qquad \left. + \left(\frac{e^{i2\pi\Delta y\, l} - e^{-i2\pi\Delta y\, l}}{2\Delta y}\right) W_{3pt}(l)\right] \\
&= i\,\frac{g}{f}\,\mathcal{F}\left[h(k,l)\right]\left[\frac{\sin(2\pi\Delta x\, k)}{\Delta x} W_{3pt}(k)\right. \\
&\qquad \left. + \frac{\sin(2\pi\Delta y\, l)}{\Delta y} W_{3pt}(l)\right] \\
&= -\,\frac{g}{f}\,\mathcal{F}\left[h(k,l)\right]\left[|W_{3pt}(k)|^2 + |W_{3pt}(l)|^2\right].
\end{aligned} \tag{I.20}$$

The last relation follows from (I.6) and (I.4).

The 2-dimensional power spectral density of the errors of SWOT estimates of vorticity obtained as the squared magnitude of the Fourier transform (I.20) is related to the power spectral density (I.1) of the SSH errors by

$$\begin{aligned}
&S^{2d}_{\zeta_g}(k,l) \\
&= \frac{g^2}{f^2}\, S^{2d}_h(k,l)\left[|W_{3pt}(k)|^4\right. \\
&\qquad \left. + 2\,|W_{3pt}(k)|^2\,|W_{3pt}(l)|^2 + |W_{3pt}(l)|^4\right]
\end{aligned} \tag{I.21a}$$

$$\begin{aligned}
&= \frac{g^2}{f^2}\,\Delta x\Delta y\,\sigma_h^2\left[|W_{3pt}(k)|^4\right. \\
&\qquad \left. + 2\,|W_{3pt}(k)|^2\,|W_{3pt}(l)|^2 + |W_{3pt}(l)|^4\right]
\end{aligned} \tag{I.21b}$$

The 1-sided, 1-dimensional alongshore spectrum of the errors of SWOT estimates of ζ_g is

$$\begin{aligned}
S^{1d}_{\zeta_g}(l) &= 2\int_{-k_{\mathcal{N}}}^{k_{\mathcal{N}}} S^{2d}_{\zeta_g}(k,l)\,dk \\
&= \frac{g^2}{f^2}\,2\Delta x\Delta y\,\sigma_h^2\left(2\int_0^{k_{\mathcal{N}}} |W_{3pt}(k)|^4\,dk\right. \\
&\qquad + 4\,|W_{3pt}(l)|^2\int_0^{k_{\mathcal{N}}} |W_{3pt}(k)|^2\,dk \\
&\qquad \left. + \frac{1}{\Delta x}\,|W_{3pt}(l)|^4\right),
\end{aligned} \tag{I.22}$$

where $k_{\mathcal{N}} = (2\Delta x)^{-1}$ is again the Nyquist wavenumber in the x dimension. The expression (I.22) uses the fact that $|W_{3pt}(k)|^2$ and $|W_{3pt}(k)|^4$ are both symmetric about $k = 0$. The second term on the right side of

(I.22) is the cross spectral term that arises from the fact that all four contributions (I.12) to the vorticity errors (I.11) are cross correlated since they share in common the SSH error $\epsilon_h(x, y)$.

The second integral on the right side of (I.22) is given by (I.9). With the same transformation of variables $k' = 2\pi\Delta x\, k$ that was used in (I.9), the first integral is

$$\int_0^{k_{\mathcal{N}}} |W_{3pt}(k)|^4 \, dk = \frac{1}{2\pi\Delta x^5} \int_0^{\pi} \sin^4(k') \, dk' = \frac{3}{16\Delta x^5}. \tag{I.23}$$

Then (I.22) becomes

$$S^{1d}_{\zeta_g}(l) = \frac{g^2}{f^2}\, 2\Delta y\, \sigma_h^2 \bigg(\frac{3}{8\Delta x^4} + \frac{1}{\Delta x^2} |W_{3pt}(l)|^2 + |W_{3pt}(l)|^4 \bigg) \tag{I.24a}$$

$$= \frac{g^2}{f^2}\, S^{1d}_h(l) \bigg(\frac{3}{8\Delta x^4} + \frac{1}{\Delta x^2} |W_{3pt}(l)|^2 + |W_{3pt}(l)|^4 \bigg), \tag{I.24b}$$

where $S^{1d}_h(l)$ is the 1-sided, 1-dimensional alongshore spectrum (I.2a) of the SSH errors.

The analytical expressions (I.2a), (I.5a), (I.10a) and (I.24a) for the 1-sided, 1-dimensional alongshore spectra of errors of the pre-processed SWOT estimates of SSH and the two velocity components and the vorticity computed geostrophically from the pre-processed SWOT data are shown for $\sigma_h^2 = (2.74 \text{ cm})^2$ by the solid green lines in Fig. 13a.

Appendix I.2. Errors of SSH and Geostrophically Computed Velocity and Vorticity from Smoothed SWOT Data

The errors of SWOT estimates of velocity and vorticity computed geostrophically from the pre-processed SWOT estimates of SSH (see Appendix G and Table 1 in Sec. 4 and the maps in the bottom left panels of Figs. 17b and 17c) are too large for the velocity and vorticity estimates to be scientifically useful. It will be necessary to estimate velocity and vorticity geostrophically from SWOT SSH fields that have been smoothed in ground-based post-processing.

Throughout this study, we use isotropic filtering with $k_c = l_c = \lambda_c^{-1}$, where k_c and l_c are the half-power filter cutoff wavenumbers in the x and y dimensions, respectively, and λ_c is the desired isotropic half-power filter cutoff wavelength in km. It is shown in Appendix C that separate 1-dimensional filtering in each dimension using the Parzen smoother is essentially equivalent to isotropic smoothing with a 2-dimensional Parzen smoother that depends only on radial distance from the estimation location. This equivalence facilitates the derivation of the theoretical wavenumber spectra of errors in this appendix. For a desired filter cutoff wavelength of λ_c, the span of the Parzen smoother in each dimension as given by (A.12b) in Appendix A is $L_4 = 0.910\, \lambda_c \approx \lambda_c$. The filter transfer function of the Parzen smoother in the x dimension, for example, is given by (A.11), which can be written in terms of the half-power filter cutoff wavelength λ_c as

$$W_{\lambda_c}(k) = \text{sinc}^4\left(\frac{kL_4}{4}\right) \approx \text{sinc}^4\left(\frac{k\lambda_c}{4}\right) = \left(\frac{\sin(\pi k\lambda_c/4)}{\pi k\lambda_c/4}\right)^4. \tag{I.25}$$

The 2-dimensional wavenumber spectrum of 2-dimensionally smoothed SSH measurement errors is obtained from the 2-dimensional wavenumber spectrum (I.1) of uncorrelated errors of the pre-processed SWOT estimates of SSH by

$$\begin{aligned}\overline{S}_h^{2d}(k,l) &= W_{\lambda_c}^2(k)\, W_{\lambda_c}^2(l)\, S_h^{2d}(k,l) \\ &= \Delta x \Delta y\, \sigma_h^2\, W_{\lambda_c}^2(k)\, W_{\lambda_c}^2(l),\end{aligned} \tag{I.26}$$

where σ_h^2 is the variance of the SSH measurement errors. The overbar distinguishes the 2-dimensional spectrum $\overline{S}_h^{2d}(k,l)$ of smoothed SSH measurement errors from the 2-dimensional spectrum (I.1) of unsmoothed errors. The 1-sided, 1-dimensional alongshore spectrum of the smoothed SSH measurement errors is

$$\begin{aligned}\overline{S}_h^{1d}(l) &= 2\int_{-k_{\mathcal{N}}}^{k_{\mathcal{N}}} \overline{S}_h^{2d}(k,l)\, dk \\ &= 4\Delta x \Delta y\, \sigma_h^2\, W_{\lambda_c}^2(l) \int_0^{k_{\mathcal{N}}} W_{\lambda_c}^2(k)\, dk.\end{aligned} \tag{I.27}$$

The right side of this equation uses the fact that $W_{\lambda_c}^2(k)$ is symmetric about $k = 0$.

For the Parzen smoother used in this study, it is shown in Appendix D that the integral of the associated squared filter transfer function on the right side of (I.27) is given by (D.12b), which can be written as

$$\int_0^{k_{\mathcal{N}}} W_{\lambda_c}^2(k)\, dk = L_4 = \frac{1}{0.910\, \lambda_c} \approx \lambda_c^{-1}. \tag{I.28}$$

The 1-dimensional wavenumber spectrum (I.27) of smoothed SSH measurement errors is therefore given approximately by

$$\overline{S}_h^{1d}(l) = \frac{4\Delta x \Delta y\, \sigma_h^2}{\lambda_c}\, W_{\lambda_c}^2(l) \tag{I.29a}$$

$$= \frac{2\Delta x}{\lambda_c}\, W_{\lambda_c}^2(l)\, S_h^{1d}(l), \tag{I.29b}$$

where $S_h^{1d}(l)$ is the 1-sided, 1-dimensional alongshore spectrum (I.2a) of the SSH errors. As discussed in Appendix E, the multiplication factor $W_{\lambda_c}^2(l)$ represents the low-pass filtering in the alongshore dimension that attenuates the spectral power $S_h^{1d}(l)$ at high wavenumbers and the multiplicative factor $2\Delta x \lambda_c^{-1}$ represents the additional attenuation of the spectral power $S_h^{1d}(l)$ at all wavenumbers from the low-pass filtering in the cross-shore dimension.

The 2-dimensional wavenumber spectrum of the errors of the geostrophically computed cross-shore velocity u_g estimated from centered alongshore differences of the smoothed SSH errors is obtained analogously to (I.3), except from the 2-dimensional spectrum (I.26) of smoothed SSH,

$$\begin{aligned}&\overline{S}_{u_g}^{2d}(k,l) \\ &\quad = \frac{g^2}{f^2}\, |W_{3pt}(l)|^2\, \overline{S}_h^{2d}(k,l) \\ &\quad = \frac{g^2}{f^2}\, \Delta x \Delta y\, \sigma_h^2\, W_{\lambda_c}^2(k)\, W_{\lambda_c}^2(l)\, |W_{3pt}(l)|^2\,.\end{aligned} \tag{I.30}$$

The 1-sided, 1-dimensional alongshore spectrum of the errors of smoothed cross-shore geostrophically computed velocity u_g is

$$\begin{aligned}&\overline{S}_{u_g}^{1d}(l) \\ &\quad = 2\int_{-k_{\mathcal{N}}}^{k_{\mathcal{N}}} \overline{S}_{u_g}^{2d}(k,l)\, dk \\ &\quad = \frac{g^2}{f^2}\, 4\Delta x \Delta y\, \sigma_h^2\, W_{\lambda_c}^2(l)\, |W_{3pt}(l)|^2 \int_0^{k_{\mathcal{N}}} W_{\lambda_c}^2(k)\, dk.\end{aligned}$$

Subsitution of (I.28) for the integral on the right side of this equation gives

$$\overline{S}^{1d}_{u_g}(l) = \frac{g^2}{f^2}\,\frac{4\Delta x\Delta y\,\sigma_h^2}{\lambda_c}\,W^2_{\lambda_c}(l)\,|W_{3pt}(l)|^2\,. \tag{I.31a}$$

From (I.29a), this can be written alternatively in terms of the 1-dimensional alongshore spectrum $\overline{S}^{1d}_h(l)$ of smoothed SSH measurement errors,

$$\overline{S}^{1d}_{u_g}(l) = \frac{g^2}{f^2}\,\overline{S}^{1d}_h(l)\,|W_{3pt}(l)|^2\,, \tag{I.31b}$$

where $\overline{S}^{1d}_h(l)$ can be expressed in terms of the 1-dimensional alongshore spectrum $S^{1d}_h(l)$ of the unsmoothed SSH measurement errors by (I.29b).

The 2-dimensional wavenumber spectrum of the errors of geostrophically computed alongshore velocity v_g estimated from centered cross-shore differences of the smoothed SSH errors is obtained analogously to (I.7), except from the 2-dimensional spectrum (I.26) of smoothed SSH,

$$\begin{aligned}
&\overline{S}^{2d}_{v_g}(k,l)\\
&\quad= \frac{g^2}{f^2}\,|W_{3pt}(k)|^2\,\overline{S}^{2d}_h(k,l)\\
&\quad= \frac{g^2}{f^2}\,\Delta x\Delta y\,\sigma_h^2\,W^2_{\lambda_c}(k)\,W^2_{\lambda_c}(l)\,|W_{3pt}(k)|^2\,.
\end{aligned} \tag{I.32}$$

The 1-sided, 1-dimensional alongshore spectrum of the errors of smoothed alongshore geostrophically computed velocity v_g is

$$\begin{aligned}
&\overline{S}^{1d}_{v_g}(l)\\
&\quad= 2\int_{-k_{\mathcal{N}}}^{k_{\mathcal{N}}}\overline{S}^{2d}_{v_g}(k,l)\,dk\\
&\quad= \frac{g^2}{f^2}\,4\Delta x\Delta y\,\sigma_h^2\,W^2_{\lambda_c}(l)\int_0^{k_{\mathcal{N}}}W^2_{\lambda_c}(k)\,|W_{3pt}(k)|^2\,dk.
\end{aligned} \tag{I.33a}$$

From (I.29a), this can be written alternatively in terms of the 1-dimensional alongshore spectrum $\overline{S}^{1d}_h(l)$ of smoothed SSH measurement errors,

$$\begin{aligned}
&\overline{S}^{1d}_{v_g}(l)\\
&\quad= \frac{g^2\lambda_c}{f^2}\,\overline{S}^{1d}_h(l)\int_0^{k_{\mathcal{N}}}W^2_{\lambda_c}(k)\,|W_{3pt}(k)|^2\,dk,
\end{aligned} \tag{I.33b}$$

where $\overline{S}^{1d}_h(l)$ can again be expressed in terms of the 1-dimensional alongshore spectrum $S^{1d}_h(l)$ of the unsmoothed SSH measurement errors by (I.29b). With $W_{3pt}(k)$ and $W_{\lambda_c}(k)$ defined by (I.6) and (I.25), there does not appear to be an analytical solution for the integral on the right sides of (I.33a) and (I.33b). The integral must therefore be evaluated numerically. The result is shown as a function of the half-power filter cutoff wavelength λ_c in Fig. I1a.

The 2-dimensional wavenumber spectrum of the errors of geostrophically computed vorticity estimated from finite differences of the smoothed SSH errors is obtained analogously to (I.21a), except from the 2-dimensional spectrum (I.26) of smoothed SSH,

$$\overline{S}^{2d}_{\zeta_g}(k,l)$$

$$= \frac{g^2}{f^2}\,\overline{S}_h^{2d}(k,l)\Big[|W_{3pt}(k)|^4 + 2\,|W_{3pt}(k)|^2\,|W_{3pt}(l)|^2 + |W_{3pt}(l)|^4\Big] \tag{I.34a}$$

$$= \frac{g^2}{f^2}\,\Delta x\Delta y\,\sigma_h^2\,W_{\lambda_c}^2(k)W_{\lambda_c}^2(l)\Big[|W_{3pt}(k)|^4 + 2\,|W_{3pt}(k)|^2\,|W_{3pt}(l)|^2 + |W_{3pt}(l)|^4\Big]. \tag{I.34b}$$

The 1-sided, 1-dimensional alongshore spectrum of the errors of smoothed geostrophically computed vorticity errors is

$$\begin{aligned}
&\overline{S}_{\zeta_g}^{1d}(l) \\
&= 2\int_{-k_{\mathcal{N}}}^{k_{\mathcal{N}}} \overline{S}_{\zeta_g}^{2d}(k,l)\,dk \\
&= \frac{g^2}{f^2}\,2\Delta x\Delta y\,\sigma_h^2\,W_{\lambda_c}^2(l) \\
&\quad\Big[2\int_0^{k_{\mathcal{N}}} W_{\lambda_c}^2(k)\,|W_{3pt}(k)|^4\,dk \\
&\qquad + 4\,|W_{3pt}(l)|^2\int_0^{k_{\mathcal{N}}} W_{\lambda_c}^2(k)\,|W_{3pt}(k)|^2\,dk \\
&\qquad + 2\,|W_{3pt}(l)|^4\int_0^{k_{\mathcal{N}}} W_{\lambda_c}^2(k)\,dk\Big].
\end{aligned} \tag{I.35a}$$

The third integral on the right side of (I.35a) is approximately λ_c^{-1} according to (I.28). Then (I.35a) can be expressed as

$$\begin{aligned}
&\overline{S}_{\zeta_g}^{1d}(l) \\
&= \frac{g^2}{f^2}\,\frac{4\Delta x\Delta y\,\sigma_h^2}{\lambda_c}\,W_{\lambda_c}^2(l) \\
&\quad\Big[\lambda_c\int_0^{k_{\mathcal{N}}} W_{\lambda_c}^2(k)\,|W_{3pt}(k)|^4\,dk \\
&\qquad + 2\lambda_c\,|W_{3pt}(l)|^2\int_0^{k_{\mathcal{N}}} W_{\lambda_c}^2(k)\,|W_{3pt}(k)|^2\,dk \\
&\qquad + |W_{3pt}(l)|^4\Big].
\end{aligned} \tag{I.35b}$$

From (I.29a), this can be written alternatively in terms of the 1-dimensional alongshore spectrum $\overline{S}_h^{1d}(l)$ of smoothed SSH measurement errors,

$$\begin{aligned}
&\overline{S}_{\zeta_g}^{1d}(l) \\
&= \frac{g^2}{f^2}\,\overline{S}_h^{1d}(l)\Big[\lambda_c\int_0^{k_{\mathcal{N}}} W_{\lambda_c}^2(k)\,|W_{3pt}(k)|^4\,dk \\
&\qquad + 2\lambda_c\,|W_{3pt}(l)|^2\int_0^{k_{\mathcal{N}}} W_{\lambda_c}^2(k)\,|W_{3pt}(k)|^2\,dk \\
&\qquad + |W_{3pt}(l)|^4\Big],
\end{aligned} \tag{I.35c}$$

where $\overline{S}_h^{1d}(l)$ can again be expressed in terms of the 1-dimensional alongshore spectrum $S_h^{1d}(l)$ of the unsmoothed SSH measurement errors by (I.29b). The second integral on the right sides of (I.35b) and (I.35c) is the same integral that appears on the right sides of (I.33a) and (I.33b) for which the solution obtained numerically is shown as a function of the half-power filter cutoff wavelength λ_c in Fig. I1a. The numerical solution for the first integral on the right sides of (I.35b) and (I.35c) is shown as a function of the λ_c in Fig. I1b. It is apparent from Figs. I1a and I1b that the value of the first integral decreases with increasing λ_c much more quickly than the value of the second integral.

The analytical expressions (I.29a), (I.31a), (I.33a) and (I.35b) for the 1-sided, 1-dimensional alongshore spectra of the residual errors of SWOT estimates of SSH and geostrophically computed velocity components and vorticity after smoothing in ground-based post-processing of the pre-processed SWOT data are applicable to any low-pass filter with a half-power filter cutoff wavelength of λ_c. The results based on the Parzen smoother are shown for $\sigma_h^2 = (2.74 \text{ cm})^2$ by the solid green lines in Fig. 13b for a half-power filter cutoff wavelength of $\lambda_c = 10$ km and in Fig. 14 for half-power filter cutoff wavelengths of $\lambda_c = 20$, 50 and 80 km. The theoretical spectra in these figures agree very well with the spectra shown iin Figs. 13b and 14 by the solid blue lines that were computed empirically from the simulated SWOT error fields generated for the analysis in Secs. 6 and 8.

Appendix I.3. Errors of Pre-Processed WaCM Estimates of Velocity and Vorticity

The baseline design for the errors of the speeds of WaCM estimates of surface ocean velocity is for isotropic smoothing of the raw WaCM data in pre-processing with a half-power filter cutoff wavelength of 10 km to achieve a standard deviation of

$$\sigma_{spd} = 0.50 \text{ m s}^{-1}. \tag{I.36}$$

The measurement errors with 10-km smoothing are essentially uncorrelated for a grid spacing of $\Delta x \times \Delta y = 5$ km $\times$ 5 km (see Appendix B.2).

If the 10-km smoothed WaCM data were subsampled on the 5 km $\times$ 5 km grid on which the errors are uncorrelated, the derivation of analytical expressions for the 1-dimensional alongshore spectra of the errors would be a straightforward modification of the derivation of the analytical expression (I.2a) for the 1-dimensional alongshore spectrum of the errors of pre-processed SWOT estimates of SSH. For WaCM estimates of vorticity $\zeta = \partial v/\partial x - \partial u/\partial y$, however, it is advantageous to grid the WaCM data on a finer grid with dimensions of $\Delta x \times \Delta y = 1$ km $\times$ 1 km. The primary advantage is that centered difference estimates of the derivatives on the finer grid retain more of the short-wavelength variability in the vorticity signal (see Appendix H). For the comparisons with geostrophically computed velocity and vorticity estimated from simulated SWOT data in this study, it is also convenient for the analysis in this study to grid the WaCM data onto the same 1 km $\times$ 1 km grid as the SWOT data.

With the 10-km smoothing assumed in the baseline design for pre-processing of WaCM data, the standard deviation of the errors of overlapping smoothed estimates of the speeds of WaCM measurements of velocity on the finer 1 km $\times$ 1 km grid is still (I.36). But the errors are no longer uncorrelated on the finer grid. As summarized below, this complicates the derivation of analytical expressions for the spectra of errors of the velocity components and vorticity estimated from pre-processed WaCM data.

The footprint size of the raw WaCM radar data will likely be of order 100 m. For the simulated WaCM data in this study, the smallest possible footprint size is the 0.5 km $\times$ 0.5 km grid spacing of the CCS model. This is a factor of 10 finer than the 5 km $\times$ 5 km grid on which the pre-processed data are uncorrelated with 10-km smoothing. To achieve the baseline design of (I.36) for the standard deviation of the speeds of 10-km smoothed errors of surface velocity measurements, the analysis in Appendix D shows that the variance of unsmoothed errors in simulated raw measurements with a footprint size of 0.5 km $\times$ 0.5 km is a factor of 100 times larger, hence the standard deviation is a factor-of-10 larger. This can be seen from the error variance reduction formula (D.5a) with the reduction factor α given by (D.14c) for the case of smoothing of the simulated raw measurements on a grid of $\delta x \times \delta y = 0.5$ km $\times$ 0.5 km using a Parzen smoother with an isotropic half-power filter cutoff wavelength of $\lambda_c = 10$ km. The standard deviation of the speeds of the

unsmoothed velocity errors on the simulated raw measurement grid is thus

$$\sigma'_{spd} = 10\,\sigma_{spd} = 5.0 \text{ m s}^{-1}, \tag{I.37}$$

where the prime distinguishes this standard deviation of the errors of the simulated raw measurements from the standard deviation (I.36) of the speed errors after smoothing isotropically with a 10-km filter cutoff.

In general, the standard deviations σ_u and σ_v of the errors of the 10-km smoothed velocity estimates differ for the two orthogonal velocity components u and v. Throughout Secs. 6 and 8–10, however, we have assumed that the speed uncertainties in the pre-processed WaCM data are equally partitioned between u and v. In this case, the standard deviations σ_u and σ_v are both equal to a value $\sigma_{u,v}$ that is related to the baseline design (I.36) by

$$\sigma_{u,v} = \frac{\sigma_{spd}}{\sqrt{2}} = 0.354 \text{ m s}^{-1}.$$

The subscript u, v is intended to indicate that the error standard deviation is the same for each velocity component. If the speed uncertainties are also equally partitioned between u and v on the simulated raw measurement grid, the standard deviations σ'_u and σ'_v of the uncorrelated errors of each velocity component in the simulated unsmoothed raw data are both equal to a value $\sigma'_{u,v}$ that is related to (I.37) by

$$\sigma'_{u,v} = \frac{\sigma'_{spd}}{\sqrt{2}} = 3.54 \text{ m s}^{-1}.$$

In the derivations that follow, we allow for the possibility of different error standard deviations for each velocity component. Parseval's Theorem for the 2-dimensional white noise wavenumber spectrum of the uncorrelated errors of the u or v velocity component on the $\delta x \times \delta y = 0.5$ km $\times$ 0.5 km simulated raw measurement grid can then be expressed as

$$S'^{\,2d}_{u;v}(k,l) = \frac{\sigma'^{\,2}_{u;v}}{4k'_{\mathcal{N}}l'_{\mathcal{N}}} = \delta x\,\delta y\,\sigma'^{\,2}_{u;v}, \tag{I.38}$$

where $k'_{\mathcal{N}} = (2\delta x)^{-1}$ and $l'_{\mathcal{N}} = (2\delta y)^{-1}$ are the Nyquist wavenumbers in the x and y dimensions. The subscript $u; v$ signifies the choice of a subscript of either u or v on both sides of (I.38), depending on which velocity component is of interest. The spectrum thus has the same form for each velocity component. The only difference is that $\sigma^2_{u;v}$ on the right side of (I.38) is replaced with $\sigma'^{\,2}_u$ or $\sigma'^{\,2}_v$, depending on whether the interest is in the spectrum $S'^{\,2d}_u(k,l)$ of u or the spectrum $S'^{\,2d}_v(k,l)$ of v on the left side of (I.38).

The form (I.38) for the spectrum of velocity component errors from WaCM data is fundamentally different from the spectra (I.5) and (I.8) of the errors of geostrophically computed velocity components estimated from SWOT data. This is because of the different filtering imposed in the case of SWOT by the filter transfer functions (I.4) and (I.6) for centered differences in orthogonal directions as summarized in Appendix I.1.

The 2-dimensional wavenumber spectrum after smoothing the simulated raw WaCM data with half-power filter cutoff wavelengths of 10 km in each dimension (which is shown in Appendix C to be essentially equivalent to isotropic smoothing for the case of the Parzen smoother considered here) is

$$\begin{aligned}\tilde{S}^{2d}_{u;v}(k,l) &= W^2_{10\text{km}}(k)\,W^2_{10\text{km}}(l)\,S'^{\,2d}_{u;v}(k,l)\\ &= \delta x\,\delta y\,\sigma'^{\,2}_{u;v}\,W^2_{10\text{km}}(k)\,W^2_{10\text{km}}(l),\end{aligned} \tag{I.39a}$$

where $W^2_{10\text{km}}(k)$ and $W^2_{10\text{km}}(l)$ are the squared values of the filter transfer functions of smoothers with half-power filter cutoff wavelengths of 10 km in the x and y dimensions, respectively. For the case of the Parzen smoother used in this study, the filter transfer function in the x dimension with a half-power filter cutoff wavelength of 10 km is given by (A.11) in Appendix A with a span of $L_4 = 9.10$ km. The filter transfer function for Parzen smoothing in the y dimension is the same, except with wavenumber k replaced with l. The tilde on the left side of (I.39a) is intended as a reminder that isotropic 2-dimensional smoothing with a half-power filter cutoff wavelength of 10 km has been applied to unsmoothed errors of the simulated raw measurements on the 0.5 km $\times$ 0.5 km grid.

With the 10-km smoothing applied to the raw WaCM data in pre-processing, the smoothed velocity component estimates could be subsampled onto a 5 km × 5 km grid with minimal aliasing that arises from the imperfect gradual rolloff of the filter transfer function through the half-power filter cutoff wavenumber of 0.1 cpkm (which is equivalent to the Nyquist wavenumber for $\Delta x = \Delta y = 5$ km). For the reasons discussed above, we assume that the raw data after 10-km smoothing are subsampled onto a $\Delta x \times \Delta y = 1$ km × 1 km grid. The 2-dimensional wavenumber spectrum of the smoothed measurement errors on this grid is the same as (I.39a), but is truncated at the Nyquist wavenumbers $k_{\mathcal{N}} = (2\Delta x)^{-1} = 0.5$ cpkm and $l_{\mathcal{N}} = (2\Delta y)^{-1} = 0.5$ cpkm that are associated with the 1 km × 1 km grid spacing. In addition to the motivations discussed previously, the subsampling onto this 1 km × 1 km grid eliminates essentially all aliasing by virtue of the fact that the Nyquist wavenumbers are five times higher than the half-power filter cutoff wavenumber of 0.1 cpkm for the 10-km smoothing applied in the pre-processing of WaCM data.

For the $\Delta x \times \Delta y = 1$ km × 1 km subsample grid, the grid spacings for our simulated raw WaCM data are related to Δx and Δy by $\delta x = 0.5\Delta x$ and $\delta y = 0.5\Delta y$. And since the variances ${\sigma'_u}^2$ and ${\sigma'_v}^2$ of the errors of these simulated raw and unsmoothed WaCM velocity component estimates are related to the variances σ_u^2 and σ_v^2 of the errors of the 10-km smoothed velocity component estimates by $\sigma'^2_{u;v} = 100\,\sigma^2_{u;v}$, the spectrum (I.39a) can be written alternatively as

$$\tilde{S}^{2d}_{u;v}(k,l) = \\ 25\,\Delta x\,\Delta y\,\sigma^2_{u;v}\,W^2_{10\mathrm{km}}(k)\,W^2_{10\mathrm{km}}(l). \tag{I.39b}$$

This expresses the 2-dimensional spectrum of the velocity component errors in terms of the grid spacing and variance after the 10-km smoothing and the $\Delta x \times \Delta y = 1$ km × 1 km subsampling that are applied in our simulated pre-processing of the WaCM data.

The 1-sided, 1-dimensional alongshore spectrum of the errors of WaCM estimates of velocity components obtained by integrating the 2-dimensional spectrum (I.39b) over all cross-shore wavenumbers k and doubling the power at each alongshore wavenumber l is

$$\begin{aligned}\tilde{S}^{1d}_{u;v}(l) &= 2\int_{-k_{\mathcal{N}}}^{k_{\mathcal{N}}} \tilde{S}^{2d}_{u;v}(k,l)\,dk \\ &= 100\,\Delta x\,\Delta y\,\sigma^2_{u;v}\,W^2_{10\mathrm{km}}(l)\int_0^{k_{\mathcal{N}}} W^2_{10\mathrm{km}}(k)\,dk.\end{aligned} \tag{I.40a}$$

This expression uses the fact that $W^2_{10\mathrm{km}}(k)$ is symmetric about $k = 0$. The integral on the right side of (I.40a) is equal to $(0.910\,\lambda_c)^{-1} \approx \lambda_c^{-1}$ according to (D.12b). Since $\lambda_c = 10$ km $= 10\Delta x$ for the smoothing applied in the pre-processing of WaCM data, the 1-dimensional alongshore spectrum (I.40a) of the errors of WaCM estimates of each velocity component on a $\Delta x \times \Delta y = 1$ km × 1 km grid is

$$\tilde{S}^{1d}_{u;v}(l) = 10\,\Delta y\,\sigma^2_{u;v}\,W^2_{10\mathrm{km}}(l). \tag{I.40b}$$

It should be noted that the multiplicative factors of 25, 100 and 10 in (I.39b), (I.40a) and (I.40b), respectively, are all specific to the choices of $\delta x = \delta y = 0.5$ km for the footprint size of the raw data as simulated in this study from the $\delta x \times \delta y = 0.5$ km × 0.5 km gridded velocity fields in the CCS model and the assumed 10-km smoothing and $\Delta x = \Delta y = 1$ km subsampling in the pre-processing of WaCM estimates of velocity. We retain Δx and Δy in these equations as a reminder of the need to keep track of units and to help facilitate adaptation of the equations to other choices of δx, δy, Δx and Δy.

For example, consider the same footprint size of $\delta x = \delta y = 0.5$ km for the raw measurements but for subsampling of the 10-km smoothed raw data onto the grid with $\Delta x = \Delta y = 5$ km on which the pre-processed WaCM estimates of velocity components are uncorrelated. Then $\delta x = 0.1\Delta x$ and $\delta y = 0.1\Delta y$ rather than $0.5\Delta x$ and $0.5\Delta y$ as in the analysis above. The multiplicative factors in (I.39b), (I.40a) and (I.40b) would then become 1, 4 and 2, respectively. If not for the imperfections of the filter transfer function

of the Parzen smoother, the values of $W_{10\mathrm{km}}(k)$ and $W_{10\mathrm{km}}(l)$ would be 1 at all wavenumbers $k < k_{\mathcal{N}}$ and $l < l_{\mathcal{N}}$ for the new Nyquist wavenumbers of $k_{\mathcal{N}} = l_{\mathcal{N}} = 0.1$ cpkm associated with the 5 km × 5 km grid. The imperfections of the filter transfer functions are nonetheless small for these ranges of k and l. The resulting analytical expression (I.39a) for the 2-dimensional spectra of velocity component errors on a $\Delta x \times \Delta y = 5$ km × 5 km would then have the same form as the 2-dimensional spectrum (I.1) of errors of pre-processed SWOT estimates of SSH. Likewise, the expressions (I.40a) and (I.40b) for the 1-dimensional spectra of velocity component errors would have the same form as the 1-dimensional spectrum (I.2a) of errors of SWOT estimates of SSH.

The 2-dimensional wavenumber spectrum of the errors of vorticity $\zeta = \partial v/\partial x - \partial u/\partial y$ estimated from the errors of pre-processed WaCM estimates of the two velocity components is obtained straightforwardly from the 2-dimensional spectrum (I.39b). For centered difference estimates of the derivatives on the $\Delta x \times \Delta y = 1$ km × 1 km subsampling grid assumed in the derivation of (I.39b), the 2-dimensional spectrum of vorticity errors is

$$\tilde{S}^{2d}_{\zeta}(k,l) = \tilde{S}^{2d}_{\partial u/\partial y}(k,l) + \tilde{S}^{2d}_{\partial v/\partial x}(k,l), \tag{I.41}$$

where

$$\tilde{S}^{2d}_{\partial u/\partial y}(k,l) = |W_{3pt}(l)|^2\, \tilde{S}^{2d}_{u}(k,l) \tag{I.42a}$$

$$\tilde{S}^{2d}_{\partial v/\partial x}(k,l) = |W_{3pt}(k)|^2\, \tilde{S}^{2d}_{v}(k,l). \tag{I.42b}$$

The tildes in the above equations again signify that 10-km smoothing has been applied in the pre-processing of WaCM data. There is no cross spectral term in (I.41) because the errors of WaCM estimates of u and v have been assumed to be uncorrelated. The response functions $W_{3pt}(k)$ and $W_{3pt}(l)$ of the centered difference estimates of the derivatives in the x and y dimensions, respectively, are given by (I.6) and (I.4) with $\Delta x = \Delta y = 1$ km.

The 1-sided, 1-dimensional alongshore spectrum of ζ errors obtained from (I.41) and (I.42) is

$$\begin{aligned}\tilde{S}^{1d}_{\zeta}(l) &= 2\int_{-k_{\mathcal{N}}}^{k_{\mathcal{N}}} \tilde{S}^{2d}_{\zeta}(k,l)\, dk \\ &= \tilde{S}^{1d}_{\partial u/\partial y}(l) + \tilde{S}^{1d}_{\partial v/\partial x}(l),\end{aligned} \tag{I.43}$$

where

$$\begin{aligned}\tilde{S}^{1d}_{\partial u/\partial y}(l) &= 2\int_{-k_{\mathcal{N}}}^{k_{\mathcal{N}}} \tilde{S}^{2d}_{\partial u/\partial y}(k,l)\, dk \\ &= 2\,|W_{3pt}(l)|^2 \int_{-k_{\mathcal{N}}}^{k_{\mathcal{N}}} \tilde{S}^{2d}_{u}(k,l)\, dk\end{aligned} \tag{I.44a}$$

$$\begin{aligned}\tilde{S}^{1d}_{\partial v/\partial x}(l) &= 2\int_{-k_{\mathcal{N}}}^{k_{\mathcal{N}}} \tilde{S}^{2d}_{\partial v/\partial x}(k,l)\, dk \\ &= 2\int_{-k_{\mathcal{N}}}^{k_{\mathcal{N}}} |W_{3pt}(k)|^2\, \tilde{S}^{2d}_{v}(k,l)\, dk.\end{aligned} \tag{I.44b}$$

According to (I.40a), the integral on the right side of (I.44a) with the multiplicative factor of 2 is equal to the 1-dimensional alongshore spectrum $\tilde{S}^{1d}_{u}(l)$ of the cross-shore velocity component errors. The contribution (I.44a) to the 1-dimensional alongshore spectrum (I.43) of vorticity errors is therefore

$$\tilde{S}^{1d}_{\partial u/\partial y}(l) = |W_{3pt}(l)|^2\, \tilde{S}^{1d}_{u}(l), \tag{I.45a}$$

where $\tilde{S}^{1d}_{u}(l)$ can be expressed alternatively in the form (I.40b) to get

$$\begin{aligned}&\tilde{S}^{1d}_{\partial u/\partial y}(l) \\ &\quad = 10\,\Delta y\,\sigma_u^2\, |W_{3pt}(l)|^2\, W^2_{10\mathrm{km}}(l).\end{aligned} \tag{I.45b}$$

From (I.39b), the contribution (I.44b) to the 1-dimensional wavenumber spectrum of vorticity errors can be written as

$$\tilde{S}^{1d}_{\partial v/\partial x}(l) = 100\,\Delta x\,\Delta y\,\sigma_v^2\,W^2_{10\mathrm{km}}(l) \int_0^{k_{\mathcal{N}}} |W_{3pt}(k)|^2\; W^2_{10\mathrm{km}}(k)\,dk. \tag{I.46a}$$

This equation uses the fact that $|W_{3pt}(k)|^2$ and $W^2_{10\mathrm{km}}(k)$ are both symmetric about $k = 0$. From (I.40b), this can be written alternatively in terms of the 1-dimensional wavenumber spectrum of alongshore velocity component errors,

$$\tilde{S}^{1d}_{\partial v/\partial x}(l) = 10\Delta x\,\tilde{S}^{1d}_{v}(l) \int_0^{k_{\mathcal{N}}} |W_{3pt}(k)|^2\; W^2_{10\mathrm{km}}(k)\,dk. \tag{I.46b}$$

The integral on the right sides of (I.46a) and (I.46b) is the same integral encountered in (I.33b) with $\lambda_c = 10$ km. Numerical solutions for this integral are shown as a function of half-power filter cutoff wavelength λ_c in Fig. I1a. For the case of $\Delta x = \Delta y = 1$ km, the integral has a value of 0.0221 at $\lambda_c = 10$ km.

The analytical expressions (I.40) and (I.43), with the latter partitioned as (I.45) and (I.46), for the 1-sided, 1-dimensional alongshore spectra of errors of WaCM estimates of the two velocity components and the vorticity computed from the pre-processed WaCM data are applicable to any low-pass filter with a half-power filter cutoff wavelength of 10 km. The results based on the Parzen smoother with $\sigma_u = \sigma_v = \sigma_{u,v} = 0.354$ m s^{-1} are shown by the solid green lines in Fig. 13c. These theoretical spectra agree very well with the spectra shown in Fig. 13c by the solid blue lines that were computed empirically from the simulated WaCM error fields generated for the analysis in Secs. 6 and 8–10.

Appendix I.4. Errors of Smoothed WaCM Estimates of Velocity and Vorticity

The errors of WaCM estimates of velocity and vorticity computed from the pre-processed WaCM data (see Appendix G and Table 1 in Sec. 4 and the bottom left panels of Figs. 19a and 19b) are too large for the velocity and vorticity estimates to be useful for most applications. It will be necessary to smooth the pre-processed WaCM data in ground-based post-processing to reduce the effects of measurement errors. As in Appendix I.3, we assume here that the pre-processed WaCM estimates of velocity have been smoothed with a filter cutoff wavelength of 10 km and subsampled from the raw measurement grid (0.5 km × 0.5 km for the simulations in this study) onto a $\Delta x \times \Delta y = 1$ km × 1 km grid.

The 2-dimensional wavenumber spectrum of WaCM estimates of each velocity component after smoothing in each dimension with a filter cutoff wavelength of λ_c in ground-based post-processing is obtained from the 2-dimensional wavenumber spectrum (I.39b) of the errors of the pre-processed estimates of the two velocity components by

$$\begin{aligned}\bar{\tilde{S}}^{2d}_{u;v}(k,l) &= W^2_{\lambda_c}(k)\,W^2_{\lambda_c}(l)\,\tilde{S}^{2d}_{u;v}(k,l) \\ &= 25\,\Delta x\,\Delta y\,\sigma^2_{u;v} \\ &\quad W^2_{10\mathrm{km}}(k) W^2_{10\mathrm{km}}(l)\,W^2_{\lambda_c}(k)\,W^2_{\lambda_c}(l).\end{aligned} \tag{I.47}$$

The subscript $u;v$ again indicates that the equation has the same form for both velocity components, differing only in the choice of a subscript u or v on both sides of (I.47). The combined tilde and overbar signify that the spectrum on the left side of (I.47) is based on WaCM velocity component estimates that have been 2-dimensionally smoothed twice, first in pre-processing with a half-power filter cutoff wavelength of 10 km

in each dimension (signified as in Appendix I.3 by the tilde) and then in ground-based post-processing with a half-power filter cutoff wavelength of λ_c in each dimension (signified by the overbar).

The 1-sided, 1-dimensional alongshore spectrum of the smoothed velocity errors is

$$\begin{aligned}\overline{\tilde{S}}^{1d}_{u;v}(l) &= 2\int_{-k_{\mathcal{N}}}^{k_{\mathcal{N}}} \overline{\tilde{S}}^{2d}_{u;v}(k,l)\,dk \\ &= 100\,\Delta x\,\Delta y\,\sigma^2_{u;v}\,W^2_{10\mathrm{km}}(l)\,W^2_{\lambda_c}(l) \\ &\qquad \int_0^{k_{\mathcal{N}}} W^2_{10\mathrm{km}}(k)\,W^2_{\lambda_c}(k)\,dk. \end{aligned} \tag{I.48a}$$

From (I.40b), this can be written alternatively in terms of the 1-dimensional alongshore spectrum $\tilde{S}^{1d}_{u;v}(l)$ of pre-processed WaCM estimates of the velocity components,

$$\begin{aligned}\overline{\tilde{S}}^{1d}_{u;v}(l) &= 10\Delta x\,\tilde{S}^{1d}_{u;v}(l)\,W^2_{\lambda_c}(l) \\ &\qquad \int_0^{k_{\mathcal{N}}} W^2_{10\mathrm{km}}(k)\,W^2_{\lambda_c}(k)\,dk. \end{aligned} \tag{I.48b}$$

When the filter cutoff wavelength λ_c in the ground-based post-processing is large compared with the 10-km filter cutoff wavelength of the smoothing applied in pre-processing of WaCM data, the filter transfer function $W_{10\mathrm{km}}(k)$ in the integrand on the right sides of (I.48a) and (I.48b) is approximately 1 across the low-wavenumber pass band of the filter transfer function $W_{\lambda_c}(k)$. In this case, the 10-km filtering in the pre-processing has relatively little effect on the integral on the right sides of (I.48a) and (I.48b). Then (I.48a), for example, reduces to the approximate form

$$\begin{aligned}\overline{\tilde{S}}^{1d}_{u;v}(l) &\approx 100\,\Delta x\,\Delta y\,\sigma^2_{u;v}\,W^2_{10\mathrm{km}}(l)\,W^2_{\lambda_c}(l) \\ &\qquad \int_0^{k_{\mathcal{N}}} W^2_{\lambda_c}(k)\,dk. \end{aligned}$$

Substitution of (I.28) simplifies this to

$$\overline{\tilde{S}}^{1d}_{u;v}(l) \approx \frac{100\,\Delta x\,\Delta y}{\lambda_c}\,\sigma^2_{u;v}\,W^2_{10\mathrm{km}}(l)\,W^2_{\lambda_c}(l). \tag{I.49}$$

More generally, the 1-dimensional alongshore spectra of velocity component errors smoothed with a half-power filter cutoff wavelength of λ_c in each dimension must be computed from (I.48). Numerical solutions for the integral on the right sides of (I.48) are shown as a function of λ_c by the solid line in Fig. I1c. The dashed line is the value of the integral when $W^2_{10\mathrm{km}}(k)$ is replaced with a value of 1 for all wavenumbers k as in (I.49). The two lines converge rapidly and the approximate solution (I.49) is accurate to better than 10% for ground-based post-processing with $\lambda_c \geq 22$ km.

The 2-dimensional wavenumber spectrum of the errors of vorticity estimated from smoothed errors of WaCM estimates of the velocity components is obtained analogously to (I.41) and (I.42), except with the 2-dimensional spectra (I.40) of the errors of pre-processed WaCM estimates of the two velocity components on the right sides of (I.42a) and (I.42b) replaced with the 2-dimensional spectra (I.47) of the two smoothed velocity component errors,

$$\overline{\tilde{S}}^{2d}_{\zeta}(k,l) = \overline{\tilde{S}}^{2d}_{\partial u/\partial y}(k,l) + \overline{\tilde{S}}^{2d}_{\partial v/\partial x}(k,l), \tag{I.50}$$

where

$$\overline{\tilde{S}}^{2d}_{\partial u/\partial y}(k,l) = |W_{3pt}(l)|^2\,\overline{\tilde{S}}^{2d}_{u}(k,l) \tag{I.51a}$$

$$\overline{\tilde{S}}^{2d}_{\partial v/\partial x}(k,l) = |W_{3pt}(k)|^2\,\overline{\tilde{S}}^{2d}_{v}(k,l). \tag{I.51b}$$

As in (I.47), the combined tilde and overbar signify spectra that are based on doubly smoothed WaCM velocity component estimates.

The 1-sided, 1-dimensional alongshore spectrum of the smoothed vorticity errors obtained from (I.50) and (I.51) is

$$\begin{aligned}\overline{\tilde{S}}^{1d}_{\zeta}(l) &= 2\int_{-k_{\mathcal{N}}}^{k_{\mathcal{N}}} \overline{\tilde{S}}^{2d}_{\zeta}(k,l)\,dk \\ &= \overline{\tilde{S}}^{1d}_{\partial u/\partial y}(l) + \overline{\tilde{S}}^{1d}_{\partial v/\partial x}(l),\end{aligned} \tag{I.52}$$

where

$$\begin{aligned}\overline{\tilde{S}}^{1d}_{\partial u/\partial y}(l) &= 2\int_{-k_{\mathcal{N}}}^{k_{\mathcal{N}}} \overline{\tilde{S}}^{2d}_{\partial u/\partial y}(k,l)\,dk \\ &= 2\,|W_{3pt}(l)|^2 \int_{-k_{\mathcal{N}}}^{k_{\mathcal{N}}} \overline{\tilde{S}}^{2d}_{u}(k,l)\,dk\end{aligned} \tag{I.53a}$$

$$\begin{aligned}\overline{\tilde{S}}^{1d}_{\partial v/\partial x}(l) &= 2\int_{-k_{\mathcal{N}}}^{k_{\mathcal{N}}} \overline{\tilde{S}}^{2d}_{\partial v/\partial x}(k,l)\,dk \\ &= 2\int_{-k_{\mathcal{N}}}^{k_{\mathcal{N}}} |W_{3pt}(k)|^2\, \overline{\tilde{S}}^{2d}_{v}(k,l)\,dk.\end{aligned} \tag{I.53b}$$

From (I.47), the first contribution (I.53a) to the 1-dimensional alongshore spectrum (I.52) of vorticity errors can be written as

$$\begin{aligned}&\overline{\tilde{S}}^{1d}_{\partial u/\partial y}(l) \\ &\quad = 100\,\Delta x\,\Delta y\,\sigma_u^2\,|W_{3pt}(l)|^2\,W^2_{10\mathrm{km}}(l)\,W^2_{\lambda_c}(l) \\ &\qquad \int_0^{k_{\mathcal{N}}} W^2_{10\mathrm{km}}(k)\,W^2_{\lambda_c}(k)\,dk.\end{aligned} \tag{I.54a}$$

The integral on the right side of this equation is the same as the integral on the right sides of (I.48a) and (I.48b). Numerical solutions for this integral are shown as a function of λ_c in Fig. I1c.

With (I.48a), the spectrum (I.54a) can be expressed more compactly in terms of the 1-dimensional alongshore spectrum $\overline{\tilde{S}}^{1d}_{u}(l)$ of the u component of smoothed velocity errors,

$$\overline{\tilde{S}}^{1d}_{\partial u/\partial y}(l) = |W_{3pt}(l)|^2\,\overline{\tilde{S}}^{1d}_{u}(l). \tag{I.54b}$$

This could be written in terms of the 1-dimensional spectrum $\tilde{S}^{1d}_{u}(l)$ of pre-processed WaCM estimates of the u component of smoothed velocity errors by substituting (I.48b) for $\overline{\tilde{S}}^{1d}_{u}(l)$ on the right side of (I.54b).

A similar procedure can be followed for the second contribution (I.53b) to the 1-dimensional alongshore spectrum (I.52) of vorticity errors. From (I.47), the expression (I.53b) can be written as

$$\begin{aligned}&\overline{\tilde{S}}^{1d}_{\partial v/\partial x}(l) \\ &\quad = 100\,\Delta x\,\Delta y\,\sigma_v^2\,W^2_{10\mathrm{km}}(l)\,W^2_{\lambda_c}(l) \\ &\qquad \int_0^{k_{\mathcal{N}}} |W_{3pt}(k)|^2\,W^2_{10\mathrm{km}}(k)\,W^2_{\lambda_c}(k)\,dk.\end{aligned} \tag{I.55a}$$

With (I.48a), this can be expressed in terms of the 1-dimensional alongshore spectrum $\overline{\tilde{S}}^{1d}_v(l)$ of the v component of smoothed velocity errors,

$$\overline{\tilde{S}}^{1d}_{\partial v/\partial x}(l) = \overline{\tilde{S}}^{1d}_v(l)\,\frac{\displaystyle\int_0^{k_{\mathcal{N}}} |W_{3pt}(k)|^2\; W^2_{10\mathrm{km}}(k)\, W^2_{\lambda_c}(k)\, dk}{\displaystyle\int_0^{k_{\mathcal{N}}} W^2_{10\mathrm{km}}(k)\, W^2_{\lambda_c}(k)\, dk}. \tag{I.55b}$$

This could be written in terms of the 1-dimensional spectrum $\tilde{S}^{1d}_v(l)$ of pre-processed WaCM estimates of the v component of velocity errors by substituting (I.48b) for $\overline{\tilde{S}}^{1d}_v(l)$ on the right side of (I.55b).

As in the case of the approximate expression (I.49) for the 1-dimensional spectrum of smoothed velocity component errors, the expression (I.55b) can be simplified when the filter cutoff wavelength λ_c in the ground-based post-processing is large compared with the 10-km filter cutoff wavelength of the smoothing applied in the pre-processing of WaCM data. Then the filter transfer function $W_{10\mathrm{km}}(k)$ in the integrands on the right sides of (I.55a) and (I.55b) is approximately 1 across the low-wavenumber pass band of the filter transfer function $W_{\lambda_c}(k)$. In this case, the 10-km filtering in the pre-processing has relatively little effect on the integral on the right side of (I.55a) and either of the two integrals on the right side of (I.55b). Then (I.55a), for example,

$$\overline{\tilde{S}}^{1d}_{\partial v/\partial x}(l) \approx 100\,\Delta x\,\Delta y\,\sigma_v^2\, W^2_{10\mathrm{km}}(l)\, W^2_{\lambda_c}(l) \int_0^{k_{\mathcal{N}}} |W_{3pt}(k)|^2\; W^2_{\lambda_c}(k)\, dk.$$

reduces to the approximate form
The integral on the right side of this equation is the same as the integral on the right sides of (I.33b) and (I.46). Numerical solutions for this integral are shown as a function of λ_c in Fig. I1a.

More generally, the 1-dimensional alongshore spectra of vorticity errors smoothed with a half-power filter cutoff wavelength of λ_c in each dimension must be computed from (I.55). Numerical solutions for the integral on the right side of (I.55a) and in the numerator of (I.55b) are shown as a function of λ_c by the solid line in Fig. I1d and numerical solutions for the integral in the denominator on the right side of (I.55b) are shown as a function of λ_c by the solid line in Fig. I1c. The dashed lines are the values of the integrals when $W^2_{10\mathrm{km}}(k)$ is replaced with a value of 1 for all wavenumbers k as in (I.56). The approximate solution to the integral is accurate to better than 10% for ground-based post-processing with $\lambda_c \geq 37$ km.

The analytical expressions (I.48) and (I.52), with the latter partitioned as (I.54) and (I.55), for the 1-sided, 1-dimensional alongshore spectra of the residual errors of WaCM estimates of the two velocity components and vorticity after smoothing in ground-based post-processing of the pre-processed WaCM data are applicable to any low-pass filter with a half-power filter cutoff wavelength of λ_c. The results based on the Parzen smoother with $\sigma_u = \sigma_v = \sigma_{u,v} = 0.354$ m s^{-1} are shown by the solid green lines in Fig. 15 for filter cutoff wavelengths of $\lambda_c = 20$, 50 and 80 km. These theoretical spectra agree very well with the spectra shown by the solid blue lines that were computed empirically from the simulated WaCM error fields generated for the analysis in Secs. 6 and 8–10.

References

Alsdorf, D., L.-L. Fu, N. Mognard, A. Cazenave, E. Rodríguez, D. Chelton and D. Lettenmaier, 2007: Measuring the global oceans and terrestrial freshwater from space. *Eos, Trans. Amer. Geophys. Union*, **88**, 253 and 257.

Arbic, B. K. R. B.Scott, D. B. Chelton, J. G. Richman, and J. F. Shriver, 2012: Effects of stencil width on surface ocean geostrophic velocity and vorticity estimation from gridded satellite data. *J. Geophys. Res.*, **117**, doi: 10.1029/2011JC007367.

Ardhuin, F., and 29 others, 2018: Measuring currents, ice drift, and waves from space: the Sea Surface KInematics Multiscale monitoring (SKIM) concept. *Ocean Science.* 10.5194/os-2017-65 (accepted).

Barnier, B., L. Siefried and P. Marchesiello 1995: Thermal forcing for a global ocean circulation model using a three-year climatolofy of ECMWF analyses. *J. Mar. Syst.*, **6**, 363–380.

Beckmann, A., and D. Haidvogel, 1993: Numerical simulation of flow around a tall isolated seamount. Part I: Problem formulation and model accuracy. *J. Phys. Oceanogr.*, **23**, 1736–1753.

Biancamaria, S., D. P. Lettenmaier and T. M. Pavelsky, 2016: The SWOT mission and it's capabilities for land hydrology. *Surv. Geophys.*, **37**, 307–337.

Bracewell, R. N., 1978: *The Fourier transform and its applications.* McGraw-Hill Book Co., New York, 444 pp.

Capet, X., J. C. McWilliams, M. J. Molemaker and F. Shchepetkin, 2008: Mesoscale to submesoscale transition in the California Current System. Part I: Flow structure, eddy flux and observational tests. *J. Phys. Oceanogr.*, **38**, 29–43.

Carton, J., and B. Giese, 2008: A reanalysis of ocean climate using Simple Ocean Data Assimilation (SODA). *Mon. Wea. Rev.*, **136**, 2999–3017.

Chapron, B., F. Collard and F. Ardhuin, 2005: Direct measurements of ocean surface velocity from space: Interpretation and validation. *J. Geophys. Res.*, **110**, C07008, doi:101029/2004JC002809.

Chelton, D. B., and M. H. Freilich, 2005: Scatterometer-based assessment of 10-m wind analyses from the operational ECMWF and NCEP numerical weather prediction models. *Mon. Wea. Rev.*, **133**, 409–429.

Chelton, D. B., M. G. Schlax, and R. M. Samelson, 2011: Global observations of nonlinear mesoscale eddies. *Prog. Oceanogr.*, **91**, 167–216, doi: 10.1016/j.pocean.2011.01.002.

Cleveland, W. S., and S. J. Devlin, 1988: Locally weighted regression: An approach to regression analysis by local fitting. *J. Amer. Stat. Assoc.*, **83**, 596–610.

Da Silva, A. M., C. Young and S. Levitus, 1994: *Algorithms and Procedures*, Vol. 1, *Atlas of Surface Marine Data 1994*, NOAA Atlas NESDIS 6, 74 pp.

Dewar, W., and G. Flierl, 1987: Some effects of the wind on rings. *J. Phys. Oceanogr.*, **17**, 16531667.

Esteban Fernandez, D., 2017: SWOT Project Mission Performance and Error Budget. Jet Propulsion Laboratory Document D-79084 Revision A, April 7, 2017, 83 pp.

Flierl, G. R., 1988: On the instability of geostrophic vorticies. *J. Fluid Mech.*, **197**, 349–388.

Fu, L.-L., and R. Ferrari, 2008: Observing oceanic submesoscale processes from space. *Eos*, **89**, 488–489.

Fu, L.-L., and E. Rodriguez, 2004: High-resolution measurement of ocean surface topography by radar interferometry for oceanographic and geophysical applications. In *The State of the Planet: Frontiers and Challenges in Geophysics, Geophys. Monogr. Ser.*, vol. 150, edited by R. S. J. Sparks and C. J. Hawkesworth, pp. 209–224, AGU, Washington, D.C.

Fu, L.-L., D. B. Chelton, P.-Y. Le Traon, and R. Morrow, 2010: Eddy dynamics from satellite altimetry: progress and challenges. *Oceanog.*, **23**, 14–25.

Gaube, P. D. B. Chelton, R. M. Samelson, M. G. Schlax and L. W. O'Neill, 2015: Satellite observations of mesoscale eddy-induced Ekman pumping. *J. Phys. Oceanogr.*, **45**, 104–132.

Gaultier, L., C. Ubelmann and L.-L. Fu, 2016: The challenge of using future SWOT data for oceanic field reconstructions. *J. Atmos. Oceanic Technol.*, **33**, 119–126.

Gaultier, L., C. Ubelmann and L.-L. Fu, 2017: SWOT Simulator Documentation. Jet Propulsion Laboratory, Release 2.3.0, March 15, 2017, 44 pp.

Gula, J. M. J. Molemaker and J. C. McWilliams, 2015: Gulf Stream dynamics along the southeastern U.S. seaboard. *J. Phys. Oceanogr.*, **45**, 690—715.

Harris, F. J., 1978: On the use of windows for harmonic analysis with the discrete Fourier transform. *Proc. IEEE*, **66**, 51–83.

Held, I. M., R. T. Pierrehumbert, S. T. Garner and K. L. Swanson, 1995: Surface quasi-geostrophic dynamics. *J. Fluid Mech.*, **282**, 1–20.

Klein, P., and G. Lapeyre, 2009: The ocean vertical pump induced by mesoscale and submesoscale turbulence. *Ann. Rev. Mar. Sci.*, **1**, 351–375.

Kloosterziel, R. C., and G. J. F. van Heijst, 1991: An experimental study of unstable barotropic vortices in a rotating fluid. *J. Fluid Mech.*, **223**, 1–24.

Kloosterziel, R. C., G. F. Carnevale, and P. Orlandi, 2007: Inertial instability in rotating and stratified fluids: barotropic vortices. *J. Fluid Mech.*, **583**, 379–412.

Le Traon, P.-Y., P. Klein, B. Lien Hua and G. Dibarboure, 2008: Do altimeter wavenumber spectra agree with the interior or surface quasigeostrophic theory? *J. Phys. Oceanogr.*, **38**, 1137–1142.

Lee, T., S. Hakkinen, K. Kelly, B. Qiu, H. Bonekamp and E. J. Lindstrom, 2010: Satellite observations of ocean circulation changes associated with climate variability. *Oceanog.*, **23**, 70–81.

Lévy, M., P. Klein and A.-M. Treguier, 2001: Impact of sub-mesoscale physics on production and subduction of phytoplankton in an oligotrophic regime. *J. Mar. Res.*, **59**, 535–565.

Mahadevan, A., L. N. Thomas and A. Tandon, 2008: Comment on "Eddy/wind interactions stimulate extraordinary mid-ocean plankton blooms." *Science*, **320**, 448.

Marchesiello, P., J. McWilliams and A. Shchepetkin, 2003: Equilibrium structure and dynamics of the California Current System. *J. Phys. Oceanogr.*, **33**, 753–783.

Martin, A. P., and K. J. Richards, 2001: Mechanisms for vertical nutrient transport within a North Atlantic mesoscale eddy. *Deep-Sea Res. II*, **48**, 757–773.

Mason, E., J. Molemaker, A. Shchepetkin, F. Colas, J. C. McWilliams and P. Sangrà, 2010: Procedures for offline grid nesting in regional ocean models. *Ocean Modell.*, **35**, 1–15.

McGillicuddy, D., and Coauthors, 2007: Eddy/wind interactions stimulate extraordinary mid-ocean plankton blooms. *Science*, **316**, 10211026.

McGillicuddy, D., J. Ledwell, and L. Anderson, 2008: Response to comments on "Eddy/wind interactions stimulate extraordinary mid-ocean plankton blooms. *Science*, **320**, 488.

Molemaker, M. J., J. C. McWilliams and W. K. Dewar, 2015: Submesoscale instability and generation of mesoscale anticyclones near a separation of the California undercurrent. *J. Phys. Oceanogr.*, **45**, 613–629.

NASEM (National Academies of Sciences, Engineering, and Medicine). 2018: *Thriving on our changing planet: A decadal strategy for Earth observation from space.* The National Academies Press, Washington, DC., 700 pages. https://doi.org.10.17226/24938.

Pascual, A., Y. Faugere, G. Larnicol, P.-Y. Le Traon, 2006: Improved description of the ocean mesoscale variability by combining four satellite altimeters. *Geophys. Res. Lett.*, **33**. doi:10.1029/2005GL024633.

Penven, P., L. Debreu, P. Marchesiello and J. McWilliams, 2006: Applications of the ROMS embedding procedure for the central California upwelling system. *Ocean Modell.*, **12**, 157–187.

Peral, E., 2016: KaRIn: Ka-Band Radar Interferometer Onboard Processor (OBP) Algorithm Theoretical Basis Document (ATBD). Jet Propulsion Laboratory Document D-79130, Initial Release, June 27, 2016, 72 pp.

Pujol, M.-I., Y. Faugère, G. Taburet, S. Dupuy, C. Pelloquin, M. Ablain and N. Picot, 2016: DUACS DT2014: The new multi-mission altimeter data set reprocessed over 20 years. *Ocean Sci.*, **12**, 1067–1090.

Pujol, M.-I., G. Dibarboure, P.-Y. Le Traon and P. Klein, 2012: Using high-resolution altimetry to observe mesoscale signals. *J. Atmos. Oceanic Technol.*, **29**, 1409–1416.

Qiu, B., S. Chen, P. Klein, C. Ubelmann, L.-L. Fu and H. Sasaki, 2016: Reconstructability of three-dimensional upper-ocean circulation from SWOT sea surface height measurements. *J. Phys. Oceanogr.*, **46**, 947–963.

Qiu, B., S. Chen, P. Klein, J. Wang, H. Torres, L.-L. Fu and D. Menemenlis, 2018: Seasonality in transition scale from balanced to unblanced motions in the world ocean. *J. Phys. Oceanogr.*, **48**, 591–605.

Rayleigh, L., 1916: On the dynamics of revolving fluids. *Proc. Roy. Soc. Lond.*, **A 93**, 148-154.

Risien, C. R., and D. B. Chelton, 2008: A global climatology of surface wind and wind stress fields from eight years of QuikSCAT scatterometer data. *J. Phys. Oceanogr.*, **38**, 2379–2413.

Rocha, C. B., T. K. Chereskin, S. T. Gille and D. Menemenlis, 2016: Mesoscale to submesoscale wavenumber spectra in Drake Passage. *J. Phys. Oceanogr.*, **46**, 601–620.

Rodríguez, E., and P. S. Callahan, 2016: Surface Water and Ocean Topography Mission (SWOT) Project Science Requirements Document. Jet Propulsion Laboratory Document D-61923, Rev A, March 18, 2016, 28 pp.

Rodríguez, E., A. Wineteer, D. Perkovic-Martin, T. Gál, B. W. Stiles, N. Niamsuwan and R. Rodriguez Monje, 2018: Estimating ocean vector winds and currents using a Ka-band pencil-beam Doppler scatterometer. *Rem. Sens.*, **10**, 576.

Savage, A. C., B. K. Arbic, M. H. Alford, J. K. Ansong, J. T. Farrar, D. Menemenlis, A. K. O'Rourke, J. G. Richman, J. F. Shriver, G. Voet, A. J. Wallcraft and L. Zamudio, 2017: Spectral decomposition of internal gravity wave sea surface height in global models. *J. Geophys. Res.*, **122**, 7803–7821.

Schlax, M. G. and D. B. Chelton, 1992: Frequency domain diagnostics for linear smoothers. JJ. Amer. Stat. Assoc., Š7, 1070–1081.

Shchepetkin, A. F., and J. C. McWilliams, 2005: The Regional Oceanic Modeling System (ROMS): A split-explicit, free-surface, topography-following-coordinate oceanic model. *Ocean Modell.*, **9**, 347–404.

Shchepetkin, A. F., and J. C. McWilliams, 2009: Correction and commentary for "Ocean forecasting in terrain-following coordinates: Formulation and skill assessment of the regional ocean modeling system" by Haidvogel et al., *J. Comput. Phys.*, **227**, pp. 3595 3624. *J. Comput. Phys.*, **228**, 8985–9000.

Smith, W., and D. Sandwell, 1997: Global seafloor topography from satellite altimetry and ship depth soundings. *Science*, **277**, 1957–1962.

Stern, M., 1965: Interaction of a uniform wind stress with a geostrophic vortex. *Deep-Sea Res.*, **12**, 355–367.

Ubelmann, C., P. Klein and L.-L. Fu, 2015: Dynamic interpolation of sea surface height and potential applications for future high-resolution altimetry mapping. *J. Atmos. Oceanic Technol.*, **32**, 177–184.

Wang, D.-P., C. N. Flagg, K. Donohue and H. T. Rossby, 2010: Wavenumber spectrum in the Gulf Stream from shipboard ADCP observations and comparisons with altimetry measurements. *J. Phys. Oceanogr.*, **40**, 840–844.

Willis, J. K., D. P. Chambers, C.-Y. Kuo and C. K. Shum, 2010: Global sea level rise. Recent progress and challenges for the decades to come. *Oceanog.*, **23**, 26–35.

Xu, Y., and L.-L. Fu, 2012: The Effects of altimeter instrument noise on the estimation of the wavenumber spectrum of sea surface height. *J. Phys. Oceanogr.*, **42**, 2229–2233.

Table 1. The standard deviations of errors of SWOT estimates of sea surface height h, the geostrophically computed cross-shore and alongshore velocity components $u_g = -gf^{-1}\partial h/\partial y$ and $v_g = gf^{-1}\partial h/\partial x$, the magnitude $(u_g^2 + v_g^2)^{1/2}$ of the geostrophically computed velocity and the geostrophically computed vorticity $\zeta_g = \partial v_g/\partial x - \partial u_g/\partial y$ normalized by the Coriolis parameter f. The calculations are all based on the value of $f = 8.77 \times 10^{-5}$ s^{-1} at the central latitude 37°N of the California Current model domain shown in Fig. 2. The results for the pre-processed SWOT estimates of SSH with 1-km footprint on a 1 km × 1 km grid and the science requirement of $\sigma_h = 2.74$ cm for the standard deviation of the uncorrelated errors of the SSH measurements are listed in the first column. The reduction of error that can be achieved by smoothing with half-power filter cutoff wavelengths of $\lambda_c = 10$ km and 50 km are listed in the second and third columns. The error estimates in the first and second columns are derived in Appendix G.1 and Appendix G.3 by propagation-of-error analysis. The error estimates in the third column were obtained by integrating the analytical expressions for the error spectra derived in Appendix I.2 with $\lambda_c = 50$ km.

Variable	SWOT with 1-km Footprint	SWOT with 5-km Footprint (10-km Smoothing)	SWOT with 50-km Smoothing
SSH	2.74 cm	0.55 cm	0.11 cm
u_g, v_g	2.17 m s^{-1}	0.26 m s^{-1}	0.013 m s^{-1}
speed	3.07 m s^{-1}	0.37 m s^{-1}	0.018 m s^{-1}
ζ_g/f	39.1	3.2	0.045

Table 2. The standard deviations of errors of WaCM estimates the cross-shore and alongshore velocity components u and v, the velocity magnitude $(u^2 + v^2)^{1/2}$ and the vorticity $\zeta = \partial v/\partial x - \partial u/\partial y$ normalized by the Coriolis parameter f at the central latitude 37°N of the California Current model domain shown in Fig. 2. The results for the pre-processed WaCM estimates of the velocity components with 5-km footprint size on a 5 km × 5 km grid and an assumed standard deviation of $\sigma_{u,v} = 0.354$ m s^{-1} for the uncorrelated measurement errors of each orthogonal component of velocity are listed in the first column. The results for the same footprint size of 5 km oversampled on a 1 km × 1 km grid are listed in the second column. The reduction of error that can be achieved by smoothing with a half-power filter cutoff wavelength of $\lambda_c = 50$ km are listed in the third column. The error estimates in the first and second columns are derived in Appendix G.2 by propagation-of-error analysis. The error estimates in the third column were obtained by integrating the analytical expressions for the error spectra derived in Appendix I.4 with $\lambda_c = 50$ km.

Variable	WaCM with 5-km Footprint and 5-km Grid	WaCM with 5-km Footprint and 1-km Grid	WaCM with 50-km Smoothing and 1-km Grid
u, v	0.35 m s^{-1}	0.35 m s^{-1}	0.071 m s^{-1}
speed	0.50 m s^{-1}	0.50 m s^{-1}	0.10 m s^{-1}
ζ/f	0.81	2.4	0.12

Table 3. The resolution capabilities deduced in Secs. 8 and 9 for SWOT and WaCM estimates of the magnitudes of surface ocean velocity and vorticity in an instantaneous snapshot and in 4-day and 14-day averages based on spatial smoothing using the Parzen and loess smoothers for measurement error standard deviations of $\sigma_h = 2.74$ cm for SWOT and $\sigma_{spd} = 0.50$ m s^{-1} equally partitioned between the two velocity components for WaCM. A horizontal line indicates that the S/N ratio did not exceed the threshold of 3.16 for any of the choices of half-power filter cutoff wavelength considered in Sec. 8. The last column shows the percent improvement of the resolution capability inferred from the loess smoother compared with the Parzen smoother. The results for WaCM are based on a swath width of 1200 km. The improved resolution capabilities if the WaCM swath can be extended to 1800 km are listed in Table 4 based on the Parzen smoother.

Velocity

Instrument	Averaging Period	Resolution from Parzen	Resolution from Loess	Percent Improvement
SWOT	Snapshot	32 km	23 km	28%
SWOT	4 days	52 km	36 km	31%
SWOT	14 days	132 km	107 km	19%
WaCM	Snapshot	130 km	99 km	24%
WaCM	4 days	60 km	52 km	13%
WaCM	14 days	28 km	25 km	11%

Vorticity

Instrument	Averaging Period	Resolution from Parzen	Resolution from Loess	Percent Improvement
SWOT	Snapshot	54 km	34 km	37%
SWOT	4 days	—	100 km	—
SWOT	14 days	—	143 km	—
WaCM	Snapshot	130 km	89 km	32%
WaCM	4 days	87 km	71 km	18%
WaCM	14 days	62 km	50 km	19%

Table 4. The resolution capabilities deduced in Secs. 6, 8 and 10 for maps of the surface ocean velocity and vorticity based on spatial smoothing of WaCM data using the Parzen smoother for: a) instantaneous snapshots of velocity; b) instantaneous snapshots of vorticity; c) 4-day averages of velocity; d) 4-day averages of vorticity; e) 14-day averages of velocity; and f) 14-day averages of vorticity. The results are listed for combinations of 1200 km and 1800 km swath widths and standard deviations of $\sigma_{spd} = 0.50$ m s^{-1} and 0.25 m s^{-1} for the uncorrelated errors of WaCM measurements of current speed. The swath width for instantaneous maps of velocity and vorticity in a) and b) is assumed to be the full CCS model domain, which is very nearly achieved with a swath width of 1800 km (see Fig. 41). Example maps with the resolutions listed in Tables a–d are shown in Figs. 48–50.

a) Instantaneous Velocity Maps

Swath Width	Measurement Noise σ_{spd} 0.50 m s^{-1}	0.25 m s^{-1}
CCS Model	130 km	50 km

b) Instantaneous Vorticity Maps

Swath Width	Measurement Noise σ_{spd} 0.50 m s^{-1}	0.25 m s^{-1}
CCS Model	130 km	74 km

c) 4-Day Averaged Velocity Maps

Swath Width	Measurement Noise σ_{spd} 0.50 m s^{-1}	0.25 m s^{-1}
1200 km	60 km	26 km
1800 km	44 km	18 km

d) 4-Day Averaged Vorticity Maps

Swath Width	Measurement Noise σ_{spd} 0.50 m s^{-1}	0.25 m s^{-1}
1200 km	87 km	59 km
1800 km	70 km	45 km

e) 14-Day Averaged Velocity Maps

Swath Width	Measurement Noise σ_{spd} 0.50 m s^{-1}	0.25 m s^{-1}
1200 km	28 km	11 km
1800 km	21 km	10 km

f) 14-Day Averaged Vorticity Maps

Swath Width	Measurement Noise σ_{spd} 0.50 m s^{-1}	0.25 m s^{-1}
1200 km	62 km	42 km
1800 km	51 km	34 km

Figure Captions

Figure 1. Snapshots for a region off the central California coast from ROMS models of the California Current System (CCS) with grid resolutions of 4, 1.5 and 0.5 km (left to right): Row a) Sea surface height; Row b) Sea surface temperature; and Row c) Normalized vorticity ζ/f, where f is the local Coriolis parameter at each grid point.

Figure 2. A representative summertime snapshot of sea surface temperature (SST) from the ROMS model of the CCS on 5 June (left panel) in latitude-longitude coordinates at the full 0.5 km $\times$ 0.5 km grid resolution of the model. The model was forced by the seasonal cycle wind stress derived from QuikSCAT scatterometer data, which is shown for the month of June in the right panel. The box in each panel delineates the truncation of the full model domain to mitigate edge effects in the analyses of spatially smoothed fields considered in this study.

Figure 3. Snapshots from the ROMS model for the same time as the SST map in Fig. 2 at the full 0.5 km $\times$ 0.5 km grid resolution of the model: Column a) the speed of the total surface velocity; and Column b) the normalized vorticity ζ/f computed from the total surface velocity, where f is the local Coriolis parameter at each grid point. The maps are for the truncated domain delineated by the boxes in Fig. 2 in the model x, y coordinate system that is rotated by a polar angle of 24° relative to latitude-longitude coordinates. The bottom panels are enlargements of the Central California Current System (CCCS) region delineated by a box in each of the top panels.

Figure 4. a) The scale dependencies of the 80^{th}, 90^{th}, 95^{th} and 99^{th} percentile points of the distributions of absolute values of the normalized vorticity ζ/f as functions of half-power filter cutoff wavelength; the dashed line corresponds to the root-mean squared value of ζ/f. b) The scale dependencies of selected percentage points symmetric about the median (i.e., the 50^{th} percentile point) in the distributions of ζ/f as functions of half-power filter cutoff wavelength; the dashed line corresponds to the mean value of ζ/f, which is indistinguishable from zero. For both panels, ζ was computed from error-free model fields of total surface velocity for the complete CCS model domain at the full 0.5 km $\times$ 0.5 km grid resolution of the model after 2-dimensional isotropic smoothing with the half-power filter cutoff wavelengths indicated along the abscissa.

Figure 5. The same as Fig. 3, except snapshots from the ROMS model for: Column a) SSH; Column b) the magnitude of geostrophically computed velocity; and Column c) normalized geostrophically computed vorticity ζ_g/f.

Figure 6. Column a) Maps of the ageostrophic velocity vectors defined to be the vector differences of the total surface velocity minus the geostrophically computed velocity with the magnitudes of the differences shown in color. Column b) The large-scale ageostrophic velocity defined to be the vector differences and their magnitudes in a) smoothed isotropically with a half-power filter cutoff wavelength of 150 km, referred to here as the Ekman ageostrophic velocity field. Column c) The magnitudes of the non-Ekman ageostrophic velocity vectors defined to be the total ageostrophic velocities in Column a) minus the large-scale ageostrophic velocities in Column b). The bottom panels are enlargements of the CCCS region delineated by a box in each of the top panels. The vectors in Columns a) and b) were subsampled on a 15 km $\times$ 15 km grid in the top panels and a 7.5 km $\times$ 7.5 km grid in the bottom panels.

Figure 7. Maps showing the scale dependence of the magnitudes of the non-Ekman ageostrophic velocities on the 0.5 km $\times$ 0.5 km model grid for the CCCS region after 2-dimensional isotropic smoothing with half-power filter cutoff wavelengths of 10, 20, 30, 40, 60 and 80 km. Note the different color bars for the upper and lower rows of panels.

Figure 8. The scale dependencies of the 80^{th}, 90^{th}, 95^{th} and 99^{th} percentile points of the distributions of the magnitudes of the non-Ekman ageostrophic velocities on the full 0.5 km $\times$ 0.5 km model grid for the full CCS model domain after 2-dimensional isotropic smoothing with the half-power filter cutoff wavelengths indicated along the abscissa. The dashed line corresponds to the root-mean squared (RMS) value of the non-Ekman ageostrophic velocities.

Figure 9. Maps of the differences (left) and ratios (right) of the normalized geostrophically computed vorticity ζ_g/f in Fig. 5c and the normalized total vorticity ζ/f in Fig. 3b after smoothing with a half-power filter cutoff wavelength of 20 km. The bottom panels show binned averages of the gridded values in the maps in the top panels. The vertical bar on each binned average represents the ± 1 standard deviation of the data values within the bin and the smooth lines correspond to the theoretical solutions derived in the text for cyclostrophic motion.

Figure 10. Snapshot maps of the magnitudes of the total velocity, the geostrophically computed velocity and the ageostrophic velocity (top to bottom) for the HF and LF simulations (left and right columns, respectively) of a region of the North Atlantic Ocean off the southeastern seaboard of the U.S. The grid resolution was 0.75 km $\times$ 0.75 km in both simulations. The HF simulation was forced with high-frequency (hourly) winds and tides. The LF simulation was forced with monthly winds and did not include tides. The ribbons of high velocity in the western and northern regions of each map are the Gulf Stream as it flows northward off the Florida coast and then turns northeastward along the continental slope to Cape Hatteras at the northern corner of the model domain. The x and y axis labels are longitude in degrees east and latitude in degrees north and the box in each panel is the area over which the non-Ekman ageostrophic velocities were computed for Figure 11.

Figure 11. Maps showing the scale dependence of the magnitudes of smoothed non-Ekman ageostrophic velocities (defined as in Fig. 6c) from the subregions of the two North Atlantic simulations indicated by the boxes in Fig. 10. The left and right columns correspond to the results for the HF and LF models, respectively, after 2-dimensional isotropic smoothing with half-power filter cutoff wavelengths of 20, 40, 60 and 80 km (top to bottom). The x and y axis labels are distance in kilometers.

Figure 12. The standard deviations of residual errors as functions of half-power filter cutoff wavelength with 2-dimensional isotropic Parzen smoothing for footprint sizes of 1 km and 5 km for SWOT and WaCM, respectively: a) SWOT estimates of SSH; b) Geostrophically computed SWOT estimates of each of the components of velocity (thin solid lines, which are indistinguishable for the two components), and WaCM estimates of each component of the total velocity (thick solid lines, which are again indistinguishable for the two components); and c) geostrophically computed SWOT estimates of vorticity (thin line) and WaCM estimates of the total vorticity (thick line), both normalized by the Coriolis parameter f at the central latitude 37°N of the CCS model domain. The standard deviations were computed from the error variances determined for SWOT and WaCM, respectively, by integrating the analytical formulas in Appendices I.3 and I.4 for each filter cutoff wavelength λ_c. The power-law dependencies on λ_c that are labeled on each curve were determined from log-log versions of each panel (not shown here).

Figure 13. Alongshore wavenumber power spectral densities of simulated satellite estimates of the signals and errors for: Column a) SWOT estimates of (top-to-bottom) SSH and geostrophically computed cross-shore and alongshore velocity and vorticity obtained from simulated pre-processed SWOT data; Column b) the same as Column a), except after isotropic smoothing using a Parzen smoother with the same half-power filter cutoff wavelength of 10 km used in the pre-processing of WaCM data; and Column c) WaCM estimates of (top-to-bottom) cross-shore velocity, alongshore velocity and vorticity obtained from simulated pre-processed WaCM data. The red lines are the signal spectra computed from the model after applying the pre-filtering for SWOT (columns a and b, with additional 10-km smoothing in the latter) and WaCM (column c). The dark blue lines are the spectra computed empirically from the simulated error fields, which were computed geostrophically based on the local value of the Coriolis parameter f at each grid point in the case of SWOT. The green lines are the theoretical spectra of errors derived in Appendix I, which are based on the constant value of f at the central latitude 37°N of the CCS model domain in the case of SWOT. All of the spectra were smoothed by ensemble averaging over the individual spectra computed from alongshore grid lines that extend the full length of the model domain with a cross-shore spacing of 5 km. For reference, selected power-law rolloff dependencies on alongshore wavenumber l are labeled in the top panels of Columns a and b. Note that the rolloff of $l^{-7/2}$ is not significantly different from the rolloff of $l^{-11/3}$ that was deduced from along-track altimeter data by Le Traon et al. (2008) and is consistent with the $l^{-5/3}$ spectral rolloff of velocity in surface quasigeostrophic (SQG) theory (Held et al., 1995).

Figure 14. Alongshore wavenumber power spectral densities of simulated satellite estimates of the signals and errors after 2-dimensional isotropic smoothing of the pre-processed SWOT data with half-power filter cutoff wavelengths of 20, 50 and 80 km (left, middle and right columns, respectively) for: Row a) SSH; Row b) geostrophically computed cross-shore velocity; Row c) geostrophically computed alongshore velocity; and Row d) geostrophically computed vorticity. The solid red lines are the signal spectra from the model after isotropic smoothing. The dark blue lines are the spectra computed empirically from the smoothed error fields constructed based on the local Coriolis parameter f at each grid point The green lines are the theoretical spectra of smoothed SWOT error fields derived in Appendix I.2 based on the constant value of f at the central latitude 37°N of the CCS model domain. For reference, the dashed red and green lines are the signal spectra and theoretical error spectra in Fig. 13a based on the pre-processed SWOT data without additional smoothing in simulated ground-based post-processing. All of the spectra were smoothed by ensemble averaging as in Fig. 13.

Figure 15. Alongshore wavenumber power spectral densities of simulated satellite estimates of the signals and errors after 2-dimensional isotropic smoothing of the pre-processed WaCM data with half-power filter cutoff wavelengths of 20, 50 and 80 km (left, middle and right columns, respectively) for: Row a) alongshore velocity; Row b) cross-shore velocity; and Row c) vorticity. The solid red lines are the signal spectra from the model after smoothing. The dark blue lines are the spectra computed empirically from the simulated error fields after smoothing and the green lines are the theoretical spectra of smoothed error fields derived in Appendix I.4. For reference, the dashed red and green lines are the signal spectra and theoretical error spectra from Fig. 13c for the pre-processed WaCM data without additional smoothing in simulated ground-based post-processing. All of the spectra were smoothed by ensemble averaging as in Fig. 13.

Figure 16. Examples showing the characteristics of noisy data after isotropic 2-dimensional smoothing to achieve signal-to-noise standard deviation ratios of 1, 2 and 3.16 (rows a, b and c, respectively). For illustration purposes, these are maps of the normalized vorticity ζ/f constructed from simulated noisy WaCM data as in Sec. 6.2 below for the case of uncorrelated speed measurement errors with a standard deviation of $\sigma_{spd} = 0.50$ m s^{-1}. The left, middle and right columns show, respectively, the noisy estimates of ζ/f, the error-free ζ/f signal and the residual errors after smoothing with the half-power filter cutoff wavelength λ_c labeled to the left of each row.

Figure 17a. Maps of simulated SWOT estimates of SSH for the CCCS region shown in the bottom panel of Fig. 5a. The top panels are the error-free fields from the pre-processed SWOT data with no additional smoothing (left), and after isotropic 2-dimensional smoothing with half-power filter cutoff wavelengths of 20, 50 and 80 km (columns 2, 3 and 4, respectively). The bottom panels show the fields computed with the addition of simulated uncorrelated SSH measurement errors with a standard deviation of $\sigma_h = 2.74$ cm but without sampling errors (i.e., as if the measurement swaths spanned the full CCS model domain on each satellite overpass). The same color bar is used for all of the panels.

Figure 17b. The same as Fig. 17a, except maps of simulated SWOT estimates of the magnitudes of geostrophically computed surface velocity for the CCCS region shown in the bottom panel of Fig. 5b. The panels in the top row were computed from error-free SSH fields and the panels in the bottom row were computed with the addition of simulated uncorrelated SSH measurement errors with a standard deviation of $\sigma_h = 2.74$ cm. The same color bar is used for all of the panels and the signal-to-noise standard deviation ratio is labeled above each of the bottom panels.

Figure 17c. The same as Fig. 17a, except maps of simulated SWOT estimates of geostrophically computed and normalized vorticity ζ_g/f for the CCCS region shown in the bottom panel of Fig. 5c. The panels in the top row were computed from error-free SSH fields and the panels in the bottom row were computed with the addition of simulated uncorrelated SSH measurement errors with a standard deviation of $\sigma_h = 2.74$ cm. The same color bar is used for all of the panels and the signal-to-noise standard deviation ratio is labeled above each of the bottom panels.

Figure 18. The scale dependencies of the ratios of the standard deviations of the signal and the uncorrelated measurement errors for a snapshot of the full CCS region from simulated a) SWOT; and b) WaCM estimates

of instantaneous surface velocity (thin lines) and vorticity (thick lines) after isotropic 2-dimensional smoothing using a Parzen smoother with the half-power filter cutoff wavelengths indicated along the abscissas. The velocity and vorticity were computed geostrophically for SWOT. The gray areas correspond to signal-to-noise (S/N) standard deviation ratios less than 3.16, which is equivalent to a signal-to-noise variance ratio of 10. The vertical dashed lines indicate the wavelengths above which the signal-to-noise standard deviation ratios exceed 3.16. The dynamic range of the abscissa is larger in b) to accommodate the lower S/N ratios of WaCM estimates of velocity and vorticity with the baseline speed standard deviation of $\sigma_{spd} = 0.5$ m s^{-1} of the uncorrelated errors of WaCM measurements of velocity. The improved resolution capabilities that would be achieved from WaCM with smaller measurement errors are summarized in Fig. 44 and Tables 4a and b.

Figure 19a. Maps of simulated WaCM estimates of the magnitudes of the total surface velocity for the CCCS region shown in the bottom panel of Fig. 3a. The top panels are the error-free fields from the pre-processed WaCM data with no additional smoothing (left), and after isotropic 2-dimensional smoothing with half-power filter cutoff wavelengths of 20, 50 and 80 km (columns 2, 3 and 4, respectively). The bottom panels show the fields computed with the addition of simulated uncorrelated velocity measurement errors with a speed standard deviation of $\sigma_{spd} = 0.5$ m s^{-1} equally partitioned between the two velocity components. The same color bar is used for all of the panels and the signal-to-noise standard deviation ratio is labeled above each of the bottom panels.

Figure 19b. The same as Fig. 19a, except maps of simulated WaCM estimates of normalized vorticity ζ/f computed from the total surface velocity for the CCCS region shown in the bottom panel of Fig. 3b. The same color bar is used for all of the panels and the signal-to-noise standard deviation ratio is labeled above each of the bottom panels.

Figure 20. Examples of the measurement swaths for single ascending and descending overpasses of SWOT (top panels) and WaCM with a swath width of 1200 km (bottom panels) overlaid on the snapshot of the normalized vorticity ζ/f from the top panel of Fig. 3b. The improved sampling coverage by WaCM with a swath width of 1800 km is shown in Fig. 41. The ground tracks for SWOT in this figure are the actual planned orbit. The ground tracks for WaCM are for illustrative purposes and could be adjusted longitudinally to optimize the sampling of any specific region of the world ocean. The details of the sampling of the CCS region would change accordingly.

Figure 21. Time and relative longitude plots of sequential ascending ground track overpasses of SWOT and WaCM measurements along a fixed latitude. There are analogous sampling patterns for the descending overpasses, except shifted approximately half a day later in time. The sampling pattern shown for SWOT is based on the orbit parameters of the planned 21-day exact repeat mission. The sampling pattern shown for WaCM is based on the orbit parameters for the 4-day exact repeat QuickSCAT mission. For reference, the vertical dashed lines in both panels indicate the longitudinal extent of the western and eastern corners of the CCS model domain and the two pairs of horizontal dotted lines in both panels indicate the two 4-day subcycles of SWOT sampling of the CCS model domain during each 21-day exact repeat period of the SWOT orbit.

Figure 22. Illustration of the two 4-day subcycles of SWOT sampling of the CCS model domain over a 14-day interval of the 21-day exact repeat period (see the left panel of Fig. 21). The swaths from the first 4-day subcycle (days 3.5–7.0) are shown in blue in the left panel and the swaths from the second 4-day subcycle (days 13.5–17.0) are shown in red in the middle panel. The combined swaths from the two 4-day subcycles are overlaid in the right panel. The intersecting diagonal lines overlaid on the right panel are the ground tracks of the 10-day exact repeat orbit of the TOPEX, Jason-1, Jason-2 and Jason-3 altimeters.

Figure 23. Histograms of the numbers of samples by SWOT and WaCM (thin and thick lines, respectively) during the first 4 days and the full 14 days (top and bottom panels, respectively) of the 14-day sampling period for the CCS model domain during each 21-day exact repeat period of the SWOT orbit. The histogram values are expressed as percentages of the total number of grid points in the CCS model domain. The

histograms for WaCM are based on a swath width of 1200 km. The improved sampling by WaCM with a swath width of 1800 km is shown later in Fig. 42.

Figure 24. An illustration of the effects of time averaging on error-free surface velocity and vorticity fields centered on the same date as the snapshots in Fig. 3: Column a) The instantaneous snapshots (the same as the top panels of Figs. 3a and b, repeated here for easy comparison with the other two panels of this figure); Column b) Four-day average maps; and Column c) Fourteen-day average maps. The averages were constructed from model output at intervals of 0.5 days. The velocity maps in the top panels of columns b) and c) are the magnitudes of the 4-day and 14-day vector-averaged velocity fields.

Figure 25. Alongshore wavenumber spectra of velocity and normalized vorticity computed from the model surface velocity fields for the instantaneous snapshot, the 4-day average and the 14-day average (thin, medium and thick lines, respectively) shown in Fig. 24. The velocity spectra for 4-day and 14-day averages were computed from the magnitudes of the vector-averaged velocity fields over the respective time periods. The smoothed spectra were computed by ensemble averaging as in Figs. 13–15, except from the raw 0.5 km × 0.5 km grid with a cross-shore spacing of 5 km.

Figure 26. Maps of 4-day averaged SSH computed from error-free and noisy simulated SWOT measurements of SSH with isotropic 2-dimensional smoothing using a Parzen smoother with a half-power filter cutoff wavelength of 25 km: Column a) The 4-day average over the full model domain computed from error-free model SSH fields at a time step of 0.5 day over the 4-day period; Column b) The 4-day average over the full model domain computed from model SSH fields at a time step of 0.5 day over the 4-day period with simulated uncorrelated measurement errors with a standard deviation of $\sigma_h = 2.74$ cm; Column c) The 4-day average computed from simulated SWOT swath sampling of error-free model SSH fields at the times and locations of each satellite observation over the 4-day period; and Column d) The 4-day average computed from simulated SWOT swath sampling of model SSH fields at the times and locations of each satellite observation over the 4-day period with simulated uncorrelated measurement errors with a standard deviation of $\sigma_h = 2.74$ cm. The bottom panels are the error maps computed by subtracting the error-free map in Column a) from the error-contaminated maps in the top row of the respective Columns b)–d).

Figure 27. The same as Fig. 26, except for 14-day averages of SSH computed from simulated SWOT measurements of SSH with isotropic 2-dimensional smoothing using a Parzen smoother with a half-power filter cutoff wavelength of 25 km.

Figure 28. Maps of the magnitudes of 4-day averages of surface velocity computed geostrophically from error-free and noisy simulated SWOT measurements of SSH with isotropic 2-dimensional smoothing using a Parzen smoother with a half-power filter cutoff wavelength of 25 km: Column a) The 4-day average over the full model domain computed geostrophically from error-free model SSH fields at a time step of 0.5 day over the 4-day period; Column b) The 4-day average over the full model domain computed geostrophically from model SSH fields at a time step of 0.5 day over the 4-day period with simulated uncorrelated SSH measurement errors with a standard deviation of $\sigma_h = 2.74$ cm; Column c) The 4-day average computed geostrophically from simulated SWOT swath sampling of error-free model SSH fields at the times and locations of each satellite observation over the 4-day period; and Column d) The 4-day average computed geostrophically from simulated SWOT swath sampling of model SSH fields at the times and locations of each satellite observation over the 4-day period with simulated uncorrelated SSH measurement errors with a standard deviation of $\sigma_h = 2.74$ cm. The bottom panels are the error maps computed by subtracting the error-free map in Column a) from the error-contaminated maps in the top row of the respective Columns b)–d).

Figure 29. The same as Fig. 28, except the magnitudes of 14-day averages of surface velocity computed geostrophically from simulated SWOT measurements of SSH with isotropic 2-dimensional smoothing using a Parzen smoother with a half-power filter cutoff wavelength of 25 km.

Figure 30. The S/N standard deviation ratios for the full CCS region for the magnitude of the vector-averaged velocity (referred to for expedience as "velocity") computed from simulated satellite estimates of

time-averaged SSH (for SWOT) and surface velocity (for WaCM) as functions of the half-power filter cutoff wavelength of 2-dimensional isotropic smoothing using a Parzen smoother: a) Geostrophically computed SWOT estimates of 4-day averaged velocity; b) Geostrophically computed SWOT estimates of 14-day averaged velocity; c) WaCM estimates of 4-day averaged velocity; and d) WaCM estimates of 14-day averaged velocity. The dotted lines correspond to estimates over the full model domain with simulated uncorrelated measurement errors ($\sigma_h = 2.74$ cm for SWOT and $\sigma_{spd} = 0.5$ m s^{-1} for WaCM). The dashed lines correspond to estimates from simulated swath sampling of error-free fields. The thick solid lines correspond to estimates from simulated swath sampling with uncorrelated measurement errors ($\sigma_h = 2.74$ cm for SWOT and $\sigma_{spd} = 0.5$ m s^{-1} for WaCM). The S/N ratios for WaCM are based on a swath width of 1200 km. The improved S/N ratios for WaCM with a swath width of 1800 km are shown later in Fig. 43a and b. The gray area in each panel indicates S/N standard deviation ratios less than 3.16, which corresponds to a S/N variance ratio of 10. The vertical dashed line in each panel indicates the wavelength above which the S/N standard deviation ratios exceed a value of 3.16 for the case of combined measurement and sampling errors.

Figure 31. Maps of the magnitudes of 4-day averages of surface velocity from error-free and noisy simulated WaCM measurements of surface velocity with a swath width of 1200 km and a standard deviation of $\sigma_{spd} = 0.5$ m s^{-1} for the speed measurement noise with isotropic 2-dimensional smoothing using a Parzen smoother with a half-power filter cutoff wavelength of 25 km: Column a) The 4-day average over the full model domain computed from error-free model surface velocity fields at a time step of 0.5 day over the 4-day period; Column b) The 4-day average over the full model domain computed from model surface velocity fields at a time step of 0.5 day over the 4-day period with simulated uncorrelated speed measurement errors with a standard deviation of $\sigma_{spd} = 0.5$ m s^{-1}; Column c) The 4-day average computed from simulated WaCM swath sampling of error-free model surface velocity fields at the times and locations of each satellite observation over the 4-day period; and Column d) The 4-day average computed from simulated WaCM swath sampling of model surface velocity fields at the times and locations of each satellite observation over the 4-day period with simulated uncorrelated speed measurement errors with a standard deviation of $\sigma_{spd} = 0.5$ m s^{-1}. The bottom panels are the error maps computed by subtracting the error-free map in Column a) from the error-contaminated maps in the top row of the respective Columns b)–d).

Figure 32. The same as Fig. 31, except the magnitudes of 14-day averages of surface velocity from WaCM with isotropic 2-dimensional smoothing using a Parzen smoother with a half-power filter cutoff wavelength of 25 km.

Figure 33. Maps of 4-day averages of normalized surface vorticity ζ_g/f computed geostrophically from error-free and noisy simulated SWOT measurements of SSH with isotropic 2-dimensional smoothing using a Parzen smoother with a half-power filter cutoff wavelength of 50 km. The various combinations of measurement and sampling errors are the same as for Columns a)–d) of Figs. 26 and 28. The bottom panels are the error maps computed by subtracting the error-free map in Column a) from the error-contaminated maps in the top row of the respective Columns b)–d). In order to see the relatively small effects of measurement errors alone, the color bar for the bottom panel of Column b differs from the color bar for the bottom panels of Columns c and d.

Figure 34. The same as Fig. 33, except for 14-day averages of normalized vorticity ζ_g/f computed geostrophically from simulated SWOT measurements of SSH with isotropic 2-dimensional smoothing using a Parzen smoother with a half-power filter cutoff wavelength of 50 km.

Figure 35. The S/N standard deviation ratios for the full CCS region from simulated satellite estimates of time-averaged surface vorticity computed from simulated satellite estimates of time-averaged SSH (for SWOT) and surface velocity (for WaCM) as functions of the half-power filter cutoff wavelength of 2-dimensional isotropic smoothing using a Parzen smoother: a) Geostrophically computed SWOT estimates of 4-day averaged vorticity; b) Geostrophically computed SWOT estimates of 14-day averaged vorticity; c) WaCM estimates of 4-day averaged total vorticity; and d) WaCM estimates of 14-day averaged total vorticity. The dotted, dashed and thick solid lines correspond to the same combinations of signal and errors as in Fig. 30 and the gray area in each panel indicates S/N standard deviation ratios less than 3.16. The

S/N ratios for SWOT in the top panels never exceed the threshold value of 3.16. The vertical dashed lines for WaCM in the bottom panels indicate the wavelengths above which the S/N standard deviation ratios exceed a value of 3.16 for the case of combined measurement and sampling errors based on a swath width of 1200 km. The improved S/N ratios for WaCM with a swath width of 1800 km are shown in Fig. 43c and d.

Figure 36. Maps of 4-day averages of normalized total surface vorticity ζ/f computed from error-free and noisy simulated WaCM measurements of surface velocity with a swath width of 1200 km and a standard deviation of $\sigma_{spd} = 0.5$ m s^{-1} for the speed measurement noise with isotropic 2-dimensional smoothing using a Parzen smoother with a half-power filter cutoff wavelength of 50 km. The various combinations of measurement and sampling errors are the same as for Columns a)–d) of Fig. 31. The bottom panels are the error maps computed by subtracting the error-free map in Column a) from the error-contaminated maps in the top row of the respective Columns b)–d).

Figure 37. The same as Fig. 36, except for 14-day averages of normalized surface vorticity ζ/f computed from simulated WaCM measurements of surface velocity with 2-dimensional isotropic smoothing using a Parzen smoother with a half-power filter cutoff wavelength of 50 km.

Figure 38. The same as Fig. 18, except the S/N standard deviation ratios from simulated satellite estimates of instantaneous snapshots of surface velocity as functions of the half-power filter cutoff wavelength of 2-dimensional isotropic smoothing using a loess smoother rather than the Parzen smoother used for Fig. 18.

Figure 39. The same as Fig. 30, except the S/N standard deviation ratios from simulated satellite estimates of time-averaged surface velocity as functions of the half-power filter cutoff wavelength of 2-dimensional isotropic smoothing using a loess smoother rather than the Parzen smoother used for Fig. 30.

Figure 40. The same as Fig. 35, except the S/N standard deviation ratios from simulated satellite estimates of time-averaged surface vorticity as functions of the half-power filter cutoff wavelength of 2-dimensional isotropic smoothing using a loess smoother rather than the Parzen smoother used for Fig. 35.

Figure 41. The same as the bottom two panels of Fig. 20, except examples of the measurement swaths for single ascending and descending overpasses of WaCM for the case of a swath width of 1800 km. The ground tracks are for illustrative purposes and could be adjusted longitudinally to optimize the sampling of any specific region of the world ocean. The details of the sampling of the CCS region would change accordingly.

Figure 42. The same as the thick lines in Fig. 23, except histograms of the number of samples by WaCM during 4 days and 14 days based on a swath width of 1800 km rather than 1200 km.

Figure 43. The same as the bottom two panels of Fig. 30 and the bottom two panels of Fig. 35, except the S/N standard deviation ratios for WaCM estimates of 4-day and 14-day averaged velocity and vorticity fields for the baseline standard deviation of $\sigma_{spd} = 0.5$ m s^{-1} for the speed measurement noise and a swath width of 1800 km rather than 1200 km.

Figure 44. The resolution capabilities of WaCM estimates of instantaneous snapshot maps of the full CCS region (which are very nearly achieved on each satellite overpass with a swath width of 1800 km – see Fig. 41) as functions of the standard deviation σ_{spd} of the uncorrelated errors of WaCM measurements of surface velocity: a) maps of velocity; and b) maps of vorticity. The solid and dashed lines in each panel correspond to the half-power filter cutoff wavelengths above which the S/N standard deviation ratios exceed a value of 3.16 using Parzen and loess smoothers, respectively. For reference, the vertical dashed line in each panel indicates a standard deviation of $\sigma_{spd} = 0.25$ m s^{-1} for the uncorrelated speed measurement errors, which corresponds to half of the baseline value of $\sigma_{spd} = 0.5$ m s^{-1}.

Figure 45. The resolution capabilities of WaCM estimates of 4-day and 14-day averages (left and right columns) of surface velocity and vorticity (top and bottom rows) as functions of the standard deviation σ_{spd} of the uncorrelated speed errors of WaCM measurements of surface velocity for swath widths of 1200 km and 1800 km (blue and red lines, respectively). The solid and dashed lines in each panel correspond to the half-power filter cutoff wavelengths above which the S/N standard deviation ratios exceed a value of 3.16 using Parzen and loess smoothers, respectively. For reference, the vertical dashed line in each panel

indicates a standard deviation of $\sigma_{spd} = 0.25$ m s^{-1} for the uncorrelated speed measurement errors, which corresponds to half of the baseline value of $\sigma_{spd} = 0.5$ m s^{-1}.

Figure 46. Maps of 30-day averaged SSH smoothed 2-dimensionally with a half-power filter cutoff wavelength of 200 km in each dimension: Column a) The "true" space-time smoothed field computed from error-free model SSH fields at a time step of 0.5 day over the 30-day period; Column b) The space-time smoothed field computed from simulated TOPEX/Poseidon and ERS-1 nadir altimeter sampling of error-free model SSH fields at the times and locations of each altimeter observation over the 30-day period; and Column c) The space-time smoothed field computed from simulated SWOT swath sampling of error-free model SSH fields at the times and locations of each SWOT observation over the 30-day period. The bottom panels are maps of the sampling errors computed by subtracting the error-free map in Column a) from the satellite-sampled maps in top row of the respective columns b) and c).

Figure 47. The standard deviations of the sampling errors in 2-dimensionally smoothed 30-day and 21-day averaged SSH fields constructed from simulated SWOT data as functions of half-power filter cutoff wavelength. The horizontal dashed line corresponds to the 1.09-cm standard deviation of the sampling errors in the simulated CLS/AVISO SSH field in the bottom panel of Fig. 46b constructed from error-free model SSH fields subsampled at the times and locations of the TOPEX/Poseidon and ERS-1 nadir altimeter observations over a 30-day period.

Figure 48. Space-time smoothed maps of the magnitudes of vector-averaged error-free surface velocity with the wavelength resolutions that can be achieved from presently available altimeter data and from 4-day averages of WaCM data with the combinations of measurement noise σ_{spd} and swath widths listed in Table 4c: a) The resolution of 200 km by 30 days that can be achieved with the geostrophic approximation from SSH maps constructed from presently available merged nadir altimetry data; b) A resolution of 60 km that could be achieved in 4-day averages of WaCM data for a swath width of 1200 km and $\sigma_{spd} = 0.50$ m s^{-1}; c) A resolution of 45 km that could be achieved in 4-day averages of WaCM data for a swath width of 1800 km and $\sigma_{spd} = 0.50$ m s^{-1}; d) A resolution of 25 km that could be achieved in 4-day averages of WaCM data for a swath width of 1200 km and $\sigma_{spd} = 0.25$ m s^{-1}; and e) A resolution of 20 km that could be achieved in 4-day averages of WaCM data for a swath width of 1800 km and $\sigma_{spd} = 0.25$ m s^{-1}.

Figure 49. Space-time smoothed maps of error-free vorticity scaled by the local Coriolis parameter f with the wavelength resolutions that can be achieved from presently available altimeter data and from 4-day averages of WaCM data with the combinations of measurement noise σ_{spd} and swath widths listed in Table 4d: a) The resolution of 200 km by 30-days that can be achieved with the geostrophic approximation from SSH maps constructed from presently available merged nadir altimetry data; b) A resolution of 90 km that could be achieved in 4-day averages of WaCM data for a swath width of 1200 km and $\sigma_{spd} = 0.50$ m s^{-1}; c) A resolution of 70 km that could be achieved in 4-day averages of WaCM data for a swath width of 1800 km and $\sigma_{spd} = 0.50$ m s^{-1}; d) A resolution of 60 km that could be achieved in 4-day averages of WaCM data for a swath width of 1200 km and $\sigma_{spd} = 0.25$ m s^{-1}; and e) A resolution of 45 km that could be achieved in 4-day averages of WaCM data for a swath width of 1800 km and $\sigma_{spd} = 0.25$ m s^{-1}.

Figure 50. Spatially smoothed maps of the magnitudes of vector-averaged error-free surface velocity (top row) and error-free vorticity scaled by the local Coriolis parameter f (bottom row) with the wavelength resolutions that can be achieved from presently available altimeter data and from instantaneous snapshot maps of WaCM data on a single satellite overpass with the combinations of measurement noise σ_{spd} and swath widths listed in Tables 4a and 4b: a) The resolution of 200 km by 30 days that can be achieved for velocity computed geostrophically from presently available merged nadir altimetry data (the same as Fig. 48a); b) A resolution of 130 km that could be achieved for velocity from a snapshot of WaCM data with $\sigma_{spd} = 0.50$ m s^{-1}; c) A resolution of 50 km that could be achieved for velocity from a snapshot of WaCM data with $\sigma_{spd} = 0.25$ m s^{-1}; d) The resolution of 200 km by 30 days that can be achieved for vorticity from presently available merged nadir altimetry data (the same as Fig. 49a); e) A wavelength resolution of 75 km that could be achieved from a snapshot of WaCM data with $\sigma_{spd} = 0.50$ m s^{-1}; and f) A wavelength resolution of 75 km that could be achieved from a snapshot of WaCM data with $\sigma_{spd} = 0.25$ m s^{-1}.

Figure A1. The weighting functions (top panels) and log-linear plots of the squared filter transfer functions (bottom panels) for uniformly weighted running-average smoothers with spans of 1 km and 0.5 km (thin lines in panels a and b, respectively) and for a Parzen weighted running average smoother with a span of 1 km (thick line in panel b).

Figure B1. The weighting functions (top panels), log-linear plots of the squared filter transfer functions (middle panels) and lagged autocorrelation functions (bottom panels) for Parzen smoothers with spans of 2 km (Column a) and 10 km (Column b) that are used in this study to simulate pre-filtering of SWOT data and WaCM data, respectively. The half-power filter cutoff wavelengths of these Parzen smoothers (shown by the dotted lines in the middle panels) are approximately 2 km and 10 km. The dotted lines in the bottom panels indicate the lags at which the autocorrelation functions decay to values of 0.5 and 0.05.

Figure C1. Log-log plots of the squared filter transfer functions of Parzen smoothers with half-power filter cutoff wavelengths of 20, 50 and 80 km (thin solid, thick solid and dashed lines, respectively). The horizontal dotted line corresponds to an ordinate value of 0.5. The half-power filter cutoff wavelengths for the Parzen smoothers are shown by the three vertical dotted lines, which are the wavenumbers at which each squared filter transfer function intersects the horizontal dotted line.

Figure C2. Log-log plots of the squared filter transfer functions with a half-power filter cutoff wavelength of 50 km for the Parzen smoother (thick line, which is the same as the thick line in Fig. C1) and a Gaussian-weighted smoother (thin line). The horizontal dotted line corresponds to an ordinate value of 0.5 and the vertical dotted line is the wavenumber at which the two squared filter transfer functions intersect the horizontal dotted line.

Figure C3. Log-log plots of the squared filter transfer functions with a half-power filter cutoff wavelength of 50 km for the Parzen smoother (thick line, which is the same as the thick line in Fig. C1), the loess smoother (thick dashed line) and the uniformly weighted running average smoother (thin dashed line). The horizontal and vertical dotted lines are the same as in Fig. C2.

Figure D1. The ratio $R_L = \sigma_4^2/\sigma_1^2$ of the residual variance σ_4^2 after filtering uncorrelated white noise using a Parzen smoother with a span of $L_4 = 4L$ and the residual variance σ_1^2 after filtering with a uniform-weighted running average with a span of $L_1 = L$. The dots correspond to the analytical approximation given by Equation (D.11) and the solid line is the exact solution obtained by numerical integration of Equation (D.8).

Figure F1. The current projected performance of the SWOT instrument. The graph shows the dependencies of the standard deviation of uncorrelated errors of SWOT measurements of SSH on significant wave height (SWH) and swath location relative to the satellite ground track. The seven solid lines correspond to SWH values increasing from 2 m to 8 m at increments of 1 m (bottom to top). The errors for 0-m SWH are essentially the same as those shown for 2-m SWH. This projected performance incorporates improvements over the baseline science requirements for SWOT. The horizontal dashed line is the estimate of the cross-swath average standard deviation of uncorrelated measurement errors derived in Appendix F from the baseline science requirements. [The solid lines in the figure are from Fig. 2.5 of Gaultier et al. (2017).]

Figure F2. The 1-sided, 1-dimensional wavenumber power spectral density of the science requirements for measurement errors of SWOT data before and after (blue and red lines, respectively) smoothing 2-dimensionally in ground-based post-processing to eliminate variability with wavelengths shorter than a half-power filter cutoff wavelength of $\lambda_c = 15$ km (shown by the black dotted line). The dotted red line corresponds to the requirement for red noise from orbit errors and long-wavelength measurement errors. The dashed red line corresponds to the requirement for residual uncorrelated errors after smoothing with an ideal filter that has a magnitude of 1 for wavelengths longer than λ_c and 0 for shorter wavelengths. The solid red line is the sum of the power spectral densities of the red noise and the ideal low-pass filtered uncorrelated errors. The dashed blue line corresponds to the uncorrelated errors in pre-processed SWOT data for a footprint size of 1 km that is derived in Appendix F without the 15-km smoothing. The integrated variance of this white noise is $\sigma_h^2 = 7.5$ cm^2, which corresponds to a noise standard deviation of $\sigma_h = 2.74$ cm. The

solid blue line is the sum of the power spectral densities of the red noise and the white noise in the pre-processed SWOT data. The thick black line is the 68^{th}-percentile SSH signal power spectral density from the SWOT Science Requirements Document (Rodriguez and Callahan, 2016). A power-law rolloff of $l^{-5/2}$ for alongshore wavenumber l is shown for reference as the thin black line. The dashed and solid green lines show, respectively, the spectra of the residual uncorrelated noise and the total noise that would be obtained if the SWOT data were smoothed 2-dimensionally using a realizable Parzen smoother with a half-power filter cutoff wavelength of $\lambda_c = 15$ km.

Figure F3. The alongshore wavenumber power spectral density of SSH computed from the CCS model. The spectrum shown by the red line was smoothed by ensemble averaging over the individual spectra computed from alongshore grid lines that extend the full length of the model domain shown in Fig. 5a with a cross-shore spacing of 5 km. The blue line is the spectrum computed empirically from simulated SSH error fields with a footprint size of 1 km and a standard deviation of $\sigma_h = 2.74$ cm after smoothing 2-dimensionally using a Parzen smoother with a half-power filter cutoff wavelength of $\lambda_c = 15$ km. The green line is the theoretical spectrum of SSH errors derived in Appendix I.1 for the same filtering. The black line is the 68^{th}-percentile SSH spectrum from Fig. F2 that is the basis for defining the science requirements for SWOT. Power-law rolloffs of $l^{-5/2}$ and $l^{-7/2}$ for alongshore wavenumber l are overlaid for reference as thin lines. As noted in the caption for Fig. 13, the rolloff of $l^{-7/2}$ is not significantly different from the rolloff of $l^{-11/3}$ that was deduced from along-track altimeter data by Le Traon et al. (2008) and is consistent with the $l^{-5/3}$ spectral rolloff of velocity in SQG theory (Held et al., 1995).

Figure F4. The wavenumber power spectral densities of SSH computed from the boxed region of the North Atlantic HF and LF simulations shown in Fig. 10 (blue and red lines, respectively). The spectra were smoothed by ensemble averaging over the individual spectra computed from "cross-shore" grid lines (southeast to northwest) over the region shown by the boxes in Fig. 10. The thick black line is the 68^{th}-percentile SSH spectrum from Figs. F2 and F3 that defines the science requirements for SWOT and the green line is the theoretical spectrum of SSH errors derived in Appendix I.1 and shown previously in Fig. F3 after smoothing 2-dimensionally using a Parzen smoother with a half-power filter cutoff wavelength of $\lambda_c = 15$ km. Power-law rolloffs of l^{-5}, l^{-3} and $l^{-5/2}$ for wavenumber l are overlaid for reference as thin lines.

Figure H1. Log-log plots of the squared filter transfer functions (also referred to as the response functions) for centered differences. The thick solid and dashed lines are for, respectively, 3-point and 9-point centered differences on a 1 km grid. The thin solid and dashed lines are for 3-point and 9-point centered differences on a 5 km grid assuming that the discretely sampled data on the 5 km grid have been filtered to attenuate variability at wavenumbers higher than the Nyquist wavenumber of 0.1 cpkm. The short dashed straight line in this log-log plot corresponds to the $(2\pi k)^2$ response function for derivatives of a continuous variable.

Figure H2. Log-log plots of the filtering from the combined effects of centered differencing and smoothing with a Parzen smoother with half-power filter cutoff wavelengths of $\lambda_c = 20$, 50 and 80 km (top to bottom). This combined filtering consists of the product of the squared filter transfer functions for each operation that are shown in Figs. C1 and H1. The thick solid and dashed lines are for Parzen smoothing of, respectively, 3-point and 9-point centered differences on a 1 km grid. The thin solid and dashed lines are for Parzen smoothing of, respectively, 3-point and 9-point centered differences on a 5 km grid assuming that the discretely sampled data on the 5 km grid have been filtered to attenuate variability at wavenumbers higher than the Nyquist wavenumber of 0.1 cpkm. The thin dashed line becomes indistinguishable from the thick solid and thick dashed lines for smoothing with half-power filter cutoff wavelengths larger than $\lambda_c = 40$ km. All four lines are barely distinguishable for $\lambda_c = 80$ km. The short dashed line corresponds to the $(2\pi k)^2$ response function for derivatives of a continuous variable without smoothing.

Figure I1. Numerical solutions as functions of half-power filter cutoff wavelength λ_c for the integrals labeled in the lower left corner of each panel that appear in the equations in Appendix I: a) The integral on the right sides of Eqs. (I.33a) and (I.33b), which also appears as the second integral on the right sides of Eqs. (I.35a), (I.35b) and (I.35c) and as the integral on the right side of Eq. (I.46b) with $\lambda_c = 10$ km; b) The first integral on the right sides of Eqs. (I.35a), (I.35b) and (I.35c); c) The integral on the right sides of Eqs. (I.48a) and

(I.48b), which also appears as the integral on the right side of Eq. (I.55a) and in the denominator on the right side of Eq. (I.55b); and d) The integral on the right side of Eq. (I.55a) and in the numerator on the right side of Eq. (I.55b). The dashed lines in panels c) and d) correspond to the approximate solutions obtained by replacing the term $W^2_{10\mathrm{km}}(k)$ in the integrands with a value of 1 for all wavenumbers k, as in Eqs. (I.49) and (I.56), respectively.

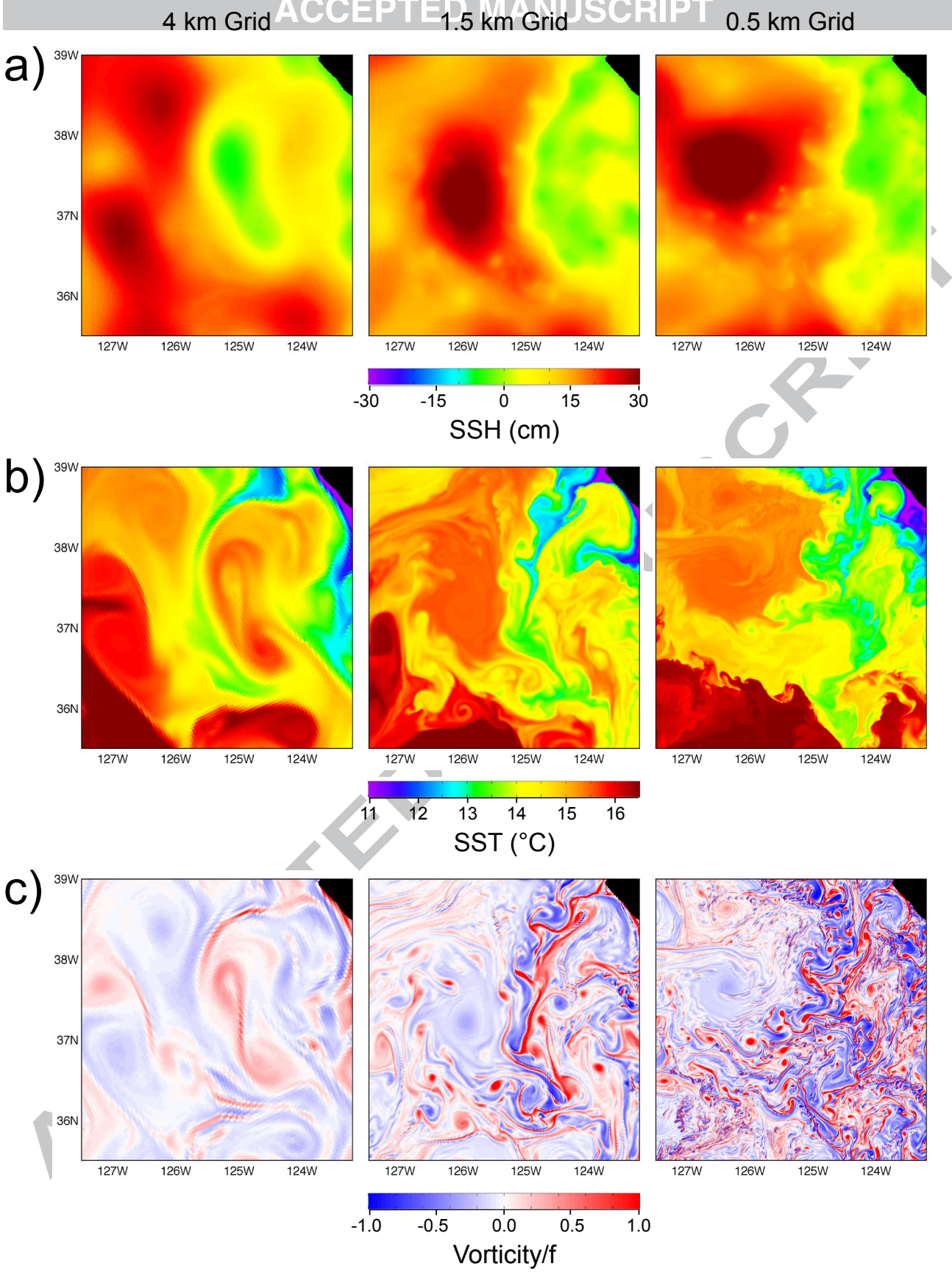

Figure 1. Snapshots for a region off the central California coast from ROMS models of the California Current System (CCS) with grid resolutions of 4, 1.5 and 0.5 km (left to right): Row a) Sea surface height; Row b) Sea surface temperature; and Row c) Normalized vorticity ζ/f, where f is the local Coriolis parameter at each grid point.

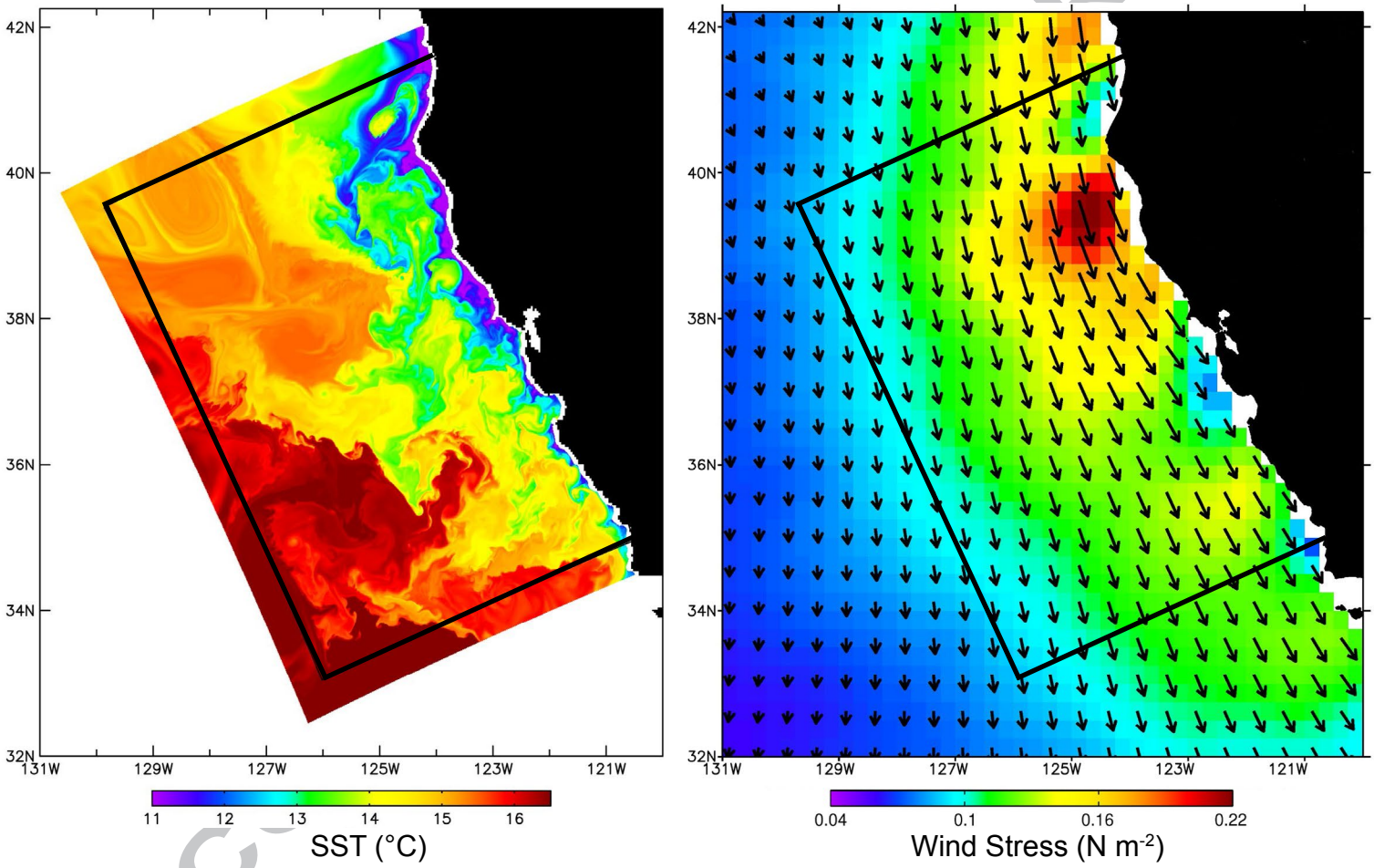

Figure 2. A representative summertime snapshot of sea surface temperature (SST) from the ROMS model of the CCS on 5 June (left panel) in latitude-longitude coordinates at the full 0.5 km × 0.5 km grid resolution of the model. The model was forced by the seasonal cycle wind stress derived from QuikSCAT scatterometer data, which is shown for the month of June in the right panel. The box in each panel delineates the truncation of the full model domain to mitigate edge effects in the analyses of spatially smoothed fields considered in this study.

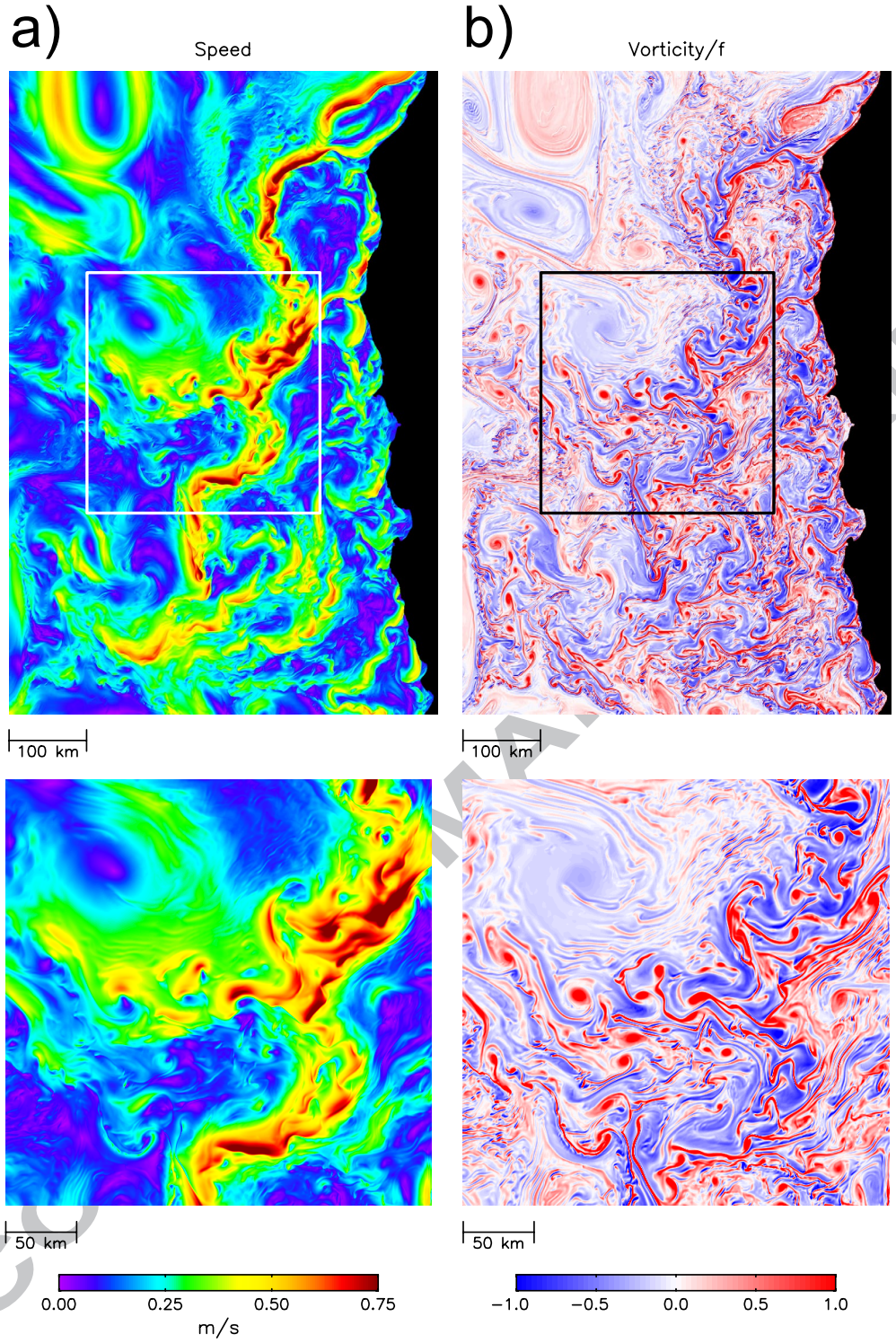

Figure 3. Snapshots from the ROMS model for the same time as the SST map in Fig. 2 at the full 0.5 km × 0.5 km grid resolution of the model: Column a) the speed of the total surface velocity; and Column b) the normalized vorticity ζ/f computed from the total surface velocity, where f is the local Coriolis parameter at each grid point. The maps are for the truncated domain delineated by the boxes in Fig. 2 in the model x, y coordinate system that is rotated by a polar angle of 24° relative to latitude-longitude coordinates. The bottom panels are enlargements of the Central California Current System (CCCS) region delineated by a box in each of the top panels.

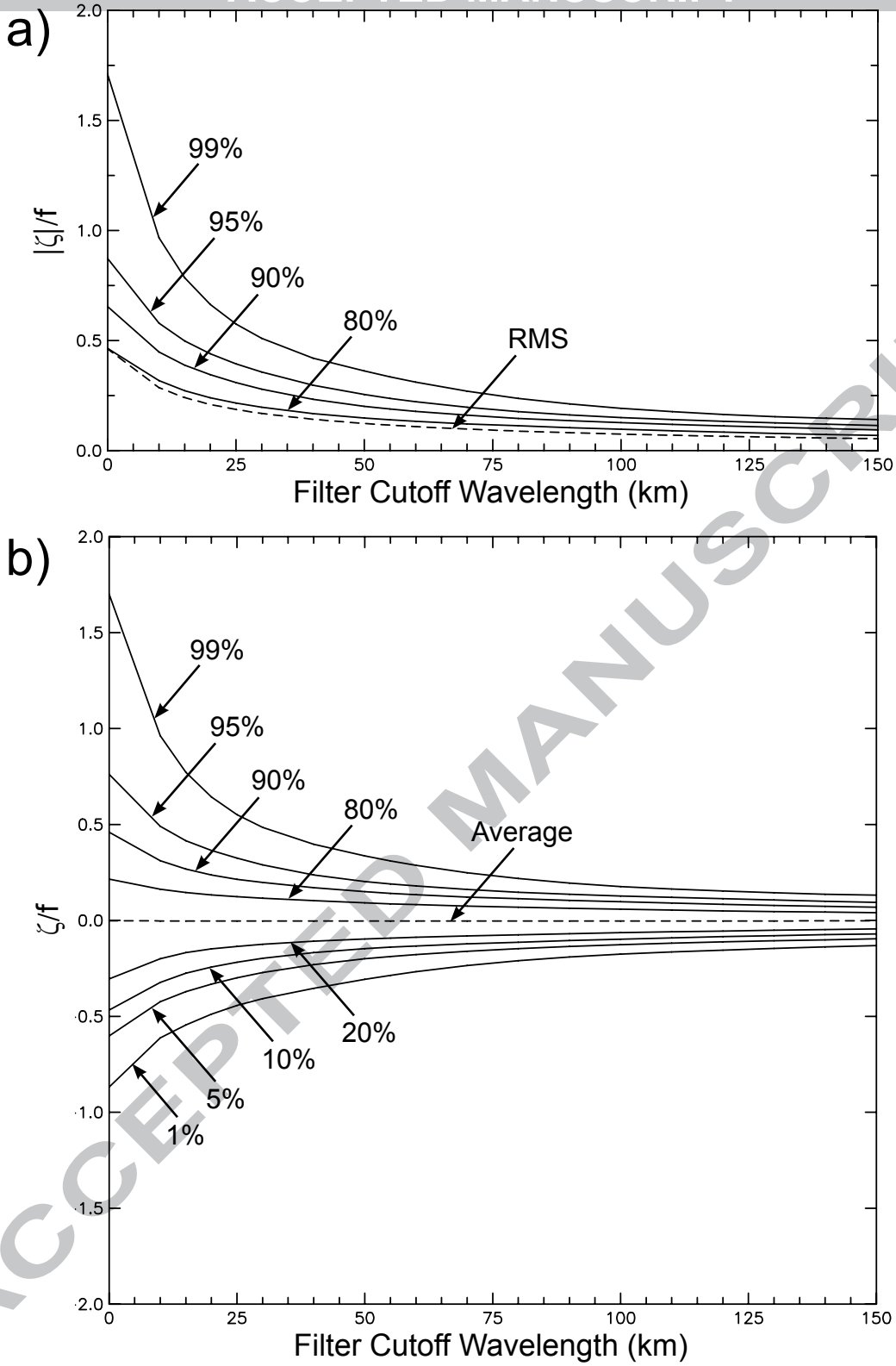

Figure 4. a) The scale dependencies of the 80^{th}, 90^{th}, 95^{th} and 99^{th} percentile points of the distributions of absolute values of the normalized vorticity ζ/f as functions of half-power filter cutoff wavelength; the dashed line corresponds to the root-mean squared value of ζ/f. b) The scale dependencies of selected percentage points symmetric about the median (i.e., the 50^{th} percentile point) in the distributions of ζ/f as functions of half-power filter cutoff wavelength; the dashed line corresponds to the mean value of ζ/f, which is indistinguishable from zero. For both panels, ζ was computed from error-free model fields of total surface velocity for the complete CCS model domain at the full 0.5 km $\times$ 0.5 km grid resolution of the model after 2-dimensional isotropic smoothing with the half-power filter cutoff wavelengths indicated along the abscissa.

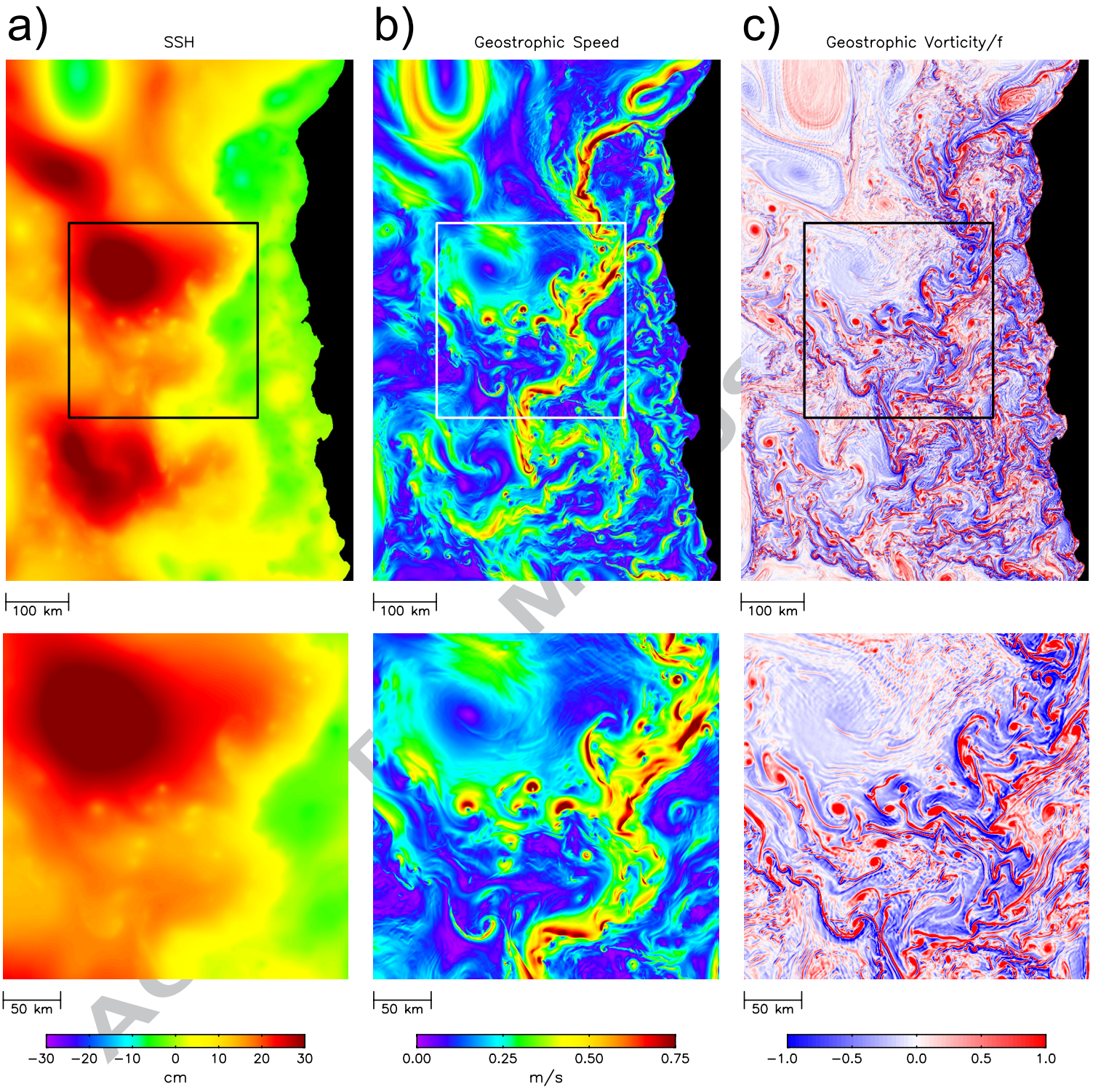

Figure 5. The same as Fig. 3, except snapshots from the ROMS model for: Column a) SSH; Column b) the magnitude of geostrophically computed velocity; and Column c) normalized geostrophically computed vorticity ζ_g/f.

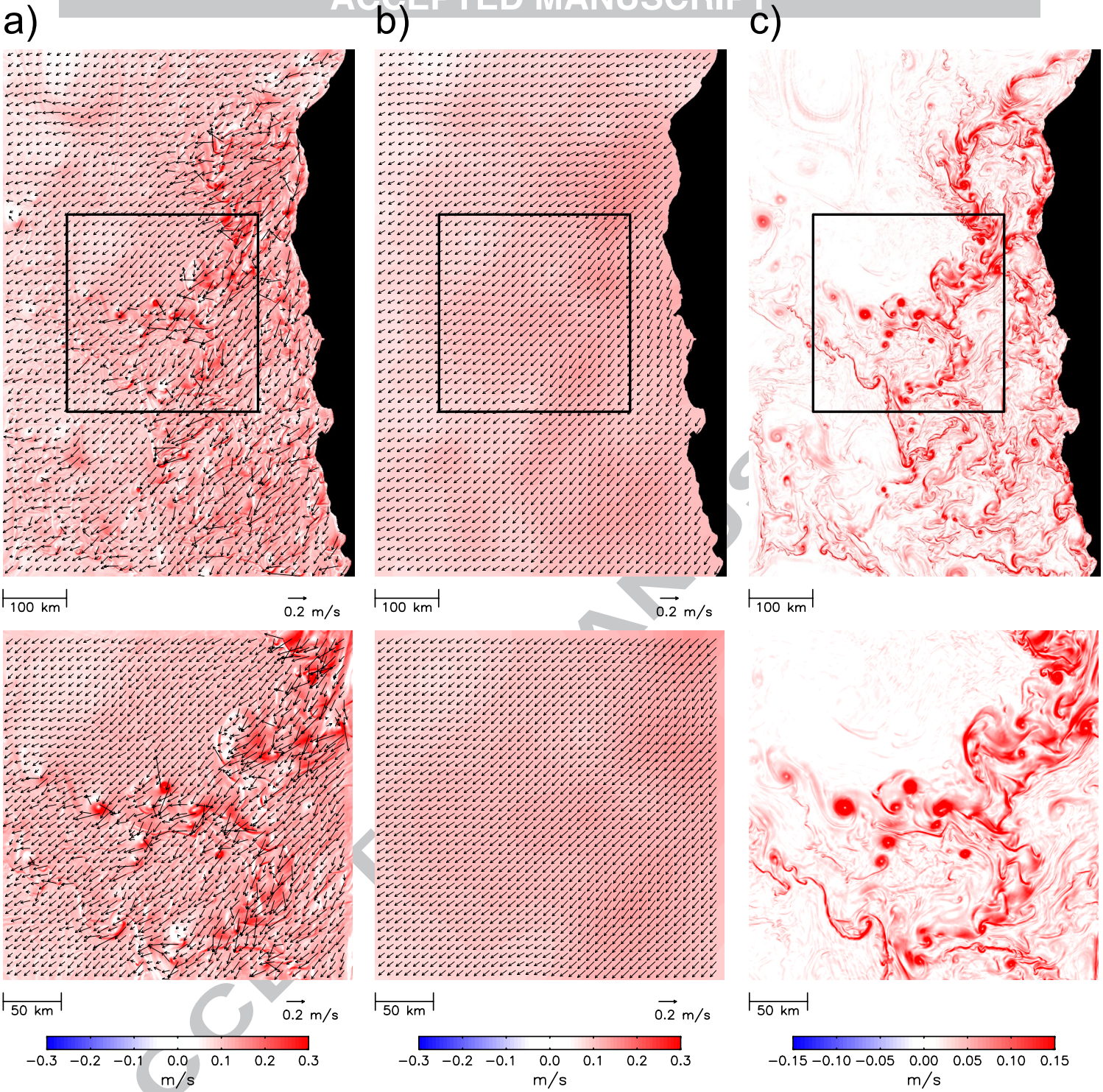

Figure 6. Column a) Maps of the ageostrophic velocity vectors defined to be the vector differences of the total surface velocity minus the geostrophically computed velocity with the magnitudes of the differences shown in color. Column b) The large-scale ageostrophic velocity defined to be the vector differences and their magnitudes in a) smoothed isotropically with a half-power filter cutoff wavelength of 150 km, referred to here as the Ekman ageostrophic velocity field. Column c) The magnitudes of the non-Ekman ageostrophic velocity vectors defined to be the total ageostrophic velocities in Column a) minus the large-scale ageostrophic velocities in Column b). The bottom panels are enlargements of the CCCS region delineated by a box in each of the top panels. The vectors in Columns a) and b) were subsampled on a 15 km × 15 km grid in the top panels and a 7.5 km × 7.5 km grid in the bottom panels.

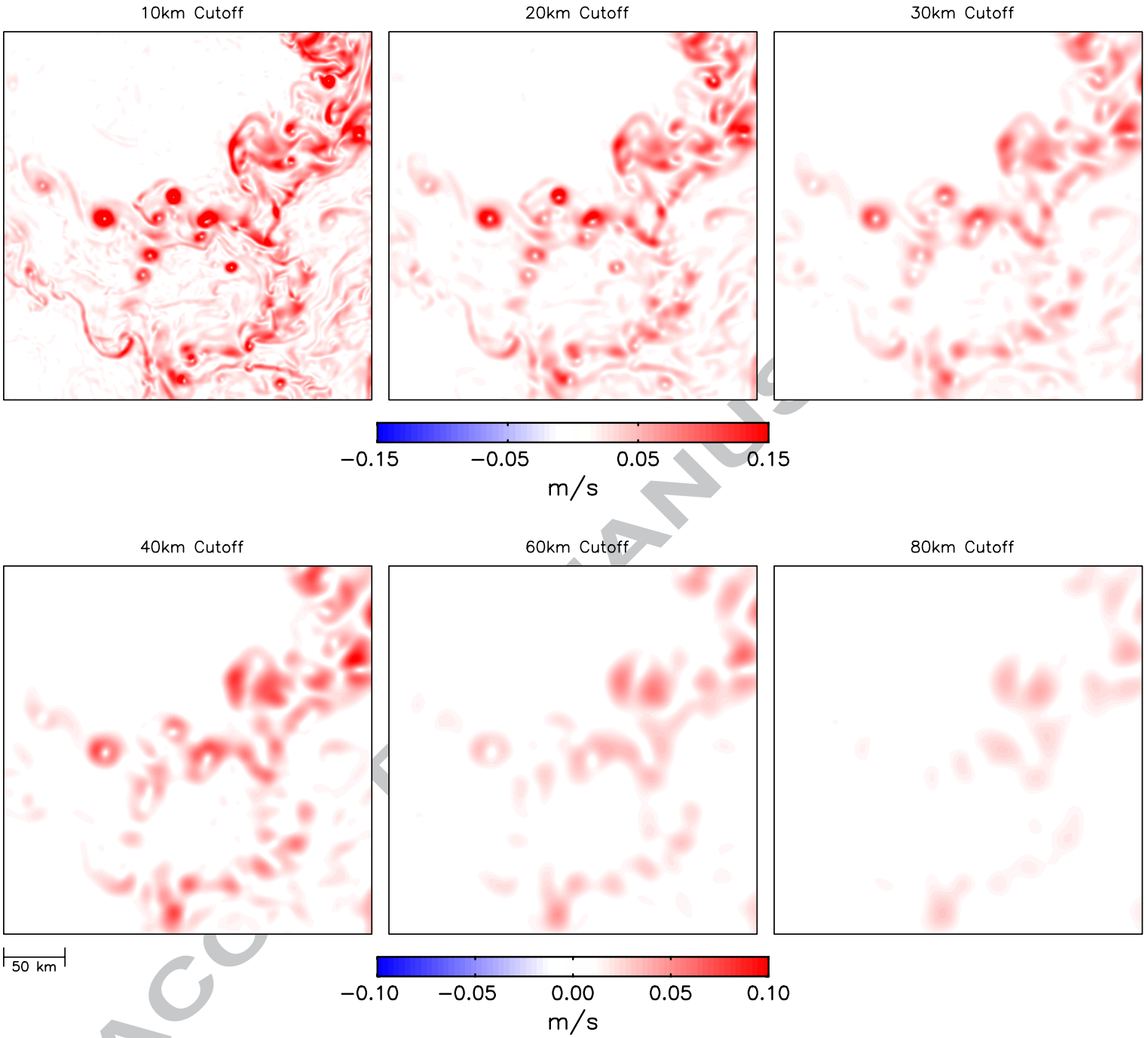

Figure 7. Maps showing the scale dependence of the magnitudes of the non-Ekman ageostrophic velocities on the 0.5 km × 0.5 km model grid for the CCCS region after 2-dimensional isotropic smoothing with half-power filter cutoff wavelengths of 10, 20, 30, 40, 60 and 80 km. Note the different color bars for the upper and lower rows of panels.

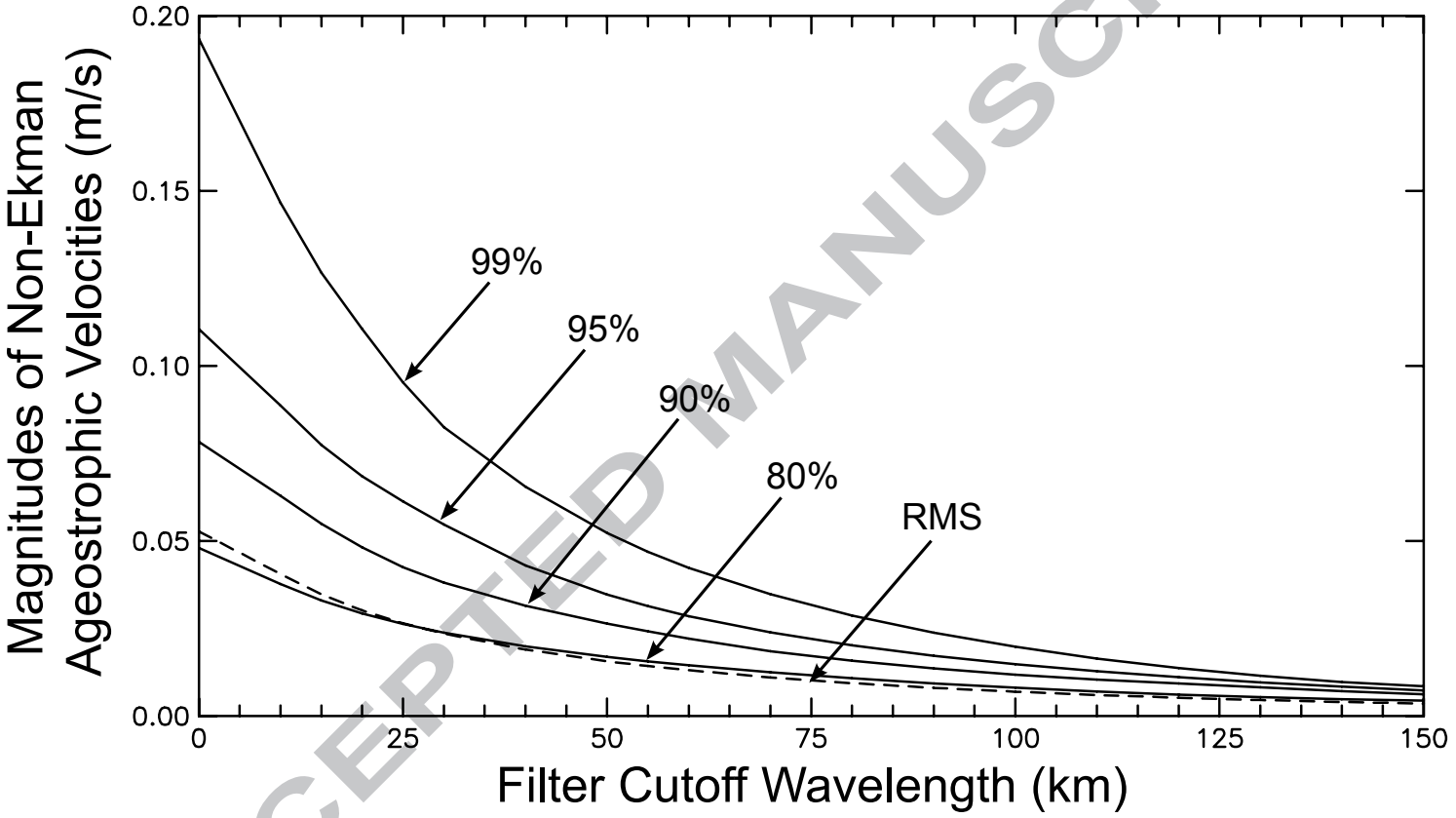

Figure 8. The scale dependencies of the 80^{th}, 90^{th}, 95^{th} and 99^{th} percentile points of the distributions of the magnitudes of the non-Ekman ageostrophic velocities on the full 0.5 km $\times$ 0.5 km model grid for the full CCS model domain after 2-dimensional isotropic smoothing with the half-power filter cutoff wavelengths indicated along the abscissa. The dashed line corresponds to the root-mean squared (RMS) value of the non-Ekman ageostrophic velocities.

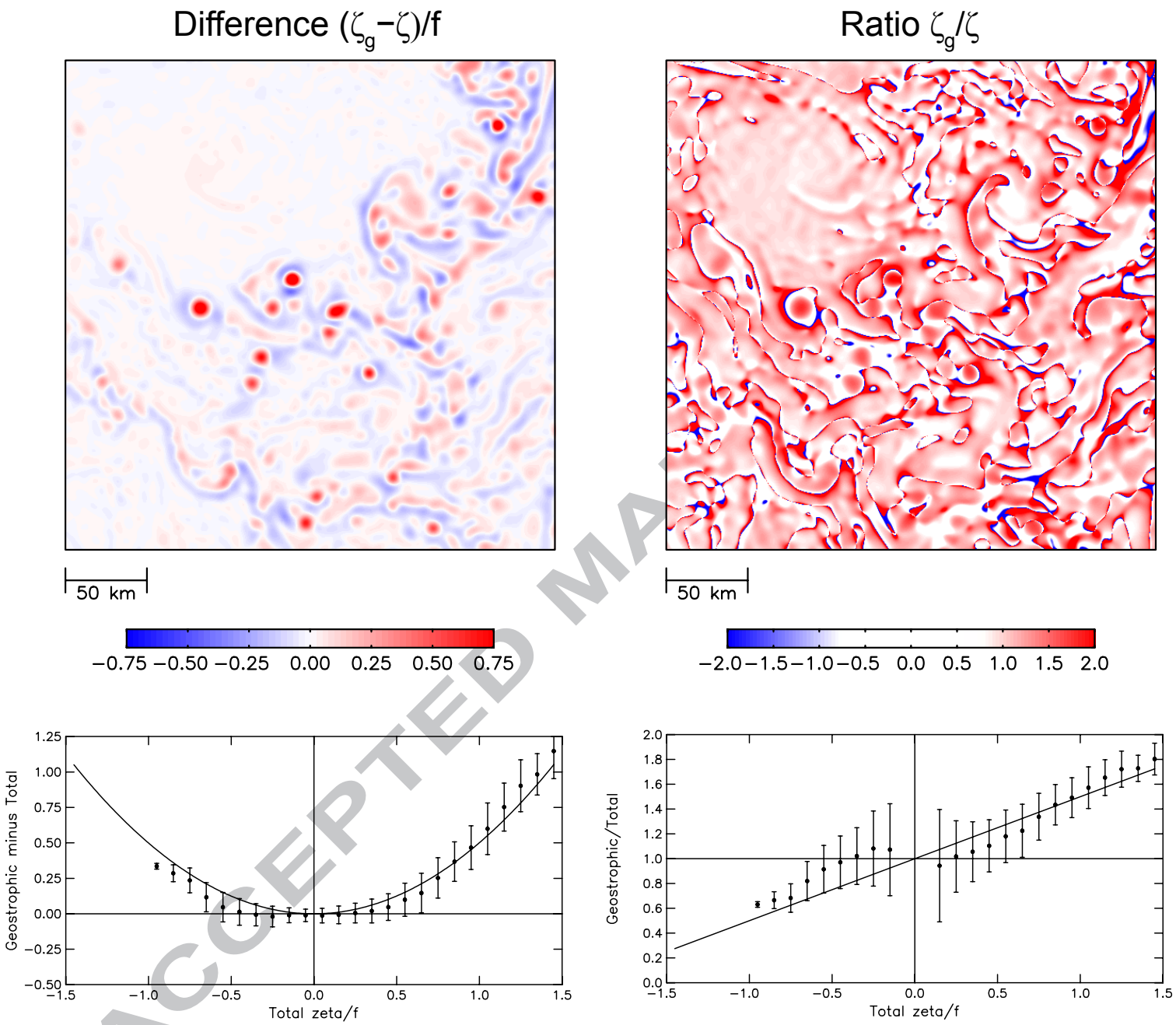

Figure 9. Maps of the differences (left) and ratios (right) of the normalized geostrophically computed vorticity ζ_g/f in Fig. 5c and the normalized total vorticity ζ/f in Fig. 3b after smoothing with a half-power filter cutoff wavelength of 20 km. The bottom panels show binned averages of the gridded values in the maps in the top panels. The vertical bar on each binned average represents the ±1 standard deviation of the data values within the bin and the smooth lines correspond to the theoretical solutions derived in the text for cyclostrophic motion.

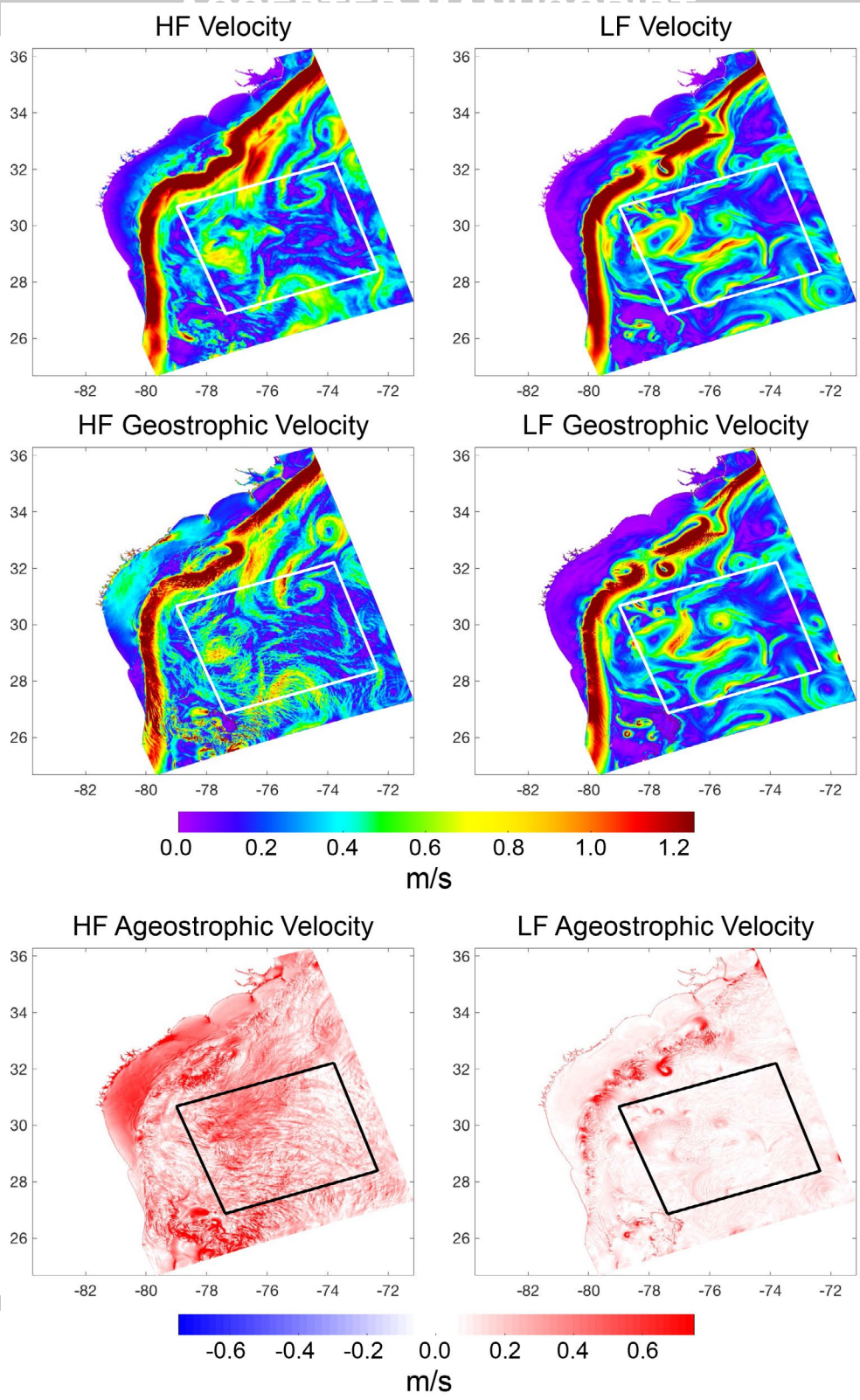

Figure 10. Snapshot maps of the magnitudes of the total velocity, the geostrophically computed velocity and the ageostrophic velocity (top to bottom) for the HF and LF simulations (left and right columns, respectively) of a region of the North Atlantic Ocean off the southeastern seaboard of the U.S. The grid resolution was 0.75 km × 0.75 km in both simulations. The HF simulation was forced with high-frequency (hourly) winds and tides. The LF simulation was forced with monthly winds and did not include tides. The ribbons of high velocity in the western and northern regions of each map are the Gulf Stream as it flows northward off the Florida coast and then turns northeastward along the continental slope to Cape Hatteras at the northern corner of the model domain. The x and y axis labels are longitude in degrees east and latitude in degrees north and the box in each panel is the area over which the non-Ekman ageostrophic velocities were computed for Figure 11.

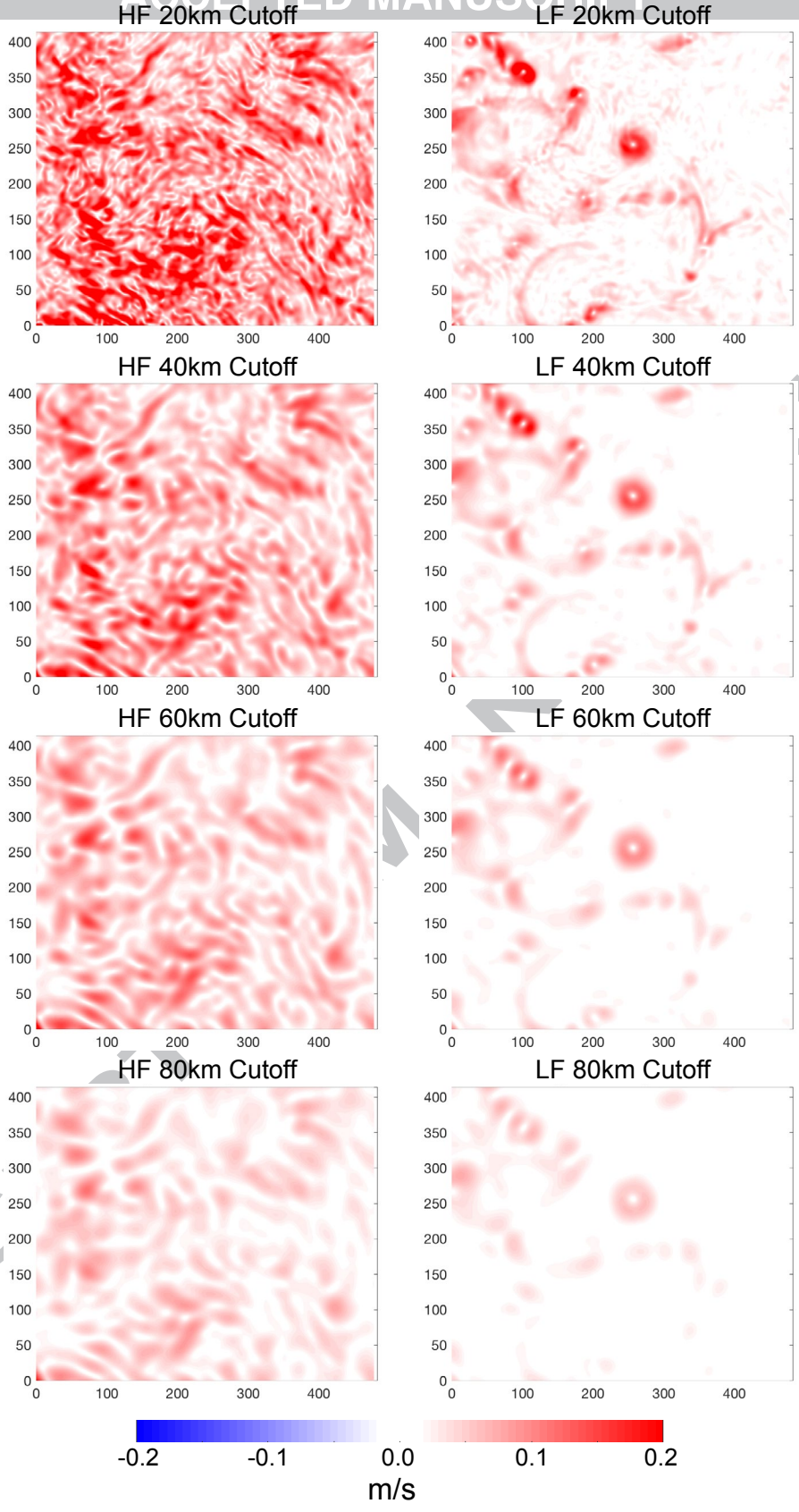

Figure 11. Maps showing the scale dependence of the magnitudes of smoothed non-Ekman ageostrophic velocities (defined as in Fig. 6c) from the subregions of the two North Atlantic simulations indicated by the boxes in Fig. 10. The left and right columns correspond to the results for the HF and LF models, respectively, after 2-dimensional isotropic smoothing with half-power filter cutoff wavelengths of 20, 40, 60 and 80 km (top to bottom). The x and y axis labels are distance in kilometers.

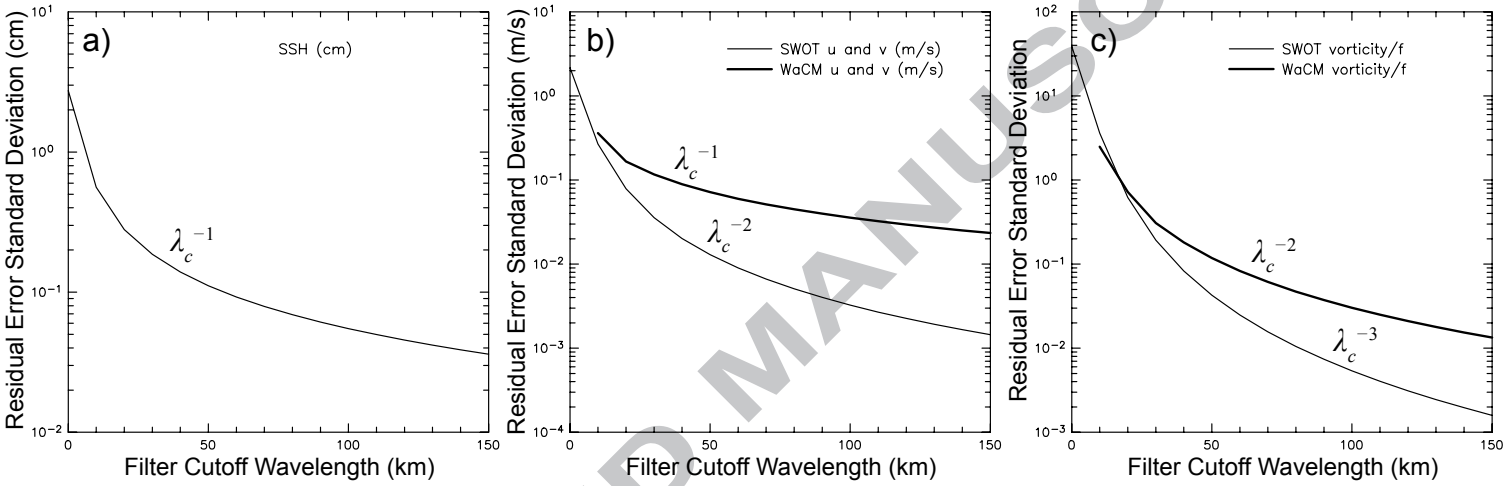

Figure 12. The standard deviations of residual errors as functions of half-power filter cutoff wavelength with 2-dimensional isotropic Parzen smoothing for footprint sizes of 1 km and 5 km for SWOT and WaCM, respectively: a) SWOT estimates of SSH; b) Geostrophically computed SWOT estimates of each of the components of velocity (thin solid lines, which are indistinguishable for the two components), and WaCM estimates of each component of the total velocity (thick solid lines, which are again indistinguishable for the two components); and c) geostrophically computed SWOT estimates of vorticity (thin line) and WaCM estimates of the total vorticity (thick line), both normalized by the Coriolis parameter f at the central latitude 37°N of the CCS model domain. The standard deviations were computed from the error variances determined for SWOT and WaCM, respectively, by integrating the analytical formulas in Appendices I.3 and I.4 for each filter cutoff wavelength λ_c. The power-law dependencies on λ_c that are labeled on each curve were determined from log-log versions of each panel (not shown here).

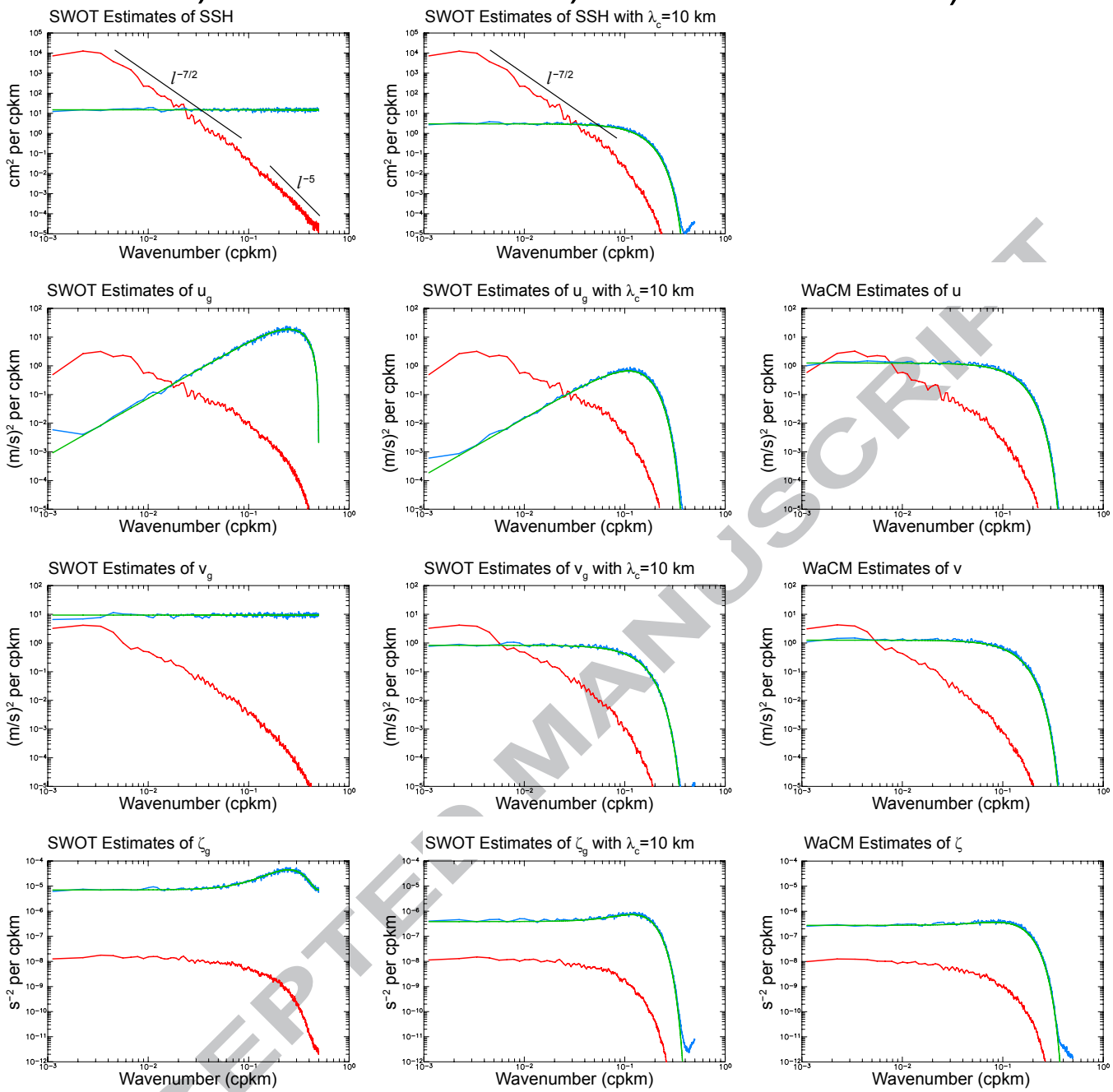

Figure 13. Alongshore wavenumber power spectral densities of simulated satellite estimates of the signals and errors for: Column a) SWOT estimates of (top-to-bottom) SSH and geostrophically computed cross-shore and alongshore velocity and vorticity obtained from simulated pre-processed SWOT data; Column b) the same as Column a), except after isotropic smoothing using a Parzen smoother with the same half-power filter cutoff wavelength of 10 km used in the pre-processing of WaCM data; and Column c) WaCM estimates of (top-to-bottom) cross-shore velocity, alongshore velocity and vorticity obtained from simulated pre-processed WaCM data. The red lines are the signal spectra computed from the model after applying the pre-filtering for SWOT (columns a and b, with additional 10-km smoothing in the latter) and WaCM (column c). The dark blue lines are the spectra computed empirically from the simulated error fields, which were computed geostrophically based on the local value of the Coriolis parameter f at each grid point in the case of SWOT. The green lines are the theoretical spectra of errors derived in Appendix I, which are based on the constant value of f at the central latitude 37°N of the CCS model domain in the case of SWOT. All of the spectra were smoothed by ensemble averaging over the individual spectra computed from alongshore grid lines that extend the full length of the model domain with a cross-shore spacing of 5 km. For reference, selected power-law rolloff dependencies on alongshore wavenumber l are labeled in the top panels of Columns a and b. Note that the rolloff of $l^{-7/2}$ is not significantly different from the rolloff of $l^{-11/3}$ that was deduced from along-track altimeter data by Le Traon et al. (2008) and is consistent with the $l^{-5/3}$ spectral rolloff of velocity in surface quasigeostrophic (SQG) theory (Held et al., 1995).

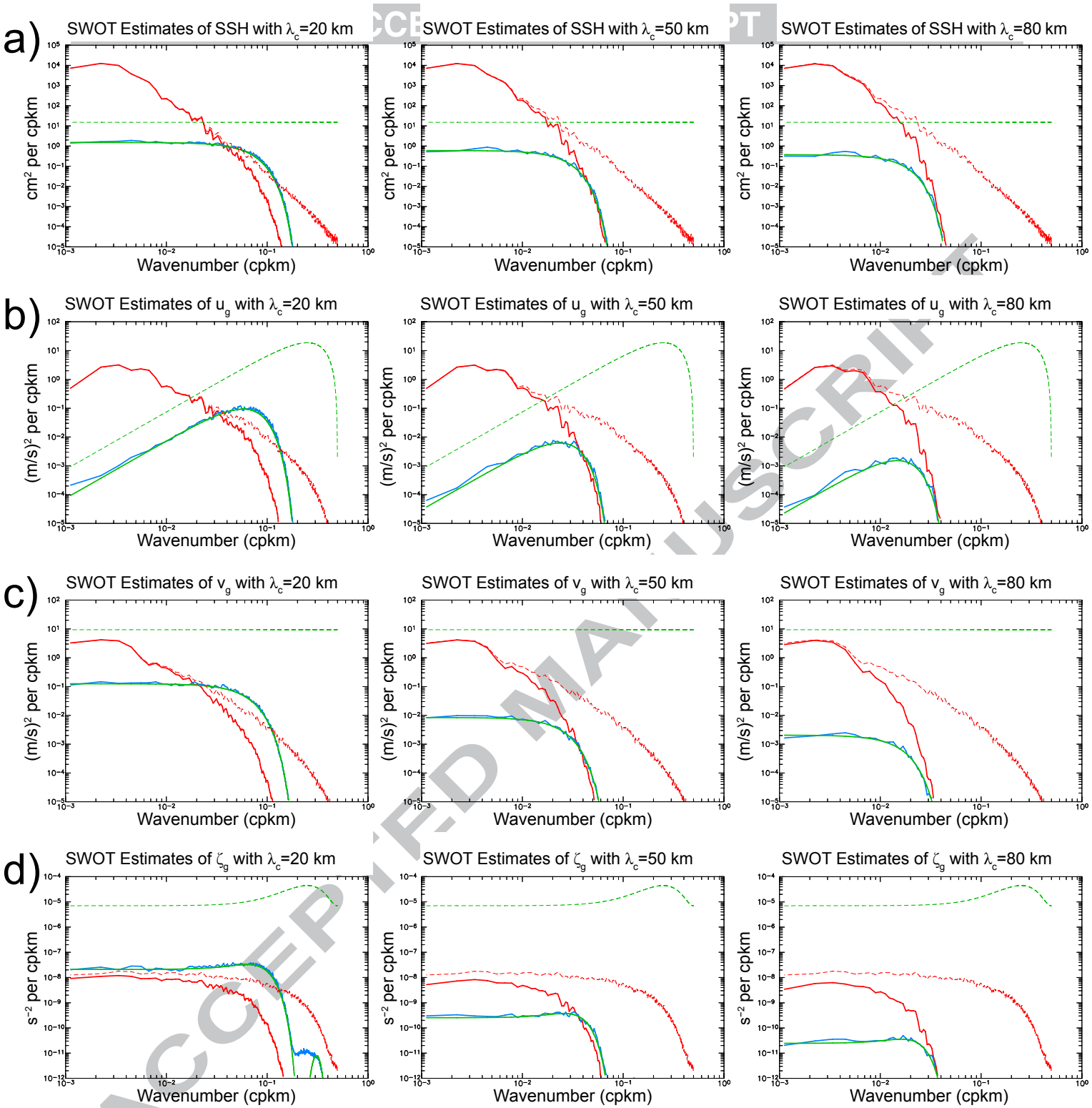

Figure 14. Alongshore wavenumber power spectral densities of simulated satellite estimates of the signals and errors after 2-dimensional isotropic smoothing of the pre-processed SWOT data with half-power filter cutoff wavelengths of 20, 50 and 80 km (left, middle and right columns, respectively) for: Row a) SSH; Row b) geostrophically computed cross-shore velocity; Row c) geostrophically computed alongshore velocity; and Row d) geostrophically computed vorticity. The solid red lines are the signal spectra from the model after isotropic smoothing. The dark blue lines are the spectra computed empirically from the smoothed error fields constructed based on the local Coriolis parameter f at each grid point The green lines are the theoretical spectra of smoothed SWOT error fields derived in Appendix I.2 based on the constant value of f at the central latitude 37°N of the CCS model domain. For reference, the dashed red and green lines are the signal spectra and theoretical error spectra in Fig. 13a based on the pre-processed SWOT data without additional smoothing in simulated ground-based post-processing. All of the spectra were smoothed by ensemble averaging as in Fig. 13.

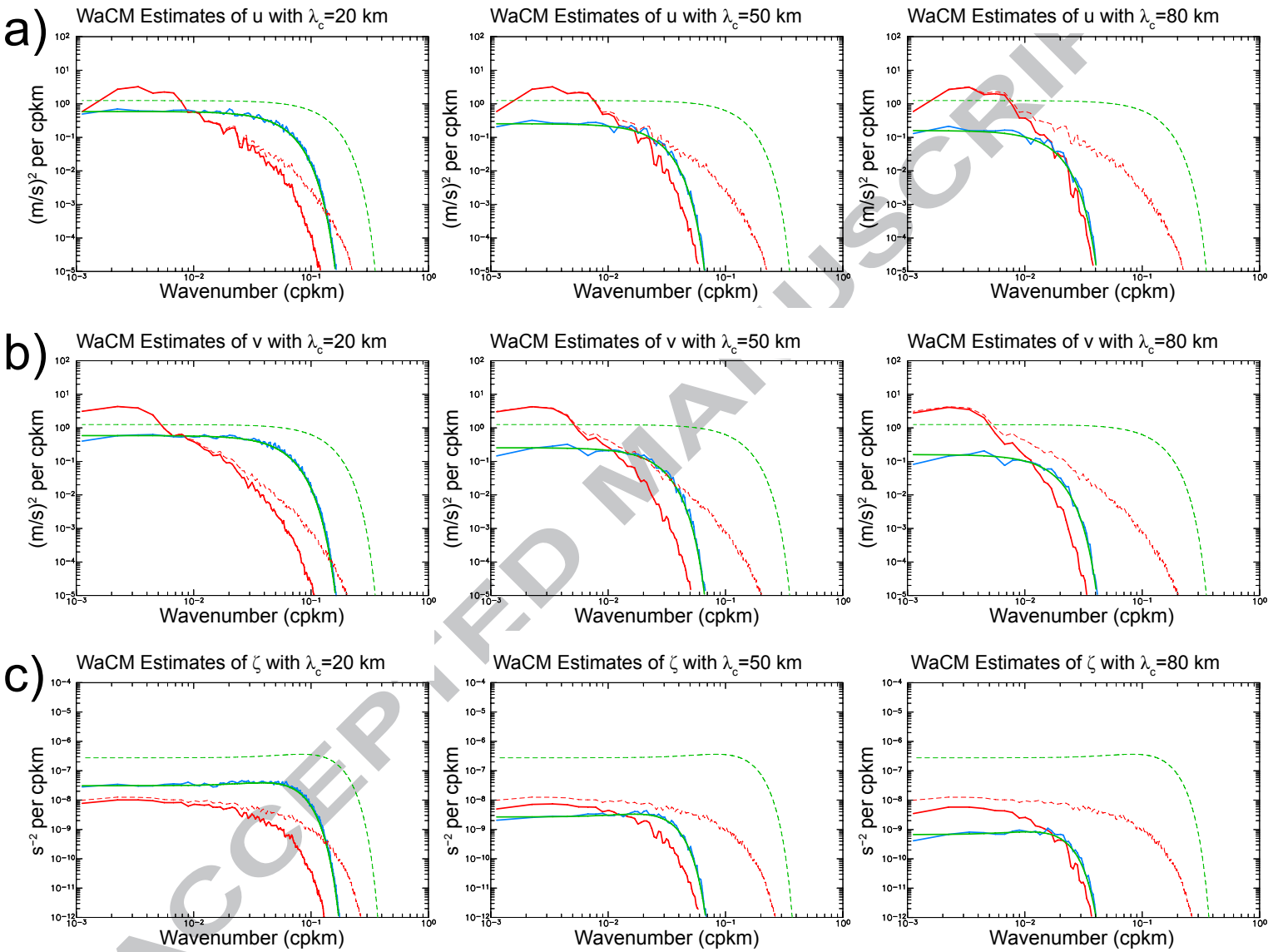

Figure 15. Alongshore wavenumber power spectral densities of simulated satellite estimates of the signals and errors after 2-dimensional isotropic smoothing of the pre-processed WaCM data with half-power filter cutoff wavelengths of 20, 50 and 80 km (left, middle and right columns, respectively) for: Row a) alongshore velocity; Row b) cross-shore velocity; and Row c) vorticity. The solid red lines are the signal spectra from the model after smoothing. The dark blue lines are the spectra computed empirically from the simulated error fields after smoothing and the green lines are the theoretical spectra of smoothed error fields derived in Appendix I.4. For reference, the dashed red and green lines are the signal spectra and theoretical error spectra from Fig. 13c for the pre-processed WaCM data without additional smoothing in simulated ground-based post-processing. All of the spectra were smoothed by ensemble averaging as in Fig. 13.

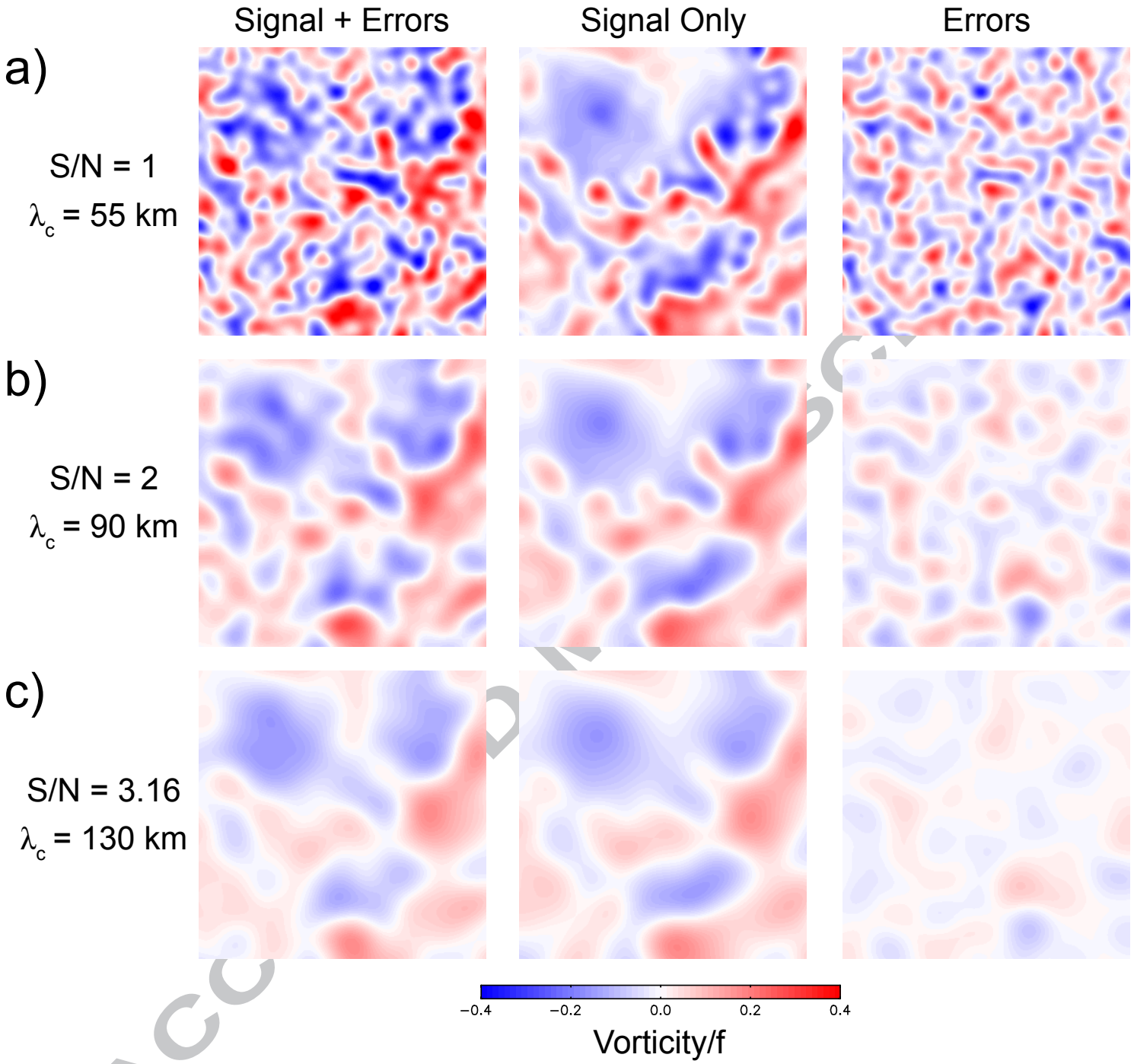

Figure 16. Examples showing the characteristics of noisy data after isotropic 2-dimensional smoothing to achieve signal-to-noise standard deviation ratios of 1, 2 and 3.16 (rows a, b and c, respectively). For illustration purposes, these are maps of the normalized vorticity ζ/f constructed from simulated noisy WaCM data as in Sec. 6.2 below for the case of uncorrelated speed measurement errors with a standard deviation of $\sigma_{spd} = 0.50$ m s^{-1}. The left, middle and right columns show, respectively, the noisy estimates of ζ/f, the error-free ζ/f signal and the residual errors after smoothing with the half-power filter cutoff wavelength λ_c labeled to the left of each row.

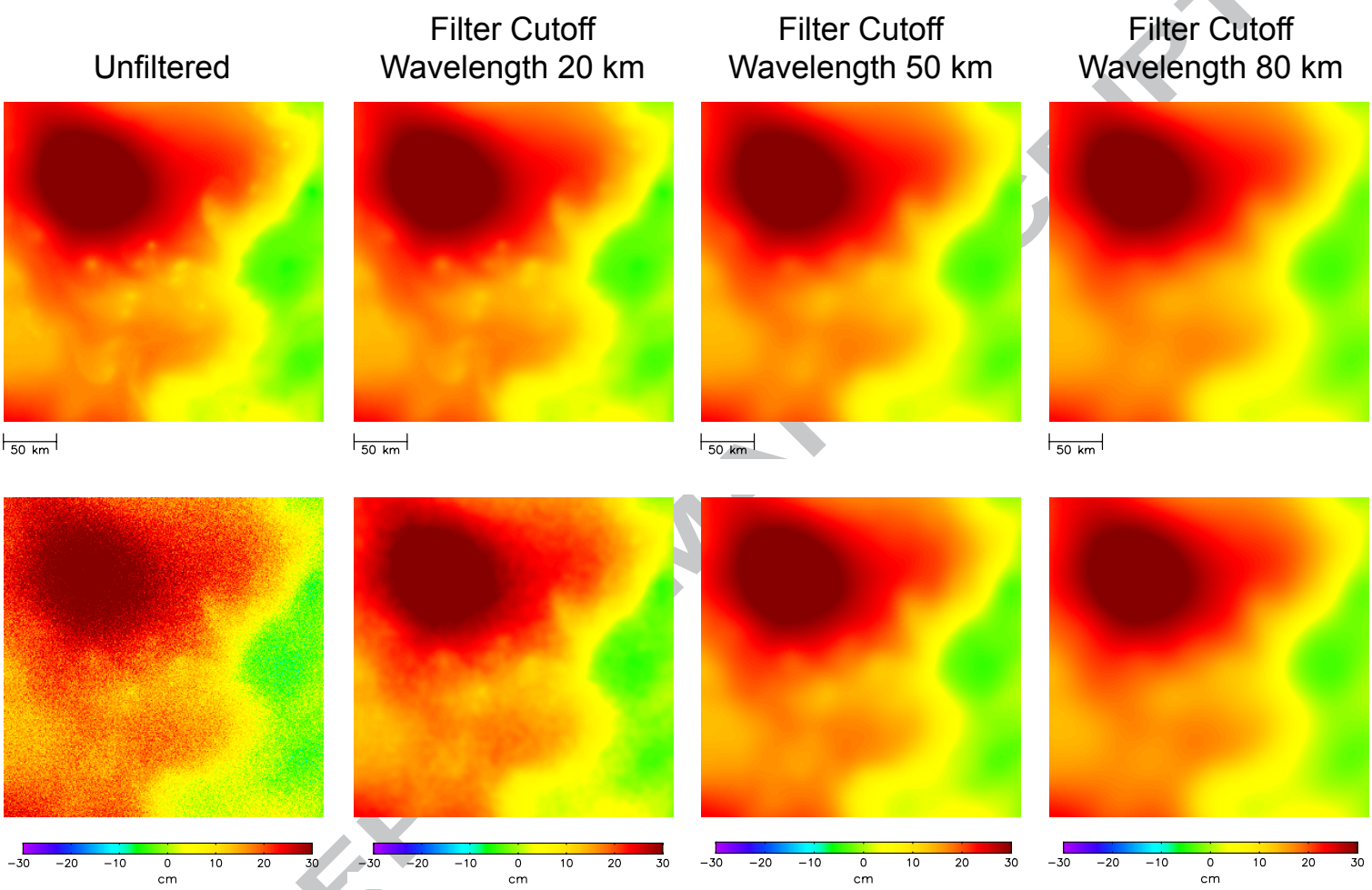

Figure 17a. Maps of simulated SWOT estimates of SSH for the CCCS region shown in the bottom panel of Fig. 5a. The top panels are the error-free fields from the pre-processed SWOT data with no additional smoothing (left), and after isotropic 2-dimensional smoothing with half-power filter cutoff wavelengths of 20, 50 and 80 km (columns 2, 3 and 4, respectively). The bottom panels show the fields computed with the addition of simulated uncorrelated SSH measurement errors with a standard deviation of $\sigma_h = 2.74$ cm but without sampling errors (i.e., as if the measurement swaths spanned the full CCS model domain on each satellite overpass). The same color bar is used for all of the panels.

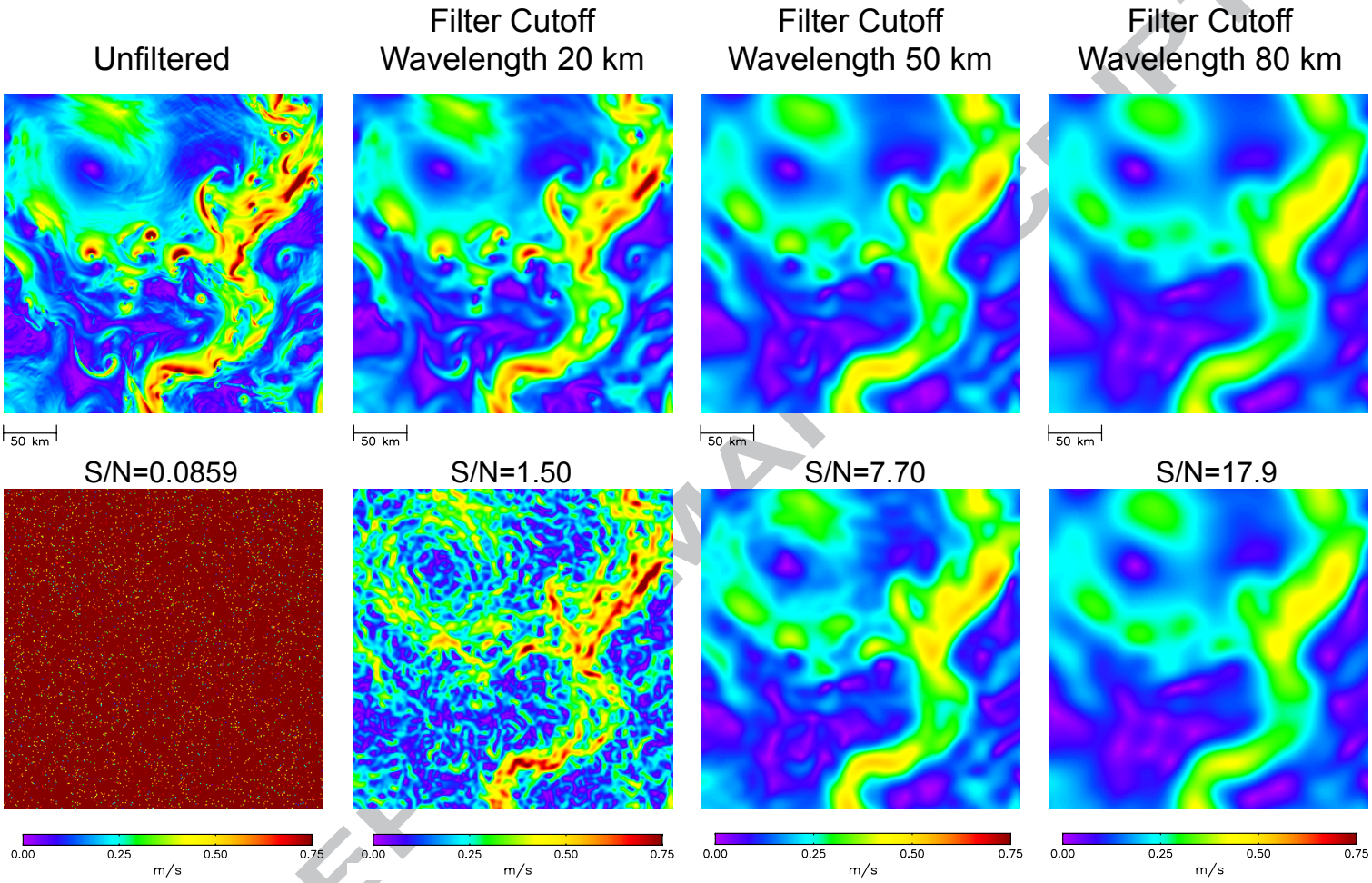

Figure 17b. The same as Fig. 17a, except maps of simulated SWOT estimates of the magnitudes of geostrophically computed surface velocity for the CCCS region shown in the bottom panel of Fig. 5b. The panels in the top row were computed from error-free SSH fields and the panels in the bottom row were computed with the addition of simulated uncorrelated SSH measurement errors with a standard deviation of $\sigma_h = 2.74$ cm. The same color bar is used for all of the panels and the signal-to-noise standard deviation ratio is labeled above each of the bottom panels.

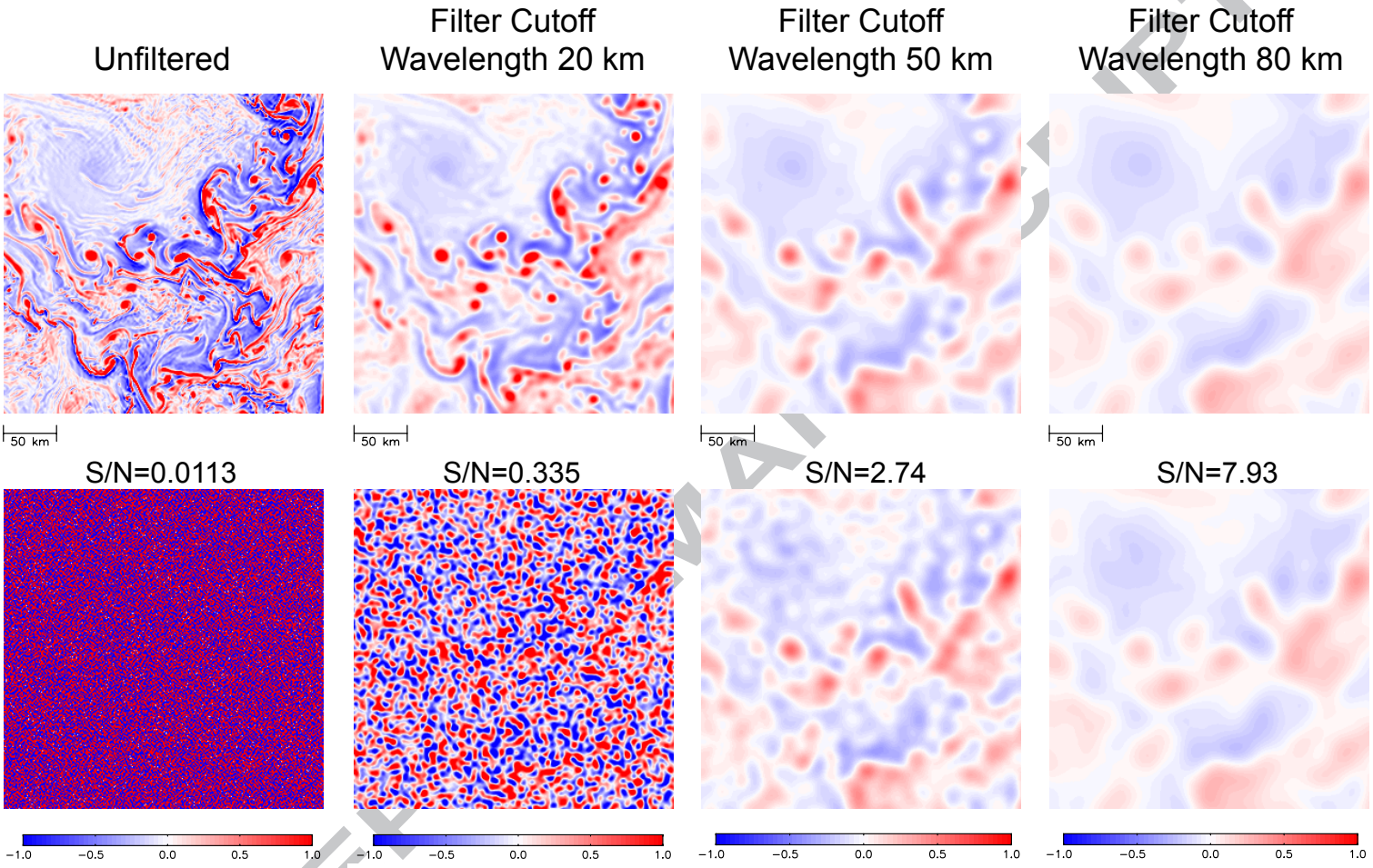

Figure 17c. The same as Fig. 17a, except maps of simulated SWOT estimates of geostrophically computed and normalized vorticity ζ_g/f for the CCCS region shown in the bottom panel of Fig. 5c. The panels in the top row were computed from error-free SSH fields and the panels in the bottom row were computed with the addition of simulated uncorrelated SSH measurement errors with a standard deviation of $\sigma_h = 2.74$ cm. The same color bar is used for all of the panels and the signal-to-noise standard deviation ratio is labeled above each of the bottom panels.

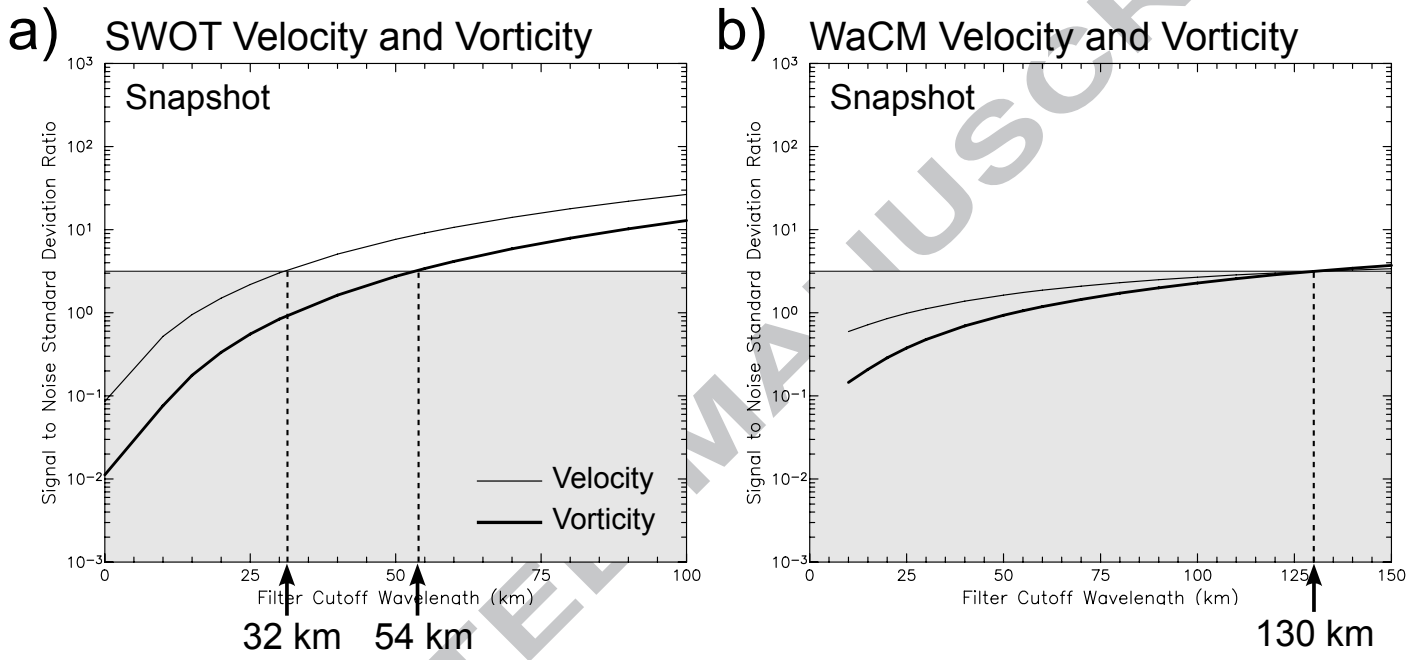

Figure 18. The scale dependencies of the ratios of the standard deviations of the signal and the uncorrelated measurement errors for a snapshot of the full CCS region from simulated a) SWOT; and b) WaCM estimates of instantaneous surface velocity (thin lines) and vorticity (thick lines) after isotropic 2-dimensional smoothing using a Parzen smoother with the half-power filter cutoff wavelengths indicated along the abscissas. The velocity and vorticity were computed geostrophically for SWOT. The gray areas correspond to signal-to-noise (S/N) standard deviation ratios less than 3.16, which is equivalent to a signal-to-noise variance ratio of 10. The vertical dashed lines indicate the wavelengths above which the signal-to-noise standard deviation ratios exceed 3.16. The dynamic range of the abscissa is larger in b) to accommodate the lower S/N ratios of WaCM estimates of velocity and vorticity with the baseline speed standard deviation of $\sigma_{spd} = 0.5$ m s^{-1} of the uncorrelated errors of WaCM measurements of velocity. The improved resolution capabilities that would be achieved from WaCM with smaller measurement errors are summarized in Fig. 44 and Tables 4a and b.

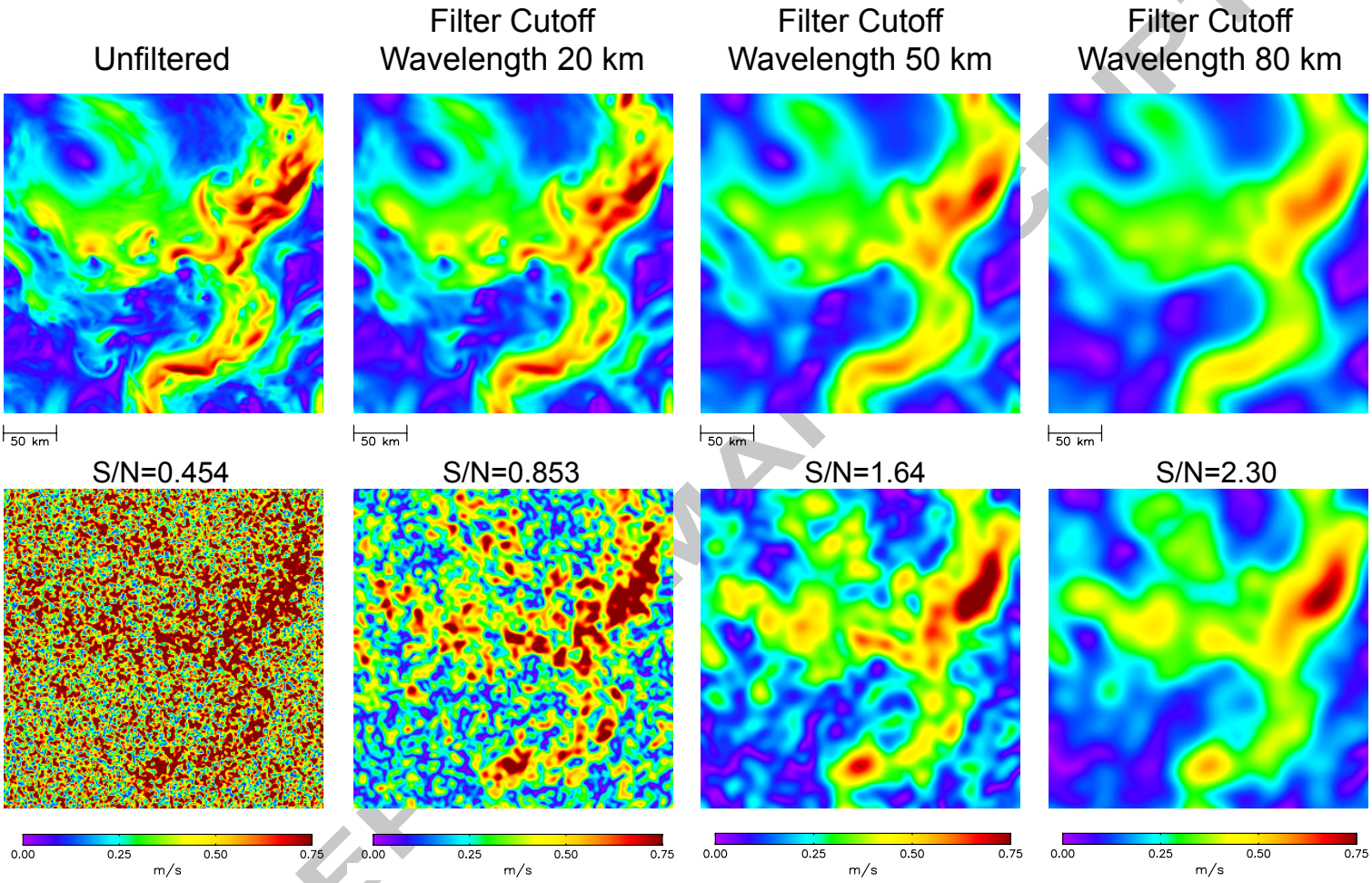

Figure 19a. Maps of simulated WaCM estimates of the magnitudes of the total surface velocity for the CCCS region shown in the bottom panel of Fig. 3a. The top panels are the error-free fields from the pre-processed WaCM data with no additional smoothing (left), and after isotropic 2-dimensional smoothing with half-power filter cutoff wavelengths of 20, 50 and 80 km (columns 2, 3 and 4, respectively). The bottom panels show the fields computed with the addition of simulated uncorrelated velocity measurement errors with a speed standard deviation of $\sigma_{spd} = 0.5$ m s^{-1} equally partitioned between the two velocity components. The same color bar is used for all of the panels and the signal-to-noise standard deviation ratio is labeled above each of the bottom panels.

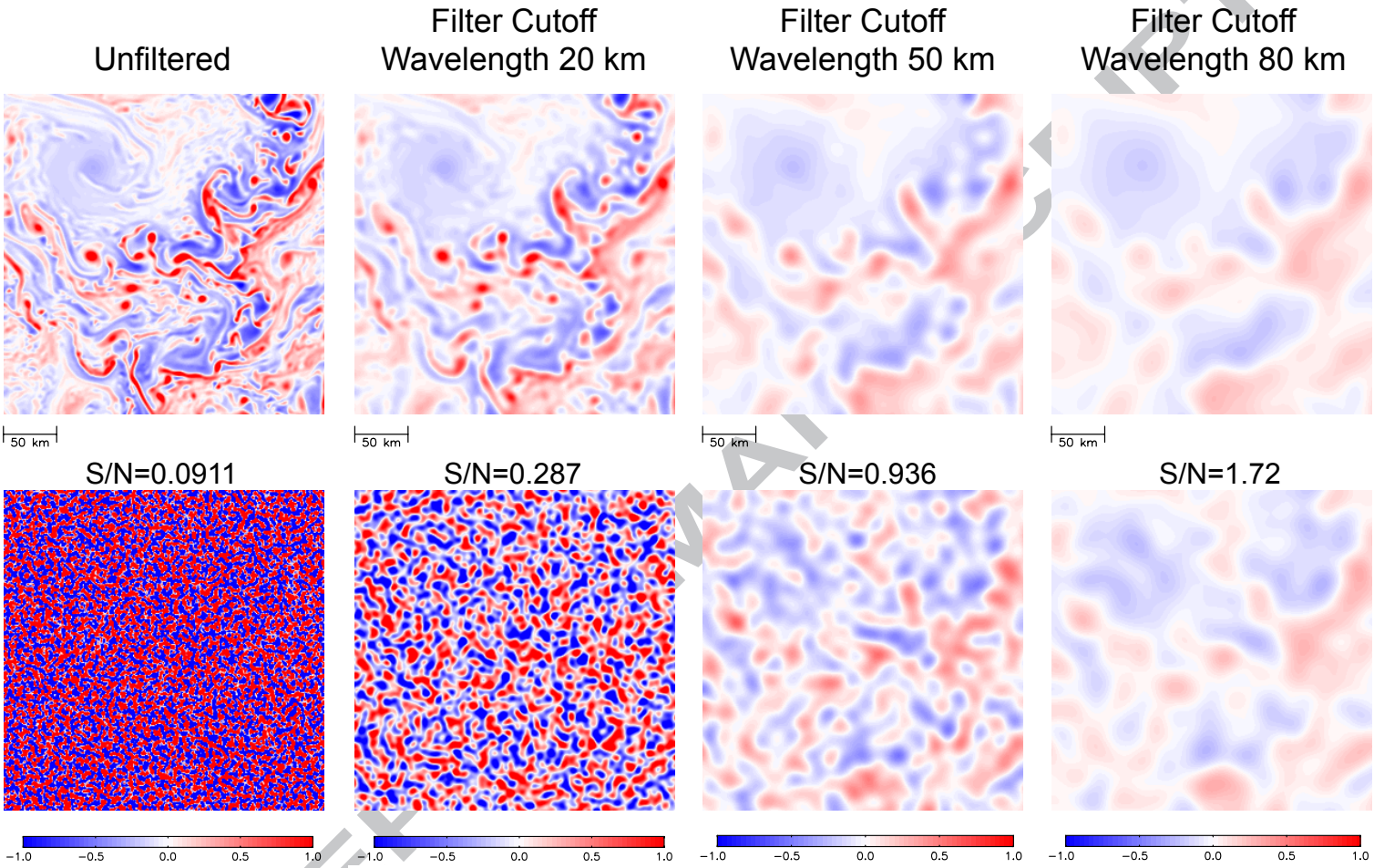

Figure 19b. The same as Fig. 19a, except maps of simulated WaCM estimates of normalized vorticity ζ/f computed from the total surface velocity for the CCCS region shown in the bottom panel of Fig. 3b. The same color bar is used for all of the panels and the signal-to-noise standard deviation ratio is labeled above each of the bottom panels.

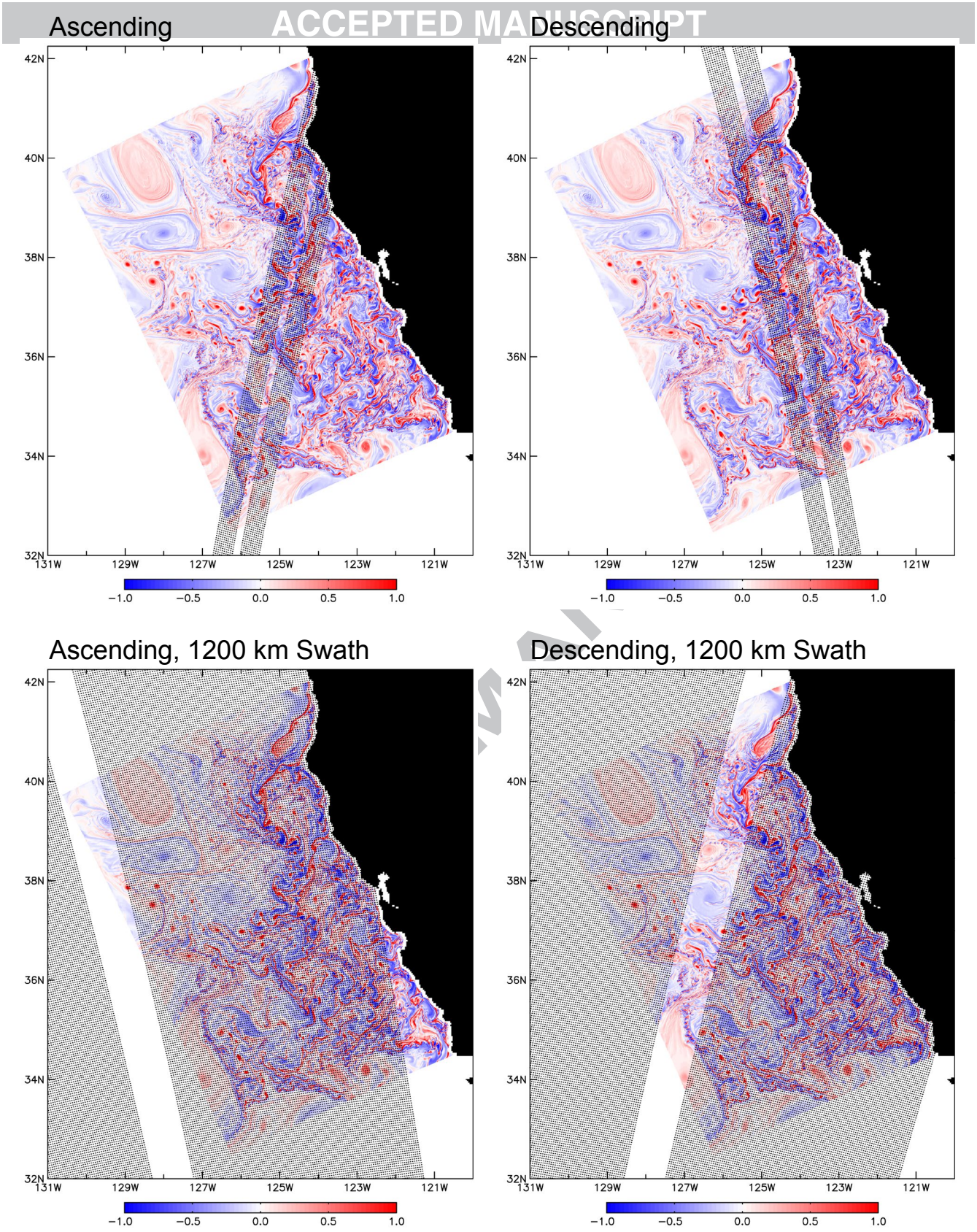

Figure 20. Examples of the measurement swaths for single ascending and descending overpasses of SWOT (top panels) and WaCM with a swath width of 1200 km (bottom panels) overlaid on the snapshot of the normalized vorticity ζ/f from the top panel of Fig. 3b. The improved sampling coverage by WaCM with a swath width of 1800 km is shown in Fig. 41. The ground tracks for SWOT in this figure are the actual planned orbit. The ground tracks for WaCM are for illustrative purposes and could be adjusted longitudinally to optimize the sampling of any specific region of the world ocean. The details of the sampling of the CCS region would change accordingly.

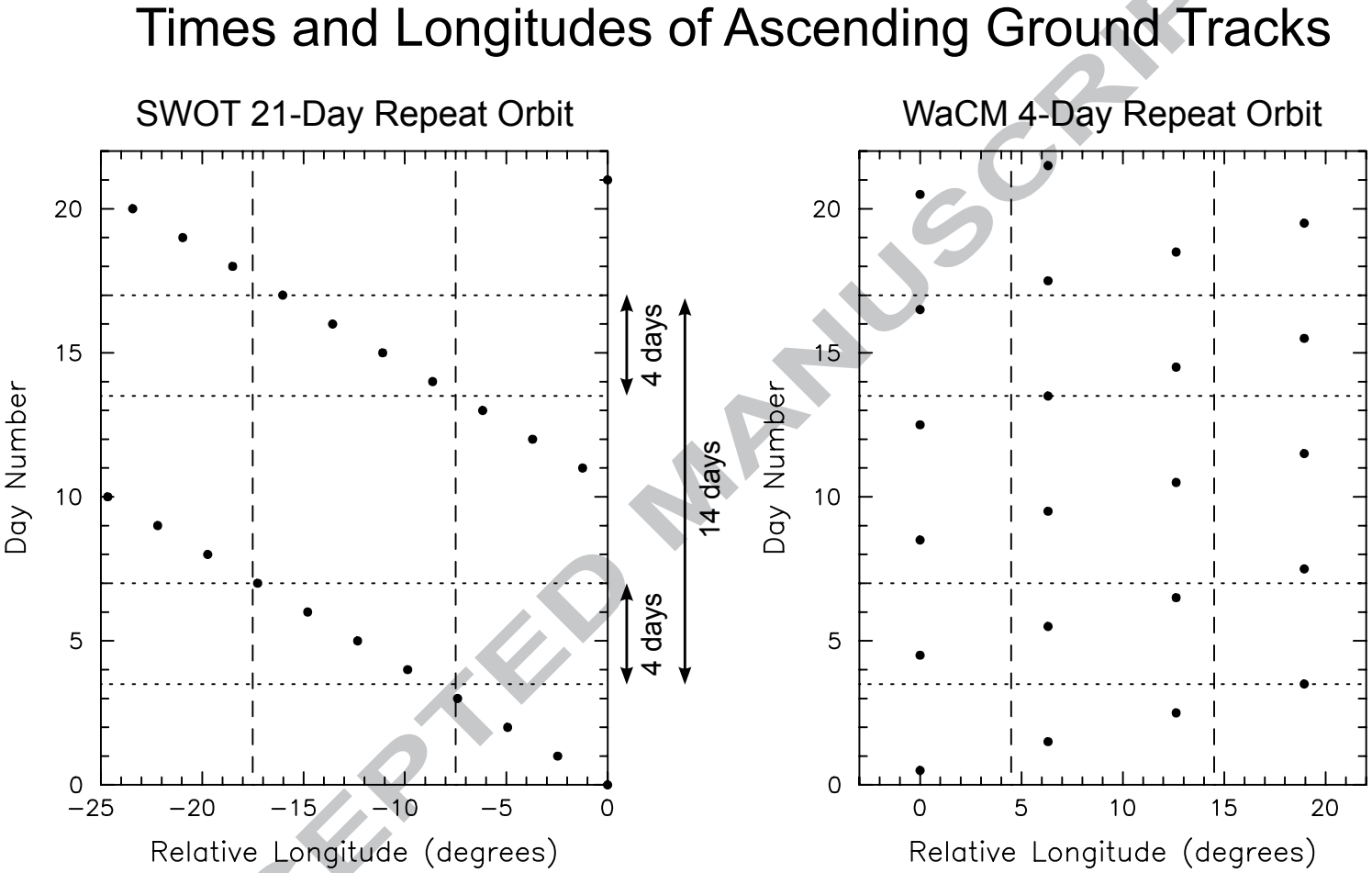

Figure 21. Time and relative longitude plots of sequential ascending ground track overpasses of SWOT and WaCM measurements along a fixed latitude. There are analogous sampling patterns for the descending overpasses, except shifted approximately half a day later in time. The sampling pattern shown for SWOT is based on the orbit parameters of the planned 21-day exact repeat mission. The sampling pattern shown for WaCM is based on the orbit parameters for the 4-day exact repeat QuickSCAT mission. For reference, the vertical dashed lines in both panels indicate the longitudinal extent of the western and eastern corners of the CCS model domain and the two pairs of horizontal dotted lines in both panels indicate the two 4-day subcycles of SWOT sampling of the CCS model domain during each 21-day exact repeat period of the SWOT orbit.

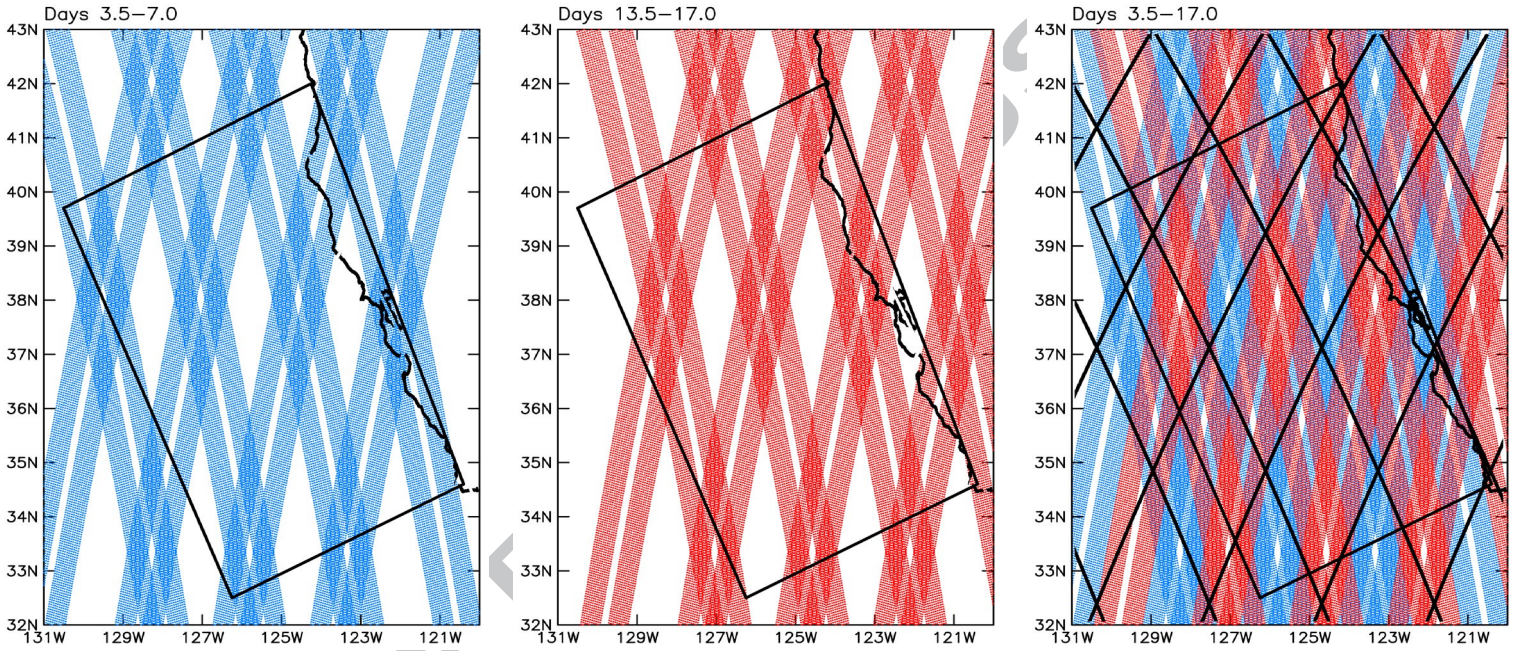

Figure 22. Illustration of the two 4-day subcycles of SWOT sampling of the CCS model domain over a 14-day interval of the 21-day exact repeat period (see the left panel of Fig. 21). The swaths from the first 4-day subcycle (days 3.5–7.0) are shown in blue in the left panel and the swaths from the second 4-day subcycle (days 13.5–17.0) are shown in red in the middle panel. The combined swaths from the two 4-day subcycles are overlaid in the right panel. The intersecting diagonal lines overlaid on the right panel are the ground tracks of the 10-day exact repeat orbit of the TOPEX, Jason-1, Jason-2 and Jason-3 altimeters.

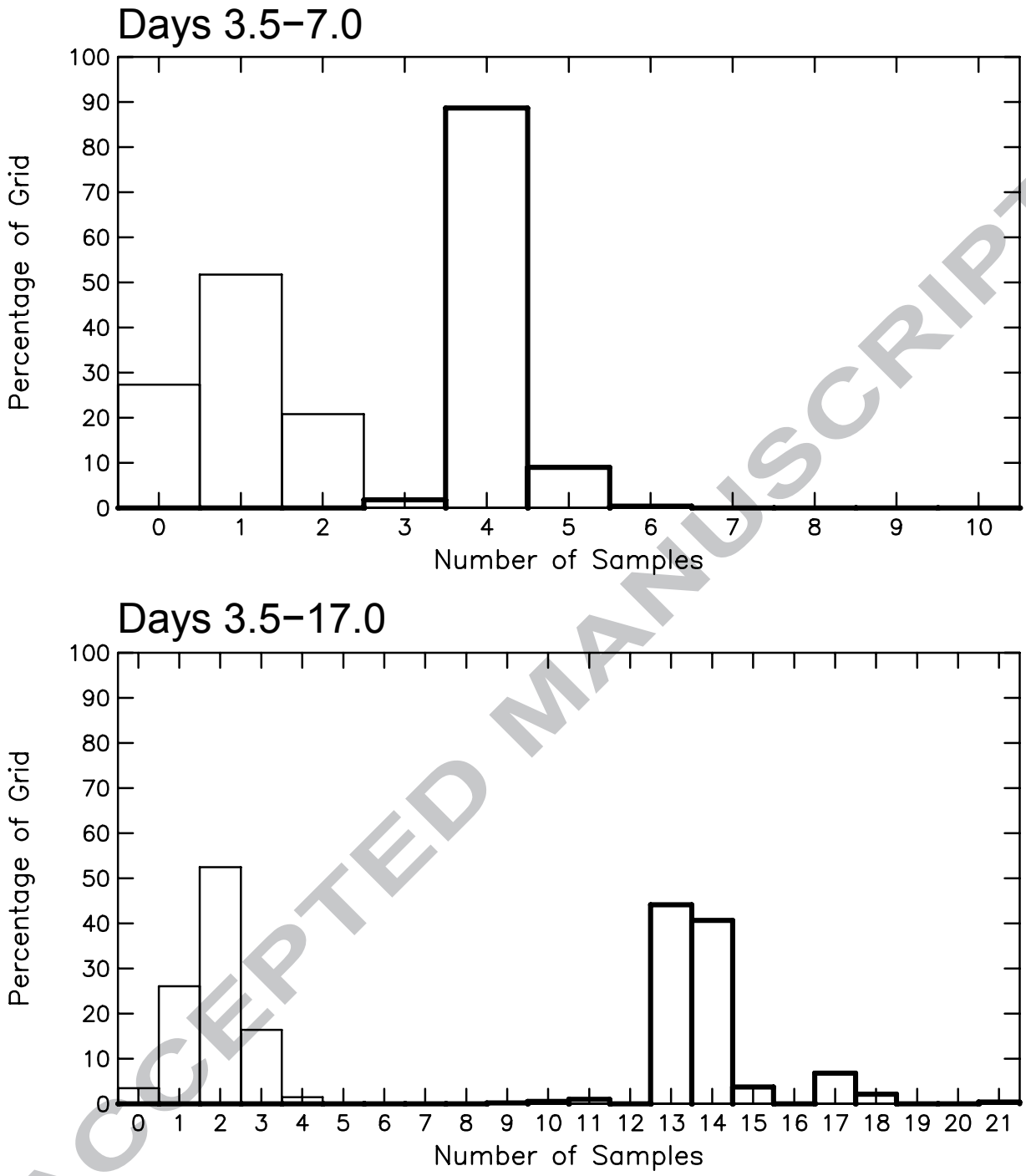

Figure 23. Histograms of the numbers of samples by SWOT and WaCM (thin and thick lines, respectively) during the first 4 days and the full 14 days (top and bottom panels, respectively) of the 14-day sampling period for the CCS model domain during each 21-day exact repeat period of the SWOT orbit. The histogram values are expressed as percentages of the total number of grid points in the CCS model domain. The histograms for WaCM are based on a swath width of 1200 km. The improved sampling by WaCM with a swath width of 1800 km is shown later in Fig. 42.

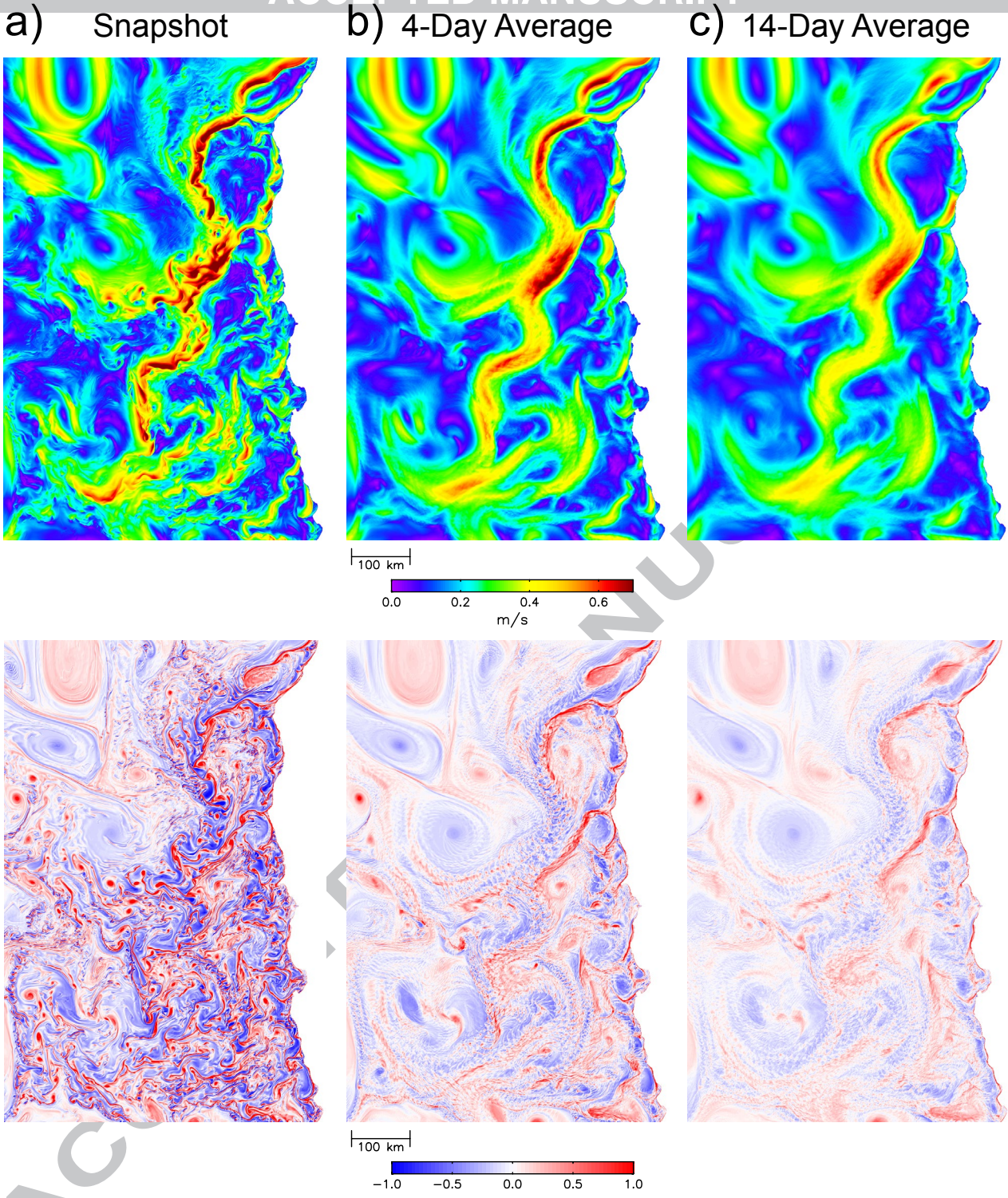

Figure 24. An illustration of the effects of time averaging on error-free surface velocity and vorticity fields centered on the same date as the snapshots in Fig. 3: Column a) The instantaneous snapshots (the same as the top panels of Figs. 3a and b, repeated here for easy comparison with the other two panels of this figure); Column b) Four-day average maps; and Column c) Fourteen-day average maps. The averages were constructed from model output at intervals of 0.5 days. The velocity maps in the top panels of columns b) and c) are the magnitudes of the 4-day and 14-day vector-averaged velocity fields.

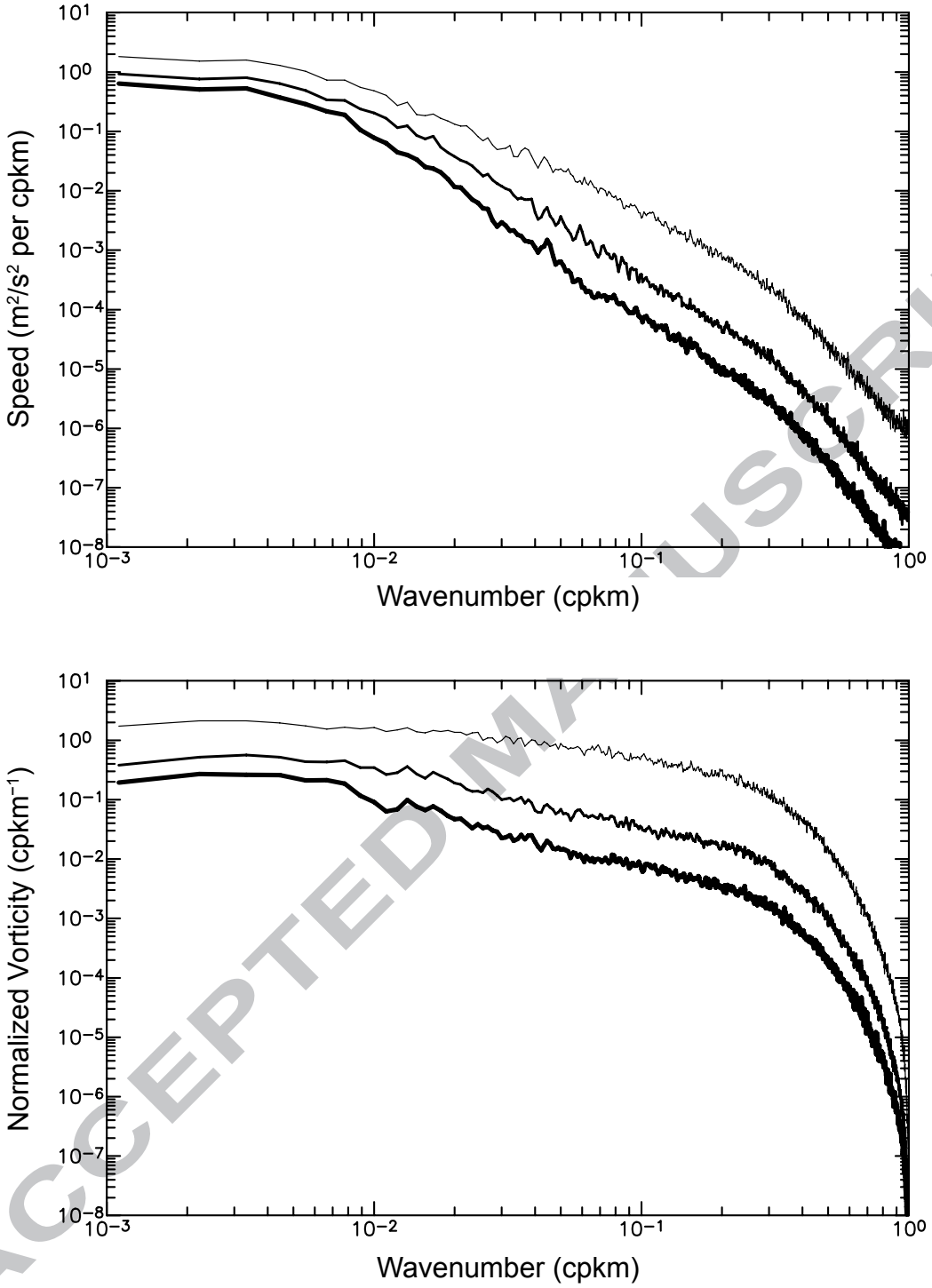

Figure 25. Alongshore wavenumber spectra of velocity and normalized vorticity computed from the model surface velocity fields for the instantaneous snapshot, the 4-day average and the 14-day average (thin, medium and thick lines, respectively) shown in Fig. 24. The velocity spectra for 4-day and 14-day averages were computed from the magnitudes of the vector-averaged velocity fields over the respective time periods. The smoothed spectra were computed by ensemble averaging as in Figs. 13–15, except from the raw 0.5 km × 0.5 km grid with a cross-shore spacing of 5 km.

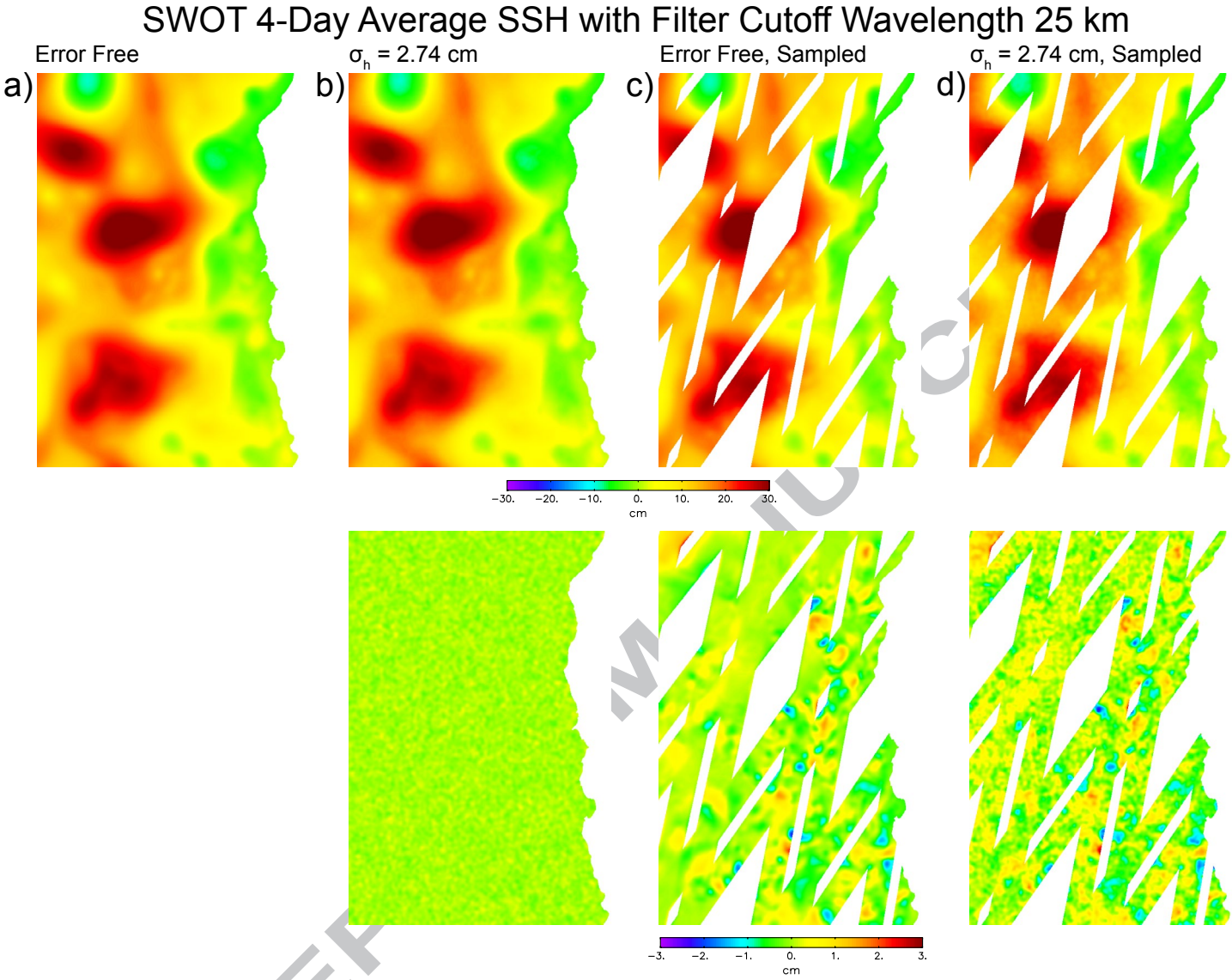

Figure 26. Maps of 4-day averaged SSH computed from error-free and noisy simulated SWOT measurements of SSH with isotropic 2-dimensional smoothing using a Parzen smoother with a half-power filter cutoff wavelength of 25 km: Column a) The 4-day average over the full model domain computed from error-free model SSH fields at a time step of 0.5 day over the 4-day period; Column b) The 4-day average over the full model domain computed from model SSH fields at a time step of 0.5 day over the 4-day period with simulated uncorrelated measurement errors with a standard deviation of $\sigma_h = 2.74$ cm; Column c) The 4-day average computed from simulated SWOT swath sampling of error-free model SSH fields at the times and locations of each satellite observation over the 4-day period; and Column d) The 4-day average computed from simulated SWOT swath sampling of model SSH fields at the times and locations of each satellite observation over the 4-day period with simulated uncorrelated measurement errors with a standard deviation of $\sigma_h = 2.74$ cm. The bottom panels are the error maps computed by subtracting the error-free map in Column a) from the error-contaminated maps in the top row of the respective Columns b)–d).

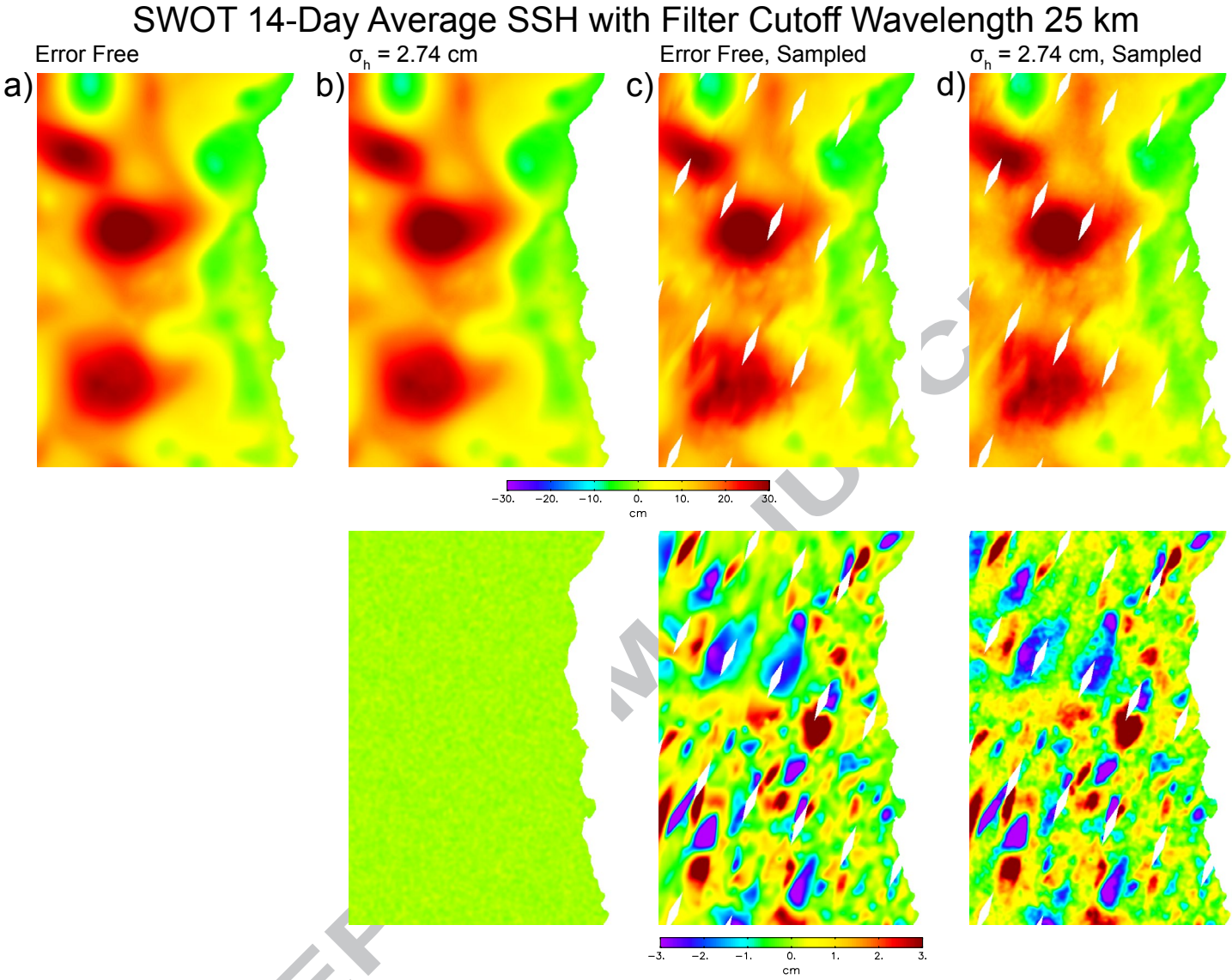

Figure 27. The same as Fig. 26, except for 14-day averages of SSH computed from simulated SWOT measurements of SSH with isotropic 2-dimensional smoothing using a Parzen smoother with a half-power filter cutoff wavelength of 25 km.

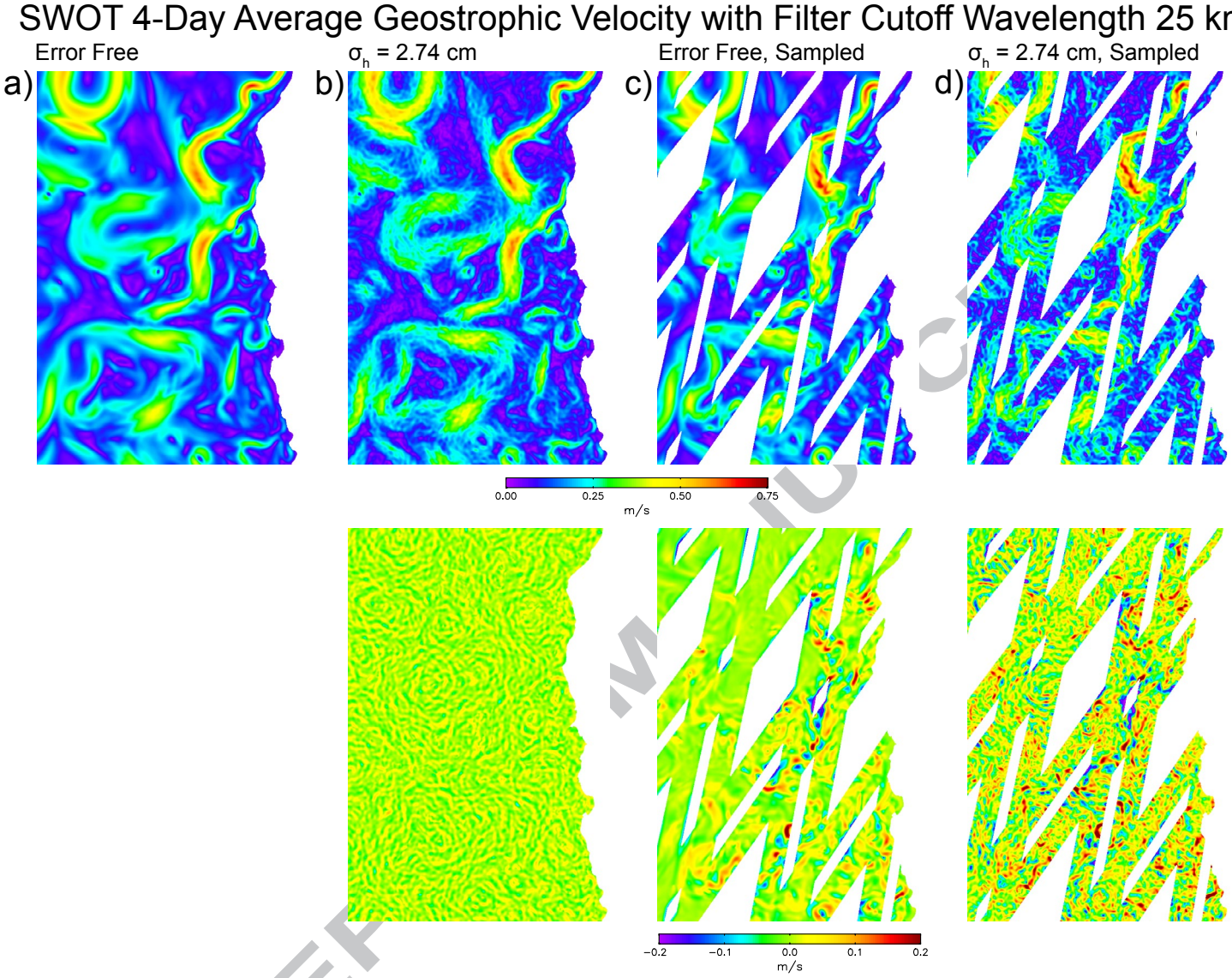

Figure 28. Maps of the magnitudes of 4-day averages of surface velocity computed geostrophically from error-free and noisy simulated SWOT measurements of SSH with isotropic 2-dimensional smoothing using a Parzen smoother with a half-power filter cutoff wavelength of 25 km: Column a) The 4-day average over the full model domain computed geostrophically from error-free model SSH fields at a time step of 0.5 day over the 4-day period; Column b) The 4-day average over the full model domain computed geostrophically from model SSH fields at a time step of 0.5 day over the 4-day period with simulated uncorrelated SSH measurement errors with a standard deviation of $\sigma_h = 2.74$ cm; Column c) The 4-day average computed geostrophically from simulated SWOT swath sampling of error-free model SSH fields at the times and locations of each satellite observation over the 4-day period; and Column d) The 4-day average computed geostrophically from simulated SWOT swath sampling of model SSH fields at the times and locations of each satellite observation over the 4-day period with simulated uncorrelated SSH measurement errors with a standard deviation of $\sigma_h = 2.74$ cm. The bottom panels are the error maps computed by subtracting the error-free map in Column a) from the error-contaminated maps in the top row of the respective Columns b)–d).

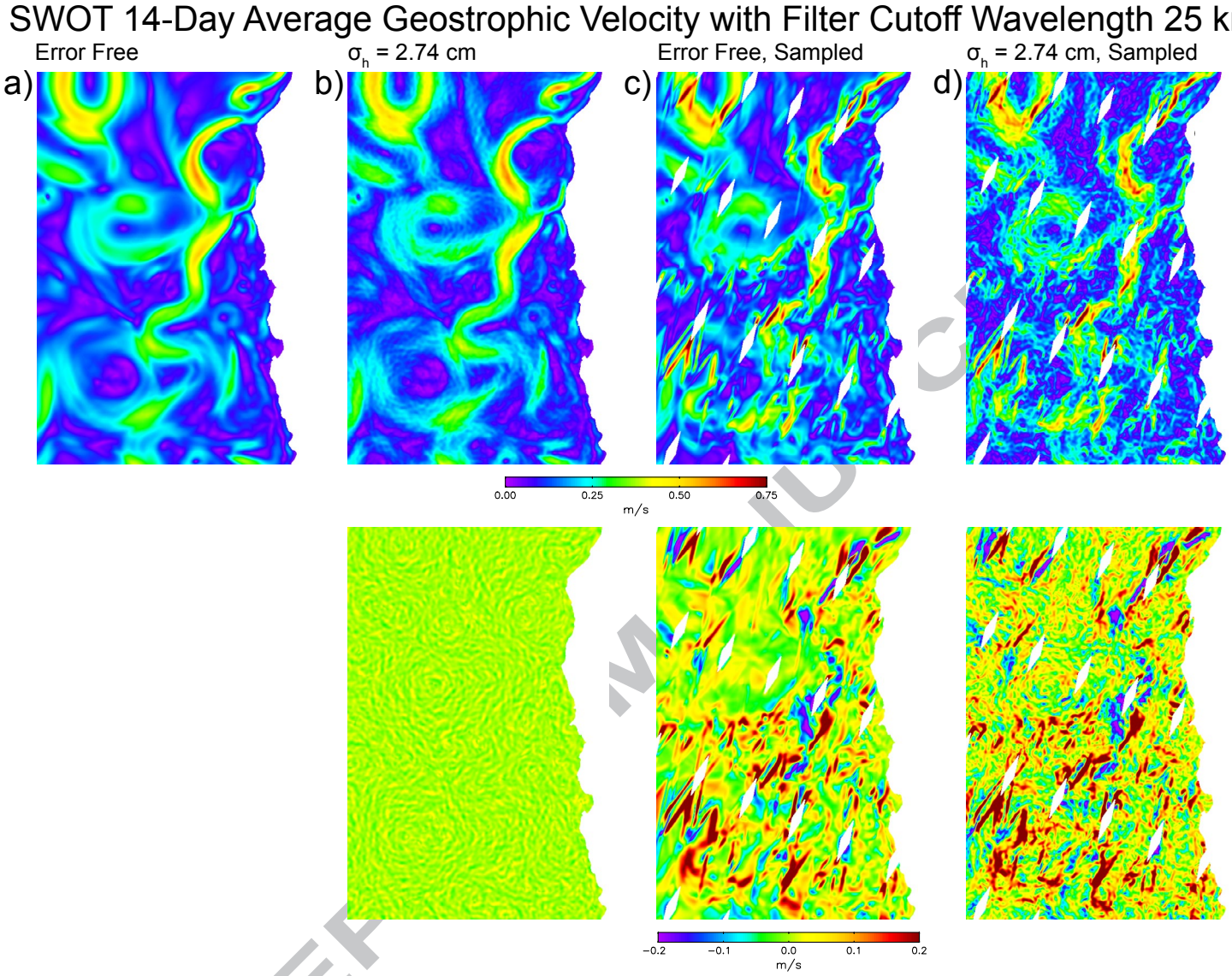

Figure 29. The same as Fig. 28, except the magnitudes of 14-day averages of surface velocity computed geostrophically from simulated SWOT measurements of SSH with isotropic 2-dimensional smoothing using a Parzen smoother with a half-power filter cutoff wavelength of 25 km.

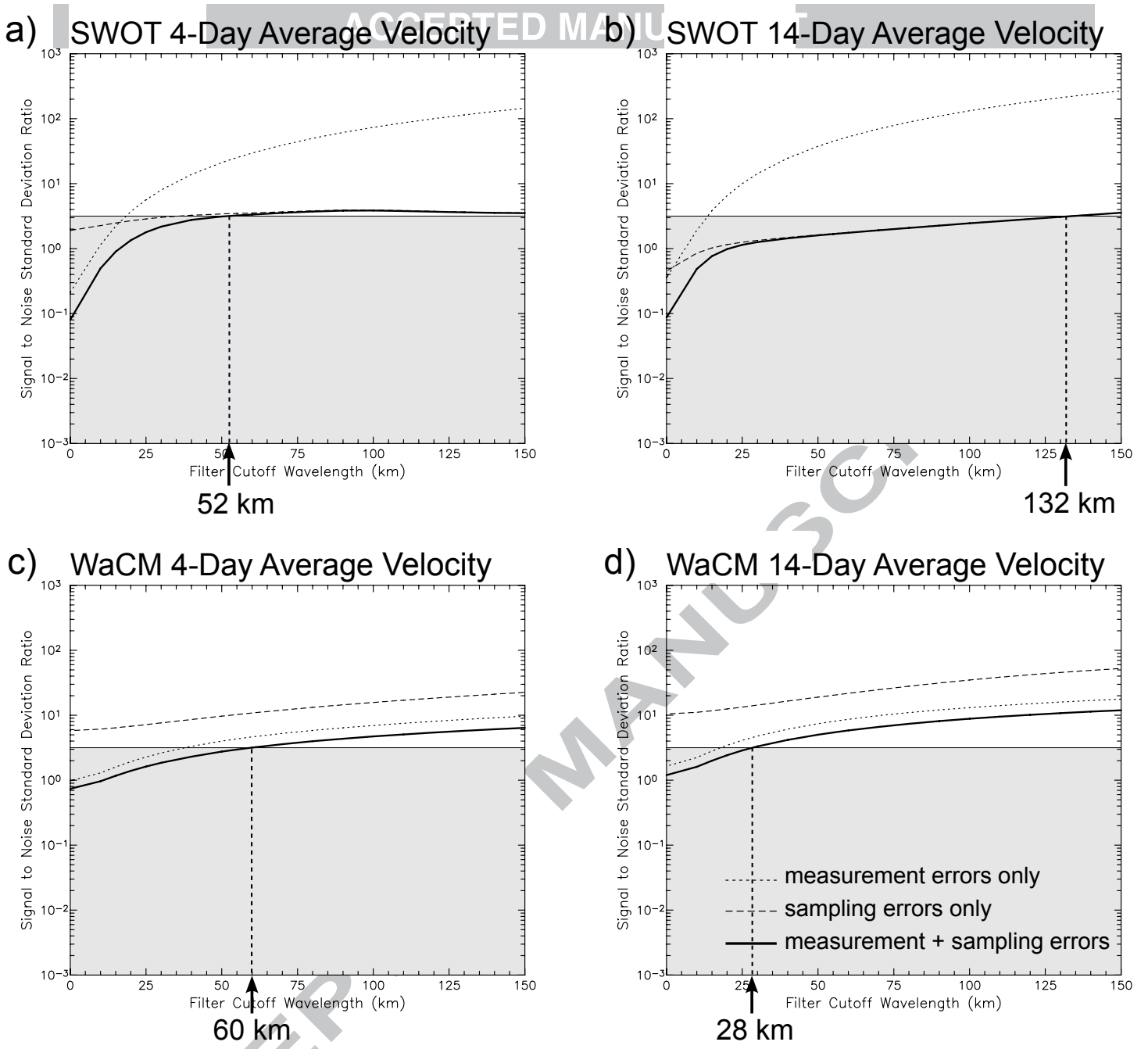

Figure 30. The S/N standard deviation ratios for the full CCS region for the magnitude of the vector-averaged velocity (referred to for expedience as "velocity") computed from simulated satellite estimates of time-averaged SSH (for SWOT) and surface velocity (for WaCM) as functions of the half-power filter cutoff wavelength of 2-dimensional isotropic smoothing using a Parzen smoother: a) Geostrophically computed SWOT estimates of 4-day averaged velocity; b) Geostrophically computed SWOT estimates of 14-day averaged velocity; c) WaCM estimates of 4-day averaged velocity; and d) WaCM estimates of 14-day averaged velocity. The dotted lines correspond to estimates over the full model domain with simulated uncorrelated measurement errors ($\sigma_h = 2.74$ cm for SWOT and $\sigma_{spd} = 0.5$ m s^{-1} for WaCM). The dashed lines correspond to estimates from simulated swath sampling of error-free fields. The thick solid lines correspond to estimates from simulated swath sampling with uncorrelated measurement errors ($\sigma_h = 2.74$ cm for SWOT and $\sigma_{spd} = 0.5$ m s^{-1} for WaCM). The S/N ratios for WaCM are based on a swath width of 1200 km. The improved S/N ratios for WaCM with a swath width of 1800 km are shown later in Fig. 43a and b. The gray area in each panel indicates S/N standard deviation ratios less than 3.16, which corresponds to a S/N variance ratio of 10. The vertical dashed line in each panel indicates the wavelength above which the S/N standard deviation ratios exceed a value of 3.16 for the case of combined measurement and sampling errors.

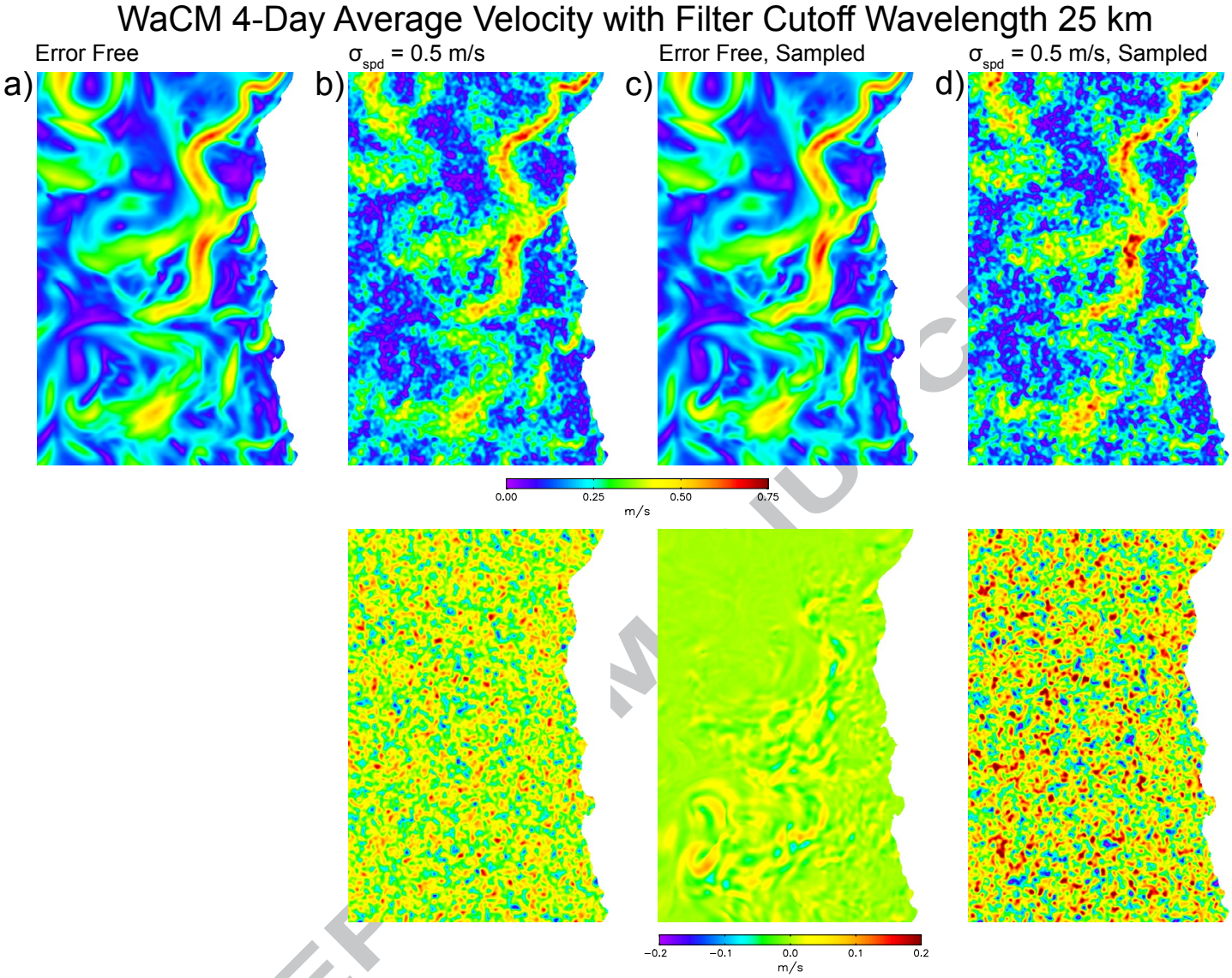

Figure 31. Maps of the magnitudes of 4-day averages of surface velocity from error-free and noisy simulated WaCM measurements of surface velocity with a swath width of 1200 km and a standard deviation of $\sigma_{spd} = 0.5$ m s^{-1} for the speed measurement noise with isotropic 2-dimensional smoothing using a Parzen smoother with a half-power filter cutoff wavelength of 25 km: Column a) The 4-day average over the full model domain computed from error-free model surface velocity fields at a time step of 0.5 day over the 4-day period; Column b) The 4-day average over the full model domain computed from model surface velocity fields at a time step of 0.5 day over the 4-day period with simulated uncorrelated speed measurement errors with a standard deviation of $\sigma_{spd} = 0.5$ m s^{-1}; Column c) The 4-day average computed from simulated WaCM swath sampling of error-free model surface velocity fields at the times and locations of each satellite observation over the 4-day period; and Column d) The 4-day average computed from simulated WaCM swath sampling of model surface velocity fields at the times and locations of each satellite observation over the 4-day period with simulated uncorrelated speed measurement errors with a standard deviation of $\sigma_{spd} = 0.5$ m s^{-1}. The bottom panels are the error maps computed by subtracting the error-free map in Column a) from the error-contaminated maps in the top row of the respective Columns b)–d).

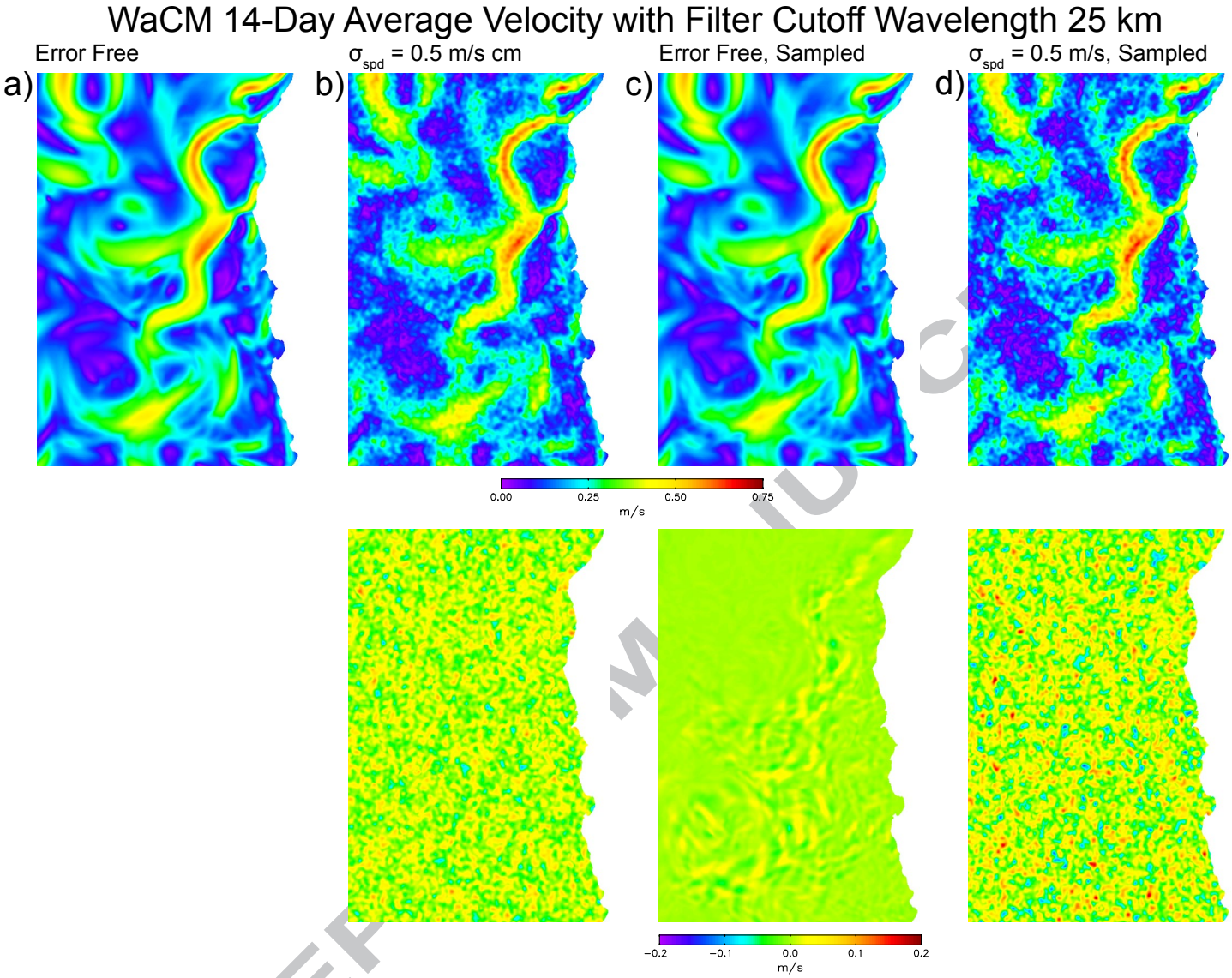

Figure 32. The same as Fig. 31, except the magnitudes of 14-day averages of surface velocity from WaCM with isotropic 2-dimensional smoothing using a Parzen smoother with a half-power filter cutoff wavelength of 25 km.

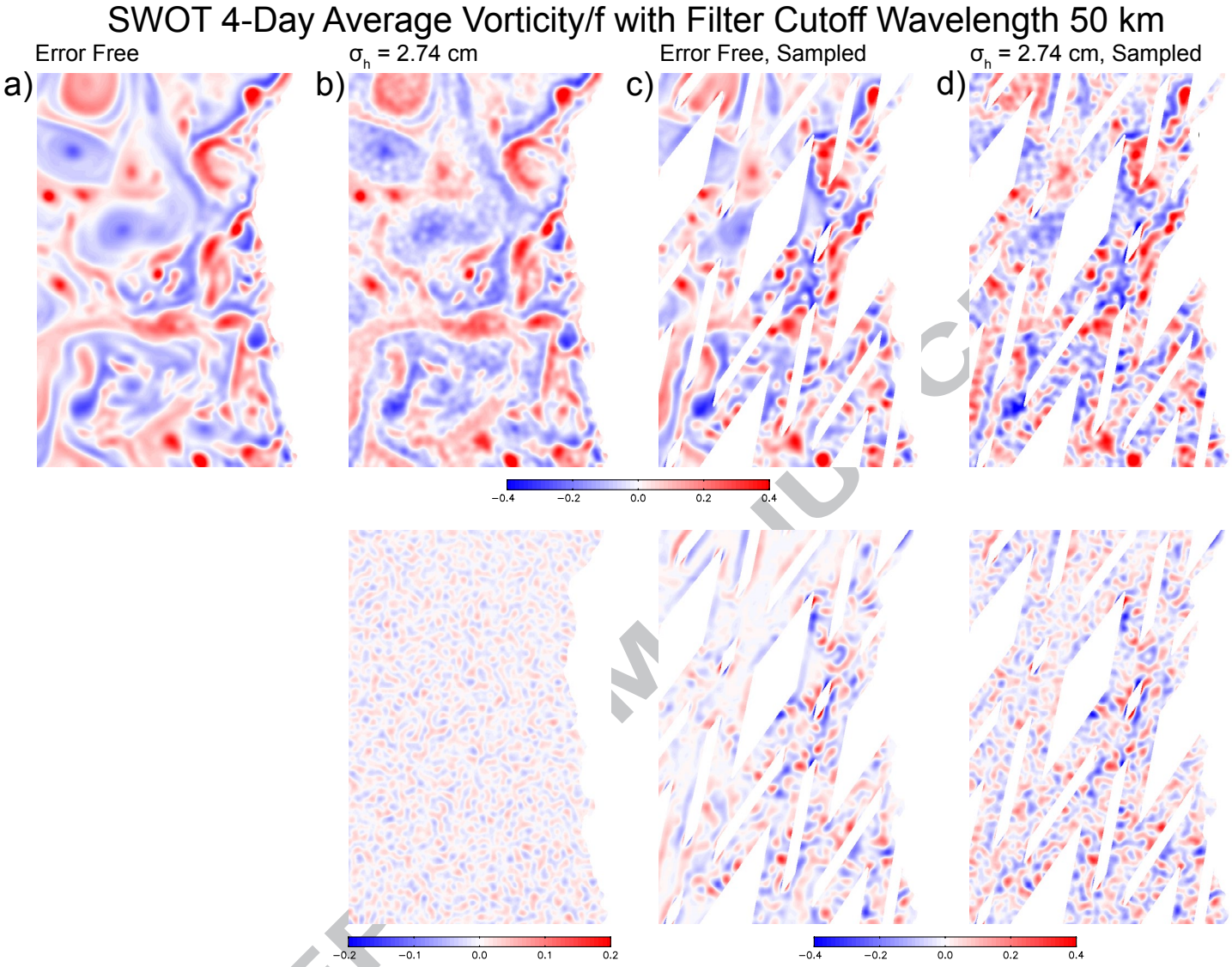

Figure 33. Maps of 4-day averages of normalized surface vorticity ζ_g/f computed geostrophically from error-free and noisy simulated SWOT measurements of SSH with isotropic 2-dimensional smoothing using a Parzen smoother with a half-power filter cutoff wavelength of 50 km. The various combinations of measurement and sampling errors are the same as for Columns a)–d) of Figs. 26 and 28. The bottom panels are the error maps computed by subtracting the error-free map in Column a) from the error-contaminated maps in the top row of the respective Columns b)–d). In order to see the relatively small effects of measurement errors alone, the color bar for the bottom panel of Column b differs from the color bar for the bottom panels of Columns c and d.

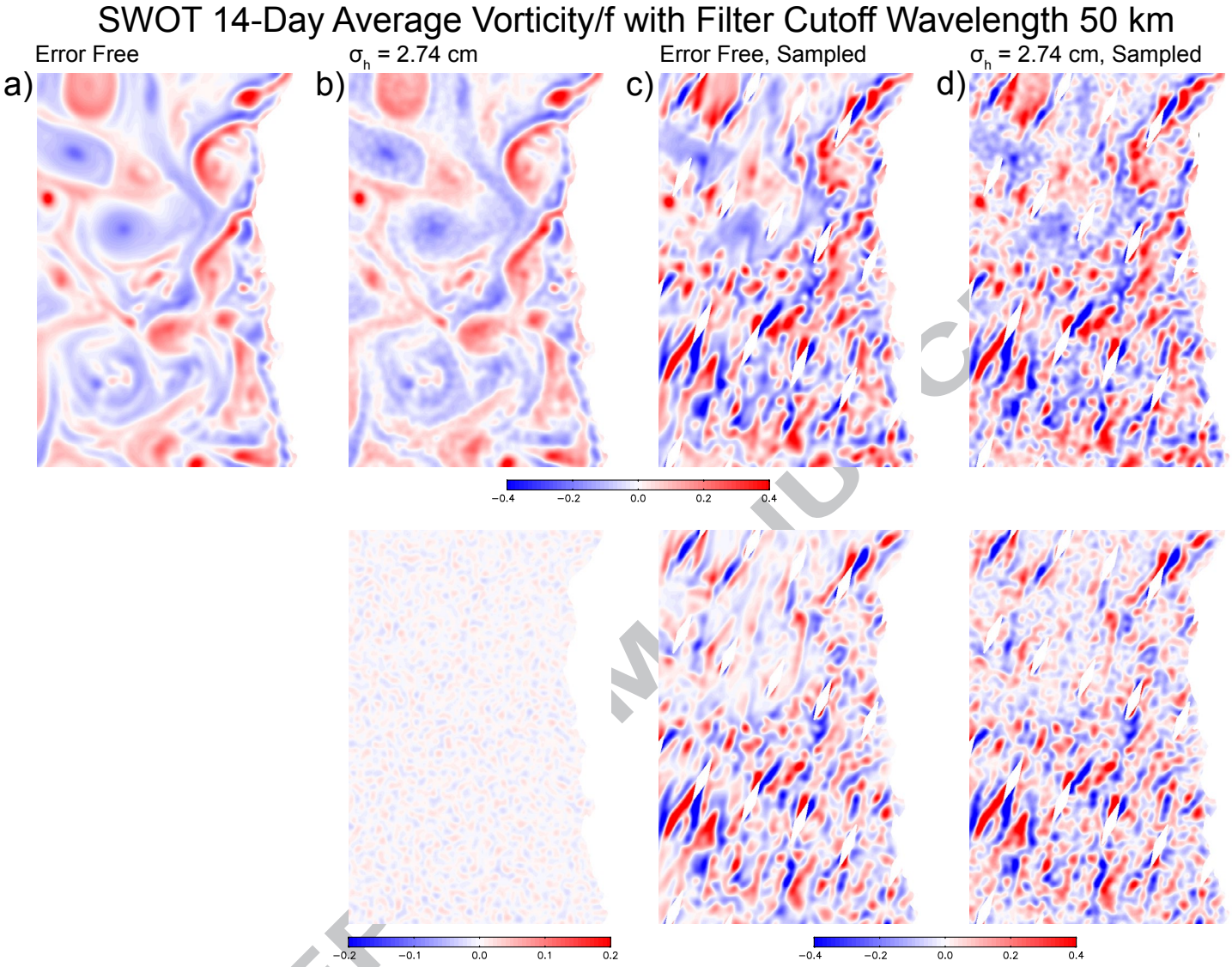

Figure 34. The same as Fig. 33, except for 14-day averages of normalized vorticity ζ_g/f computed geostrophically from simulated SWOT measurements of SSH with isotropic 2-dimensional smoothing using a Parzen smoother with a half-power filter cutoff wavelength of 50 km.

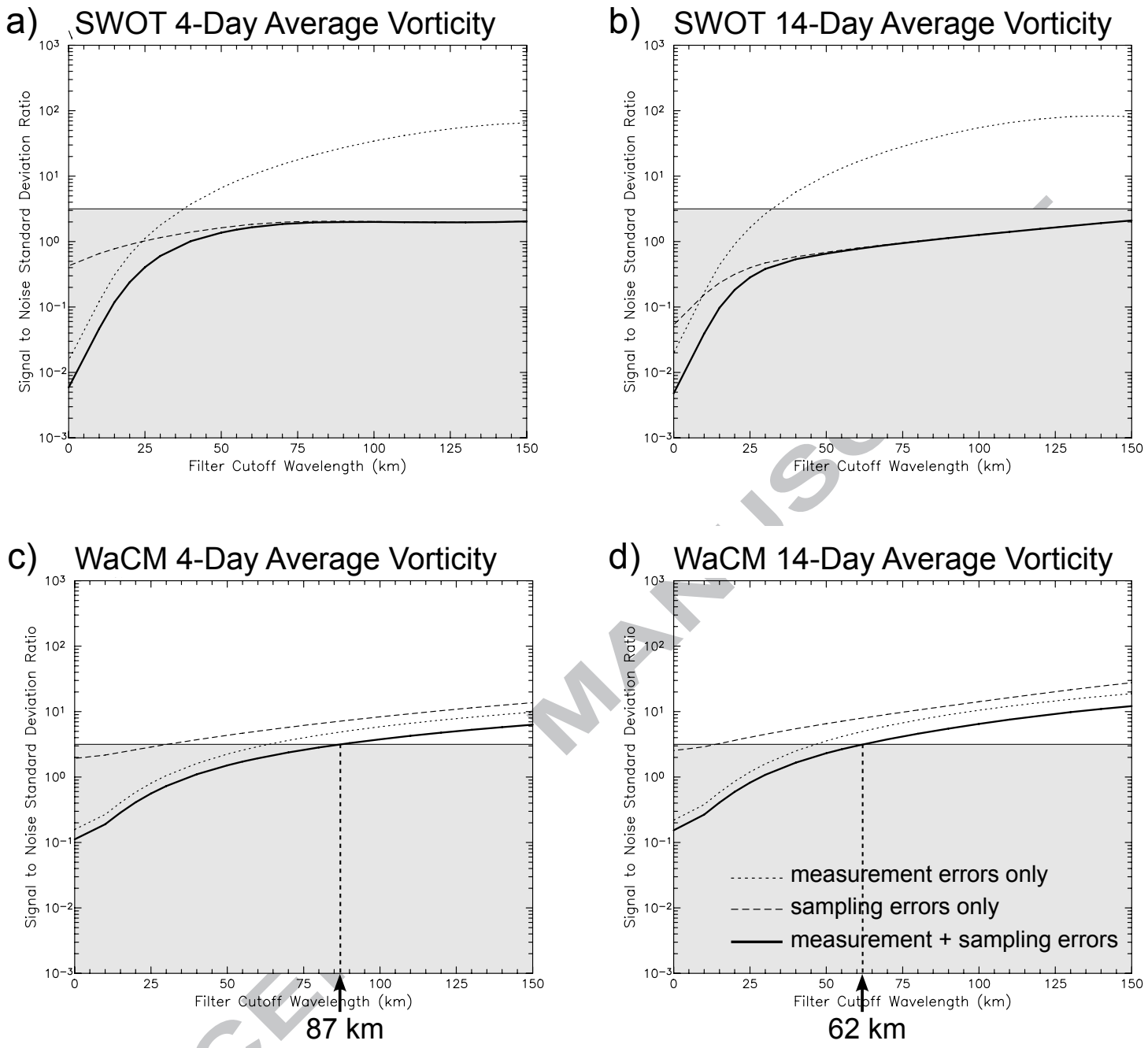

Figure 35. The S/N standard deviation ratios for the full CCS region from simulated satellite estimates of time-averaged surface vorticity computed from simulated satellite estimates of time-averaged SSH (for SWOT) and surface velocity (for WaCM) as functions of the half-power filter cutoff wavelength of 2-dimensional isotropic smoothing using a Parzen smoother: a) Geostrophically computed SWOT estimates of 4-day averaged vorticity; b) Geostrophically computed SWOT estimates of 14-day averaged vorticity; c) WaCM estimates of 4-day averaged total vorticity; and d) WaCM estimates of 14-day averaged total vorticity. The dotted, dashed and thick solid lines correspond to the same combinations of signal and errors as in Fig. 30 and the gray area in each panel indicates S/N standard deviation ratios less than 3.16. The S/N ratios for SWOT in the top panels never exceed the threshold value of 3.16. The vertical dashed lines for WaCM in the bottom panels indicate the wavelengths above which the S/N standard deviation ratios exceed a value of 3.16 for the case of combined measurement and sampling errors based on a swath width of 1200 km. The improved S/N ratios for WaCM with a swath width of 1800 km are shown in Fig. 43c and d.

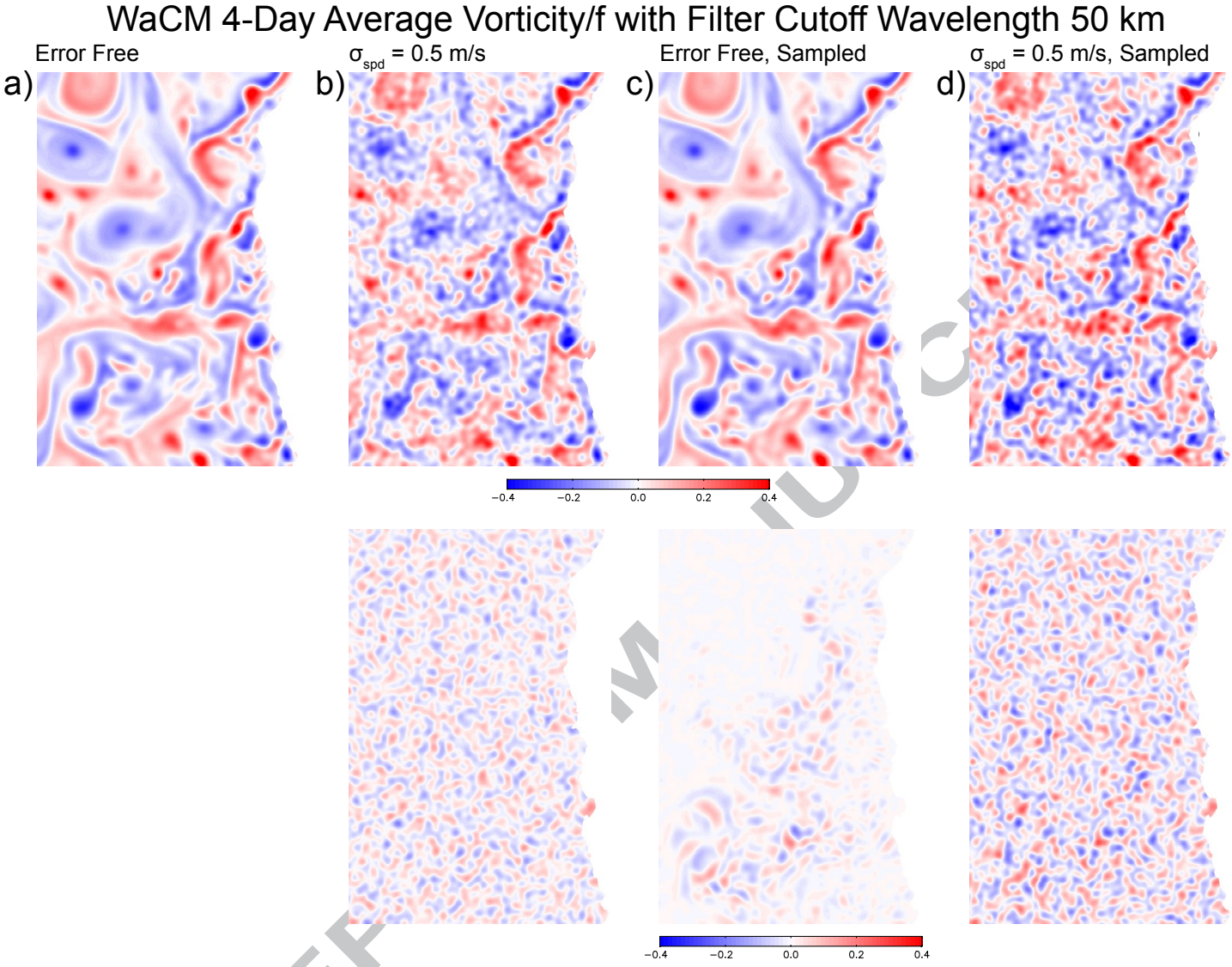

Figure 36. Maps of 4-day averages of normalized total surface vorticity ζ/f computed from error-free and noisy simulated WaCM measurements of surface velocity with a swath width of 1200 km and a standard deviation of $\sigma_{spd} = 0.5$ m s^{-1} for the speed measurement noise with isotropic 2-dimensional smoothing using a Parzen smoother with a half-power filter cutoff wavelength of 50 km. The various combinations of measurement and sampling errors are the same as for Columns a)–d) of Fig. 31. The bottom panels are the error maps computed by subtracting the error-free map in Column a) from the error-contaminated maps in the top row of the respective Columns b)–d).

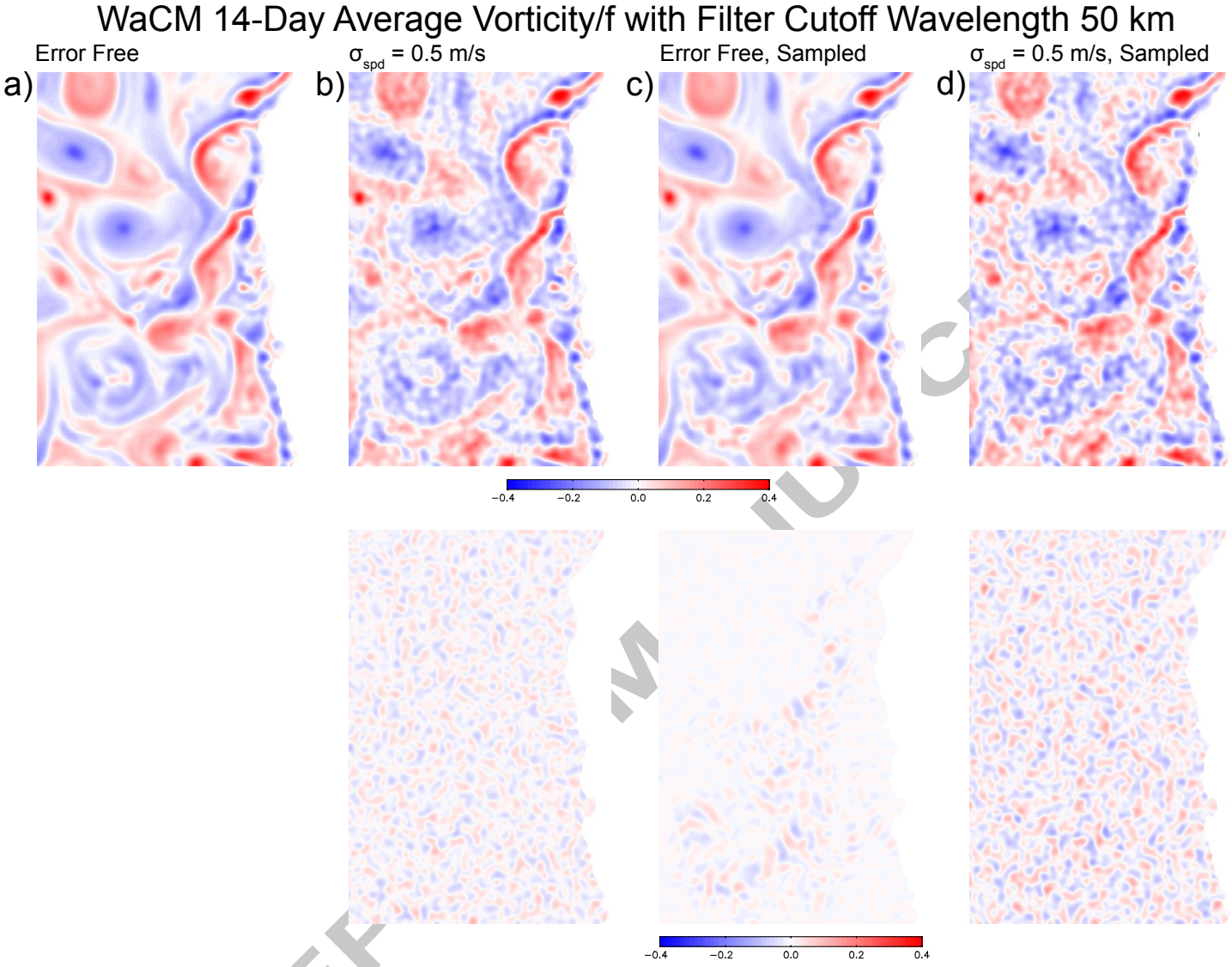

Figure 37. The same as Fig. 36, except for 14-day averages of normalized surface vorticity ζ/f computed from simulated WaCM measurements of surface velocity with 2-dimensional isotropic smoothing using a Parzen smoother with a half-power filter cutoff wavelength of 50 km.

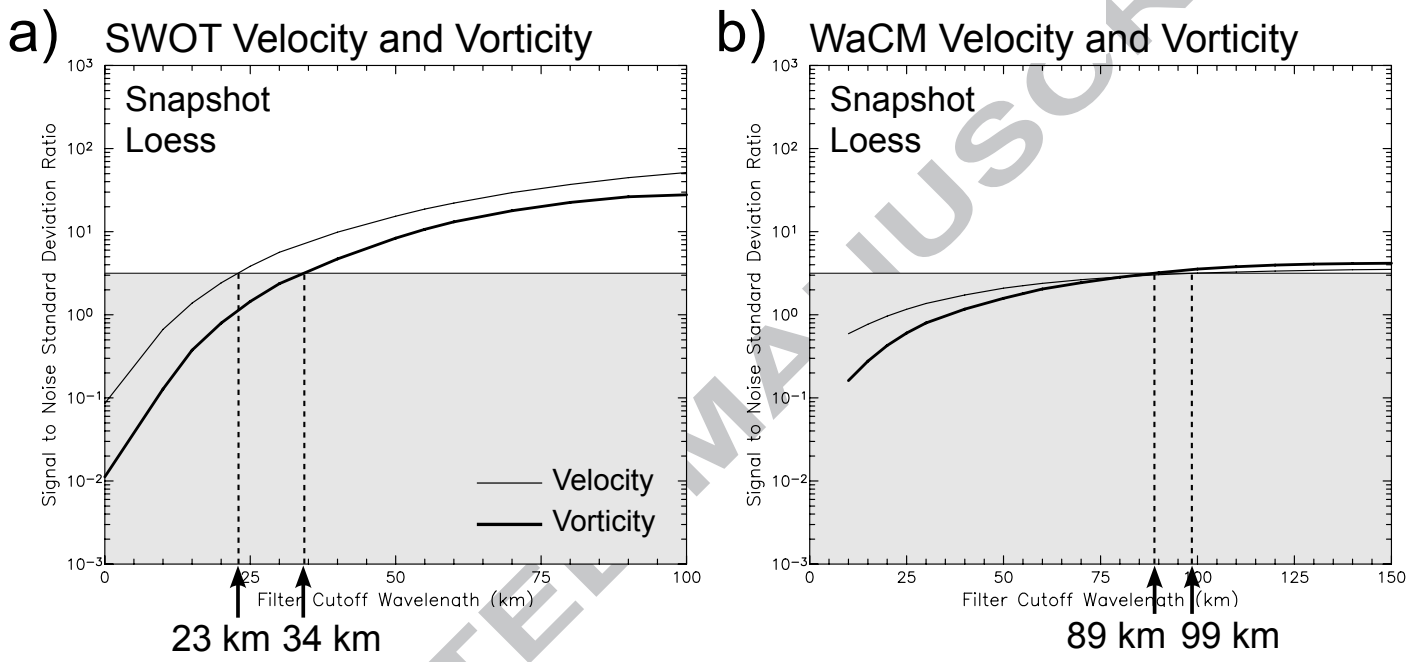

Figure 38. The same as Fig. 18, except the S/N standard deviation ratios from simulated satellite estimates of instantaneous snapshots of surface velocity as functions of the half-power filter cutoff wavelength of 2-dimensional isotropic smoothing using a loess smoother rather than the Parzen smoother used for Fig. 18.

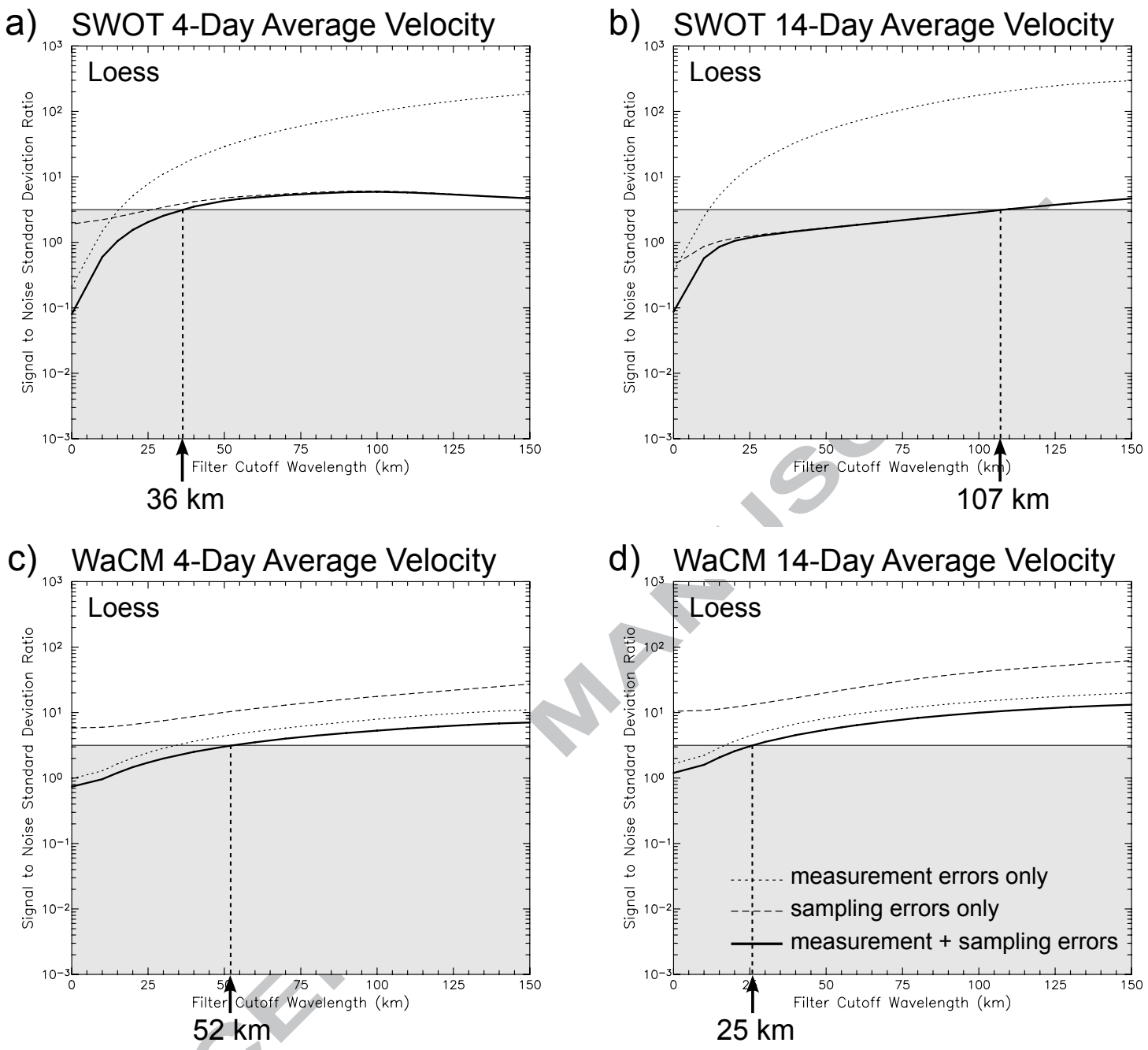

Figure 39. The same as Fig. 30, except the S/N standard deviation ratios from simulated satellite estimates of time-averaged surface velocity as functions of the half-power filter cutoff wavelength of 2-dimensional isotropic smoothing using a loess smoother rather than the Parzen smoother used for Fig. 30.

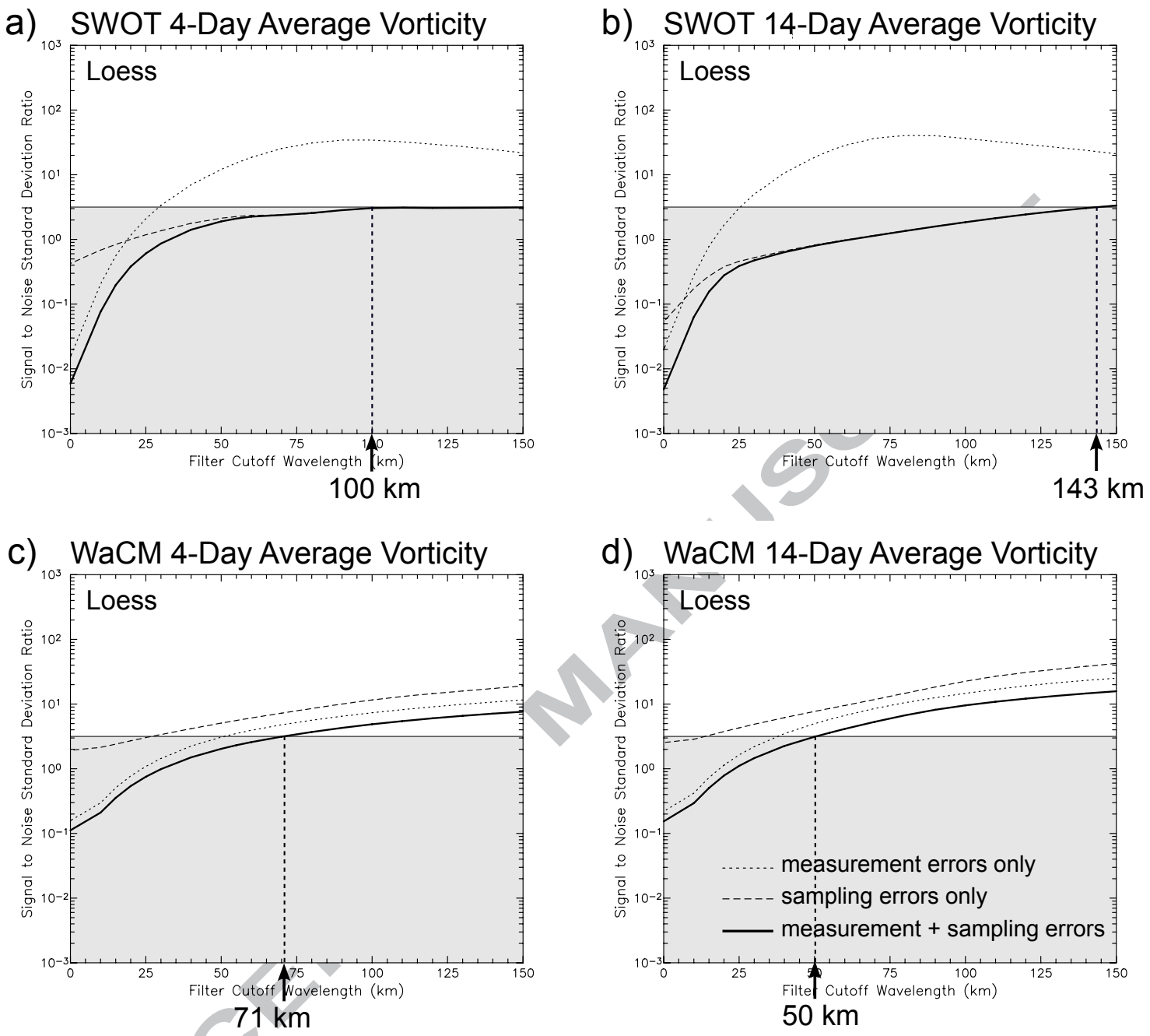

Figure 40. The same as Fig. 35, except the S/N standard deviation ratios from simulated satellite estimates of time-averaged surface vorticity as functions of the half-power filter cutoff wavelength of 2-dimensional isotropic smoothing using a loess smoother rather than the Parzen smoother used for Fig. 35.

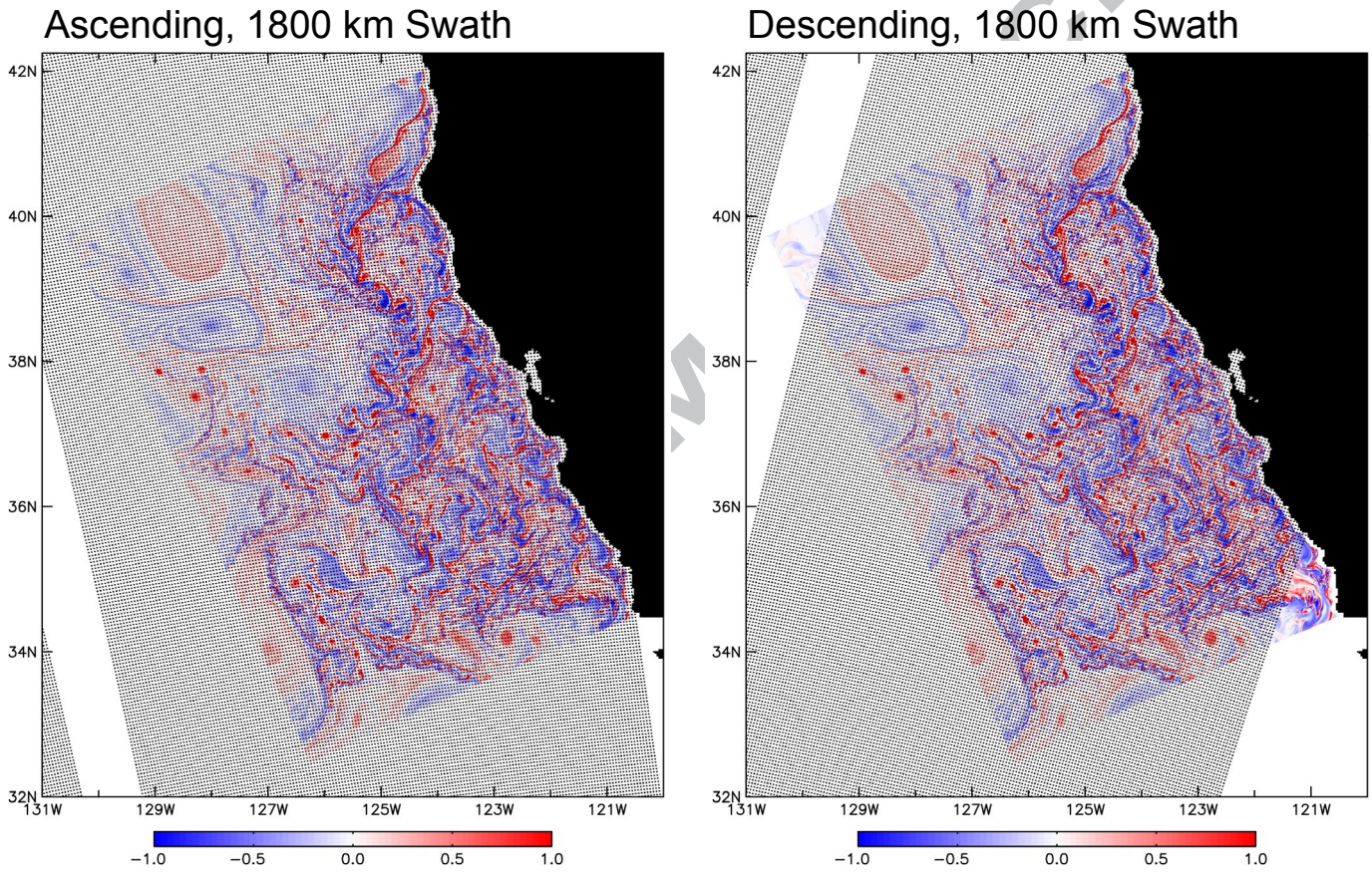

Figure 41. The same as the bottom two panels of Fig. 20, except examples of the measurement swaths for single ascending and descending overpasses of WaCM for the case of a swath width of 1800 km. The ground tracks are for illustrative purposes and could be adjusted longitudinally to optimize the sampling of any specific region of the world ocean. The details of the sampling of the CCS region would change accordingly.

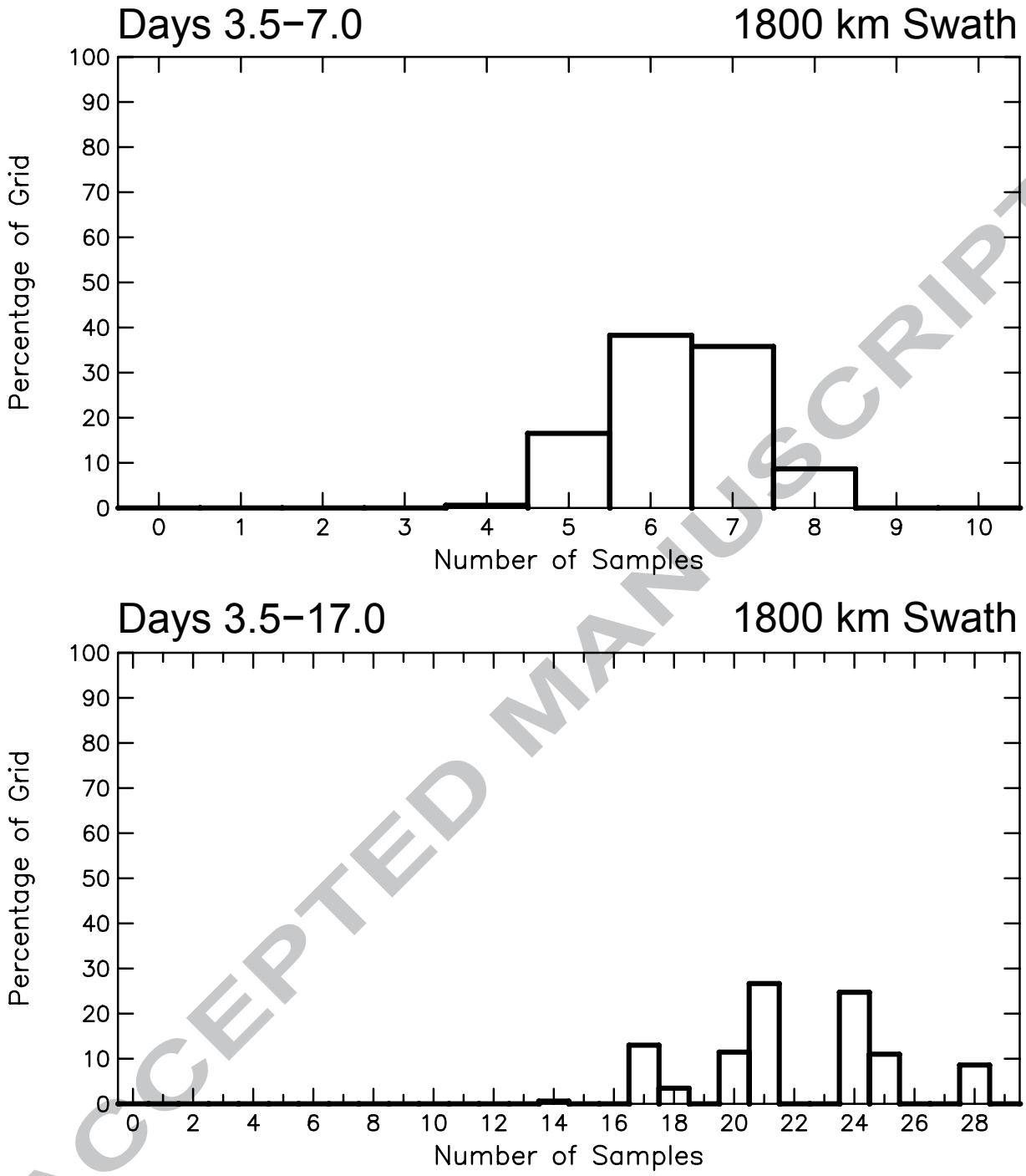

Figure 42. The same as the thick lines in Fig. 23, except histograms of the number of samples by WaCM during 4 days and 14 days based on a swath width of 1800 km rather than 1200 km.

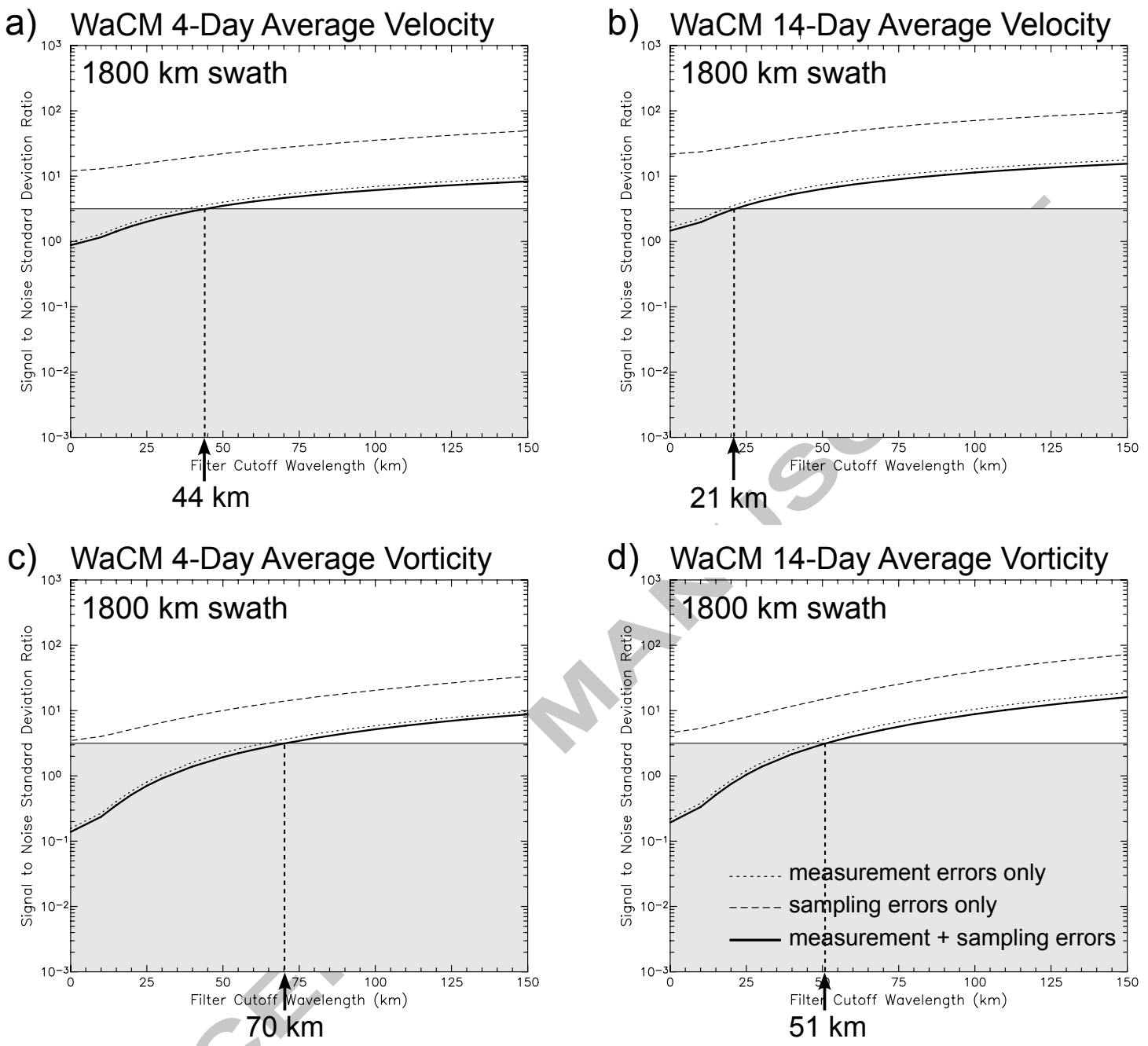

Figure 43. The same as the bottom two panels of Fig. 30 and the bottom two panels of Fig. 35, except the S/N standard deviation ratios for WaCM estimates of 4-day and 14-day averaged velocity and vorticity fields for the baseline standard deviation of $\sigma_{spd} = 0.5$ m s^{-1} for the speed measurement noise and a swath width of 1800 km rather than 1200 km.

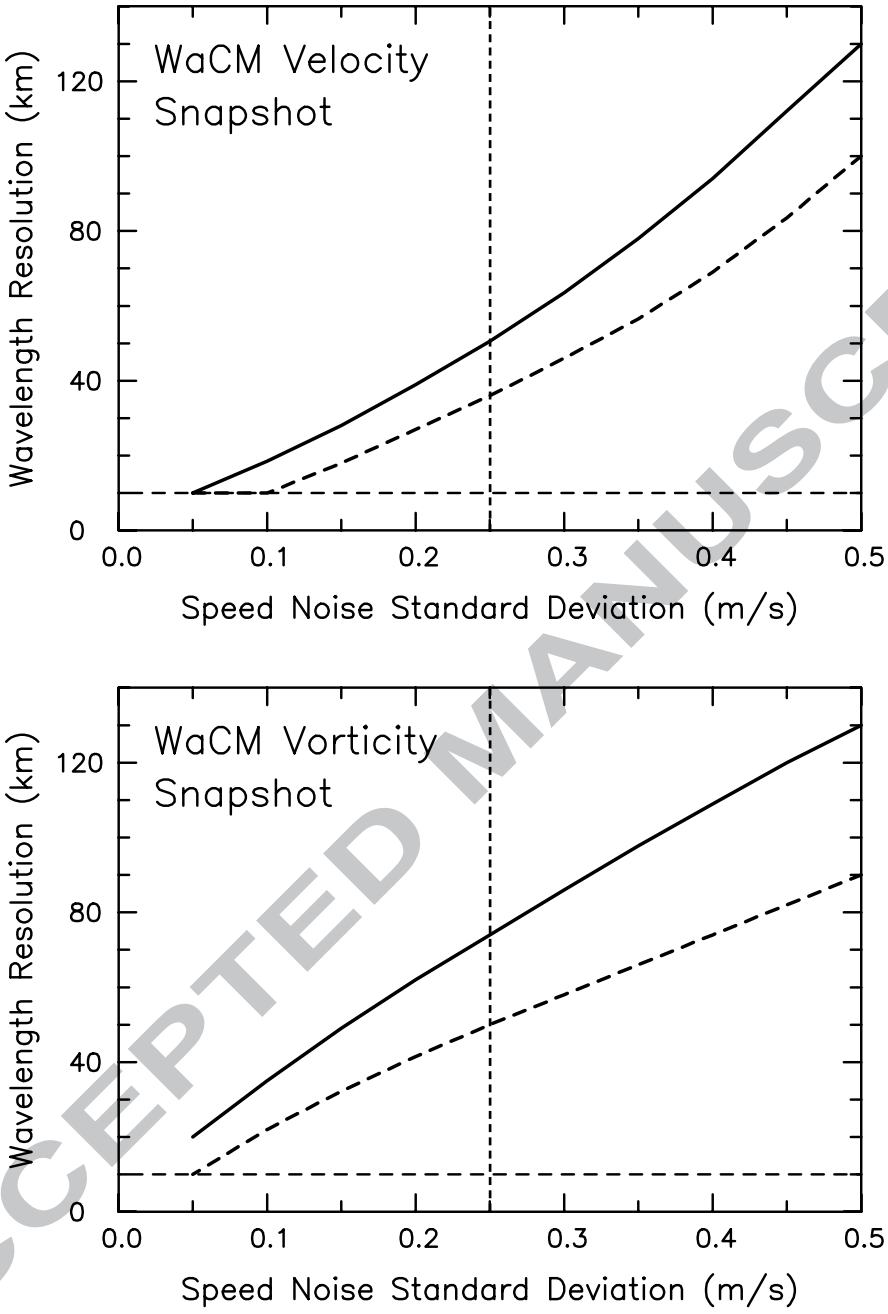

Figure 44. The resolution capabilities of WaCM estimates of instantaneous snapshot maps of the full CCS region (which are very nearly achieved on each satellite overpass with a swath width of 1800 km – see Fig. 41) as functions of the standard deviation σ_{spd} of the uncorrelated errors of WaCM measurements of surface velocity: a) maps of velocity; and b) maps of vorticity. The solid and dashed lines in each panel correspond to the half-power filter cutoff wavelengths above which the S/N standard deviation ratios exceed a value of 3.16 using Parzen and loess smoothers, respectively. For reference, the vertical dashed line in each panel indicates a standard deviation of $\sigma_{spd} = 0.25$ m s^{-1} for the uncorrelated speed measurement errors, which corresponds to half of the baseline value of $\sigma_{spd} = 0.5$ m s^{-1}.

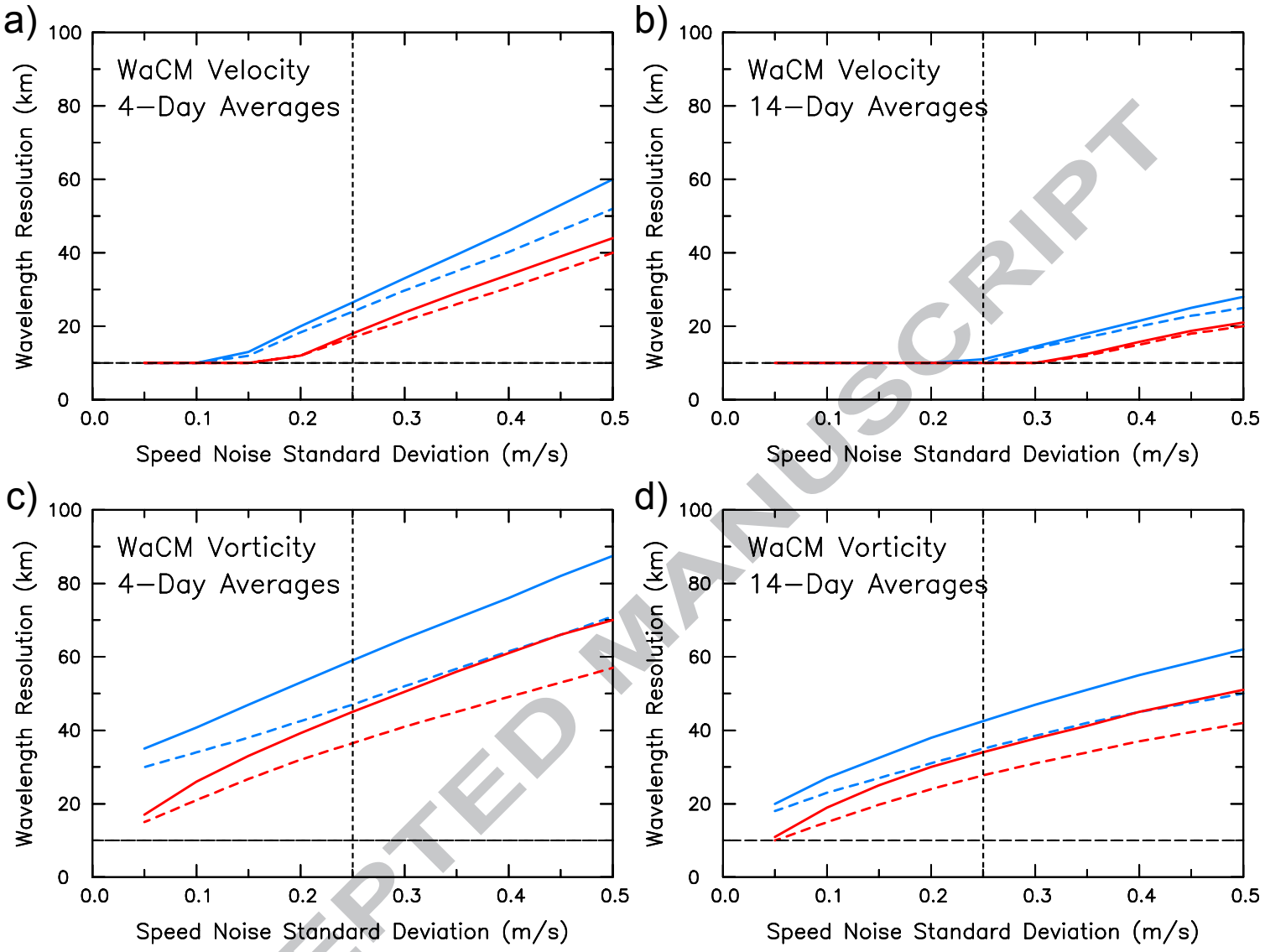

Figure 45. The resolution capabilities of WaCM estimates of 4-day and 14-day averages (left and right columns) of surface velocity and vorticity (top and bottom rows) as functions of the standard deviation σ_{spd} of the uncorrelated speed errors of WaCM measurements of surface velocity for swath widths of 1200 km and 1800 km (blue and red lines, respectively). The solid and dashed lines in each panel correspond to the half-power filter cutoff wavelengths above which the S/N standard deviation ratios exceed a value of 3.16 using Parzen and loess smoothers, respectively. For reference, the vertical dashed line in each panel indicates a standard deviation of $\sigma_{spd} = 0.25$ m s^{-1} for the uncorrelated speed measurement errors, which corresponds to half of the baseline value of $\sigma_{spd} = 0.5$ m s^{-1}.

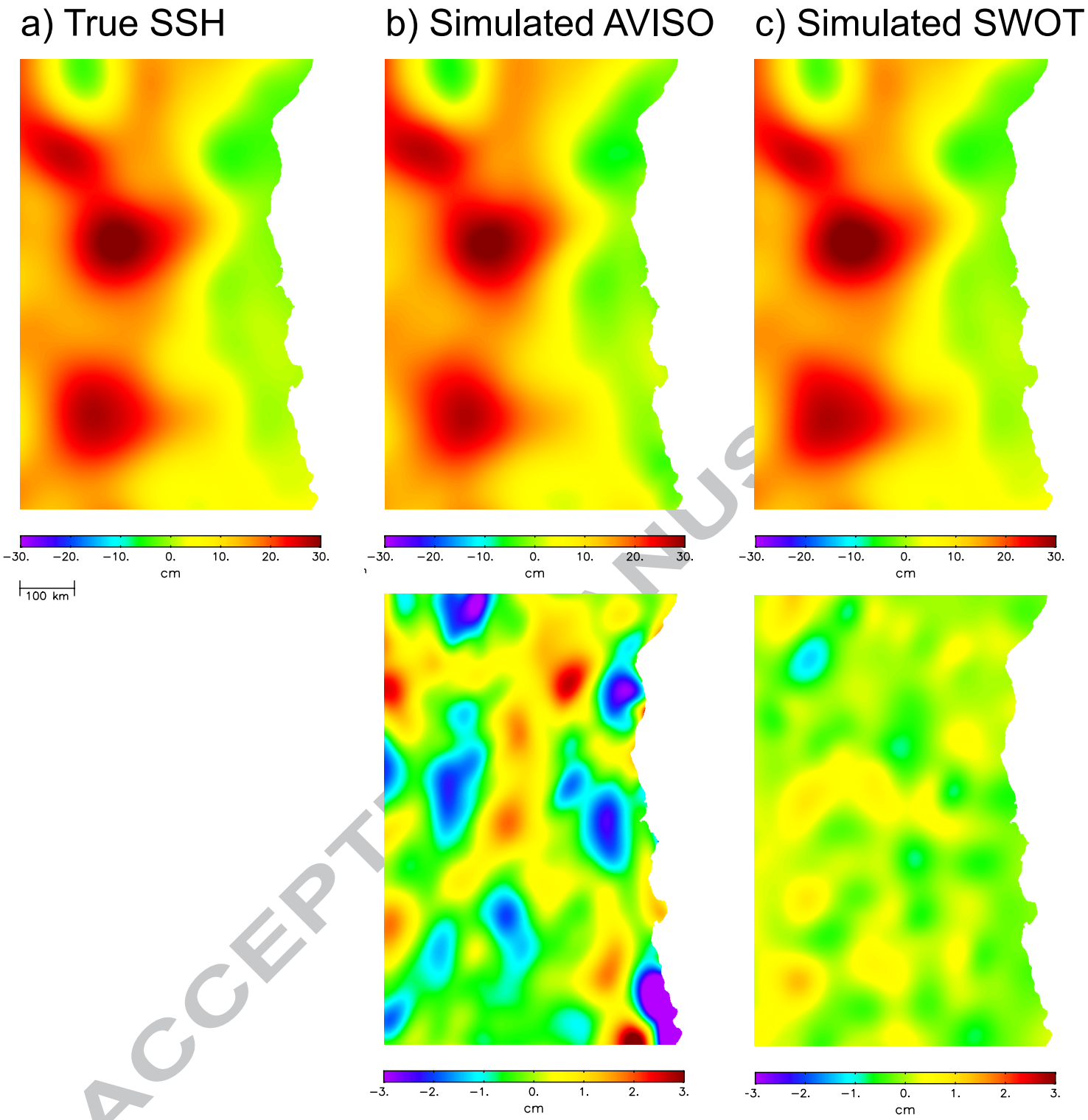

Figure 46. Maps of 30-day averaged SSH smoothed 2-dimensionally with a half-power filter cutoff wavelength of 200 km in each dimension: Column a) The "true" space-time smoothed field computed from error-free model SSH fields at a time step of 0.5 day over the 30-day period; Column b) The space-time smoothed field computed from simulated TOPEX/Poseidon and ERS-1 nadir altimeter sampling of error-free model SSH fields at the times and locations of each altimeter observation over the 30-day period; and Column c) The space-time smoothed field computed from simulated SWOT swath sampling of error-free model SSH fields at the times and locations of each SWOT observation over the 30-day period. The bottom panels are maps of the sampling errors computed by subtracting the error-free map in Column a) from the satellite-sampled maps in top row of the respective columns b) and c).

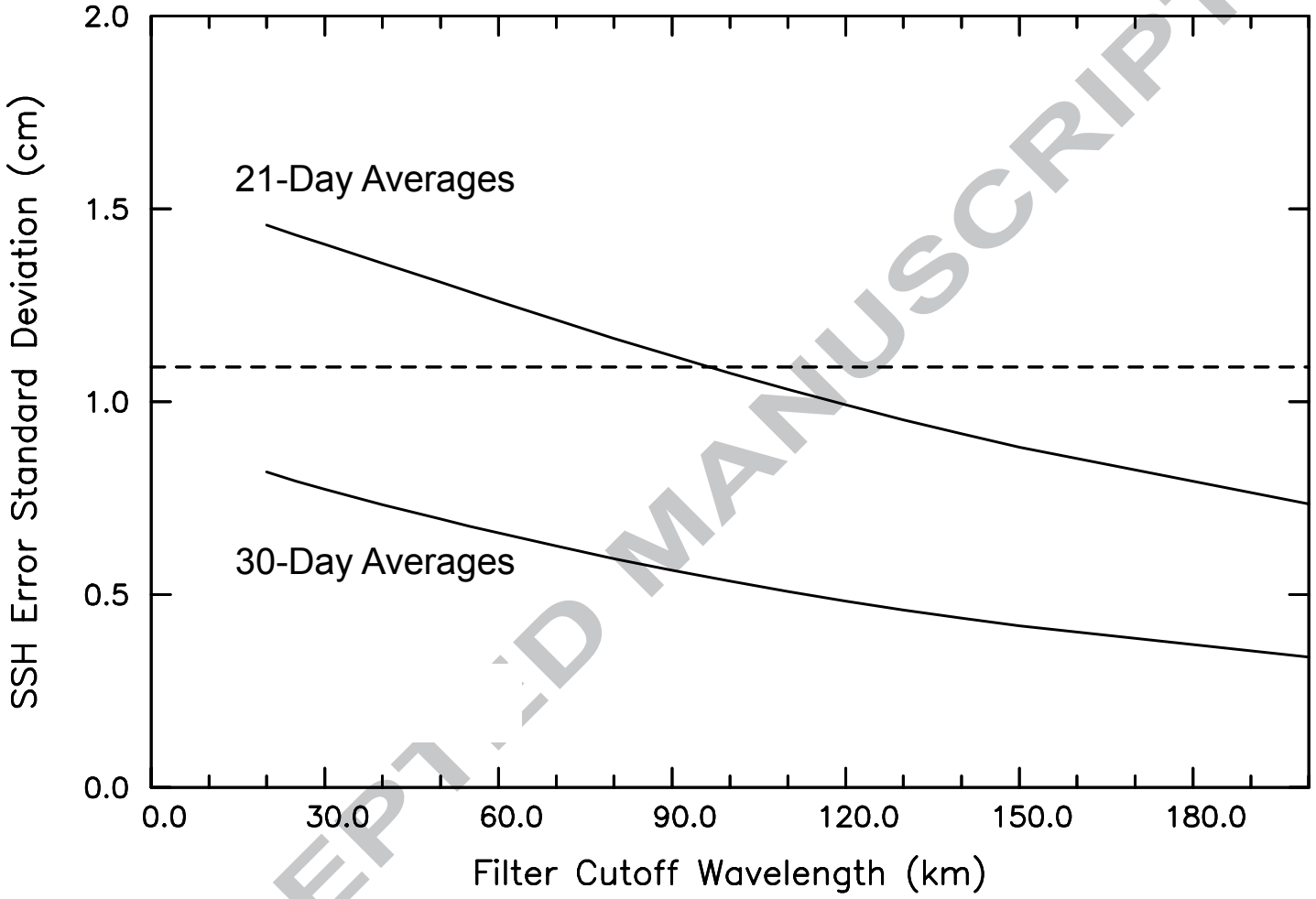

Figure 47. The standard deviations of the sampling errors in 2-dimensionally smoothed 30-day and 21-day averaged SSH fields constructed from simulated SWOT data as functions of half-power filter cutoff wavelength. The horizontal dashed line corresponds to the 1.09-cm standard deviation of the sampling errors in the simulated CLS/AVISO SSH field in the bottom panel of Fig. 46b constructed from error-free model SSH fields subsampled at the times and locations of the TOPEX/Poseidon and ERS-1 nadir altimeter observations over a 30-day period.

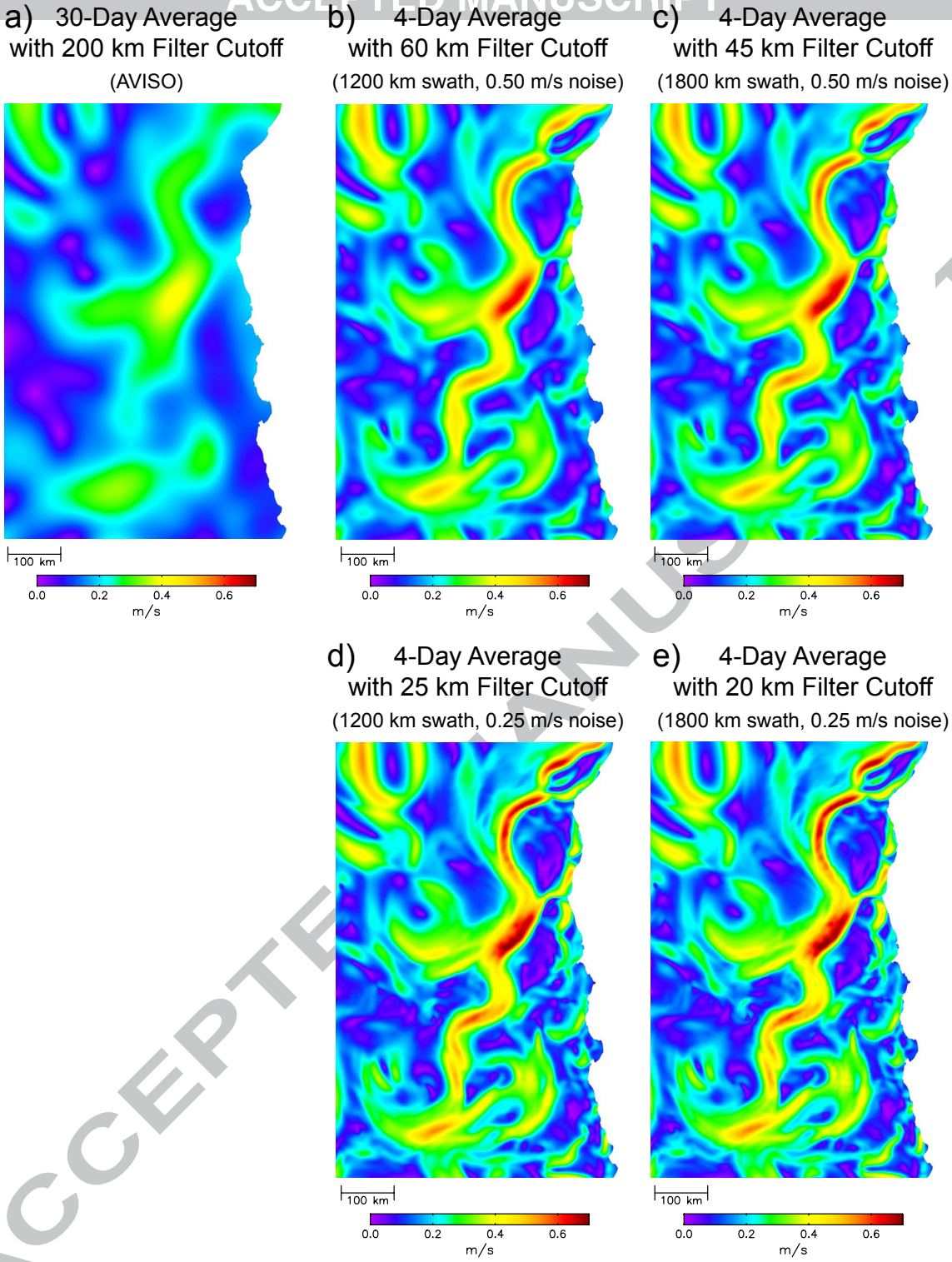

Figure 48. Space-time smoothed maps of the magnitudes of vector-averaged error-free surface velocity with the wavelength resolutions that can be achieved from presently available altimeter data and from 4-day averages of WaCM data with the combinations of measurement noise σ_{spd} and swath widths listed in Table 4c: a) The resolution of 200 km by 30 days that can be achieved with the geostrophic approximation from SSH maps constructed from presently available merged nadir altimetry data; b) A resolution of 60 km that could be achieved in 4-day averages of WaCM data for a swath width of 1200 km and $\sigma_{spd} = 0.50$ m s^{-1}; c) A resolution of 45 km that could be achieved in 4-day averages of WaCM data for a swath width of 1800 km and $\sigma_{spd} = 0.50$ m s^{-1}; d) A resolution of 25 km that could be achieved in 4-day averages of WaCM data for a swath width of 1200 km and $\sigma_{spd} = 0.25$ m s^{-1}; and e) A resolution of 20 km that could be achieved in 4-day averages of WaCM data for a swath width of 1800 km and $\sigma_{spd} = 0.25$ m s^{-1}.

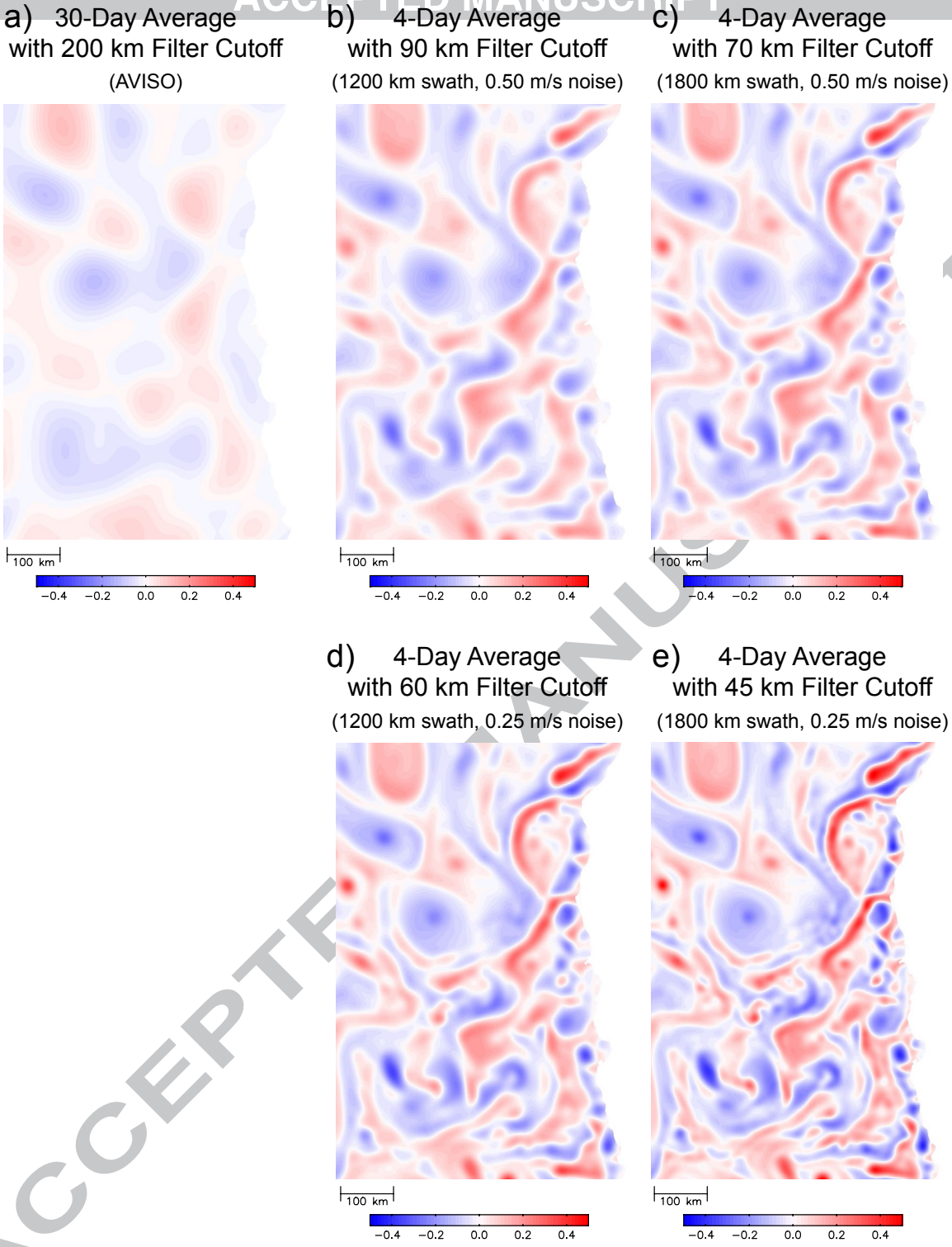

Figure 49. Space-time smoothed maps of error-free vorticity scaled by the local Coriolis parameter f with the wavelength resolutions that can be achieved from presently available altimeter data and from 4-day averages of WaCM data with the combinations of measurement noise σ_{spd} and swath widths listed in Table 4d: a) The resolution of 200 km by 30-days that can be achieved with the geostrophic approximation from SSH maps constructed from presently available merged nadir altimetry data; b) A resolution of 90 km that could be achieved in 4-day averages of WaCM data for a swath width of 1200 km and $\sigma_{spd} = 0.50$ m s^{-1}; c) A resolution of 70 km that could be achieved in 4-day averages of WaCM data for a swath width of 1800 km and $\sigma_{spd} = 0.50$ m s^{-1}; d) A resolution of 60 km that could be achieved in 4-day averages of WaCM data for a swath width of 1200 km and $\sigma_{spd} = 0.25$ m s^{-1}; and e) A resolution of 45 km that could be achieved in 4-day averages of WaCM data for a swath width of 1800 km and $\sigma_{spd} = 0.25$ m s^{-1}.

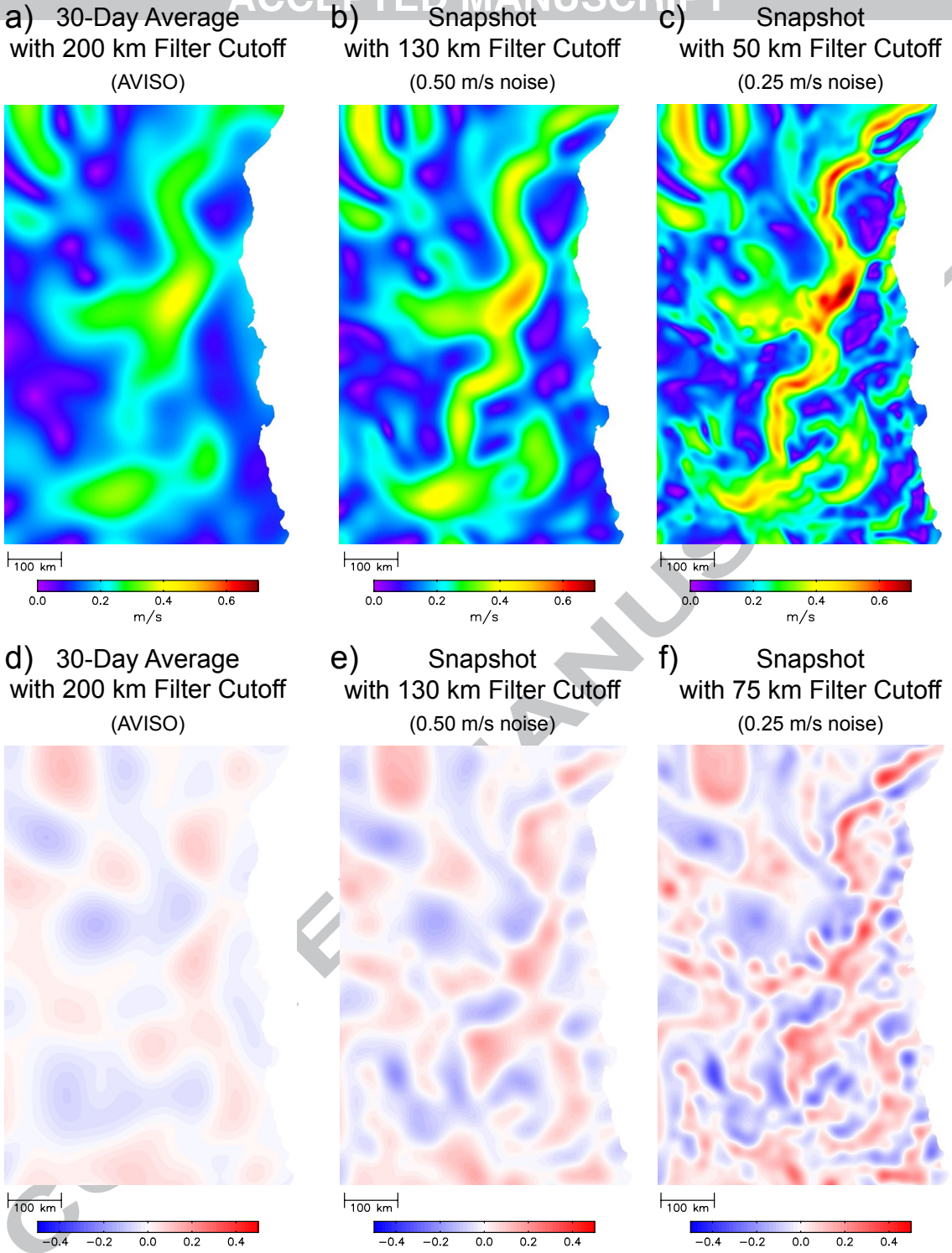

Figure 50. Spatially smoothed maps of the magnitudes of vector-averaged error-free surface velocity (top row) and error-free vorticity scaled by the local Coriolis parameter f (bottom row) with the wavelength resolutions that can be achieved from presently available altimeter data and from instantaneous snapshot maps of WaCM data on a single satellite overpass with the combinations of measurement noise σ_{spd} and swath widths listed in Tables 4a and 4b: a) The resolution of 200 km by 30 days that can be achieved for velocity computed geostrophically from presently available merged nadir altimetry data (the same as Fig. 48a); b) A resolution of 130 km that could be achieved for velocity from a snapshot of WaCM data with $\sigma_{spd} = 0.50$ m s^{-1}; c) A resolution of 50 km that could be achieved for velocity from a snapshot of WaCM data with $\sigma_{spd} = 0.25$ m s^{-1}; d) The resolution of 200 km by 30 days that can be achieved for vorticity from presently available merged nadir altimetry data (the same as Fig. 49a); e) A wavelength resolution of 75 km that could be achieved from a snapshot of WaCM data with $\sigma_{spd} = 0.50$ m s^{-1}; and f) A wavelength resolution of 75 km that could be achieved from a snapshot of WaCM data with $\sigma_{spd} = 0.25$ m s^{-1}.

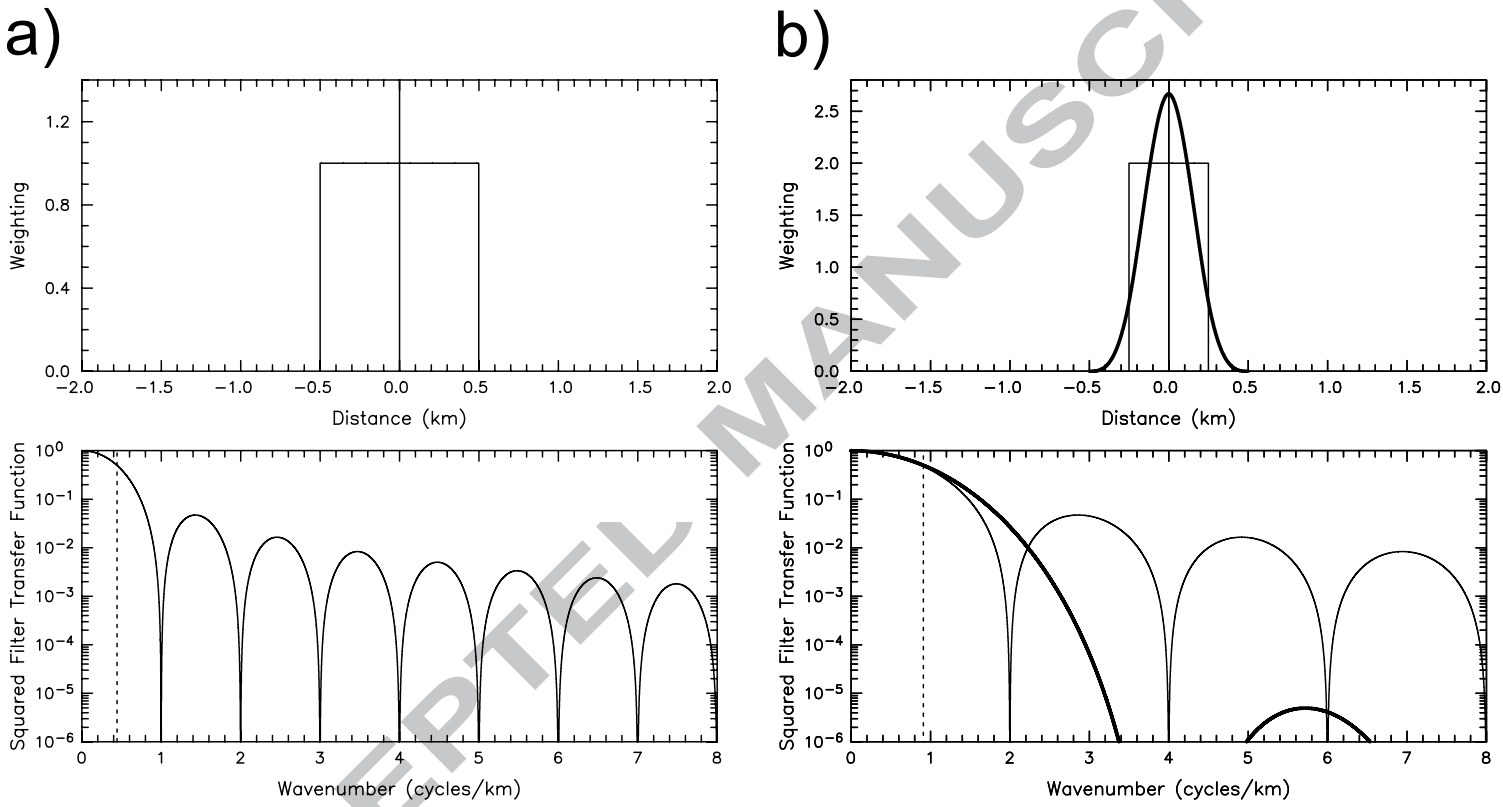

Figure A1. The weighting functions (top panels) and log-linear plots of the squared filter transfer functions (bottom panels) for uniformly weighted running-average smoothers with spans of 1 km and 0.5 km (thin lines in panels a and b, respectively) and for a Parzen weighted running average smoother with a span of 1 km (thick line in panel b).

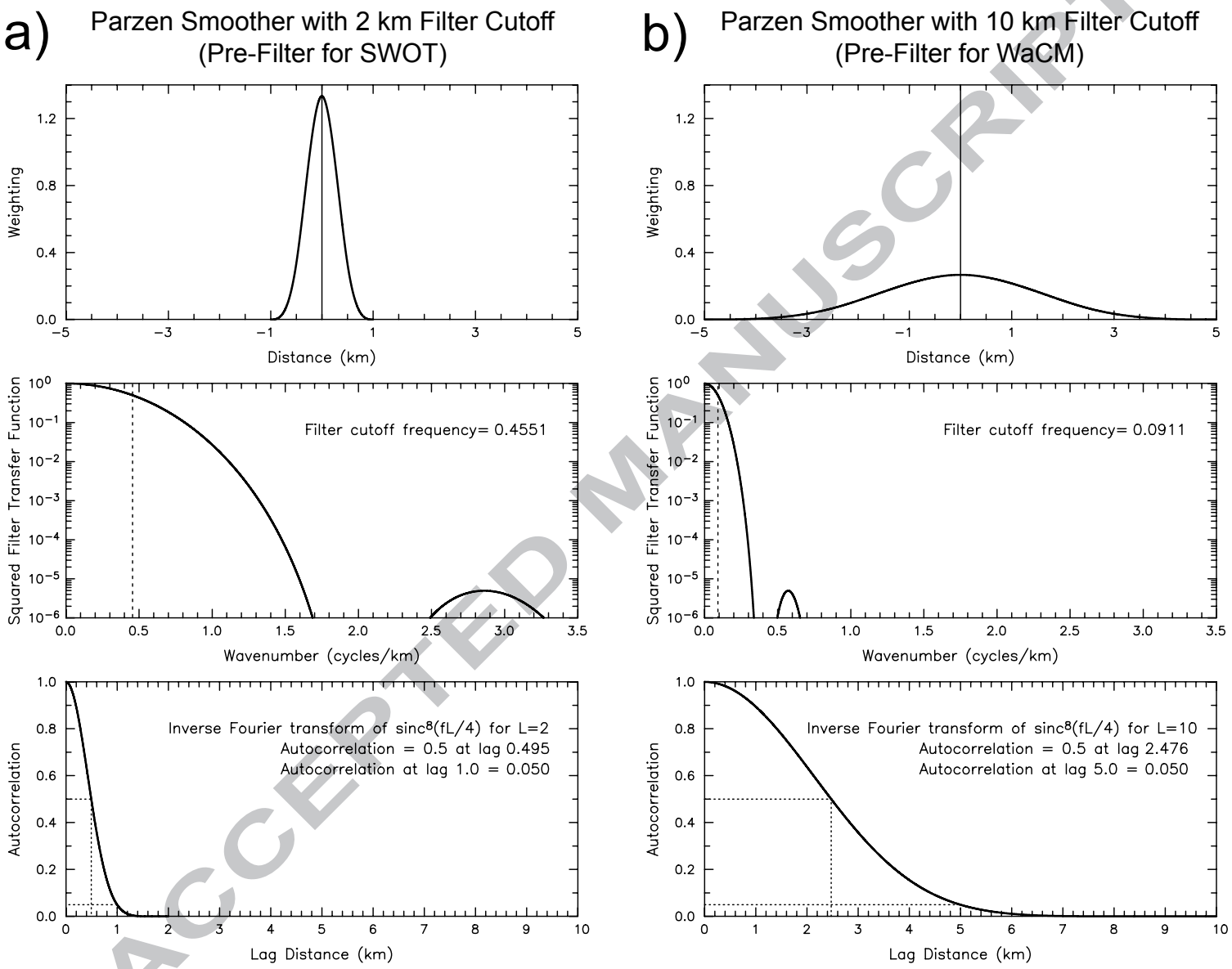

Figure B1. The weighting functions (top panels), log-linear plots of the squared filter transfer functions (middle panels) and lagged autocorrelation functions (bottom panels) for Parzen smoothers with spans of 2 km (Column a) and 10 km (Column b) that are used in this study to simulate pre-filtering of SWOT data and WaCM data, respectively. The half-power filter cutoff wavelengths of these Parzen smoothers (shown by the dotted lines in the middle panels) are approximately 2 km and 10 km. The dotted lines in the bottom panels indicate the lags at which the autocorrelation functions decay to values of 0.5 and 0.05.

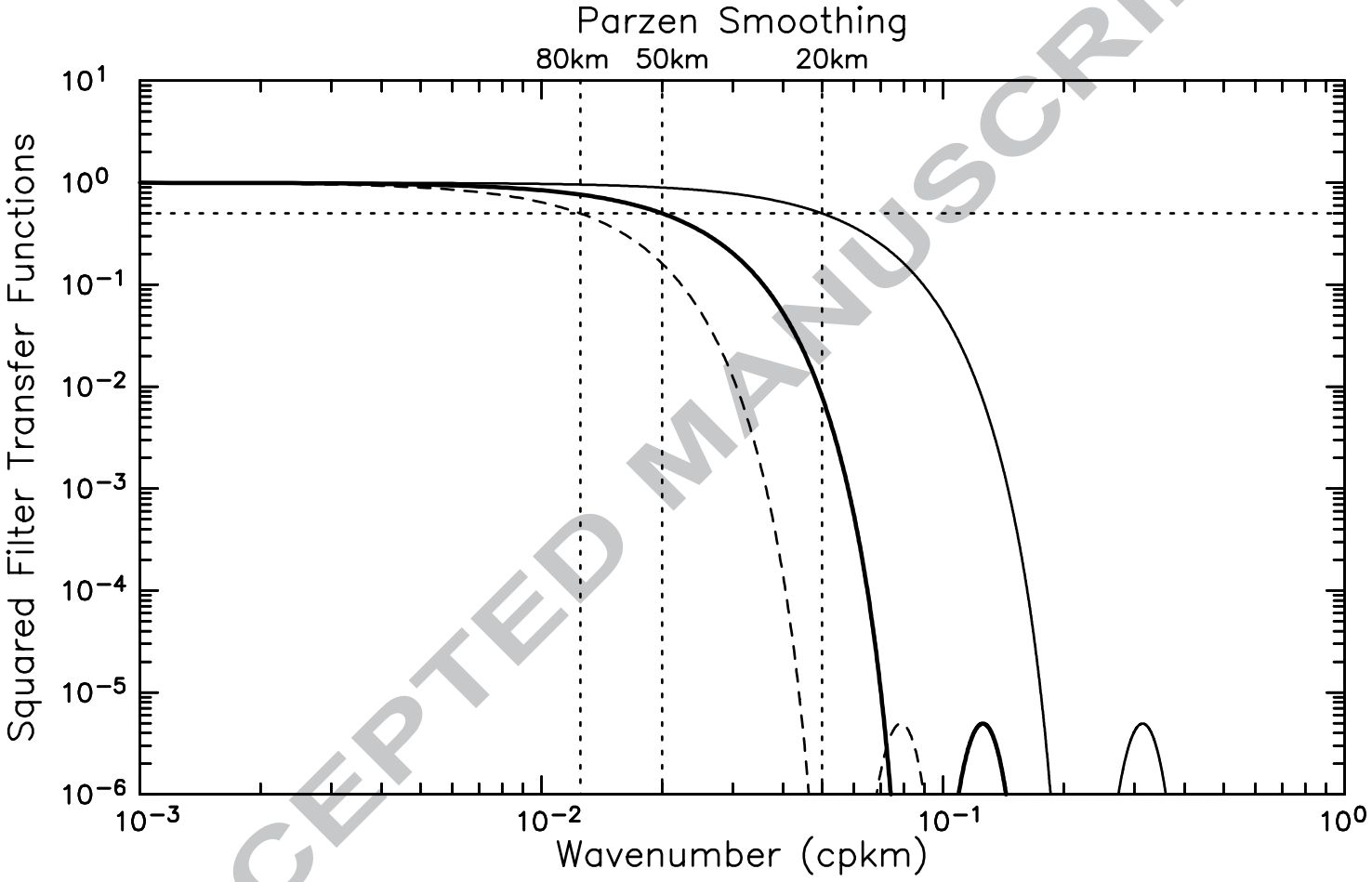

Figure C1. Log-log plots of the squared filter transfer functions of Parzen smoothers with half-power filter cutoff wavelengths of 20, 50 and 80 km (thin solid, thick solid and dashed lines, respectively). The horizontal dotted line corresponds to an ordinate value of 0.5. The half-power filter cutoff wavelengths for the Parzen smoothers are shown by the three vertical dotted lines, which are the wavenumbers at which each squared filter transfer function intersects the horizontal dotted line.

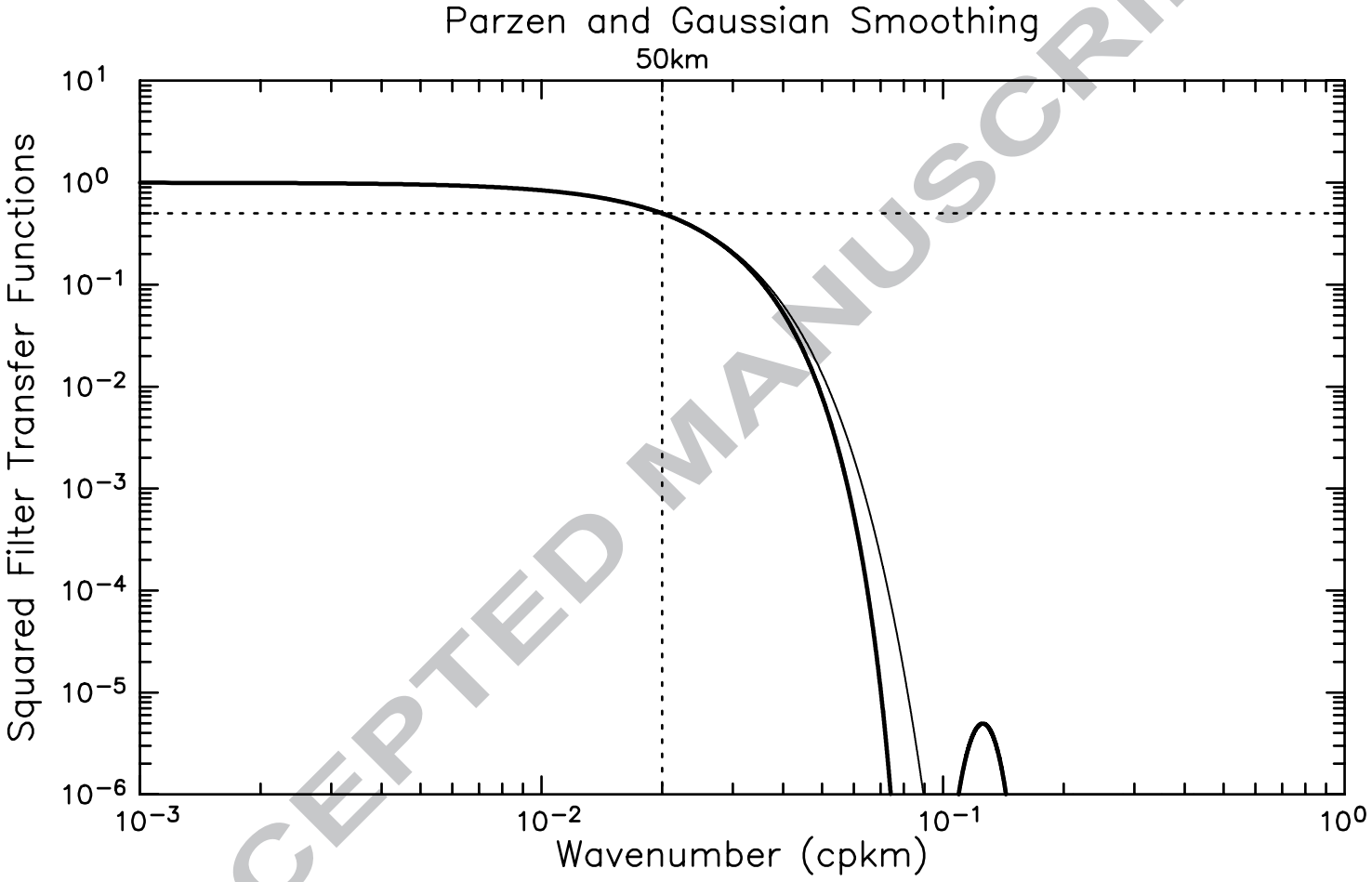

Figure C2. Log-log plots of the squared filter transfer functions with a half-power filter cutoff wavelength of 50 km for the Parzen smoother (thick line, which is the same as the thick line in Fig. C1) and a Gaussian-weighted smoother (thin line). The horizontal dotted line corresponds to an ordinate value of 0.5 and the vertical dotted line is the wavenumber at which the two squared filter transfer functions intersect the horizontal dotted line.

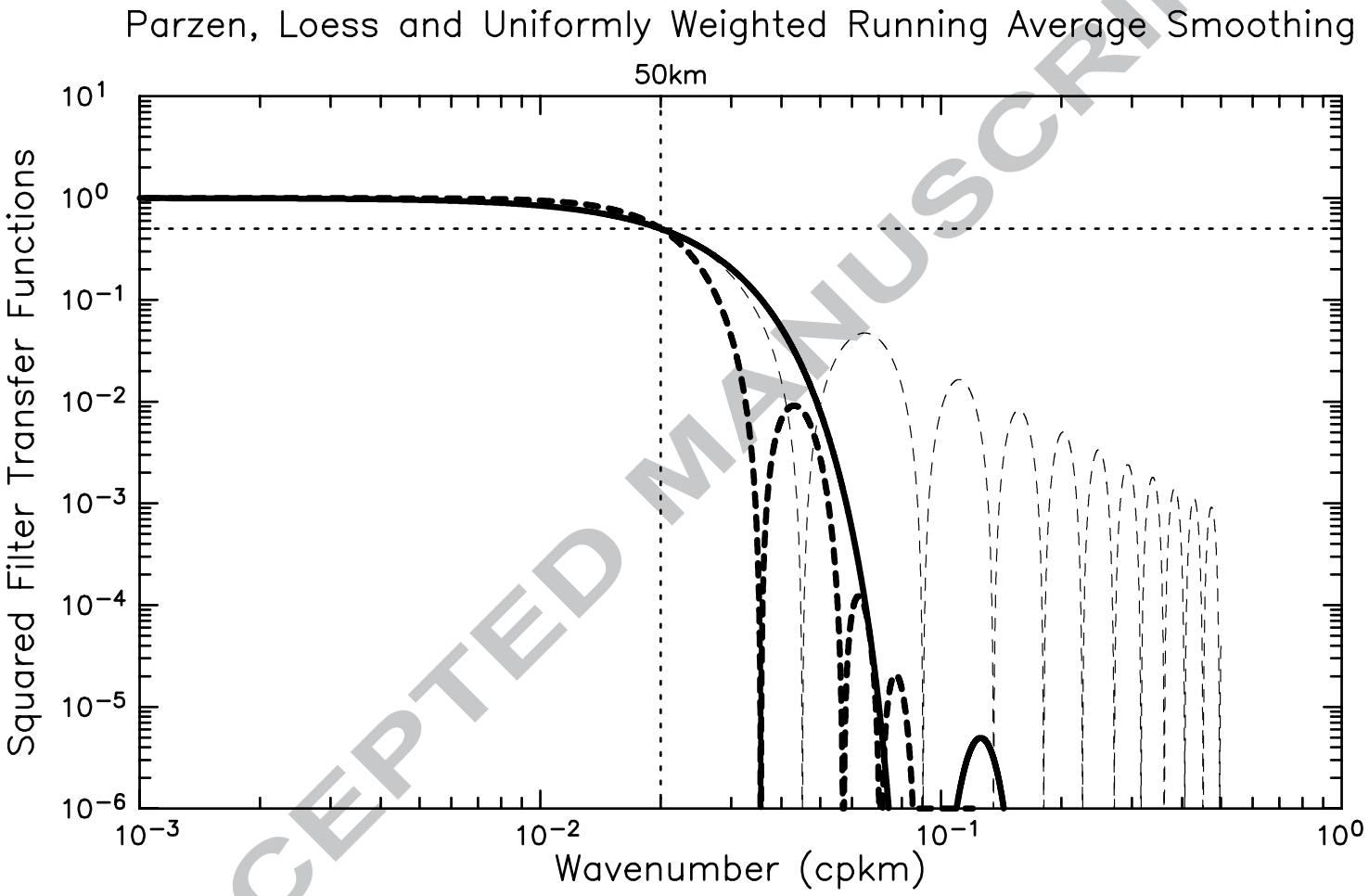

Figure C3. Log-log plots of the squared filter transfer functions with a half-power filter cutoff wavelength of 50 km for the Parzen smoother (thick line, which is the same as the thick line in Fig. C1), the loess smoother (thick dashed line) and the uniformly weighted running average smoother (thin dashed line). The horizontal and vertical dotted lines are the same as in Fig. C2.

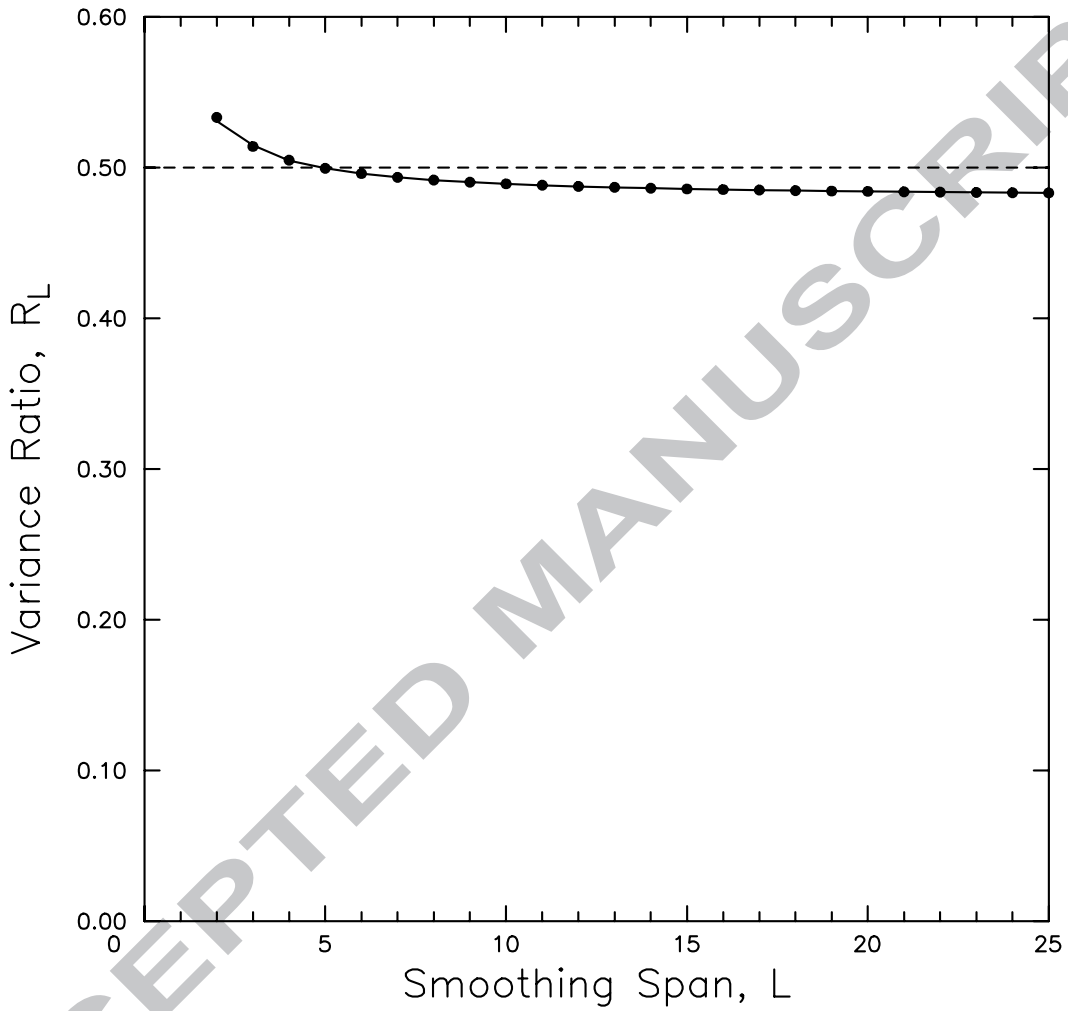

Figure D1. The ratio $R_L = \sigma_4^2/\sigma_1^2$ of the residual variance σ_4^2 after filtering uncorrelated white noise using a Parzen smoother with a span of $L_4 = 4L$ and the residual variance σ_1^2 after filtering with a uniform-weighted running average with a span of $L_1 = L$. The dots correspond to the analytical approximation given by Equation (D.11) and the solid line is the exact solution obtained by numerical integration of Equation (D.8).

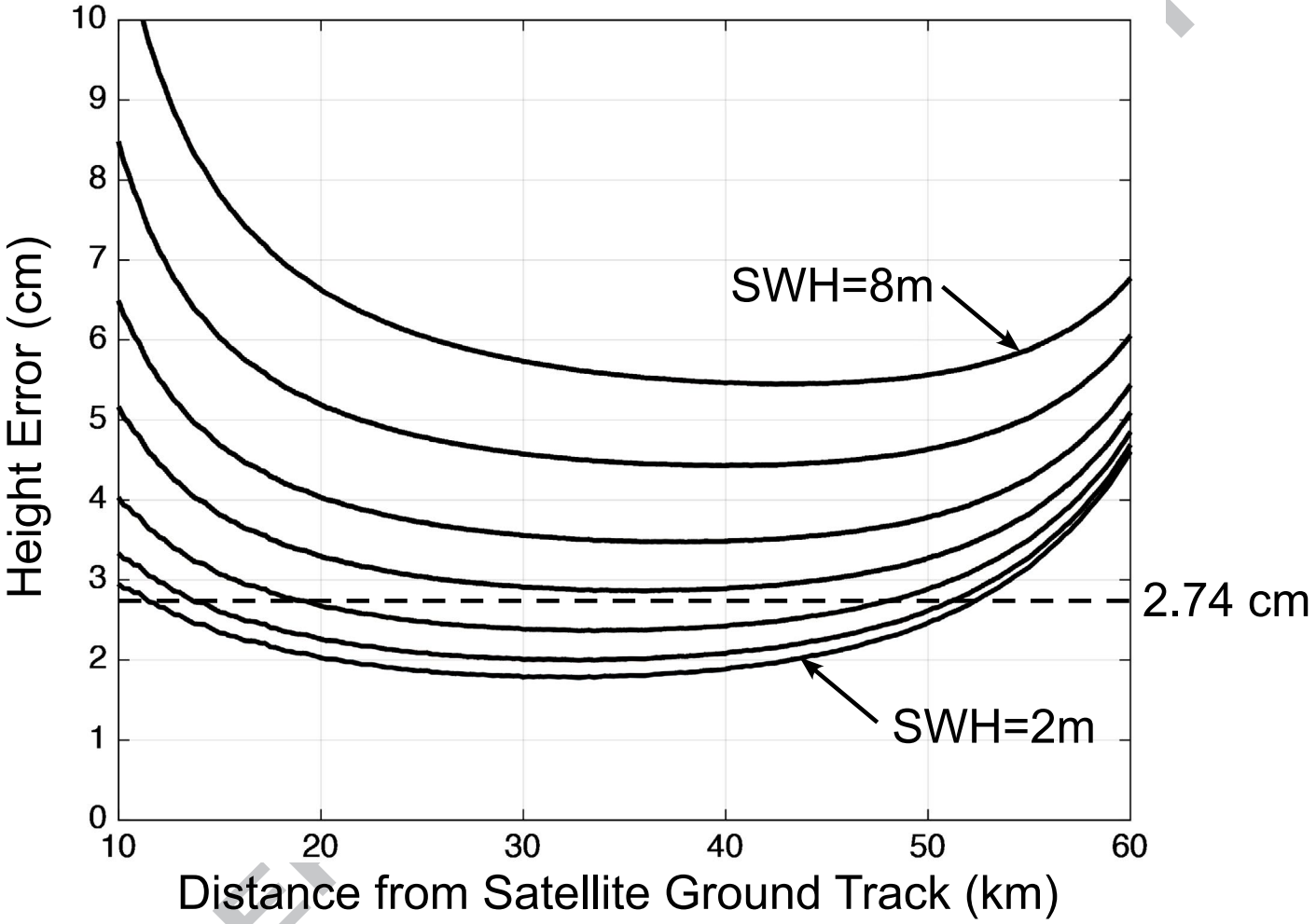

Figure F1. The current projected performance of the SWOT instrument. The graph shows the dependencies of the standard deviation of uncorrelated errors of SWOT measurements of SSH on significant wave height (SWH) and swath location relative to the satellite ground track. The seven solid lines correspond to SWH values increasing from 2 m to 8 m at increments of 1 m (bottom to top). The errors for 0-m SWH are essentially the same as those shown for 2-m SWH. This projected performance incorporates improvements over the baseline science requirements for SWOT. The horizontal dashed line is the estimate of the cross-swath average standard deviation of uncorrelated measurement errors derived in Appendix F from the baseline science requirements. [The solid lines in the figure are from Fig. 2.5 of Gaultier et al. (2017).]

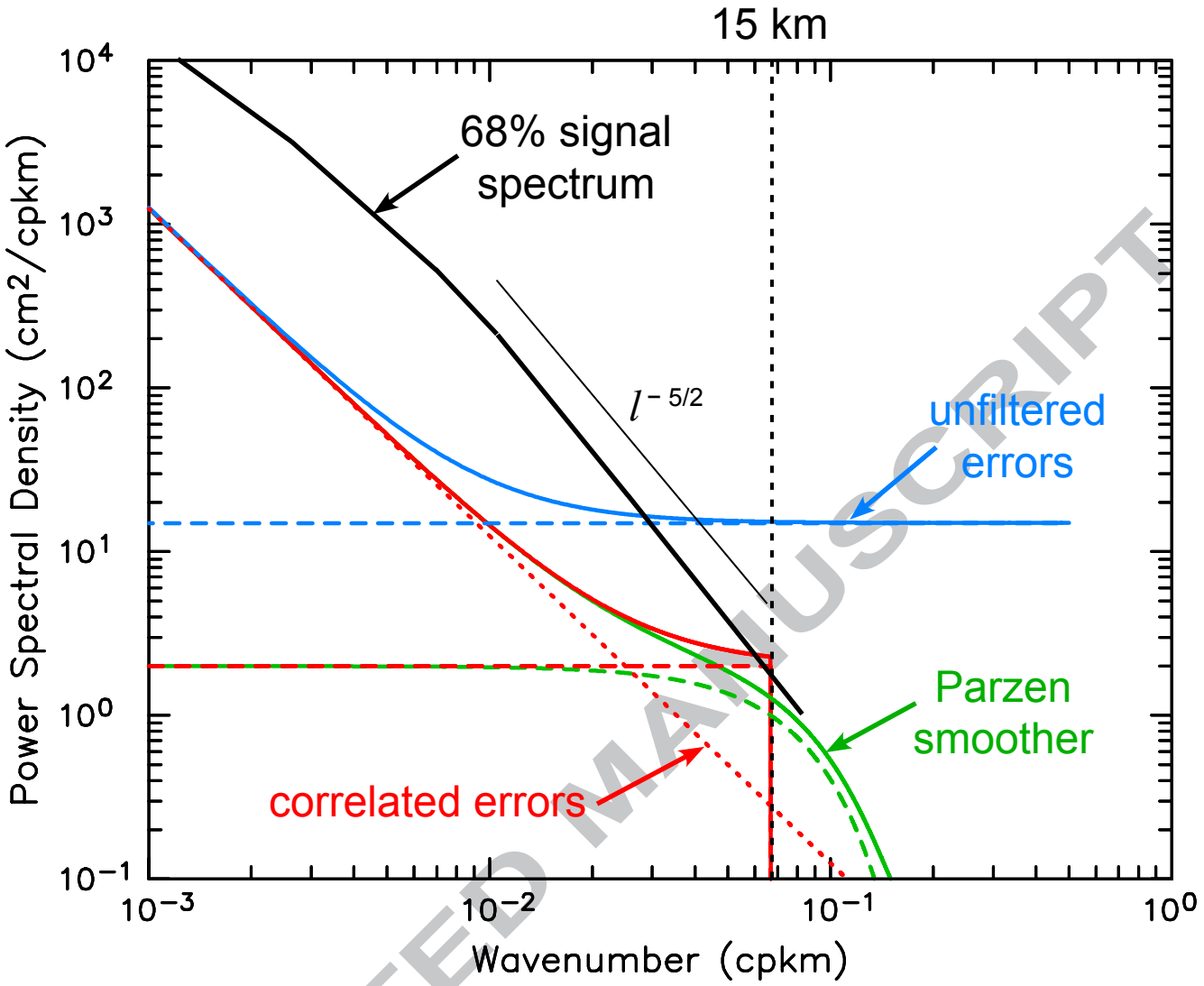

Figure F2. The 1-sided, 1-dimensional wavenumber power spectral density of the science requirements for measurement errors of SWOT data before and after (blue and red lines, respectively) smoothing 2-dimensionally in ground-based post-processing to eliminate variability with wavelengths shorter than a half-power filter cutoff wavelength of $\lambda_c = 15$ km (shown by the black dotted line). The dotted red line corresponds to the requirement for red noise from orbit errors and long-wavelength measurement errors. The dashed red line corresponds to the requirement for residual uncorrelated errors after smoothing with an ideal filter that has a magnitude of 1 for wavelengths longer than λ_c and 0 for shorter wavelengths. The solid red line is the sum of the power spectral densities of the red noise and the ideal low-pass filtered uncorrelated errors. The dashed blue line corresponds to the uncorrelated errors in pre-processed SWOT data for a footprint size of 1 km that is derived in Appendix F without the 15-km smoothing. The integrated variance of this white noise is $\sigma_h^2 = 7.5$ cm^2, which corresponds to a noise standard deviation of $\sigma_h = 2.74$ cm. The solid blue line is the sum of the power spectral densities of the red noise and the white noise in the pre-processed SWOT data. The thick black line is the 68$^{\text{th}}$-percentile SSH signal power spectral density from the SWOT Science Requirements Document (Rodriguez and Callahan, 2016). A power-law rolloff of $l^{-5/2}$ for alongshore wavenumber l is shown for reference as the thin black line. The dashed and solid green lines show, respectively, the spectra of the residual uncorrelated noise and the total noise that would be obtained if the SWOT data were smoothed 2-dimensionally using a realizable Parzen smoother with a half-power filter cutoff wavelength of $\lambda_c = 15$ km.

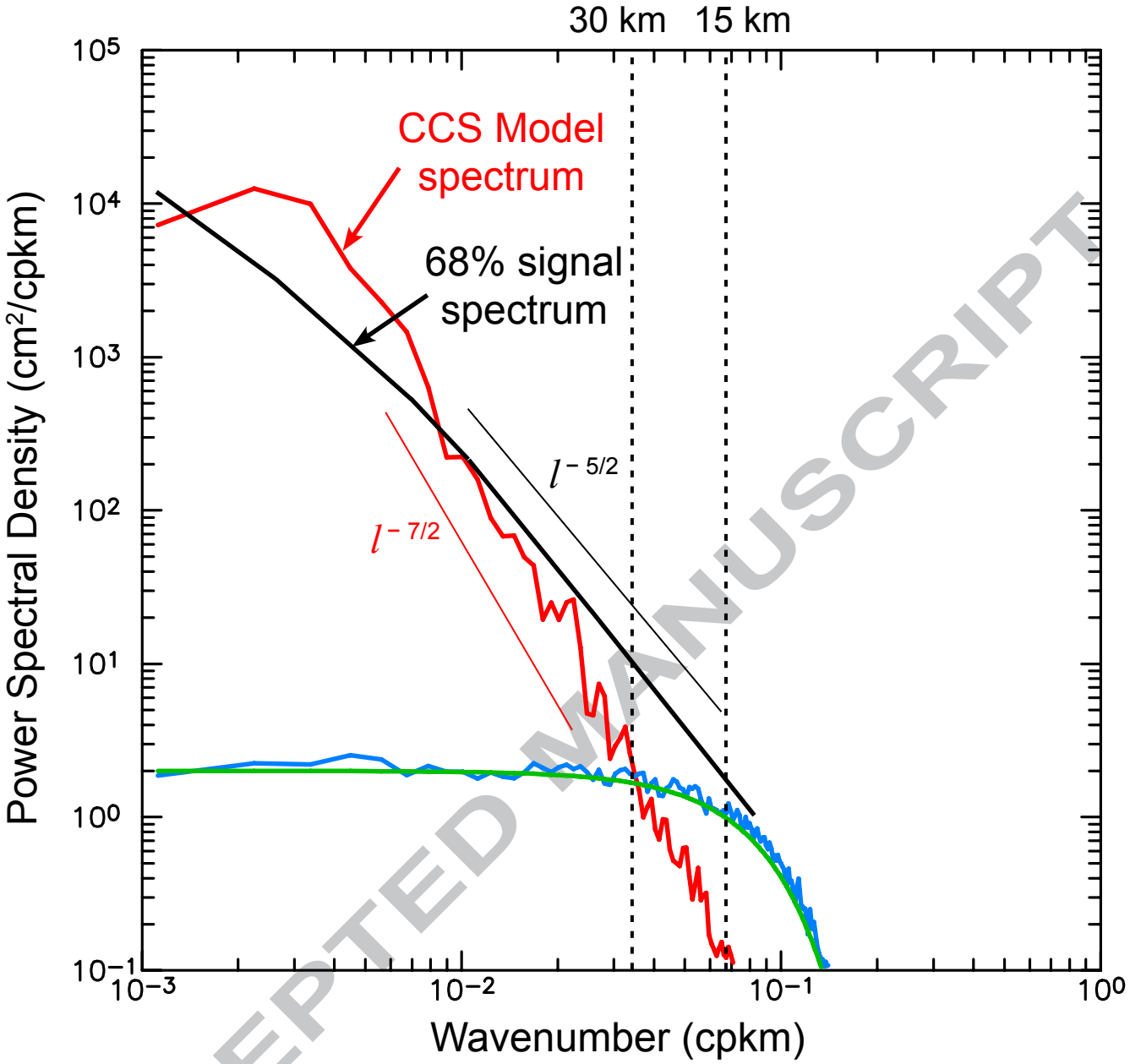

Figure F3. The alongshore wavenumber power spectral density of SSH computed from the CCS model. The spectrum shown by the red line was smoothed by ensemble averaging over the individual spectra computed from alongshore grid lines that extend the full length of the model domain shown in Fig. 5a with a cross-shore spacing of 5 km. The blue line is the spectrum computed empirically from simulated SSH error fields with a footprint size of 1 km and a standard deviation of $\sigma_h = 2.74$ cm after smoothing 2-dimensionally using a Parzen smoother with a half-power filter cutoff wavelength of $\lambda_c = 15$ km. The green line is the theoretical spectrum of SSH errors derived in Appendix I.1 for the same filtering. The black line is the 68$^{\text{th}}$-percentile SSH spectrum from Fig. F2 that is the basis for defining the science requirements for SWOT. Power-law rolloffs of $l^{-5/2}$ and $l^{-7/2}$ for alongshore wavenumber l are overlaid for reference as thin lines. As noted in the caption for Fig. 13, the rolloff of $l^{-7/2}$ is not significantly different from the rolloff of $l^{-11/3}$ that was deduced from along-track altimeter data by Le Traon et al. (2008) and is consistent with the $l^{-5/3}$ spectral rolloff of velocity in SQG theory (Held et al., 1995).

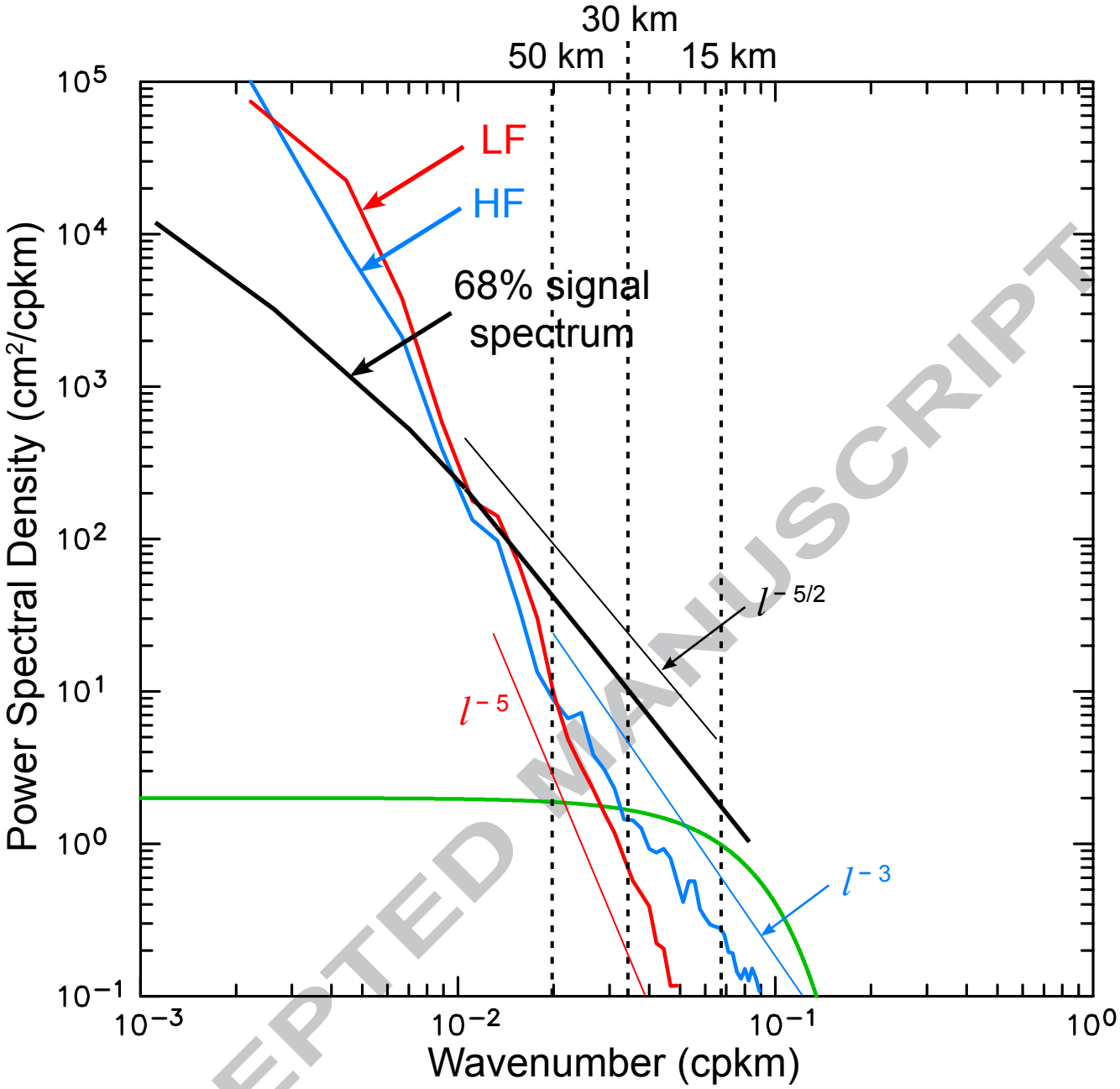

Figure F4. The wavenumber power spectral densities of SSH computed from the boxed region of the North Atlantic HF and LF simulations shown in Fig. 10 (blue and red lines, respectively). The spectra were smoothed by ensemble averaging over the individual spectra computed from "cross-shore" grid lines (southeast to northwest) over the region shown by the boxes in Fig. 10. The thick black line is the 68$^{\text{th}}$-percentile SSH spectrum from Figs. F2 and F3 that defines the science requirements for SWOT and the green line is the theoretical spectrum of SSH errors derived in Appendix I.1 and shown previously in Fig. F3 after smoothing 2-dimensionally using a Parzen smoother with a half-power filter cutoff wavelength of $\lambda_c = 15$ km. Power-law rolloffs of l^{-5}, l^{-3} and $l^{-5/2}$ for wavenumber l are overlaid for reference as thin lines.

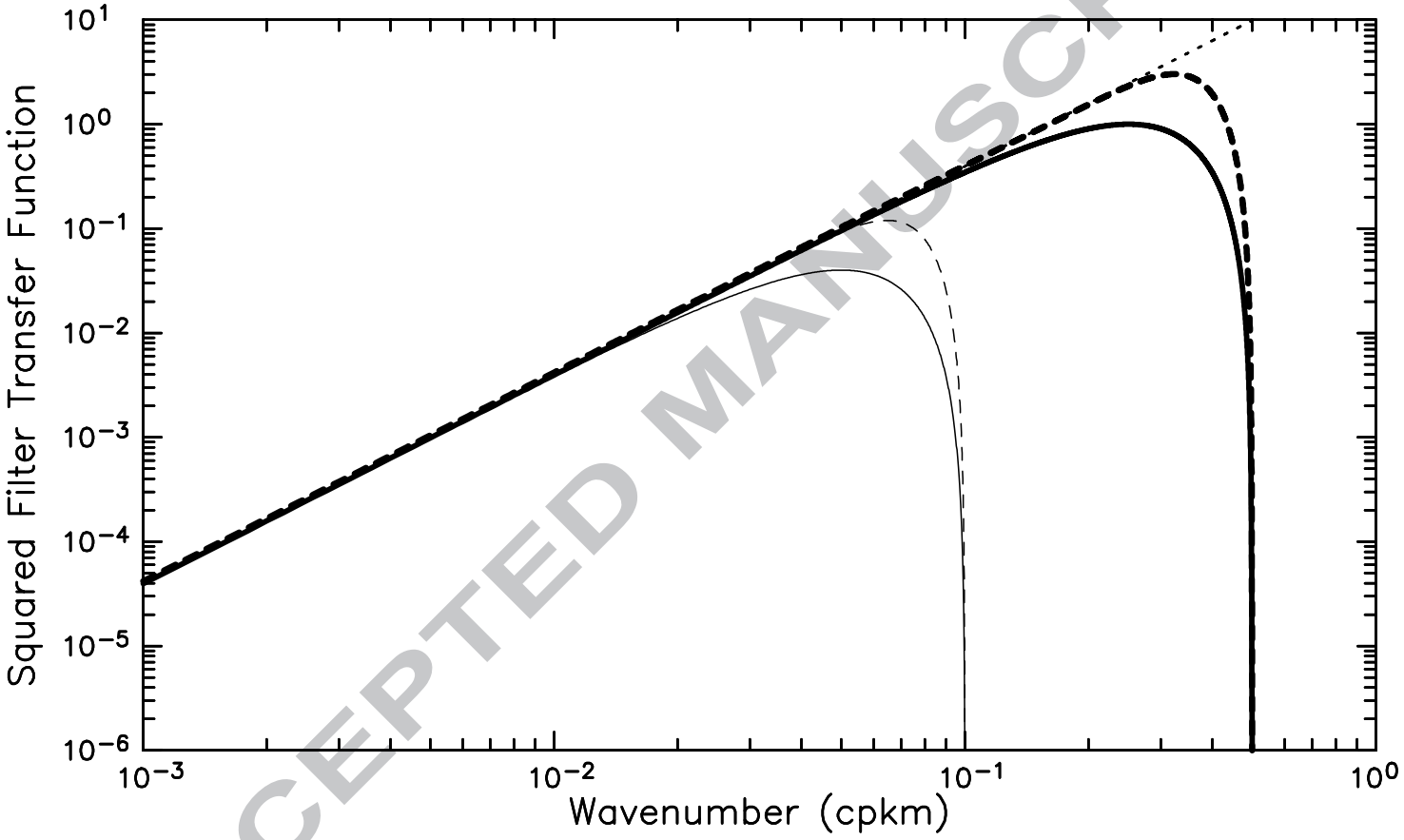

Figure H1. Log-log plots of the squared filter transfer functions (also referred to as the response functions) for centered differences. The thick solid and dashed lines are for, respectively, 3-point and 9-point centered differences on a 1 km grid. The thin solid and dashed lines are for 3-point and 9-point centered differences on a 5 km grid assuming that the discretely sampled data on the 5 km grid have been filtered to attenuate variability at wavenumbers higher than the Nyquist wavenumber of 0.1 cpkm. The short dashed straight line in this log-log plot corresponds to the $(2\pi k)^2$ response function for derivatives of a continuous variable.

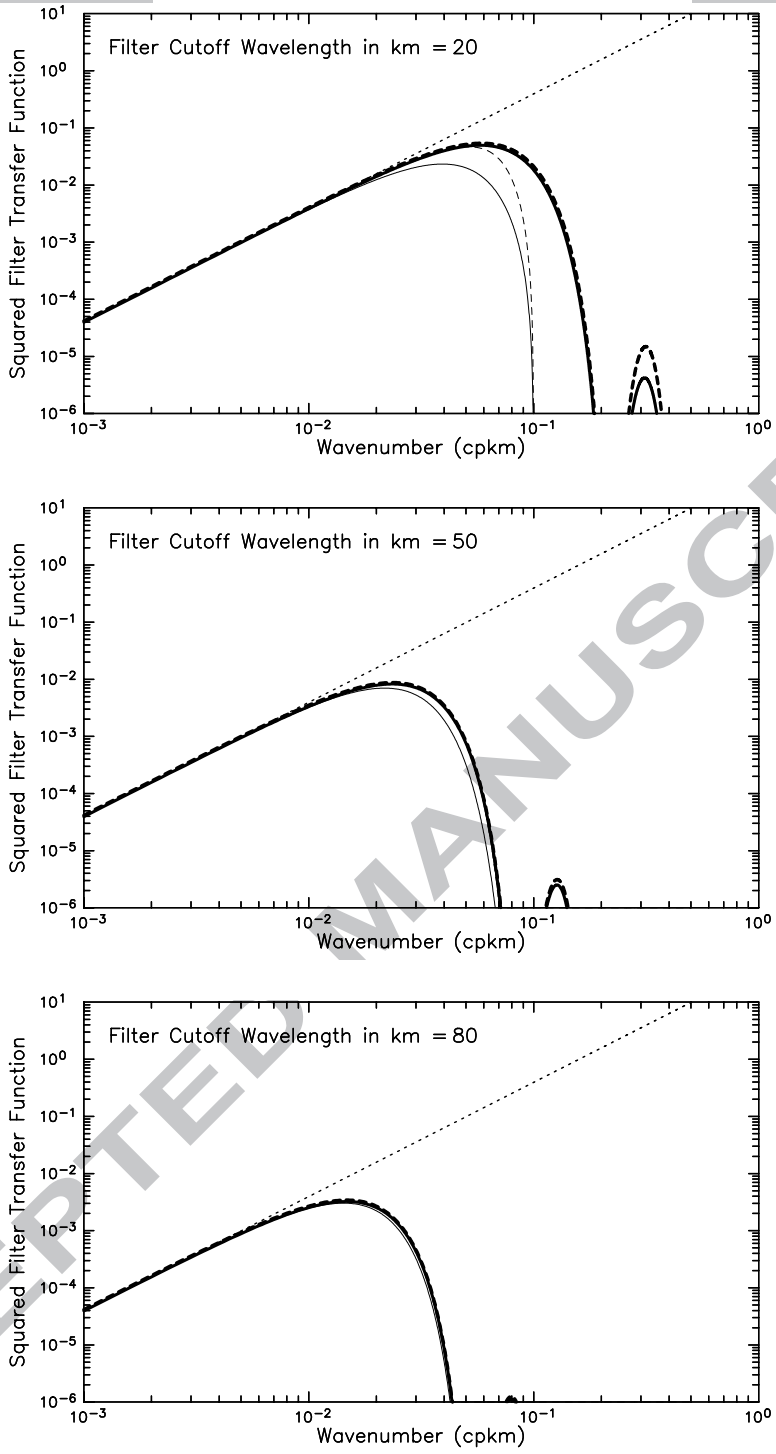

Figure H2. Log-log plots of the filtering from the combined effects of centered differencing and smoothing with a Parzen smoother with half-power filter cutoff wavelengths of $\lambda_c = 20$, 50 and 80 km (top to bottom). This combined filtering consists of the product of the squared filter transfer functions for each operation that are shown in Figs. C1 and H1. The thick solid and dashed lines are for Parzen smoothing of, respectively, 3-point and 9-point centered differences on a 1 km grid. The thin solid and dashed lines are for Parzen smoothing of, respectively, 3-point and 9-point centered differences on a 5 km grid assuming that the discretely sampled data on the 5 km grid have been filtered to attenuate variability at wavenumbers higher than the Nyquist wavenumber of 0.1 cpkm. The thin dashed line becomes indistinguishable from the thick solid and thick dashed lines for smoothing with half-power filter cutoff wavelengths larger than $\lambda_c = 40$ km. All four lines are barely distinguishable for $\lambda_c = 80$ km. The short dashed line corresponds to the $(2\pi k)^2$ response function for derivatives of a continuous variable without smoothing.

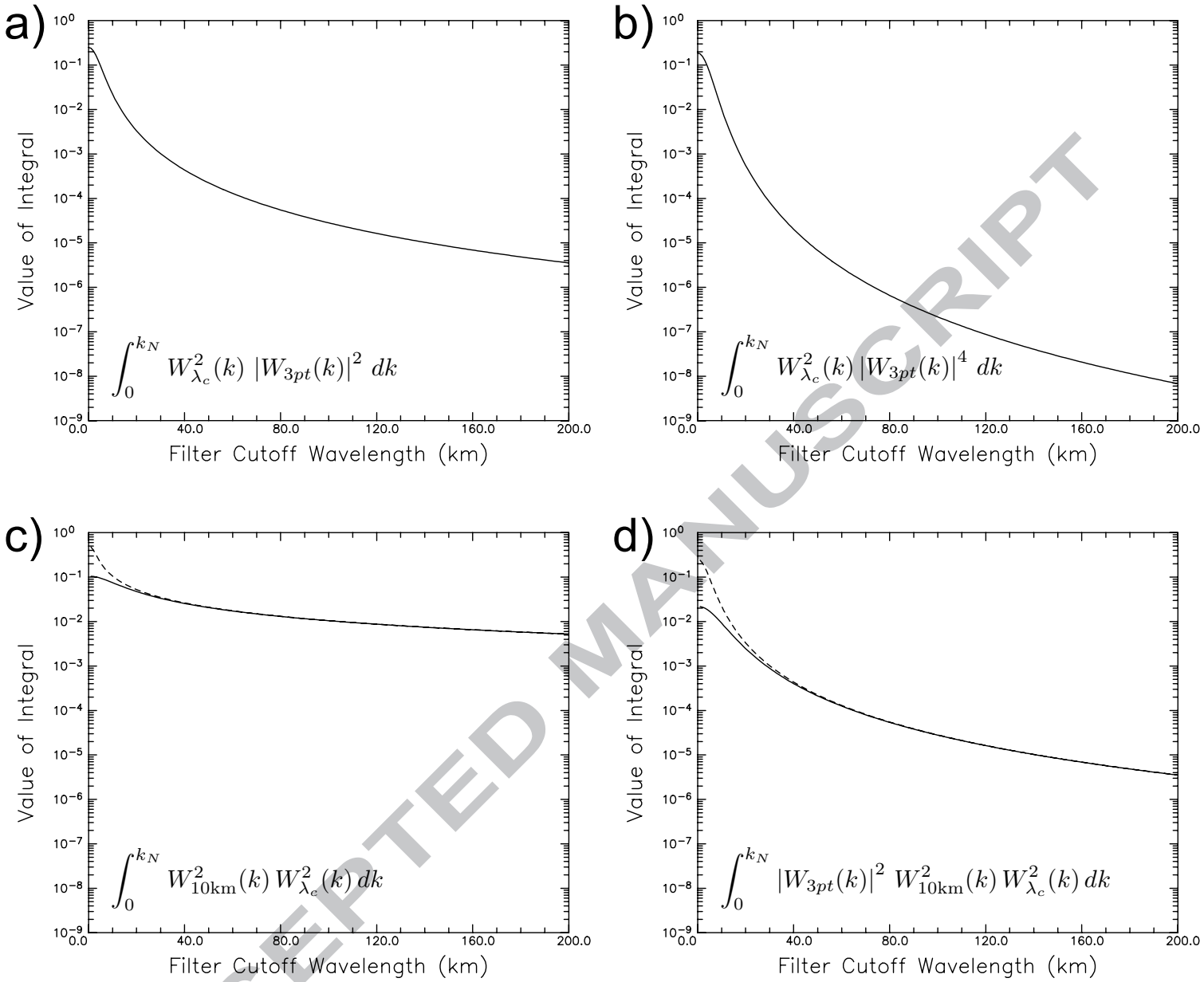

Figure I1. Numerical solutions as functions of half-power filter cutoff wavelength λ_c for the integrals labeled in the lower left corner of each panel that appear in the equations in Appendix I: a) The integral on the right sides of Eqs. (I.33a) and (I.33b), which also appears as the second integral on the right sides of Eqs. (I.35a), (I.35b) and (I.35c) and as the integral on the right side of Eq. (I.46b) with $\lambda_c = 10$ km; b) The first integral on the right sides of Eqs. (I.35a), (I.35b) and (I.35c); c) The integral on the right sides of Eqs. (I.48a) and (I.48b), which also appears as the integral on the right side of Eq. (I.55a) and in the denominator on the right side of Eq. (I.55b); and d) The integral on the right side of (I.55a) and in the numerator on the right side of Eq. (I.55b). The dashed lines in panels c) and d) correspond to the approximate solutions obtained by replacing the term $W^2_{10\mathrm{km}}(k)$ in the integrands with a value of 1 for all wavenumbers k, as in Eqs. (I.49) and (I.56), respectively.